

Bioimpedance spectroscopy methods for analysis and control of neurostimulation dose

by

Herschel Binyomin Caytak

Thesis submitted to the
Faculty of Graduate and Postdoctoral Studies
In partial fulfillment of the requirements
For the Ph.D. degree in
Electrical and Computer Engineering

School of Electrical Engineering and Computer Science
Faculty of Engineering
University of Ottawa

© Herschel Binyomin Caytak, Ottawa, Canada, 2018

Abstract

TDCS is a form of non-invasive neurostimulation that is comprised of injection of current via strategically placed scalp electrodes into targeted areas of the brain. TDCS has shown therapeutic benefit for numerous clinical applications. This technique has not however been widely adopted due to high variability of response to the stimulation. Current state of the art methods for optimizing tDCS are based on FEM models that generally model tissue as isotropic and homogeneous and do not take into account inter subject variability of head tissue electrical properties. We therefore develop an in-vivo method of measuring and analyzing bioimpedance spectroscopy measurements of the head to estimate change to tDCS dose in neural tissues for different subjects.

Finite element simulations are implemented on a realistic MRI derived head model. 5% random Gaussian noise is added. Experimental bioimpedance measurements are taken of the heads of 8 subjects. We simulate sensitivity distribution and impedance for a variety of 2 and 4 electrode configurations over a wide frequency range. We also extract Cole parameters and implement PCA on simulated and experimental impedance.

We demonstrate that the Cole model of the head can be accurately approximated by the sum in series of Cole systems of each tissue. Comparison of Cole parameters from various simulated electrode configurations show statistical differences (paired t test $p < .05$). PCA shows that close to 100% of the variance between two impedance spectra is described along a single principal component. Variation described by the second principal component increases as a function of increasing inter electrode gap which may be related to changes in dose. FEM and experimentally derived Cole parameters show different trends for various electrode configurations, good agreement is however shown for the PCA results.

The outcome of this research may lead to a higher tDCS efficacy by improving standardization and control of stimulation by relation of dose and bioimpedance spectra characteristics.

Acknowledgements

I would like to thank my supervisors, Prof. Miodrag Bolic and Prof. Andrew Adler, for all their help, resources, including lab and equipment use, and encouragement I received while working on this thesis. I want to express my gratitude to Dr. Izmail Batkin and Dr. Daniel Shapiro for their invaluable advice and mentorship. I would like to acknowledge all the assistance I received from Dr. Isar Nejadgholi especially in regards to PCA and Cole analysis. I would also like to thank Dr. Abeye Mekonnen for helping me with the FEM head model.

I want to especially thank my parents, Dr. Joseph and Devora Caytak, for all their support during the course of my research. Last but not least I want to mention my gratitude to my wife Aliza and my children, who have patiently encouraged me during my long years of study.

Table of Contents

List of Tables	xii
List of Figures	xiv
I Introduction	1
1 Thesis Motivation, Goals and Outline	2
1.1 Research Motivation	2
1.2 Research Goals and Objectives	4
1.2.1 Objective 1	7
1.2.2 Objective 2	8
1.2.3 Objective 3	9
1.2.4 Objective 4	10
1.2.5 Objective 5	10
1.2.6 Objective 6	11
1.3 Thesis Outline	12
1.4 Publications	14

II	Literature Review	16
2	Literature Review	17
2.1	TDCS dose optimization methods	17
2.2	TDCS Background	17
2.2.1	TDCS effect on cortical excitation	18
2.2.2	Proposed mechanisms of action	20
2.3	FEM based optimization methods	22
2.3.1	Electric field optimization	24
2.3.1.1	Genetic Algorithms	24
2.3.1.2	Multi-Electrode Arrays and Linear Superposition	26
2.3.1.3	Interior Point Optimization Method	27
2.3.2	Reciprocity approach	28
2.3.3	Experimental Validation of Reciprocity Principle	31
2.3.4	Reciprocity vs. Error Fitting Algorithms	32
2.4	Summary	33
III	FEM Modelling	34
3	FEM Model Description	35
3.1	Model Description	35
3.2	Summary	36
4	Simulation of Bioimpedance Spectroscopy Measurements	40
4.1	Electrode montages	40

4.1.1	Bipolar Electrode montages	40
4.1.2	Tetrapolar Electrode montages	42
4.2	Region of Interest Setup	44
4.2.1	Cortical grey matter ROI	44
4.2.2	Sub-Cortical white matter ROI	45
4.2.3	Whole Brain	47
4.3	Spherical Coordinates	47
4.4	Boundary conditions	50
4.5	Material Properties and Frequency Range	51
4.6	Probe setup and Simulated Noise	53
4.7	Simulated noise	54
4.8	Calculated Dose and Measurement Parameters	55
4.8.1	Electric Field	55
4.8.2	Current Density	56
4.8.3	Sensitivity and Impedance	57
4.8.4	Focality	59
4.9	Summary	60
5	Solver configuration	61
5.1	Solver Types	62
5.1.1	Linear Solvers	62
5.1.2	Jacobi and Gauss-Seidel Iterative Solvers	63
5.1.3	Biconjugate Gradient Solvers	64

5.2	Solver configuration used for FEM Simulations	66
5.2.1	Generalized Minimal Residual Method Solver	66
5.2.2	Nested Generalized Minimal Residual Method and Multigrid Solver Configuration	67
5.3	Summary	69
6	Multi-frequency Sensitivity Field Simulations	71
6.1	Two electrode configuration	74
6.1.1	Head Tissue Sensitivity	74
6.1.1.1	Scalp	80
6.1.1.2	Skull	82
6.1.1.3	CSF	83
6.1.1.4	GM	84
6.1.1.5	GM ROI	85
6.1.1.6	WM	86
6.1.1.7	WM ROI	87
6.1.1.8	Eye Matter	87
6.1.1.9	Log-Log Plots of Head Tissue Sensitivity	88
6.1.2	Sensitivity vs. Dose and Measurement Parameters	92
6.1.2.1	Sensitivity vs Current Density	93
6.1.2.2	Sensitivity vs Electric Field	95
6.1.3	Focality	97
6.1.4	Discussion	99

6.2	Four electrode configuration	103
6.2.1	Head Tissue Sensitivity	103
6.2.1.1	Scalp	104
6.2.1.2	Skull	107
6.2.1.3	CSF	108
6.2.1.4	GM	109
6.2.1.5	GM ROI	110
6.2.1.6	WM	110
6.2.1.7	WM ROI	111
6.2.1.8	Eye Matter	112
6.2.1.9	All Head Tissues	112
6.2.2	Sensitivity vs. Dose and Measurement Parameters	115
6.2.2.1	Sensitivity vs Current Density	115
6.2.2.2	Sensitivity vs Electric Field	116
6.2.3	Focality	118
6.2.4	Discussion	120
6.3	Summary	122
7	Multi-frequency Transfer Impedance Simulations	124
7.1	Relationship between Transfer Impedance, and Sensitivity	124
7.2	Head Tissue Impedance	126
7.2.1	Two Electrode Configuration	126
7.2.1.1	Discussion	129

7.2.2	Four Electrode Configuration	131
7.2.2.1	Discussion	133
7.3	Summary	134
8	Cole model and Principal Component Analysis	136
8.1	Head Tissue Cole Model	136
8.2	Two electrode configuration	137
8.2.1	Nyquist plots	138
8.2.2	Cole parameters	144
8.2.2.1	Cole Parameter fitting and extraction	144
8.2.2.2	Cole Parameter Comparison	149
8.2.3	Principal component analysis	149
8.2.3.1	PCA parameters	156
8.2.4	Discussion	161
8.3	Four electrode configuration	166
8.3.1	Nyquist Plots	166
8.3.1.1	Cole parameters	173
8.3.2	Principal component analysis	179
8.3.3	Discussion	182
8.4	Summary	186
IV	Experimental study	187
9	In-Vivo Experiments	188
9.1	Study Research Goals	188

9.2	Instrumentation	189
9.2.1	Experimental Configuration	189
9.2.2	Calibration	191
9.3	Study Description	193
9.3.1	Study recruitment	193
9.3.2	Procedure	194
9.4	Data Analysis	196
9.4.0.1	Experimental Cole fitting	196
9.5	Results	197
9.5.1	Individual Subjects	197
9.5.1.1	Bode Plots	197
9.5.1.2	Discussion	202
9.5.1.3	Cole Plots and Parameters	205
9.5.2	Across Subject Mean	224
9.5.2.1	Bode Plots	225
9.5.2.2	Bode Plots Features and Outliers	228
9.5.2.3	Cole Plots and Parameters	229
9.5.2.4	PCA parameters of experimental spectra	232
9.5.3	Discussion	234
9.6	Summary	239
10	Comparison of FEM and Experimental Results	240
10.1	Comparison of Nyquist plots and Cole Parameters	243

10.2 Comparison of PCA parameters	247
10.3 Discussion	250
10.4 Summary	255
11 Conclusions	257
11.1 Discussion	257
11.1.1 Objective 1 Results	257
11.1.2 Objective 2 Results	259
11.1.3 Objective 3 Results	261
11.1.4 Objective 4 Results	262
11.1.5 Objective 5 Results	264
11.1.6 Objective 6 Results	264
11.2 Conclusions and Future Work	265
11.2.1 Limitations and Future Work	266
11.3 Summary of Contributions	271
Appendices	273
A Ethics clearance	274

List of Tables

3.1	Description of Model Components/Tissues	37
4.1	List of ROI and electrode Cartesian and spherical coordinates	50
5.1	Solver performance details	69
6.1	Coefficient and p-values of correlation of head tissue sensitivity and current density	95
6.2	Coefficient and p-values of correlation of head tissue sensitivity and electric field.	96
6.3	Coefficient and p-values of correlation of head tissue sensitivity and current density for the C3-C1-CZ-C2 montage.	116
6.4	Coefficient and p-values of correlation of head tissue sensitivity and electric field for the C3-C1-CZ-C2 montage.	117
8.1	P-values showing statistical significance for differences between α Cole parameters. α significance level is Bonferroni corrected for $n = 6$ pairwise comparisons.	151
8.2	P-values showing statistical significance for differences between β Cole parameters. α significance level is Bonferroni corrected for $n = 6$ pairwise comparisons.	152

8.3	P-values showing statistical significance for differences between γ Cole parameters. α significance level is Bonferroni corrected for $n = 6$ pairwise comparisons.	153
8.4	P-values showing statistical significance for differences between α Cole parameters. α significance level is Bonferroni corrected to $n = 3$ pairwise comparisons.	175
8.5	P-values showing statistical significance for differences between β Cole parameters. α significance level is Bonferroni corrected to $n = 3$ pairwise comparisons.	177
8.6	P-values showing statistical significance for differences between γ Cole parameters. α significance level is Bonferroni corrected to $n = 3$ pairwise comparisons.	178
10.1	Correlation coefficients and p-values for FEM and experimental real and imaginary impedance.	242

List of Figures

3.1	View of the head model in 3D Cartesian Space (units [mm]). Electrodes C2 and CZ are shown to the right of and at the scalp vertex. Locations of other electrodes are indicated by circles on the scalp.	38
3.2	Sub-figures (a)-(f) show the principal tissues/components of the head model	39
4.1	Plane view of four electrode montages used for 2 electrode simulations. The head model is oriented such that the nasion is shown at the top of the figure. Each electrode pair is shown highlighted. CZ-T7 (c) is shown tilted in order to clearly show temporal electrode T7. Electrode spacing is increased from (a) CZ-C1 to (d) T7-T8 (electrodes shown on the temporal sides of the head).	41
4.2	Illustration of electrode montages used for 4 electrode simulations. Each electrode part of the montage is shown highlighted. Electrode spacing is increased from (a) C3-CZ-C1-C2 (electrodes all adjacent) to (b) T7-C3-CZ-C2 (gap increased between voltage electrode pair C3-CZ and current-voltage pair T7-C3) to (c) T7 C3 C4 T8 (large gap between current pair C3-C4, and gap between voltage pairs T8-C4 and T7-C3) (electrodes shown on the temporal sides of the head).	43
4.3	View of the grey matter cortical ROI positioned under the CZ electrode coordinate.	45
4.4	View of the white matter cortical ROI positioned under the Cz electrode coordinate.	46

4.5	Transparent image of the brain showing the structure of the grey and white matter.	48
4.6	\vec{r} , representing electrode and ROI location, can be defined by radial distance r , inclination angle, θ and azimuthal angle ϕ	48
5.1	Convergence graphs of the V Multigrid algorithm nested in the GMRES iterative solver.	70
6.1	Sagittal plane view of sensitivity field from the CZ-C1 montage. Model is oriented such that the face is facing forward. Plots are shown in the mm scale with units as $[1/mm^4]$. Sensitivity is shown with a maximum scale of 10^{-7} . Sensitivity distributions are shown for 4 frequencies (a) 1 Hz, (b) 1 KHz, (c) 100 KHz, (d) 1 MHz.	75
6.2	Sagittal plane view of sensitivity field from the CZ-C3 montage. Model is oriented such that the face is facing forward. Plots are shown in the mm scale with units as $[1/mm^4]$. Sensitivity is shown with a maximum scale of 10^{-7} . Sensitivity distributions are shown for 4 frequencies (a) 1 Hz, (b) 1 KHz, (c) 100 KHz, (d) 1 MHz.	76
6.3	Sagittal plane view of sensitivity field from the CZ-T7 montage. Model is oriented such that the face is facing forward. Plots are shown in the mm scale with units as $[1/mm^4]$. Sensitivity is shown with a maximum scale of 10^{-7} . Sensitivity distributions are shown for 4 frequencies (a) 1 Hz, (b) 1 KHz, (c) 100 KHz, (d) 1 MHz.	78

6.4	Sagittal plane view of sensitivity field from the T7-T8 montage. Model is oriented such that the face is facing forward. Plots are shown in the mm scale with units as $[1/mm^4]$. Sensitivity is shown with a maximum scale of 10^{-7} . Sensitivity distributions are shown for 4 frequencies (a) 1 Hz, (b) 1 KHz, (c) 100 KHz, (d) 1 MHz.	79
6.5	Mean sensitivity integrated across the scalp domain for all electrode montages, (a) without error bars and (b) with error bars (SEM).	81
6.6	Mean sensitivity integrated across the skull domain for all electrode montages.	82
6.7	Mean sensitivity integrated across the CSF domain for all electrode montages.	83
6.8	Mean sensitivity integrated across the GM domain for all electrode montages.	84
6.9	Mean sensitivity integrated across the GM ROI domain for all electrode montages.	85
6.10	Mean sensitivity integrated across the WM domain for all electrode montages.	86
6.11	Mean sensitivity integrated across the WM ROI domain for all electrode montages.	87
6.12	Mean sensitivity integrated across the eye domain (optical nerves and eye sockets) for all electrode montages.	88
6.13	Log-Log graph of CZ-C1 head tissues sensitivity vs frequency with error bars (SEM).	89
6.14	Log-Log graph of CZ-C3 head tissues sensitivity vs frequency with error bars	90
6.15	Log-Log graph of CZ-T7 head tissues sensitivity vs frequency with error bars.	90
6.16	Log-Log graph of T7-T8 head tissues sensitivity vs frequency with error bars.	91
6.17	Log-Log graph of CZ-C1 head tissues current density vs frequency with error bars (SEM).	93

6.18	Log-Log graph of CZ-C1 head tissues electric field vs. frequency.	95
6.19	GM_{ROI} focality of all electrode montages vs. frequency.	97
6.20	WM_{ROI} focality of all electrode montages vs. frequency.	98
6.21	Brain focality of all electrode montages vs. frequency.	99
6.22	Sagittal plane view of sensitivity field from the C3-C1-CZ-C2 montage. Model is oriented such that the face is facing forward. Plots are shown in the mm scale with units as $[1/mm^4]$. Sensitivity is shown with a maximum scale of 10^{-7} . Sensitivity distributions are shown for 4 frequencies (a) 1 Hz, (b) 1 KHz, (c) 100 KHz, (d) 1 MHz.	103
6.23	Sagittal plane view of sensitivity field from the T7-C3-CZ-C2 montage. Model is oriented such that the face is facing forward. Plots are shown in the mm scale with units as $[1/mm^4]$. Sensitivity is shown with a maximum scale of 10^{-7} . Sensitivity distributions are shown for 4 frequencies (a) 1 Hz, (b) 1 KHz, (c) 100 KHz, (d) 1 MHz.	105
6.24	Sagittal plane view of sensitivity field from the T7-C3-C4-T8 montage. Model is oriented such that the face is facing forward. Plots are shown in the mm scale with units as $[1/mm^4]$. Sensitivity is shown with a maximum scale of 10^{-7} . Sensitivity distributions are shown for 4 frequencies (a) 1 Hz, (b) 1 KHz, (c) 100 KHz, (d) 1 MHz.	106
6.25	Mean scalp sensitivity vs. frequency for all electrode montages.	107
6.26	Mean skull sensitivity vs. frequency for all electrode montages	108
6.27	Mean CSF sensitivity vs. frequency for all electrode montages.	108
6.28	Mean grey matter sensitivity vs. frequency for all electrode montages.	109
6.29	Mean grey matter ROI sensitivity vs. frequency for all electrode montages.	110
6.30	Mean white matter sensitivity vs. frequency for all electrode montages	111

6.31	Mean white matter ROI sensitivity vs. frequency for all electrode montages.	111
6.32	Mean eye sensitivity vs. frequency for all electrode montages.	112
6.33	Log-Log graph of C3-C1-CZ-C2 head tissues sensitivity vs frequency with error bars (SEM).	113
6.34	Log-Log graph of T7-C3-CZ-C2 head tissues sensitivity vs frequency with error bars (SEM)	114
6.35	Log-Log graph of T7-C3-C4-T8 head tissues sensitivity vs frequency with error bars (SEM).	114
6.36	Log-Log graph of C3-C1-CZ-C2 head tissue current density vs frequency with error bars (SEM).	115
6.37	Log-Log graph of C3-C1-CZ-C2 head tissue current density vs frequency with error bars (SEM).	117
6.38	GM_{ROI} focality of all electrode montages vs. frequency.	118
6.39	WM_{ROI} focality of all electrode montages vs. frequency	119
6.40	Brain focality of all electrode montages vs. frequency.	119
7.1	Log-Log graph of CZ-C1 head tissue impedance vs. frequency.	126
7.2	Log-Log graph of CZ-C3 head tissue impedance vs. frequency.	127
7.3	Log-Log graph of CZ-T7 head tissue impedance vs. frequency.	128
7.4	Log-Log graph of T7-T8 head tissue impedance vs. frequency.	129
7.5	Log-Log graph of C3-C1-CZ-C2 head tissue impedance vs. frequency.	131
7.6	Log-Log graph of T7-C3-CZ-C2 head tissue impedance vs. frequency.	132
7.7	Log-Log graph of T7-C3-C4-T8 head tissue impedance vs. frequency.	132
8.1	Nyquist plot of total and added real and imaginary impedance.	138

8.2	Total Nyquist plots for all electrode montages. Mean values with error bars are shown.	139
8.3	Nyquist plot of scalp for all electrode montages. Mean values with error bars are shown.	140
8.4	Skull Nyquist plots for all electrode montages. Mean values with error bars are shown.	141
8.5	CSF Nyquist plots for all electrode montages. Mean values with error bars are shown.	141
8.6	GM Nyquist plots for all electrode montages. Mean values with error bars are shown.	142
8.7	WM Nyquist plots for all electrode montages. Mean values with error bars are shown.	143
8.8	Eye tissue Nyquist plots for all electrode montages. Mean values with error bars are shown.	143
8.9	Cole plots shown for all bipolar electrode montages. The first, second and third semi circle represent the α , β and γ frequency distributions respectively. Markers show the locations of fitted Cole parameters (R_0 , f_c and R_∞). . . .	148
8.10	Bar graphs showing mean Cole parameters of 2 electrode configurations for the α dispersion. Comparisons between mean values is made with a paired t test. Significance level is shown by number of stars.	150
8.11	Bar graphs showing mean Cole parameters of 2 electrode configurations for the β dispersion. Comparisons between mean values is made with a paired t test. Significance level is shown by number of stars.	150

8.12	Bar graphs showing mean Cole parameters of 2 electrode configurations for the γ dispersion. Comparisons between mean values is made with a paired t test. Significance level is shown by number of stars.	154
8.13	Principal components, scores and coefficients shown of real and imaginary components of electrode montages CZ-C1 and CZ-C3.	157
8.14	Percent of total variance of first and second principal components of real and imaginary components, shown for electrode montages CZ-C1 and CZ-C3. . .	158
8.15	Principal components, scores and coefficients shown of real and imaginary components of electrode montages CZ-C1 and CZ-T7.	159
8.16	Percent of total variance of first and second principal components of real and imaginary components. Shown for electrode montages CZ-C1 and CZ-T7 . .	160
8.17	Principal components, scores and coefficients shown of real and imaginary components of electrode montages CZ-C1 and T7-T8.	160
8.18	Percent of total variance of first and second principal components of real and imaginary components, shown for electrode montages CZ-C1 and T7-T8. . .	161
8.19	Nyquist plot of Total and Added real and imaginary impedance.	167
8.20	Total Nyquist plots for all electrode montages. Mean values with error bars are shown.	168
8.21	Nyquist plot of scalp for all electrode montages. Mean values with error bars are shown.	169
8.22	Skull Nyquist plots for all electrode montages. Mean values with error bars are shown.	170
8.23	CSF Nyquist plots for all electrode montages. Mean values with error bars are shown.	171

8.24 GM Nyquist plots for all electrode montages. Mean values with error bars are shown.	171
8.25 WM Nyquist plots for all electrode montages. Mean values with error bars are shown.	172
8.26 Eye tissue Nyquist plots for all electrode montages. Mean values with error bars are shown.	172
8.27 Cole plots shown for all 3 tetrapolar electrode montages. The first, second and third semi circle represent the α , β and γ frequency distributions respectively. Markers show the locations of fitted Cole parameters (R_0 , F_c and R_∞). . . .	173
8.28 FEM 4 electrode alpha dispersion Cole parameter comparison. Stars show significance level of paired t-tests.	174
8.29 FEM 4 electrode beta dispersion Cole parameter comparison. Stars show significance level of paired t-tests.	176
8.30 FEM 4 electrode beta dispersion Cole parameter comparison. Stars show significance level of paired t-tests.	179
8.31 Principal components, scores and coefficients shown of real and imaginary components of electrode montages C3-C1-CZ-C2 and T7-C1-CZ-C2	180
8.32 Percent of total variance of first and second principal components of real and imaginary components, shown for electrode montages C3-C1-CZ-C2 and T7-C1-CZ-C2.	180
8.33 Principal components, scores and coefficients shown of real and imaginary components of electrode montages C3-C1-CZ-C2 and T7-C3-C4-T8.	181
8.34 Percent of total variance of first and second principal components of real and imaginary components, shown for electrode montages C3-C1-CZ-C2 and T7-C3-C4-T8	182

9.1	Components of the measurement configuration shown, the double head arrows show the communication pathways between the different elements of the frequency sweep experiment.	190
9.2	Bode and Nyquist plot of impedance shown for calibration measurement of the Solatron.	192
9.3	Subject 1 and 2 impedance magnitude vs frequency.	198
9.4	Subject 3 and 4 impedance magnitude vs frequency.	200
9.5	Subject 5 and 6 impedance magnitude vs frequency.	201
9.6	Subject 7 and 8 impedance magnitude vs frequency.	203
9.7	Nyquist plots shown of electrode montages. Cole parameter location of R_0, F_c and R_∞ , shown in the α (red circles) and β range (blue diamonds).	206
9.8	Bar graphs showing mean Cole parameters of 4 electrode configuration measurements obtained from subject 1. Comparisons between mean values is made with a paired t test. Significance level is shown by number of stars. . .	207
9.9	Bar graphs showing mean Cole parameters of 4 electrode configuration measurements obtained from subject 1. Comparisons between mean values is made with a paired t test. Significance level is shown by number of stars. . .	207
9.10	Nyquist plots shown of electrode montages. Cole parameter location of R_0, F_c and R_∞ , shown in the α (red circles) and β range (blue diamonds).	209
9.11	Bar graphs showing mean Cole parameters of 4 electrode configuration measurements obtained from subject 2. Comparisons between mean values is made with a paired t test. Significance level is shown by number of stars. . .	209
9.12	Bar graphs showing mean Cole parameters of 4 electrode configuration measurements obtained from subject 2. Comparisons between mean values is made with a paired t test. Significance level is shown by number of stars. . .	210

9.13	Nyquist plots shown of electrode montages. Cole parameter location of R_0, F_c and R_∞ , shown in the α (red circles) and β range (blue diamonds).	211
9.14	Bar graphs showing mean Cole parameters of 4 electrode configuration measurements obtained from subject 3. Comparisons between mean values is made with a paired t test. Significance level is shown by number of stars. . .	212
9.15	Bar graphs showing mean Cole parameters of 4 electrode configuration measurements obtained from subject 3. Comparisons between mean values is made with a paired t test. Significance level is shown by number of stars. . .	212
9.16	Nyquist plots shown of electrode montages. Cole parameter location of R_0, F_c and R_∞ , shown in the α (red circles) and β range (blue diamonds).	213
9.17	Bar graphs showing mean Cole parameters of 4 electrode configuration measurements obtained from subject 4. Comparisons between mean values is made with a paired t test. Significance level is shown by number of stars. . .	214
9.18	Bar graphs showing mean Cole parameters of 4 electrode configuration measurements obtained from subject 4. Comparisons between mean values is made with a paired t test. Significance level is shown by number of stars. . .	214
9.19	Nyquist plots shown of electrode montages. Cole parameter location of R_0, F_c and R_∞ , shown in the α (red circles) and β range (blue diamonds).	216
9.20	Bar graphs showing mean Cole parameters of 4 electrode configuration measurements obtained from subject 5. Comparisons between mean values is made with a paired t test. Significance level is shown by number of stars. . .	216
9.21	Bar graphs showing mean Cole parameters of 4 electrode configuration measurements obtained from subject 5. Comparisons between mean values is made with a paired t test. Significance level is shown by number of stars. . .	217
9.22	Nyquist plots shown of electrode montages. Cole parameter location of R_0, F_c and R_∞ , shown in the α (red circles) and β range (blue diamonds). . . .	218

9.23	Bar graphs showing mean Cole parameters of 4 electrode configuration measurements obtained from subject 6. Comparisons between mean values is made with a paired t test. Significance level is shown by number of stars. . .	219
9.24	Bar graphs showing mean Cole parameters of 4 electrode configuration measurements obtained from subject 6. Comparisons between mean values is made with a paired t test. Significance level is shown by number of stars. . .	219
9.25	Nyquist plots shown of electrode montages. Cole parameter location of R_0 , F_c and R_∞ , shown in the α (red circles) and β range (blue diamonds). . . .	220
9.26	Bar graphs showing mean Cole parameters of 4 electrode configuration measurements obtained from subject 7. Comparisons between mean values is made with a paired t test. Significance level is shown by number of stars. . .	221
9.27	Bar graphs showing mean Cole parameters of 4 electrode configuration measurements obtained from subject 7. Comparisons between mean values is made with a paired t test. Significance level is shown by number of stars. . .	221
9.28	Nyquist plots shown of electrode montages. Cole parameter location of R_0 , F_c and R_∞ , shown in the α (red circles) and β range (blue diamonds). . . .	222
9.29	Bar graphs showing mean Cole parameters of 4 electrode configuration measurements obtained from subject 8. Comparisons between mean values is made with a paired t test. Significance level is shown by number of stars. . .	223
9.30	Bar graphs showing mean Cole parameters of 4 electrode configuration measurements obtained from subject 8. Comparisons between mean values is made with a paired t test. Significance level is shown by number of stars. . .	224
9.31	Across Subject Mean Bode plots shown with and without error bars.	225
9.32	Across Subject Mean phase plots shown with and without error bars.	227
9.33	Across Subject Mean Cole plots shown with and without error bars.	230

9.34	Mean across subject α Cole parameter comparison across electrode montages.	231
9.35	Mean across subject β Cole parameter comparison across electrode montages.	231
9.36	Principal components, scores and coefficients shown of real and imaginary components of electrode montages C3-C1-CZ-C2 and T7-C1-CZ-C2	233
9.37	Percent of total variance of first and second principal components of real and imaginary components, shown for electrode montages C3-C1-CZ-C2 and T7-C1-CZ-C2.	233
9.38	Principal components, scores and coefficients shown of real and imaginary components of electrode montages C3-C1-CZ-C2 and T7-C3-C4-T8.	234
9.39	Percent of total variance of first and second principal components of real and imaginary components, shown for electrode montages C3-C1-CZ-C2 and T7-C3-C4-T8.	235
10.1	Comparison of mean experimental and FEM impedance. From upper left clockwise, Sum of all real impedance across all electrode montages, real impedance of C3-C1-CZ-C2, real impedance of T7-C3-CZ-C2, real impedance of T7-C3-C4-T8.	240
10.2	Comparison of mean experimental and FEM impedance. From upper left clockwise, Sum of all imaginary impedance across all electrode montages, imaginary impedance of C3-C1-CZ-C2, imaginary impedance of T7-C3-CZ-C2, imaginary impedance of T7-C3-C4-T8.	241
10.3	FEM Nyquist plots across all electrode montages up until 1 MHz.	243
10.4	Mean Bode plot across all subjects with no error bars.	244
10.5	FEM α Cole parameter comparison across electrode montages.	244
10.6	FEM β Cole parameter comparison across electrode montages up until 1 MHz.	245

10.7 Mean inter-subject α Cole parameter comparison across electrode montages.	246
10.8 Mean inter-subject β Cole parameter comparison across electrode montages.	246
10.9 Principal components, scores and coefficients shown of real and imaginary components of FEM electrode montages C3-C1-CZ-C2 and T7-C1-CZ-C2. .	248
10.10 Principal components, scores and coefficients shown of real and imaginary components of FEM electrode montages C3-C1-CZ-C2 and T7-C3-C4-T8. . .	248
10.11 Principal components, scores and coefficients shown of real and imaginary components of experimental electrode montages C3-C1-CZ-C2 and T7-C1-CZ-C2.	249
10.12 Principal components, scores and coefficients shown of real and imaginary components of experimental electrode montages C3-C1-CZ-C2 and T7-C3-C4-T8	249

Part I

Introduction

Chapter 1

Thesis Motivation, Goals and Outline

1.1 Research Motivation

Over the past decade interest has greatly increased in the research of non-invasive brain stimulation methods for a wide variety of clinical applications [1]. The most popular form of non-invasive brain stimulation is called transcranial Direct Current Stimulation (tDCS) [1]. This technique is comprised of application of weak direct current via external electrodes (commonly saline soaked sponges) to specific sites in the human brain associated with specific neuropsychologic, psychophysiologic, and motor activity [2]. The growth of tDCS research is due largely to its ease-of use and non-invasive profile combined with a reported ability to significantly alter and modulate neural plasticity [1,3].

TDCS is potentially a very attractive form of treatment; it is non-invasive, has low side effect profile and is relatively low cost [2]. Results of clinical research of potential therapeutic effects of tDCS have been encouraging; it has shown potential as a substitutive treatment for pharmacotherapy (for patients with poor drug tolerability) [4], and as a restorative or augmentative treatment (i.e. stroke [5], chronic pain [6] and depression [7]). TDCS has also demonstrated beneficial effects in the treatment of disorders associated with stroke [8,9], epilepsy [10], and chronic pain [11]. Studies have shown that tDCS can reduce nicotine [12], alcohol [13] and food craving [14]. In addition tDCS is increasingly being explored as a method of augmenting performance of specific cognitive tasks such as

motor learning [15], working memory [16], and language performance [17].

Despite increasing evidence of tDCS efficacy for a wide range of disorders, a number of barriers have prevented the emergence of tDCS as a mainstream clinical therapy. A recent review paper [18] discussed some of the experimental and technical challenges of tDCS research. Specifically, a large between- [19] and within- [20] group variation of tDCS effect on motor evoked potential (MEP) amplitude has been reported. Inter-subject variability is shown in Fricke et. al. [21] who reported MEP amplitude increase of 93.2% and 9.2% for two different groups who received stimulation with the same protocol (0.0286mA/cm² current density; anode M1/cathode contralateral orbit; 5 min duration). Nitsche et al. reported in studies using identical protocols MEP amplitude inhibition after stimulation of 30 minutes of 42.9% [22] and 20 % [23] respectively; other studies by Nitsche et al. showed inter-group variation of MEP enhancement of 54.4% [24] and 19.3% [25]. Example of intra-subject (within a single group) are found in Nitsche and Paulus [26] and Tremblay et al. [27] who reported differences in MEP amplitude of around 290 %. In addition to high variability, tDCS effects may not be reproducible as demonstrated in two studies where a second session of tDCS using an identical stimulation protocol caused a decrease [28] and even inhibition [29] of MEP amplitude. Some meta-analyses have described tDCS efficacy (chronic pain, cognition) as inconclusive [30] or non-existent [31, 32].

In manner analogous to pharmacokinetics and drug-bioavailability, treatment dose is defined as the interaction of the active agent (electromagnetic field) and the therapeutic target (brain). According to Peterchev et al. [33] transcranial electro-magnetic (EM) stimulation dose is defined by all factors that define the EM field in the body i.e. electrode size and montage (placement of electrodes on the scalp based on EEG coordinates for the purpose of neurostimulation [34]) and stimulation parameters (current intensity, polarity, session number and duration).

The difficulty in achieving a consistent response to tDCS may thus be related to difficulties in controlling factors related to dose. For instance, intracranial dose which is correlated to

tDCS response [35], is affected by factors unique to individual physiology and anatomy such as skin thickness, skull conductivity, intracranial tissue conductivity and brain tissue conductivity [36]. Horvath et al. [37], listed inter- and intra- subject variability, and electric current influences (hair, method of electrode attachment) as factors that affect treatment reliability and efficacy.

It is known that head tissues (scalp, skull, cerebrospinal fluid CSF, grey matter and white matter) have unique anatomical and physiological characteristics which are reflected in different multi-frequency conductivity [38] and permittivity values for these tissues [39,40]. Our motivation is thus to develop a new method of improving control and optimization of tDCS dose by measuring and analyzing multi-frequency electrical properties of individual subjects head tissues that affect the flow and distribution of current to the brain. We have already explored the potential of using bioimpedance spectroscopy as form of in-vivo feedback during tDCS relating changes in dose, to shifts in the measured multi-frequency impedance characteristics [41,42]. We now wish to investigate the potential of relating the characteristics of dielectric spectra of the head to dose-related parameters such as the intracranial current density and electric field distribution.

1.2 Research Goals and Objectives

The overall goal of this thesis is to analyze the impedance spectra of the head tissues and relate characteristics of the impedance spectra to dose in the brain. The core of our approach is the in-vivo spectroscopic measurement of the head impedance, analysis of the impedance parameters using classical explanatory and descriptive models (Cole model and multivariate analysis) and comparison of these parameters to results derived from FEM to infer distribution of dose in the brain.

Previous work has shown that the resistivity of regional head tissues can be estimated by injection of current through a pair of electrodes and measuring the resulting potential

distribution through a network of electrodes strategically placed on the scalp [38, 43, 44]. The motivation of these studies were to improve source localization of brain electrical activity. The approach used in these studies involves the use of an analytic model of a head usually consisting of a number of spheres representing the primary head tissues. The regional head conductivities are then estimated by minimizing the error (with some variation of the simplex method [38, 44]) between the computed and measured scalp potentials. This method has had good results, with one author showing model and measurement error could be reduced to a few percent even when noise had been added to the model to account for experimental error [38, 44]. Although these studies have focused on the EEG localization problem, results of this method could easily be applied to the forward problem of calculating current density in the brain which is essential for estimation of neurostimulation dose. In fact some authors have already shown a clear relationship, using the principle of reciprocity, between EEG and the forward tDCS problem [45–47].

We believe however that this approach suffers from some important shortcomings. First of all simple analytic models shaped as concentric shells as used in [38] are quite different than the intricate anatomy of the human head and may contribute to error [43]. In [38] it was shown that the simplex minimization only provided relatively accurate agreement with measured values when initial inputs fed to the algorithm were based on a range of conductivity values found in the literature. In addition it was shown that the performance of the algorithm was dependent on the angle between the injecting electrodes, as the angle is increased the error also increases [38]. In [43] the boundary element method (BEM) is used for solving a realistic head model. Results are shown to be sensitive to the distributions of points in the different model compartments, this potentially reduces the generalizability of the method. In [44] data sets are only obtained from 2 patients. In addition in [44] only the ratio $\frac{\rho_{brain}}{\rho_{skull}}$ are considered, effects of other tissues, such as the CSF, are ignored. Finally all these authors only consider the use of a single low ($> kHz$) frequency. Spectroscopic measurements contain more information of tissue structure and

electrical properties and for some applications (such as estimation of total body water [48]) are shown to achieve a higher accuracy than single frequency measurements.

In the context of our work, we are interested in relating unique characteristics of an impedance spectra to a particular dose distribution resulting from defined arrangement of electrodes (referred to as montage) and boundary conditions. The DC or low end frequency applications can be thought of as occupying the beginning of the spectra. By analyzing a wide frequency range we investigate the entire head tissue frequency response over the α , β and γ relaxation zones which can be fitted be to multiple Cole models [49].

Our proposed methodology involves comparison and analysis of multi-frequency spectra data characteristics across multiple independent (simulation and experimental) platforms for estimation of neurostimulation dose. Unlike much of previous work in this field, we do not entirely rely on FEM modeling results. Instead FEM work provides a baseline and a theoretical framework for comparison to experimental data. In addition we analyze in detail trends and patterns within and across subject impedance spectra. This avoids the problem of the very limited generalizability of pure simulation results.

The applications of this work may go beyond the tDCS form of neurostimulation. Indeed many applications of bipolar montages are using frequencies well above DC. Examples include studies of neuro plasticity using transcranial alternating current stimulation (tACS) that include stimulation up until 5 kHz [50] and the use of alternating electric fields at 200 kHz for the treatment of brain tumors [51]. In addition transcranial random noise stimulation (tRNS), has been used between 0.1 and 640 Hz [52]. Furthermore bioimpedance studies are generally in the high kHz range due the generally high frequencies needed to measure the dielectric properties of common biological tissue [53–56].

Overall we use AC analysis for investigation of DC properties of the head since we can extrapolate DC properties using the Cole model. In addition DC measurements are prone to error and can significantly change the conductivity of the tissue [57]. The use of AC

(depending on frequency) should minimally change skin impedance [57] and thus should provide near identical measurements for repeated scans. In addition impedance measurements should be near identical irrespective of the order of the frequencies used in the sweep.

Geselowitz [58] used the reciprocity theorem to show that the sensitivity of a tetrapolar impedance measurement is defined as the scalar product of the vector current densities (the lead fields) for unit current injection between the two pairs of current and voltage electrodes. The concept of the sensitivity field based on the formulation of [58] is an important part of our work as it relates the measured output, transfer impedance, to the distribution of vector current densities - which are in turn related to dose parameters.

The detailed research goals can then be stated as follows:

1.2.1 Objective 1

1. Use of a realistic head FEM to investigate the effect of electrode montage (different configurations of bipolar and tetrapolar montages), head tissue properties and frequency on sensitivity and focality

We use a realistic MRI derived head FEM for all our simulations. Each simulation is comprised of 6 measurements of all tissues with 5% of normally distributed Gaussian random noise added to the model.

We are interested in analyzing how changing the distance between the electrodes changes the dose in the brain. This FEM study will show how the sensitivity contribution of each tissue (analogous to dose) shifts as a result of varying electrode position. This work lays the foundation of relating unique impedance characteristics of various montages to the resulting dose distribution.

We expect to see that sensitivity and focality are dependent on electrode distance. As electrode gap is increased we should observe a higher overall sensitivity and

focality in the brain. We also analyze changes of sensitivity and focality in defined regions of interest (ROIs) in the brain. The change of dose and sensitivity in ROIs will depend on their location relative to the electrodes.

We also want to investigate the proportion of sensitivity field distribution in each head tissue. This is important since we want to know how much each tissue contributes to the total impedance measurement of the head. If the brain sensitivity is large compared to other tissues then it can be easily detected in the impedance measurement. We do however expect that the sensitivity measurement of the head to be dominated ($> 95\%$) by more superficial tissues such as the scalp and CSF due to their relatively small volume and high conductivity.

In addition we wish to investigate the dependence of sensitivity and focality on frequency. The frequency response of tissues may be an important determinant in optimizing dose. Although tDCS is set at DC, other forms of neurostimulation are used at higher frequencies.

We also will examine the effect of changing electrode configuration (different positions of bipolar and tetrapolar electrodes) on sensitivity and dose. This is an important part of optimizing neurostimulation since the distribution of dose is dependent on the number and position of electrodes. tDCS modeling work is exploring the use electrode arrays to optimize dose [59]. We expect that the sensitivity field distributions of the tetrapolar measurements will be more sensitive to deeper tissues than the bipolar measurement since the current and voltage electrodes are separated. This has important implications for relating impedance measurement characteristics to dose in the brain.

1.2.2 Objective 2

2. Investigating the linear correlation of sensitivity to dose

We want to explore the relationship between sensitivity and dose (electric field and current density). We explore if these variables are linearly correlated over frequency. Statistical significance is measured with a paired t-test. We expect here that sensitivity and dose are significantly correlated (p-value below an $\alpha = .05$) and that correlation is high ($> .9$)

1.2.3 Objective 3

3. Use of a realistic head FEM to investigate the effect of electrode montage (different configurations of bipolar and tetrapolar montages), head tissue properties and frequency on impedance

We now wish to examine how all these parameters affect the impedance measurement of head and its constituent tissues. Impedance is related to sensitivity and the conductivity of each tissue. Thus we expect that the high impedance skull tissue will have a large contribution to the total impedance of the head. We also expect that the scalp and the CSF will have large contributions to the total impedance. Other tissues will contribute less than 1% of the impedance.

The frequency dependence of the head tissue impedance is also important. For instance we expect that the contribution of CSF on impedance will decrease and conversely the brain contribution to impedance will increase as frequency is increased.

We wish to investigate the affect of increasing the gap between the electrodes, as electrodes are moved apart we expect that the total impedance will increase and that the contribution of the brain tissues to the total impedance will increase.

Finally we also want to compare the bioimpedance spectra resulting from various tetrapolar and bipolar montages. We expect that the for tetrapolar montages, the scalp impedance will be greatly decreased and that the brain impedance will be increased. Conversely the impedance of the bipolar montages will be mainly

comprised of scalp impedance ($> 90\%$).

1.2.4 Objective 4

4. Extract Cole model and PCA parameters from simulated data and compare the results across bipolar and tetrapolar montages

Here we use Cole model and PCA parameters to characterize the impedance spectra. This is necessary to reduce the data dimensionality to a small number of parameters. We expect that there will be significant differences (p-value below an $\alpha = .05$) between the Cole and PCA parameters of each electrode montage. We also expect that most of the variance ($< 99\%$) between two impedance spectra can be described by a single principal component. This shows an almost linear relationship between two sets of impedance spectra. We expect as the gap between the electrodes are increased this relationship will become increasingly non-linear and that the variance described by a second principal component will increase.

We also wish to investigate that the linear superposition approximation is valid for bioimpedance spectra. We will show this by demonstrating that the sum in series of each tissues Cole system (characteristic semi-circle in the Nyquist plot of real vs. negative imaginary) is equal (within an error of 1%) to the total Cole system measured across all the tissues.

These linear properties of the impedance spectra have important implications since we may now consider linear operations such subtraction to remove the impedance of undesired tissue such as the scalp.

1.2.5 Objective 5

5. Extract Cole and PCA parameters from measurements on human subjects. Compare parameters for different tetrapolar montages

We are looking here to see if the experimental data will be consistent across all montages and that a clear trend of statistically significant differences can be observed which is the same for all subjects.

We expect that there will be a very high degree of variability between results for different subjects due to measurement error and natural physiological differences.

In order to quantify this variability we compare the mean Cole parameters of all the subjects for the different montages. An unpaired t-test will be used to measure significance at $\alpha = 0.05$. We expect that there will be mean Cole parameters with statistically significant differences for the different electrode montages. This shows that there certain patterns in the impedance spectra that are not canceled out by inter-subject variability.

1.2.6 Objective 6

6. Compare experimental and FEM impedance characteristics

Our final goal is to compare various impedance characteristics (Nyquist plots, Cole and PCA) of the FEM and the mean experimental data. Similarities can be used to infer relationships between impedance spectra and dose as calculated by the FEM.

The main expected contributions of the thesis can therefore be summarized as:

1. Development and analysis of a novel methodology of relating tissue impedance spectra to neurostimulation dose. This includes:
 - Analysis of the effect of changing dose-related parameters (frequency, electrode configuration) on simulated spectra of sensitivity, impedance and dose
 - Use of Cole model and multivariate analysis to describe and compare changes to the impedance spectra for different electrode montages as well as to relate these changes to variation in dose

- Analysis and comparison of FEM and experimental impedance spectra parameters to infer dose distribution

1.3 Thesis Outline

The following is an outline of the sections of this thesis.

Chapter 2 provides a literature review of the state of the art of the field of optimization of tDCS dose.

Chapter 3 describes the realistic head FEM. Topics discussed included a description of model layers, components and number of nodes.

Chapter 4 provides a detailed description of the setup and physics of a simulated multi-frequency impedance measurements. Subsections of this chapter include; a discussion of the material properties of the head tissues and electrodes (impedance and reactance), boundary conditions, addition of noise, electrode montage (2 and 4 electrode measurements), region of interest (ROI) setup, dose and measurement parameters measured and probe setup.

Chapter 5 describes in detail the solver configuration used for the modeling work. We discuss some background of solver types and the considerations that determined the best choice of solver for our model (nested multigrid and generalized minimal residual method).

Chapter 6 shows the results of sensitivity field calculation for various 2 and 4 electrode configuration. We describe the tissues which have the highest concentration of sensitivity.

The concept of the negative sensitivity field is discussed. Finally we describe the relationship between sensitivity and dose and measurement parameters.

Chapter 7 describes impedance simulation results. We show here the principle of superposition by demonstrating that sum of all tissue's impedance added in series is equivalent to the total measured impedance. We then show how each tissue behaves as a

Cole system which add together in series to a total Cole system. We show how the transfer impedance can be modeled as a weighted sum of impedances where the sensitivity provides the weight. We also demonstrate how the total impedance can be approximated by the impedance of 3 tissues (scalp, skull and CSF).

Chapter 8 provides a description of Cole modeling and PCA analysis. We extract Cole parameters for the 2 and 4 electrode configurations. A description is provided of the fitting and extraction method. We show how the Cole parameters can be related to sensitivity distribution and dose and measurement parameters. We demonstrate how the variance between two measurements can be decomposed into primarily a single principal component demonstrating the linearity of the problem.

Chapter 9 describes the experimental protocol and results. We analyze the impedance using Cole model and PCA.

Chapter 10 compares FEM and the pilot study results and provides discussion of results, proposed future work and a summary of contributions.

1.4 Publications

The list below includes all my publications, including those in preparation, related to my thesis. I have also included a patent related to some of the topics discussed.

1. **H. Caytak**, A. Adler, M. Bolic, "A FEM and experimental analysis of impedance spectra of the human head for optimization of neurostimulation dose," in preparation.
2. **H. Caytak**, A. Boyle, A. Adler, M. Bolic, "Bioimpedance Spectroscopy Processing and Denoising Methods." Encyclopedia of Biomedical Engineering Elsevier, 2017.
3. I Nejadgholi, **H. Caytak**, M Bolic,"Using Bioimpedance Spectroscopy parameters as real-time feedback during tDCS," IEEE Engineering in Medicine and Biology, 2016 IEEE pp. 5246-5249
4. **H. Caytak**, I Nejadgholi, I Batkin, M Bolic,"Bioimpedance Spectroscopy method for investigating changes to intracranial dose during transcranial direct current stimulation," IEEE Engineering in Medicine and Biology, Milan, Italy, August 2015, pp. 3448-3451.
5. I. Nejadgholi, **H. Caytak**, M. Bolic, I. Batkin, S. Shirmohammadi, Preprocessing and Parameterizing of Bioimpedance Spectroscopy Measurements By Singular Value Decomposition. Journal of Physiological Measurements, 2015.
6. A. Mekonnen, I. Batkin, S. Golami, **H. Caytak**, M. Bolic, "Temperature induced enhancement of tDCS efficacy." Poster, NYC Neuromodulation Conference 2015.
7. D. Shapiro, **H. Caytak**, M. Bolic, "Voltage drop during tDCS, Problem and potential solution." Poster presented at the Engineering and Computer Science Graduate Poster Competition University of Ottawa, March 31 2015.

8. **H. Caytak**, I. Batkin, A. Mekonnen, D. Shapiro, S. Hassoun, G. Li, H. R. Dajani, M. Bolic, Superabsorbent polymer electrode for transcranial direct current stimulation, in Medical Measurements and Applications Proceedings (MeMeA), 2013 IEEE International Symposium on. IEEE, 2013, pp. 320324.
9. **H. Caytak**, D Shapiro, A. Borisenko, and M. Bolic, "Advances in tDCS could provide a safer clinical tool for neuromodulation," IEEE Pulse March 2015.
10. **H. Caytak**, A. Mekonnen, I. Batkin, "Method and device for determining brain and scalp state," US Patent Publication number US20150025352 A1 Publication date 22 Jan 2015.

Part II
Literature Review

Chapter 2

Literature Review

2.1 TDCS dose optimization methods

In section 1.1 we described our motivation for developing a method of improving control of tDCS (transcranial direct current stimulation) dose. In this chapter we review current state of the art methods for optimization of tDCS dose.

We now describe the organization of this chapter. To provide context for our work we provide a review of the of tDCS research as well as proposed mechanisms of action of tDCS. We then review state of the art methods for optimization of tDCS dose. This review includes a detailed discussion of optimization methods implemented on MRI derived realistic head models. Other discussion includes algorithmic based methods (evolutionary strategy, genetic algorithms, interior point optimization for non-linear minimization) and methods based on the linear supposition approximation and the principal of reciprocity.

2.2 TDCS Background

Transcranial direct current stimulation (tDCS) is a form of neural electrostimulation whereby low intensity DC current is delivered to the cortex via surface electrodes placed strategically on the scalp [2]. Typically tDCS devices are battery-powered current generators that are capable of outputting a fixed electrical current of up to 2 mA; device

lead wires are attached to electrodes (usually carbon inserted in saline or water soaked sponges 20-35 cm² in area) that are fixed to the scalp with a non conducting strap or cap [60]. TDCS stimulation is generally defined by the following parameters: current density (current intensity/electrode size), duration, polarity and montage [60]. (Montage is defined as a particular configuration of electrodes on the scalp for the purpose of neurostimulation [34])

Investigation of the effect of brain stimulation began with the work Giovanni Aldini in 1802 who reported that cortical stimulation of decapitated prisoners resulted in muscular grimaces on the side of the head contralateral to the stimulation. In 1804 Aldini reported the successful treatment using neural stimulation of patients with melancholia [60]. Batholow (1874), Sciamanna (1882) and Alberti (1883) carried out a series of pioneering experiments comprised of stimulating cortical tissue of conscious patients with exposed brain tissue due to illness or trauma; the investigators described the electrical current eliciting muscular contraction of various parts of the body in some cases contralateral to brain hemisphere being stimulated (see description of tDCS history in [2, 60, 61]. The work of these early researchers served as the foundation of numerous clinical studies (ranging from the end of 19th and beginning of 20th centuries) investigating and mapping the physical effect of stimulating the motor cortex. Despite early progress, interest in DC or galvanic stimulation as a research and therapeutic tool was superseded by introduction of electroconvulsive therapy in 1930 by Lucino Bino and Ugo Cerletti [62], other factors that detracted from interest in the field included the popularity of psychopharmacologic drugs and a lack of reliable neurophysiologic markers necessary for accurate measurement and reproduction of the stimulation effect [2].

2.2.1 TDCS effect on cortical excitation

At the turn of the century a series of studies by Priori et al. [63] and Nitsche Paulus [35] used transmagnetic stimulation (TMS) evoked motor potentials as a method of measuring

tDCS induced cortical excitability. Both studies found that the DC current was capable of modulating significant lasting changes in excitability. Priori reported that anodal scalp DC in humans significantly alters reaction times but cathodal DC does not [63], whereas Nitsche and Paulus found that DC stimulation significantly increased motor-cortical excitability during anodal stimulation and caused a similar significant decrease during cathodal stimulation; effect size was approximately 20% [35]. Specifically, experimental results showed that the interaction of current polarity with electrode position, as well as interactions between current duration, stimulation intensity and time course after current stimulation, all had a significant effect on MEP size [35]. These findings suggested that DC stimulation could be an effective method of non-invasively reversibly modulating cortex excitability especially if the effect duration could be extended as already shown successfully in animal studies involving rats [64,65]. This is significant since changes in baseline cortical excitation may affect performance of many neural functions.

Additional studies appeared to confirm the polarity dependent cortical excitation properties of DC stimulation [66]. In a 2001 paper Nitsche and Paulus showed 9 to 13 minute sessions of tDCS increased motor cortical excitability about 150% above baseline for up to 90 minutes after the end of stimulation thus demonstrating the potential long lasting nature of the stimulation effect [26]. In 2003 Antal et al. [67] showed that DC stimulation could modulate the visual cortex excitability; anodal stimulation resulted in an increase of the phosphene threshold (PT) as measured by short TMS pulses, conversely cathodal current resulted in a decrease of the PT. Nitsche et al. showed that cathodal current applied to the motor cortex resulted in a reduction of MEP size; 5-7 minutes of stimulation resulted in a return to MEP baseline whereas 9 minutes of applied DC resulted in MEP reduction up to one hour post stimulation [68]. A more recent study published in 2016 demonstrated that paired electrical stimulation of the median nerve resulted in a reduced paired-pulse suppression (PPS) of somatosensory evoked potentials after anodal stimulation indicating cortical excitation; cathodal stimulation resulted in an increased

PPS thus showing an inhibitory effect [66].

The relative success of studies demonstrating the ability of tDCS to modulate cortical excitability has provided motivation for researchers attempting to demonstrate the viability of tDCS as a tool capable of providing controlled therapeutic neuromodulation and plasticity. A large number of tDCS studies have now been published, investigating the potential of using this stimulation for a wide range of motor, cognitive and neuropsychiatric disorders (for example see the following reviews [2, 69, 70]).

2.2.2 Proposed mechanisms of action

A number of mechanisms of action have been proposed to explain the basic effect of tDCS on cortical excitability. Nitsche et al. [68] suggested that cortical excitation reported for anodal stimulation is caused by neuronal depolarisation and a resulting shift in resting membrane potential; conversely cathodal stimulation causes an inhibitory response due to neuronal hyperpolarization. This effect is only reliably reported in that paper for the anodal-motor and cathodal contralesional orbit; it is suggested that other electrode montages can result in anodal hyperpolarization and cathodal depolarization since the direction of polarization depends on the relative orientation of the electric field versus the neural cell axons and dendrites [60, 68]. The duration of the effect after several minutes post stimulation is thought to result from changes in changes in the spontaneous discharge rate of the neuronal action potentials [68]. Modelling work has indeed shown that DC stimulation can change neuronal transmembrane potential without triggering an action potential [71, 72]. Some controversy exists if the tDCS stimulation effects are due to changes in the physiology of the neuronal membrane, or rather tDCS mediates changes more indirectly by altering the balance of local ionic concentrations [60].

There is evidence that tDCS modulates glutamatergic and GABAergic neurotransmitters responsible for an excitatory and inhibitory neural response respectively. Some studies have shown that tDCS effect can be abolished by blocking of glutamatergic NMDA

receptors, conversely the stimulation effect can be prolonged through the action of the NMDA receptor agonist D-cycloserine [24, 73]. Additionally it has been shown that both anodal and cathodal tDCS reduce GABA as measured by magnetic resonance spectroscopy (MRS) [74]; this is consistent with the observation that GABA reduction increases glutamatergic plasticity in animal slice experiments and may be the basis of the plasticity effect induced in humans [75]. Glutamate release activates NMDA receptors which in turn can cause an increase of intraneuronal calcium (Ca^{2+}) concentration through a dedicated ligand-gated channel. At specific Ca^{2+} concentration thresholds, enzyme cascades cause insertion or removal of glutamatergic AMPA receptors; quantity of these receptors control the post-synaptic activation threshold. Modification of the AMPA receptors is considered the basis for long term potentiation (LTP) and long term depression (LTD) [75]. Other neurotransmitters (GABA, dopamine, acetylcholine, serotonin, adrenaline, and noradrenaline) also affect the post-synaptic activation threshold by modifying the transmembrane potential via receptors including glutamergic and ion channels [75]. The basis of tDCS effect thus appears to be primarily related to activation of the glutamergic excitatory system whereas the reduction of GABA serves to remove inhibition to glutamergic excitation [75].

Other studies have shown that tDCS effects are nonsynaptic and may cause transient changes in protein channel density in the region of the stimulating electrode [2, 76, 77]. Since the tDCS induced field causes polar molecule migration, including of many neurotransmitters, it is theorized that the stimulation effects are caused by displacement and alteration of the neurochemical environment [74, 77]. Evidence of these changes is a demonstrated in a magnetic resonance spectroscopy study that showed that anodal tDCC altered myoinositol but didn't change n-acetyl-aspartate [78]. Constant electrical fields are known to affect various kinds of biological tissues and physiological mechanisms (inflammation, cell migration) [2]. In line with these observations it has been observed that anodal tDCS can induce prolonged brain vasodilatation [79]

Research has shown that tDCS effect is not strictly limited to areas directly under and adjacent to the scalp electrodes; rather the stimulation may affect distant structures likely through connections between the stimulated neurons and other neural networks [60]. A number of studies have demonstrated that stimulation effects can be measured at sites distant to yet functionally connected to targeted regions [80–83]. It has been shown tDCS modulates neuronal oscillations as evidenced by increases of EEG activity in the theta and delta range [76]. Simulation studies have shown that conventional tDCS provided by large electrodes is non-focal due to current spread in the brain [84]; this may provide an alternative explanation for non-local effects observed subsequent to stimulation [75].

Since tDCS effect is hypothesized to depend on orientation of current flow relative to neural orientation [75], electrode position is critically important in determining stimulation efficacy. It has been shown in fact that the position of the return electrode, a factor that determines the induced electrical field orientation and magnitude, influences the directionality and effect size for motor, and visual cortex stimulation [35, 63, 85]. A study that investigated a stimulation protocol with the return electrode placed on the shoulder or arm reported reduced efficacy [86], this provides further support to the centrality of electric field magnitude in determining stimulation effect. A proper balance must be sought in electrode placement to ensure that the electrode field intensity is sufficient while avoiding excessive shunting through the superficial scalp layers [75].

2.3 FEM based optimization methods

FEM head models are the primary tool used for developing tDCS optimization methodologies. Early work by Rush and Driscoll [87] derived an analytical solution of current flow through a model consisting of concentric spheres representing the scalp, skull and brains. The model solution was shown to be similar to results achieved by measuring current spread in a realistic phantom (human skull suspended in a receptacle filled with

saline.

Miranda et. al [71] continued this work by implementing the Rush and Driscoll model parameters in a finite element model developed in Comsol. In this spherical head model radii and electrical conductivity values were set for 3 domains representing the scalp, skull and brain. Sponge electrode sizes are modeled at $6.5 \times 15 \text{ cm}^2$ and $5 \times 5 \text{ cm}^2$ respectively. Four electrode configurations are investigated comprised of a single anode and one or two cathodes (left M1, right contralateral; left Dlpfc, right contralateral; symmetrical above the eyebrows, and 2 small cathodes placed on the mastoids) total DC passed through the anode is set to 2 mA. Results showed that for all montage a significant portion of the current was shunted through the scalp (41%, 49%, 61%, and 53% respectively for the four montages corresponding to inter anode cathode distances of 12.4, 6.5, 3.2 and 6.3 cm). The study showed, in accordance with Rush and Driscoll [87], that for electrodes placed far apart a significant part of the current penetrates the brain whereas for electrodes placed close together (less than 5 cm) current is primarily shunted through the scalp. Results also showed that the current density in the brain during the simulated tDCS is around 0.1 A/m^2 which corresponds to an electric field of 0.22 V/m ; current density at this order of magnitude have to be linked to significant physiological effects [88, 89].

Shortcomings of the spherical models included lack of geometrical accuracy and sometimes omission of critical layers such as the cerebral spinal fluid (CSF) [71]. To achieve better accuracy modelling efforts concentrated on developing and solving realistic MRI-derived head models [71, 84, 90–97]. Wagner et al. in 2007 [90] describes an MRI-derived FE for simulating tDCS currents applied to brain. The Ansoft solver was used for solving all FEM calculations. The FEM mesh was generated using specialized CAD software [98] rendering of human head MRI images. As part of the mesh construction, the various types of human head tissues (skin, skull, cerebrospinal fluid (CSF) were segmented into discrete domains. Tissue conductivity were assigned based values found in the literature (skin: 0.465 S/m ; bone: 0.010 S/m ; CSF: 1.654 S/m ; gray matter: 0.276 S/m ; white matter: 0.126 S/m).

Various electrode pairs were investigated ($7 * 7cm^2$, $7 * 5cm^2$, $5 * 5cm^2$ and $1 * 1cm^2$); each electrode pair was placed on the scalp at the right M1 (anode) and the contralateral supra-orbital region (cathode). The model was solved and current density magnitude and distribution was analyzed for each montage. Parameters analyzed included maximum cortical current surface area, current density variation and current shunting. Results showed that increasing the electrode size resulted to a less focal current distribution with the greatest difference seen between the $7 * 7cm^2$ and $1 * 1cm^2$. Other significant findings showed that current density varied significantly between the tissues with the largest current magnitudes in the skin and CSF volumes, in addition shunting increased greatly for the $1 * 1cm^2$ electrodes when compared to larger electrodes.

Other parameters analyzed in MRI-derived FEM head model studies include stroke [90,94], tinnitus [95], fibromyalgia [99], anisotropic properties of head tissues [96,100–102], head fat and obesity [103], skull defects and skull plates [104] and electrode area and inter-electrode distance [105]. Analysis of customized FE models of individual subjects have shown the importance of modelling idiosyncratic physiological and anatomical details as these parameters may greatly influence current dose and distribution [94,106–108].

2.3.1 Electric field optimization

In order to improve current focality, increasing current density at a desired neurological target while reducing current density throughout other brain regions, a number of computational algorithm based methods are proposed.

2.3.1.1 Genetic Algorithms

Im et al. [109] demonstrated the principle of using an evolutionary strategy (es) for computing the optimal positions of an electrode pair for generating maximal current in a target brain area. The study used a 3D head model, comprised of scalp skull and CSF

extracted from structural MRI data of a standard brain atlas; scalp electrodes were modeled as two boundary nodes with Dirichlet-type boundary values of 0 and 1 V. The model was first converted to a best fitting sphere; based on the center of the sphere, angles (θ and ψ) are evaluated for all the boundary nodes. Four boundary angles (θ_1 , ψ_1 , θ_2 and ψ_2) are designated as optimization variables representing the scalp electrodes. Range of θ and ψ was set as (0, 120) and (0, 360) respectively. Target position was chosen arbitrarily around the occipital and temporal lobe areas. A (2+6) (parent offspring) evolution strategy [110] was then used iteratively until the solution quality did not improve or mutation range was lower than a predefined level. Execution of the ES algorithm showed selection of electrode position such that the solution converged to a maximum electric field at the target (0.117 Am^{-2} and 0.077 Am^{-2} for the shallow (occipital) and deep brain (temporal lobe) target respectively). The authors have also indicated that the ES algorithm has advantages over other optimization algorithms, genetic algorithm (GA) and simulated annealing (SA), due to its greater speed and greater likelihood of not being trapped in a local minima [110].

Another example of the application of a genetic algorithm towards tDCS optimization is presented by Ruffini et al. [111]. Electric field calculations are performed on the MRI-derived realistic head model described in Miranda et al. [112]. The model is multi-layered comprised of scalp, skull, CSF including ventricles, and brain (grey and white matter). Values for tissue conductivity were taken from the literature. Electric field computation is performed on a set of 27 electrodes (diameter 1 cm, height 2.5 mm) (see discussion of multi-electrode array design in section 3.2.2) with the anodal electrode placed on C_z . The principle of superposition - the solution of a N-electrode problem can be stated as a linear combination of N-1 electrode pairs - is used; thus the total electrode field is calculated as the consecutive solutions of 26 unique anode-cathode pairs. The authors assumed that the electric field component pointing into the cortex (positive normal component) is excitatory whereas the component directed out of the cortex is inhibitory

(negative normal component). The problem is thus defined as optimization of the component of the electrical field normal to the cortex; this can be written as $[E(x) * \dots * E_{n-1}(x)] * I = E_0(x)$ where $E_n(x)$ is a basis function of the normal components the electric field, I is an array of components currents and $E_0(x)$ is the desired electric field at the target. A constrained least squared method is used to minimize the error at each mesh point [111]. A genetic algorithm (GA) was implemented to determine which electrodes should be used for the optimization; solution "offspring" fitness was evaluated by error magnitude and by a weighted cross correlation coefficient (between 1 and -1) between the target and the electric field.

2.3.1.2 Multi-Electrode Arrays and Linear Superposition

Results showed that increasing the number of electrodes beyond 8 provided only marginal gains. Analysis showed that a traditional bipolar montage has a relatively limited ability (low cross correlation coefficients, high error) of focusing an electric field at a target compared to an optimized 8 electrode montage. Results also showed the superior fitting properties of the 8 electrode montage for a variety of target maps based on various clinical imaging modalities (rs-fcMRI, PET).

Optimization of a multi-electrode array is described in detail in a 2011 paper by Dmochowski et al. [59]. As described in other papers [109, 111], field optimization is based on the principle of linear superposition of electric fields resulting from different electrode pairs. Optimization is considered with a 64 electrode array (1.2 cm diameter) situated (using the 10/10 coordinate system) on a MRI T1 image-derived head model; gel is interposed between the electrodes and the scalp surface. The model is segmented into brain, skull, CSF and scalp tissues, conductivity of the tissues and electrodes are assigned based on values found in the literature. A target is defined on a gyrus on the posterior side of the central sulcus. The net electric field e of M electrodes (64 minus a reference electrode) at location r_n can be written as $e(r_n) = \sum_{m=1}^M e_m(r_n) = \sum_{m=1}^M s_m a_m(r_n)$ where

s_m is applied current density and a_m is resistivity. Optimization is achieved by fine-tuning the coefficients s_m in a manner analogous to beam forming in array signal applications [113]. The study considers a variety of algorithms (least squares, weighted least squares with a constraint on the maximum current applied to each electrode, linearly constrained minimum variance (lcmv) (enforced gain in a given direction), and optimizing for intensity).

The performance metric is defined as electric field focality in a sphere of increasing radius around the target; half max radius is defined as the radius that contains half of the electric field magnitude. Focality is demonstrated for both radial and tangential currents of a variety electrode montages (5 large pad electrodes, 2 ad hoc arrays of small electrodes (including 4 by 1 and bipolar arrangements); the weighted least squares (wls) and lcmv algorithms performed similarly for radial currents however wls enabled greater intensity for tangential current. Results showed the trade-off between focality and intensity - as the latter was increased the former decreased as measured by the half max radius. The authors noted that for both radial and tangential currents the lcmv (unconstrained) algorithm provided the best focality-intensity tradeoff, while the maximum intensity algorithm provided the highest electric field intensity at the target. In all cases it is demonstrated that optimal stimulation parameters are affected by field orientation at the target (radial or tangential), trade-off between focality and intensity as well as safety criteria.

2.3.1.3 Interior Point Optimization Method

Sadleir et al. [114] describes another method of non-linear optimization of intra-cranial current. As part of this analysis a head model was obtained from the Re-Sliced Adam (RA) dataset from the DTI White Matter atlas repository (Johns Hopkins Medical Institutes). The model, based on T1 weighted MR images, includes white matter anisotropy vectors. The model consists of 10 tissue types, cancellous bone, cortical bone, blood, CSF, sclera, fat, muscle, brain, and skin; conductivities are assigned based on measurements

under 1 kHz reported in the literature. Large electrodes (22 cm²) are used for this simulation; one electrode is sited close to the targeted brain region whereas the other (reference) electrode are placed elsewhere on the scalp or extra-cranially. A total of 19 montages (10-20 EEG system) are considered. Voltage data was calculated for each electrode after simulation of current injection of 1 mA. An interior point optimization method (used for solving general non-linear minimization problems subject to linear and non-linear restraints [115]) was used for optimizing current flow by calculating the weight or coefficient determining the appropriate stimulation intensity to be delivered to each electrode. This method is similar to that described in [59] with the fundamental difference being that their general non-linear algorithm explicitly specifies avoidance areas (current only allowed below a set threshold) instead of minimizing current flow in all areas outside the target. Optimal current flow is calculated without the constraint of all electrodes being placed on the head as extracranial electrodes may be attached to compensate for additional uncompensated current. Three problems are considered: 1. preferential delivery to the left inferior frontal gyrus (IFG) while avoiding the accumbens, 2. maximal current delivery to the accumbens, and 3. maximum current delivery to the accumbens while avoiding current flow to the left inferior frontal gyrus (IFG).

Results showed that current could be preferentially delivered to the IFG while avoiding the accumbens (current magnitude in the target is greater by a factor of 10). The latter 2 problems were solved, however many more iterations were required to converge to solution than the first case. In addition it was shown that when targeting deep brain structures current flow through peripheral brain structures (cortex) can not be avoided solutions and that these problems may not yield a unique solution.

2.3.2 Reciprocity approach

Another optimization approach utilizes the principle of reciprocity to guide tDCS stimulation to cortical targets mapped by EEG signals [45, 46, 116–120].

Dutta et al. [116] first explored the potential of using the electromagnetic reciprocity theorem to reciprocally energize the EEG electrodes. The foundation of this approach relies on the fact that the EM lead-field resulting from current dipole sources in the brain recorded at an EEG electrode, is the same as that generated by a unit of current injected in that electrode. In lead field formulation the reciprocity theorem can be stated as [116] $\vec{u}_{1,NME_j} \cdot \left(\vec{J}_{2,NME_j} \right) = \left(\vec{c}_{1,\bar{r}_{anode},NME_j} - \vec{c}_{1,\bar{r}_{cathode},NME_j} \right) \cdot \vec{u}_{1,NME_j}$ where \vec{u}_{1,NME_j} is a vector representing a unit dipole generated signal by the j^{th} neural mass ensemble (NME) (average event related activity), \vec{J}_{2,NME_j} is a unit of current (brain stimulation) flowing through the NME, and $\left(\vec{c}_{1,\bar{r}_{anode},NME_j} - \vec{c}_{1,\bar{r}_{cathode},NME_j} \right)$ is the dipole lead field in the j^{th} NME between the cathode and anode. This equation shows the equivalency of the dipole and current lead field thus demonstrating the principle of reciprocity. One shortcoming of this method is the lack of accurate conductivity values required for precise forward solving of computational head model. Dutta et al. thus proposes the use of magnetic resonance current density imaging [121] where the current lead field can be determined *in vivo* allowing for estimation of appropriate conductivity values using a regularized least square method.

Ruffini et al. [117] described EEG and transcranial electric stimulation (TES) (voltage space to dipole space) as a pair linear systems linked by a common transfer matrix. Based on the reciprocity principle, the scalp voltage at point a with respect to b can be written for a volume mesh with n points as $V_{ab} = - \sum_n \vec{E}_n^0 \cdot \vec{J}_n \delta V_n$ where \vec{E}_n^0 is the electric field induced by reciprocal montage at point a and b . Since each component of a triangular mesh is defined by 3 points each mesh point is divided by 3 resulting in a $3N$ dipole space. The number of voltage functions (defined as basis functions) is equivalent to the number of electrodes minus 1; in this example case equivalent to 26. The transfer or forward mapping matrix, referred to as K , then results in a $26 \times 3N$ matrix. Ruffini et al. then describes a number of methods of smoothing the data for inversion including minimizing the curvature of the solution subject to data constraints [122]. This approach would allow inversion of EEG potentials to dipole (source) space which can be used to define a dipole field map;

multichannel stimulation (MtCS) can then be optimized to align or anti-align with the dipole electric field using the methods described in [111]. Potential applications of this method include: online optimization and close-loop monitoring of MtCS from EEG as well as playing back EEG from the MtCS currents.

The concept of the linear reciprocal relationship between EEG and TES has been further explored by Dmochowski et al. [120]. The relationship is formalized through a common transfer matrix linking the 2 linear systems; this can be written as $R^T = S$ where R is the electrical path between neural current sources and recording electrodes, S is the relationship between the stimulation currents and the resulting electric field and T is the matrix transposition. The stated optimization problem is to modulate sources of neural activity; it is thus desirable to achieve $E = cD$ whereby E is the induced electric field, D is the field resulting from neural sources and c is a proportionality scalar. The optimization minimization problem can then be written as $I = arg\ min\ ||kE - cD||^2 = c(RR^T)^{-1}V$. This spatially decorrelated V is not identical to merely "naively" reversing the scalp voltage by using $I = V$. Thus in order to target neural structures it is only necessary to locate the scalp voltage projections of the sources as opposed to determining the spatial location of the EEG dipoles. Dmochowski et al. demonstrated use of this derived reciprocity principle on a boundary element (BEM) problem solved on a MRI derived model. Four regions of interest were defined using a variety of electrode montages; dipolar current sources of an average radius of 1.03 cm were simulated and generated scalp potentials were transformed to stimulation current using both "naive" and true reciprocity. Stimulation performance was computed as the ratio of the electric field strength at the targeted region to the field strength outside this zone. True reciprocity achieved higher focality by a factor of 10 (ratio of 10.67 ± 8.68 vs 1.76 ± 0.61 for naive reciprocity) at the price of lower field strength at the targeted regions (0.086 ± 0.054 V/m for true reciprocity vs. $0.200.087 \pm V/m$ for naive reciprocity). Some considerations with this approach that are discussed include safety constraints (maximum allowable current), focality limits (dependent on electrode number,

size and position) and potential for an optimized close-loop stimulation.

2.3.3 Experimental Validation of Reciprocity Principle

Luu et al. [119] continued the approach of using the reciprocity principle to guide targeting of slow frequency pulsed stimulation. The study was comprised of several stages; first MRI images were acquired of 12 healthy individuals, next TMS (transmagnetic stimulation) mapping was used to determine the primary motor cortex location that provided the highest intensity index finger EMG response. The latter part of the study was comprised of generating an anatomically accurate FE head model for all the individuals and then providing stimulation (placebo, anodal or cathodal protocols) counter-balanced across participants using a 3*3 latin square design. The stimulation sessions were double blind (TMS operator and participants) separated by a maximum of 48 hours.

To generate the head model, each voxel of the the structural MRI data was segmented into one of seven tissue/material types: eyeball, flesh, skull, cerebral-spinal fluid (CSF), grey matter (GM), white matter, and air. 256 electric sensors are modeled as attached to the scalp surface. The cortical tissue mesh was divided into 1200 dipole patches with each patch about $1cm^2$ in size. current flow is calculated as the average perpendicular orientation of vertices within each patch. Calculation of a lead-field matrix (LFM) using the finite difference method (FDM) was used to compute current flow from each cortical path to all the sensor coordinates.

An optimal current injection setup was determined by using the Lorentz reciprocity theorem which relates injected current densities and their resulting electromagnetic fields in a complex resistive volume [123]. This is applied to TES (transcranial electric stimulation) through the principle that current injection based on a scalp voltage field generated by a dipole at a target will maximize current density at the target. The scalp voltage was mapped, injected current patterns were then shaped to conform to the scalp voltage amplitudes (generated by target dipoles) using 8 anodal and 8 cathodal electrodes

for a total of 16 electrodes. Electrode values were normalized so the maximum source (anode) and sink (cathode) were assigned weights of 1 and -1 respectively.

Pulsed, direct current stimulation was then applied with the voltages and electrical montage defined with the reciprocity theorem. Stimulation was driven by the prototype GTEN 100 system with a 256- channel HC GSN 100 which controls a network of evenly spaced Ag-Ag Cl electrodes. The GTEN uses a balancing circuit capable of maintaining a constant current (source-sink) configuration. Stimulation was comprised of pulses of 100 ms duration delivered at 0.5 Hz for 17 minutes. Lidocaine was used to minimize physical sensation caused by the current.

Relative to placebo, 8 participants who received cathodal stimulation and 5 participants who received anodal stimulation had a reduction of MEPs relative to placebo. These results showed that an inhibitory response, measured by a reduction of MEPs,(long term depression -LTD) was induced with low-charge reciprocity guide pulse with greater consistency than reported in prior research.

2.3.4 Reciprocity vs. Error Fitting Algorithms

M. Fernandez-Corazza compared reciprocity based optimization to traditional error fitting algorithms [118]. Four different cortical targets were defined in a 7 tissue FE head model. The performance of the reciprocity method in optimizing stimulation parameters (electrode density, targeting error, focality, intensity and directionality) is compared to the performance of least square (LS) and linearly constrained minimum variance (LCMV) algorithms. Results showed that the reciprocity approach performed comparably (improved intensity and directionality) to the LS and LCMV algorithms. Increasing the electrode mesh from 128 to 256 improved performance in all parameters (focality, density, and intensity).

Cancelli et al. [45] proposes the use of EEG data for reciprocity targeted stimulation without the computationally demanding use of anatomical head models for both source

localization and current injection modelling. The authors demonstrate a two step process where EEG signal topography is used to select locations for stimulation as well as to determine the amount of current to be injected in each electrode. This method is verified by use of FE model simulation that incorporates both head anatomy and dipole location. The study investigated a number of montages while varying the number of electrodes from a few to greater than 300. Results showed that model free use of EEG data could provide comparable results (as measured by performance parameters intensity, focality and directionality) to that provided with FE models with relatively few (2-8) electrodes.

2.4 Summary

This section of the thesis has provided a review of neurostimulation background, proposed mechanism of action and dose optimization methods. The focus of this review is on optimization methods in the simulation space that have generally not been compared to experimental data. We discuss here results of tDCS optimization methods that include genetic algorithms, linear superposition of electrode field using multiple electrodes, interior point optimization methods and reciprocity based approaches.

Part III

FEM Modelling

Chapter 3

FEM Model Description

This chapter describes in detail the realistic head finite element model that was used for the simulation work in this thesis.

3.1 Model Description

We adapt a realistic head model, described in [112, 124], for use as a platform for our simulation work. We used an already developed head FEM model geometry (segmentation and development work was not performed by the author). We however describe the process of model generation below (for further details see [112, 124]).

The realistic head model was generated from T1 and PD weighted MRI images aligned to MNI stereotaxic space of the single-subject template Colin27¹. The Brainsuite software package² was used to segment these images at a resolution of $1 \times 1 \times 1 \text{ mm}^3$. Segmentation resulted in 5 surface meshes; scalp, skull, CSF (cerebral spinal fluid), GM (grey matter) and WM (white matter). WM, GM and CSF were generated from T1 images whereas skull and scalp meshes were obtained from PD images. Segmentation of the cortex accurately captured the intricate cortical gyri and sulci.

The segmented mesh was then imported into Mimics³. Further refinement operations in

¹obtained from BrainWeb <http://brainweb.bic.mni.mcgill.ca/brainweb>)

²version 9.01, <http://www.loni.ucla.edu/Software/BrainSuite>

³version 14, <http://www.materialise.com/mimics>

Mimics included smoothing irregularities in the CSF outer surface and adding 2 cylindrical plugs (cross section of 100 mm^2) at the superior orbital fissures and the optic foramina representing eyeballs. Optical nerves were added to the optic canal; the optic chiasm (crossover point of the right and left medial retina fibres) was modeled in the intra-cranial fossa simulating the paths of the optical tracts. In addition the lateral ventricles were manually defined by thresholding operations. Twenty round 2 cm diameter electrodes were affixed to various locations on the scalp (defined by 10-20 EEG coordinates) electrodes. Finally a volume mesh (comprised of tetrahedral elements) was generated and exported to Comsol for FE analysis.

A 3D view of the realistic FE model with some electrodes is shown in Fig. 3.1. Fig. 3.2 shows the components/tissue layers of the model. Table 3.1 provides a basic quantitative description of each model component/tissues.

3.2 Summary

This chapter describes the FEM head model used as the basis of our simulation work. Details include a quantitative description of all the model components (layers, domains, surfaces, nodes...).

Model Component/Tissue	Description
Complete Model	<p>Quantities: Tetrahedral mesh element number: 2230952, Degrees of freedom: 3013088, Average tetrahedral mesh quality: 0.4512, Domains: 37, Faces: 106, Edges: 148, Points: 132, Volume: 3894 cm³</p> <p>Layers/Components: 26 electrodes, 6 tissue sub-layers/components (scalp, skull, csf, gm, wm, eye tissue)</p>
Quantities	<p>Statistics: Tetrahedral mesh element number: 542, Volume: .739 cm³, Surface area: 7.798 cm², Cylinder shape: Top of cylinder boundary surface area: 3.106 cm², Side of cylinder boundary surface area: 1.577 cm²,</p> <p>Location (10-20 EEG Coordinates): 26 positions: p07, c4, f4, c1, f7, fPz, c3, f8, pz, fz, o2, p4, fP2, po8, oz, o1, Af8, Af7, T8, fp1, p3, c2, t7, p7, cz, f3</p>
Scalp	<p>Quantities: Tetrahedral mesh element number: 314033, Volume: 1125 cm³, Surface area: 2448 cm².</p>
Skull	<p>Quantities: Tetrahedral mesh element number: 214599, Volume: 544 cm³, Surface area: 1969 cm².</p>
Cerebral Spinal Fluid	<p>Quantities: Tetrahedral mesh element number: 342772, Volume: 534.4 cm³, Surface area: 2687 cm².</p>
Grey Matter	<p>Quantities: Tetrahedral mesh element number: 873675, Volume: 931.2 cm³, Surface area: 3791 cm².</p>
White Matter	<p>Quantities: Tetrahedral mesh element number: 450684, Volume: 696.1 cm³, Surface area: 2063 cm².</p>
Eyeballs and Optical Nerves	<p>Quantities: Tetrahedral mesh element number: 19095, Volume: 41.11 cm³, Surface area: 140 cm².</p>

Table 3.1: Description of Model Components/Tissues

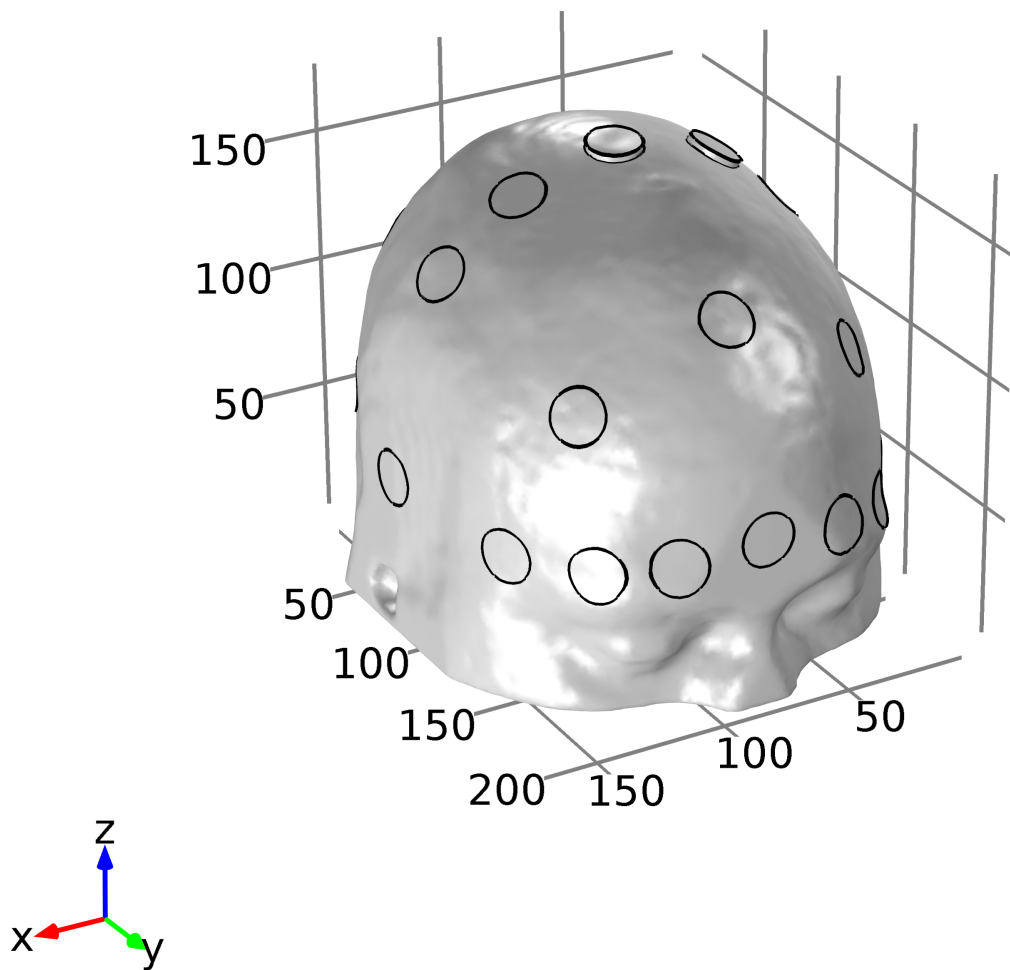
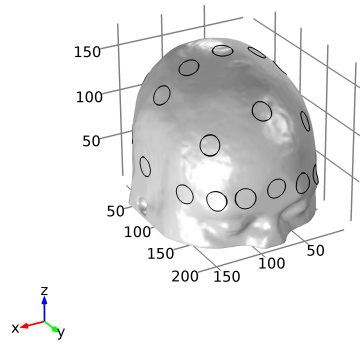
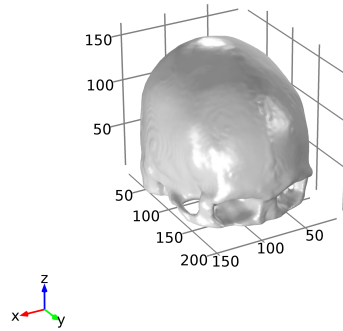


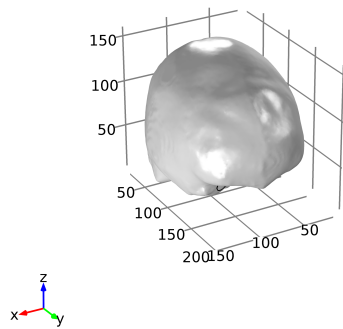
Figure 3.1: View of the head model in 3D Cartesian Space (units [mm]). Electrodes C2 and CZ are shown to the right of and at the scalp vertex. Locations of other electrodes are indicated by circles on the scalp.



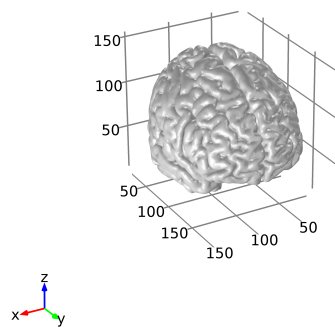
(a) Scalp



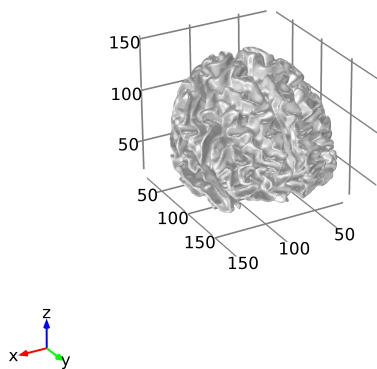
(b) Skull



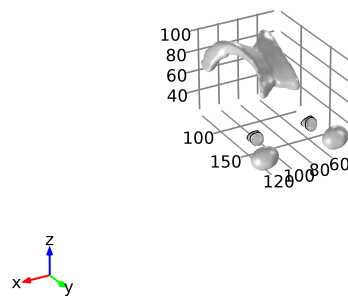
(c) Cerebral Spinal Fluid



(d) Grey Matter



(e) White Matter



(f) Eyeballs and Optical Nerves

Figure 3.2: Sub-figures (a)-(f) show the principal tissues/components of the head model

Chapter 4

Simulation of Bioimpedance Spectroscopy Measurements

We used Comsol Multiphysics ver. 5.1 for implementation of simulated multi-frequency measurements of the realistic human head FEM model described in Sec. 3.1. Section 4 provides a detailed description of the simulation setup and solution parameters.

4.1 Electrode montages

In the following section we describe the bipolar (2-electrode) and tetrapolar (4-electrode) montages used in our simulation work (Chapters 6–8). Electrode sites are provided using the International EEG 10 20 system [125] as well as in Cartesian and Spherical coordinates (Table 4.1).

4.1.1 Bipolar Electrode montages

Fig. 4.1 shows the four montages used to simulate bipolar spectroscopy measurements. We begin our simulations with the electrodes spaced closely together - montage CZ-C1 - as shown in Fig. 4.1 (a). The electrode pair is then separated as shown to the coordinates CZ-C3 as shown in Fig. 4.1 (b). The inter-electrode gap is further increased to CZ-T7 (Fig. 4.1 (c)). Finally we simulate the T7-T8 montage where electrodes are placed on diametrically opposed sites on opposite sides of the model head ((Fig. 4.1 (d)).

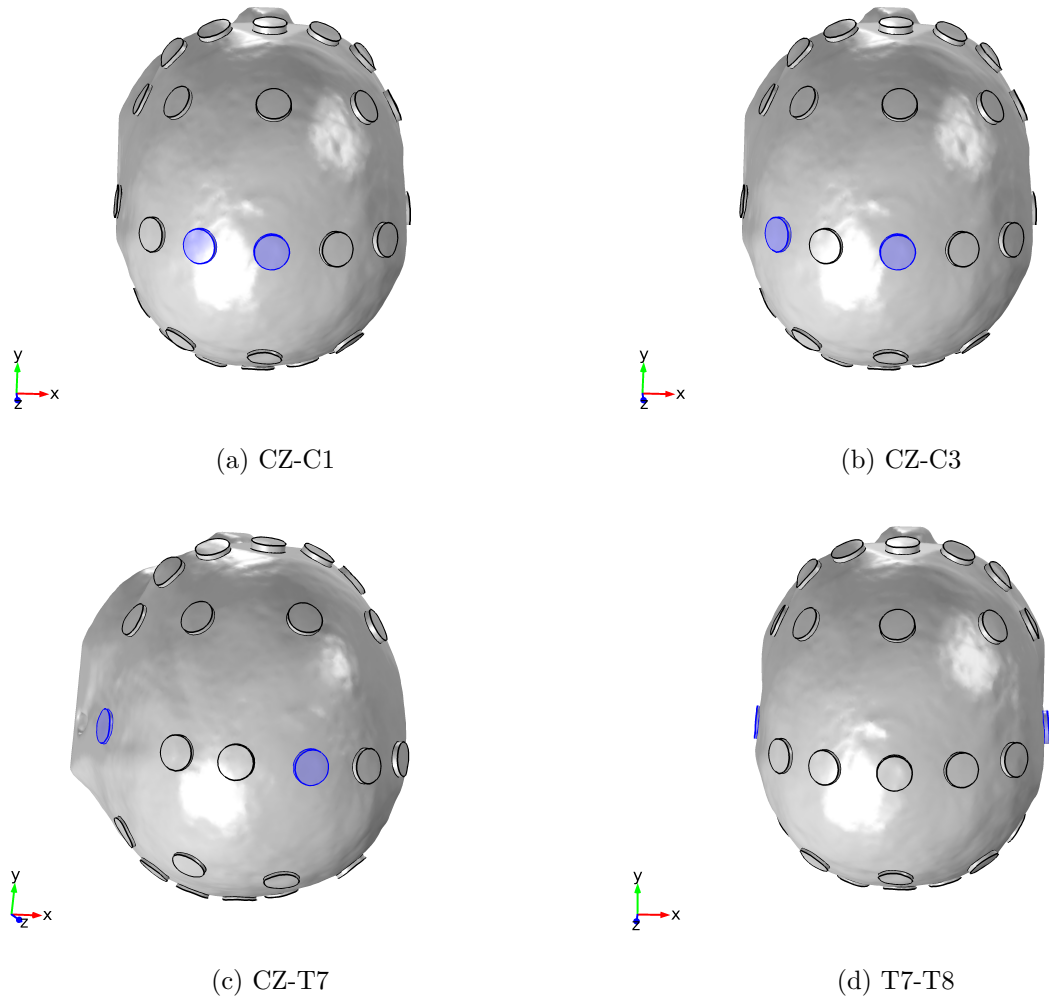


Figure 4.1: Plane view of four electrode montages used for 2 electrode simulations. The head model is oriented such that the nasion is shown at the top of the figure. Each electrode pair is shown highlighted. CZ-T7 (c) is shown tilted in order to clearly show temporal electrode T7. Electrode spacing is increased from (a) CZ-C1 to (d) T7-T8 (electrodes shown on the temporal sides of the head).

As described in section 4.4 we set one of the electrodes to positive potential and one to negative to drive current through the head tissues.

For the bipolar electrode montages we set CZ as the the negative electrodes (with the exception of the T7-T8 montage where T7 is set to a negative potential). The motivation for this was based on trial and error simulation work that showed a higher concentration of current density and sensitivity under the sink (cathode) than the source (anode). Thus our strategy targeting the cortical and sub-cortical ROIs (see section 4.2) is to place the cathode directly above these regions.

4.1.2 Tetrapolar Electrode montages

In addition to the bipolar configurations discussed above, we also simulate tetrapolar (four) electrode measurements. Specifically we simulate the C3-C1-CZ-C2 montage (Fig. 4.2 (a)), T7-C3-CZ-C2 (Fig. 4.2 (b)), and T7-C3-C4-T8 (Fig. 4.2 (c)).

For our tetrapolar measurements the outer electrodes are current drive and the inner ones are designated for voltage measurements. The electrode pair on the left side of the model head (relative to the face) are all set positive and those further to the left are set as negative (see section 4.4). Thus for the first montage C3 (+) and C2 (-) are a pair of current electrodes and C1 (+) and CZ (-) are a voltage measurement pair. For the second montage T7 (+) and C2 (-) are the current electrodes and C3 (+) and CZ (-) serve as the voltage pair. Finally our last montage consists of a current pair T7 (+), T8 (-) and a voltage pair C3 (+) and C4 (-).

Like for the bipolar montages, we simulate the spectra of a number of montages whereby the gap between the electrodes are systematically increased. First, the C3-C1-CZ-C2 montage is comprised of electrodes all sited on adjacent 10-20 coordinates. For the next montage, a gap is introduced between the current electrodes (so they are sited on C3 and CZ) and between the positive current and voltage electrodes (now sited on T7 and C3

respectively). Finally for the last montage the gap between the current electrodes is further increased (C3-C4) and the negative current and voltage electrodes are separated (C4-T8).

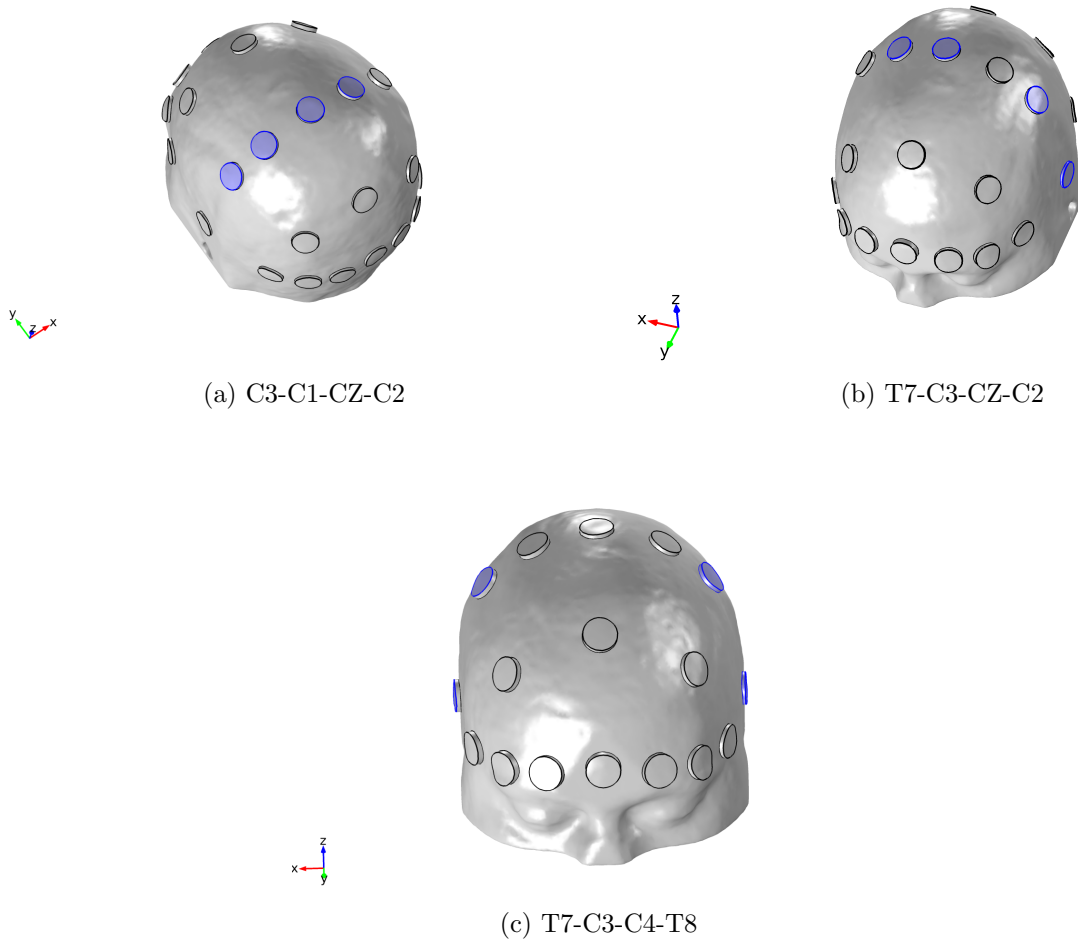


Figure 4.2: Illustration of electrode montages used for 4 electrode simulations. Each electrode part of the montage is shown highlighted. Electrode spacing is increased from (a) C3-CZ-C1-C2 (electrodes all adjacent) to (b) T7-C3-CZ-C2 (gap increased between voltage electrode pair C3-CZ and current-voltage pair T7-C3) to (c) T7 C3 C4 T8 (large gap between current pair C3-C4, and gap between voltage pairs T8-C4 and T7-C3) (electrodes shown on the temporal sides of the head).

4.2 Region of Interest Setup

In order to demonstrate the focality and resolution of current stimulation and impedance measurement we simulate regions of interest (ROIs) in various intracranial areas as described below.

4.2.1 Cortical grey matter ROI

It is challenging to directly determine the realm of influence of non-invasive electrical treatments such as tDCS (transcranial direct stimulation) due to the wide spread of current throughout the brain and the low-intensity sub-action potential threshold interaction of current with neurons [106]. In general however, current flow through the brain, affected in part by electrode montage, is associated with neuro-physiological effect [35].

The cerebral cortex, the most exterior part of the brain, is a common target for neuro-stimulation paradigms such tDCS [126]. Studies have shown that tDCS can modify the physiological properties of cortices related to the visual, somatosensory and prefrontal areas [16, 85, 127–129].

Fortuitously, the close location of the cortex to the electrode stimulation site on the scalp, ensure that current can be delivered to cortical targets with sufficient strength to drive physiologically significant changes [35].

As part of our analysis we simulate a cortical ROI in the frontal lobe motor cortex region at the CZ or apex of the brain. Although the physiological function of the brain area associated with CZ may not be significant, it is simply our intent to simulate a cortical ROI in a region easy to locate. The ROI may be simulated in any other cortical region.

The ROI (see Fig. 4.3) is set in the grey matter domain across the boundary separating the right and left hemispheres. The ROI was simulated approximately in a cube shape with x and y dimensions of 20 mm across and about 10 mm along the z axis. Dimensions of the ROI in the XYZ space are defined as ($z > .14$), ($x > .08, x < .1$), and

($y > .1, y < .12$) where units are meters. Due to the position of the grey matter ROI across the fissure separating the right and left hemisphere, the ROI is segmented into 3 parts.

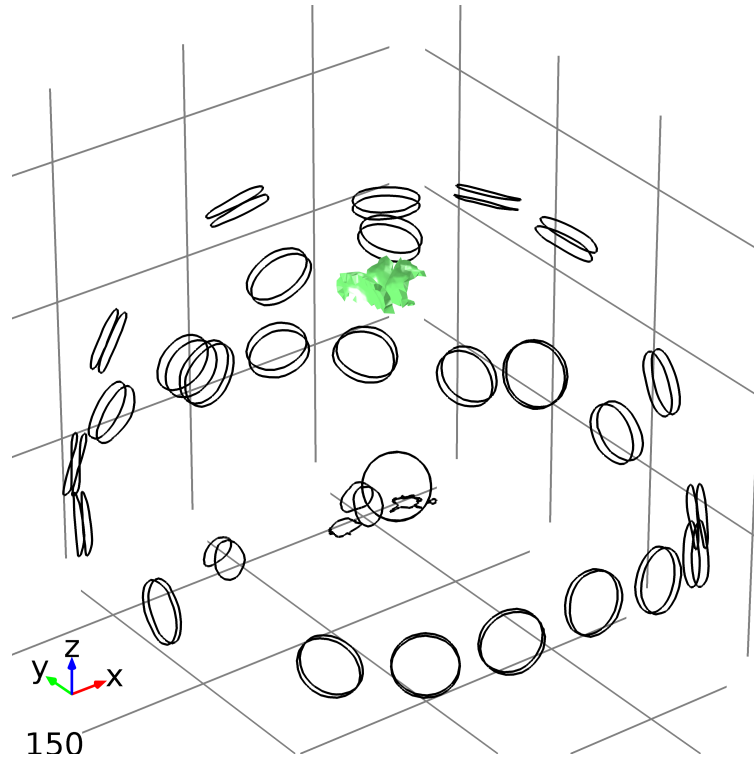


Figure 4.3: View of the grey matter cortical ROI positioned under the CZ electrode coordinate.

4.2.2 Sub-Cortical white matter ROI

We explore the possibility of targeting deeper (non-cortical) brain structures such as the surface of the white matter. Many neuro-physiological disorders, such as Parkinson’s, affect deep brain structures. It is thus important to assess the ability to focus and target these structures with sufficient intensity to induce beneficial effect. Indeed some authors have demonstrated that stimulation current flow can be steered towards deep brain structures such as the left inferior frontal gyrus (IFG) [130]. Others have investigated the spread of tDCS current in neural areas such as white matter, the cerebellum, the hippocampus, the medulla oblongata, the pons, the midbrain, and the thalamus [92].

We select white matter as a meaningful target due to its critical role in brain function. It has been shown that white matter is associated with learning, control of nerve transmission by acting as a relay between various neural regions and by modulation of action potential [131]. The position of the white matter, inferior to grey matter, does allow us somewhat to assess the ability to target non-superficial neural regions.

We set the sub-cortical ROI in the white matter domain, see Fig. 4.4. Dimensions of the white matter ROI are the same as described in section 4.2.1 except that the ROI is shifted 10 mm lower on the Z axis. Dimensions in the XYZ space are thus ($z > .13$), ($x > .08, x < .1$), and ($y > .1, y < .12$). Like the grey matter target, the white matter ROI is segmented into 3 parts due its' location on fissure dividing the brain hemispheres.

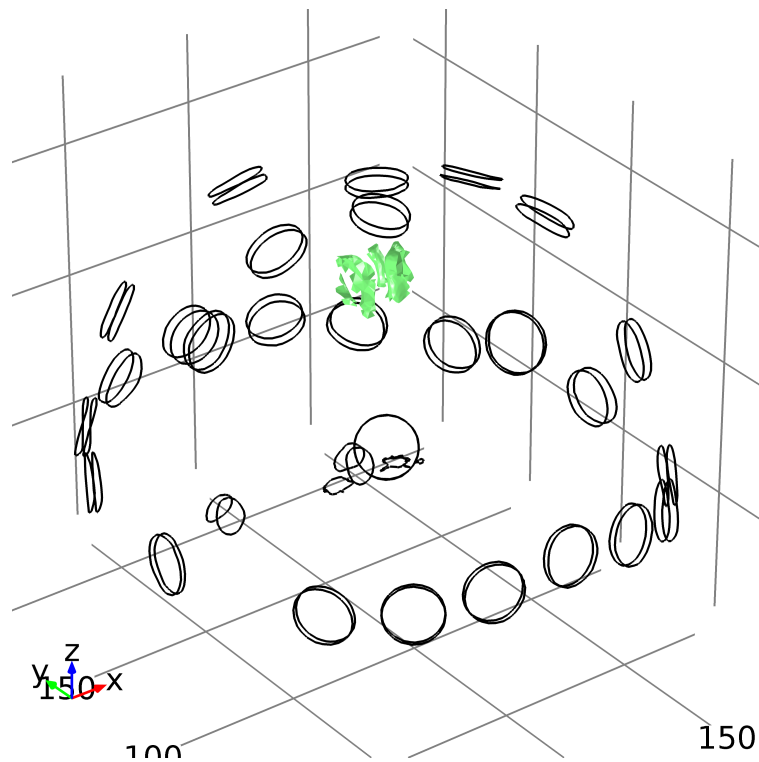


Figure 4.4: View of the white matter cortical ROI positioned under the Cz electrode coordinate.

4.2.3 Whole Brain

We also assess the ability of stimulation and measurement current to target the entire brain. In some clinical applications, such as impedance measurement of effect of stroke [132, 133] and brain activity [134, 135], a large neural target provides sufficient resolution.

In fact, despite the relatively large anatomical dimensions of the brain, direct electrical measurement/stimulation of this organ provides a set of challenges due to the attenuation and shaping of the electrode field caused by surrounding tissue layers including the scalp [71, 136, 137], CSF [106, 137] and skull [136, 137].

We therefore analyze a simulated BIS measurement on the entire functional region of the brain (see Fig. 4.5 for an illustration of the total brain ROI). We investigate if the measurement sensitivity to neural tissue and if this measurement can be separated from the total measured impedance.

4.3 Spherical Coordinates

The shape of the human head approximates a sphere, thus electrode and ROI positions can be expressed in spherical coordinates [138] defined by θ , ϕ and r (Fig.4.6).

Due to the symmetry of the head, as well as our desire to simplify this analysis we restrict our simulated montages to coordinates that vary along the polar θ angle.

This angle can be defined through an imaginary line extending through the central vertex CZ to temporal areas of the head (T7 and T8) which can be defined in terms of radial distance from this point of origin. The point of origin itself is defined as having a null θ angle. We define r as positive so that $r \geq 0$.

The bipolar montages (described in section 4.1.1 essentially consist of fixing one electrode the pair at the center vertex CZ. The position of the second electrode is varied along a line

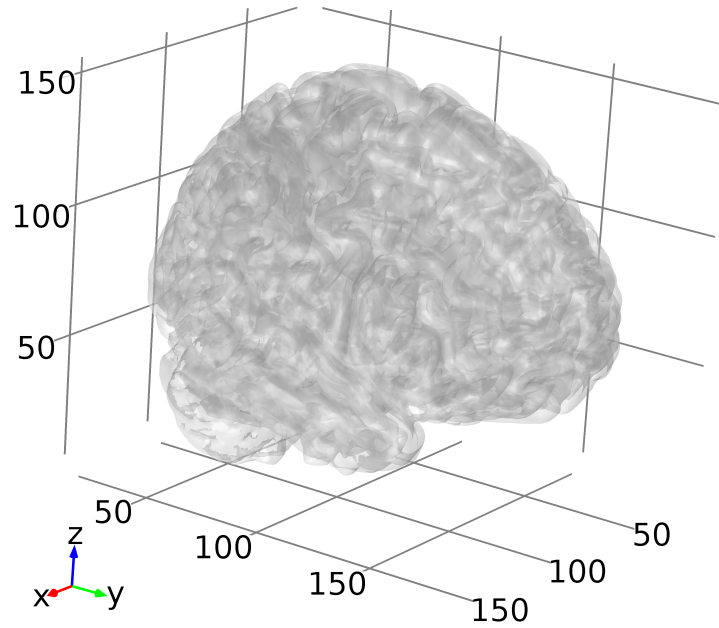


Figure 4.5: Transparent image of the brain showing the structure of the grey and white matter.

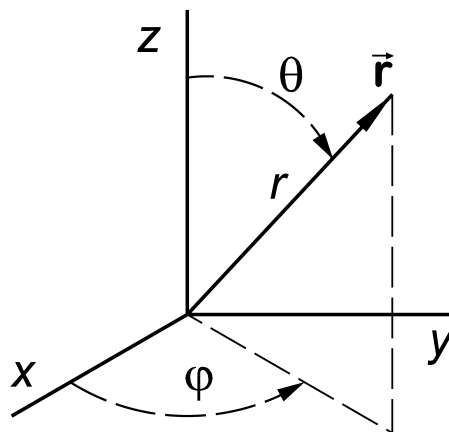


Figure 4.6: \vec{r} , representing electrode and ROI location, can be defined by radial distance r , inclination angle, θ and azimuthal angle ϕ .

extending from the center vertex to the temporal scalp above the left ear. This represents changing electrode position along the angle θ of the spherical head. The final bipolar montage (T7-T8) is varied such that each electrode is placed on the the temporal scalp above the right and left ear respectively.

The tetrapolar montages (see section 4.1.2) are also varied as a function of changes to θ . As described in section 4.1.2 the angle between different combinations of current and voltage electrodes are systematically increased.

We therefore show all electrode and ROI locations converted from xyz cartesian coordinates to spherical coordinates - r and angles θ and ϕ . (ϕ is included since the electrodes are not points sources and thus can be described along the azimuthal ϕ angle as well).

Cartesian xyz coordinates are first determined using the **measure** function in the **evaluate** tab of Comsol 5.1. Coordinates are provided with reference to a point of origin outside the FEM model. We translate the coordinates so that the origin of reference is located at the base of the head model.

We then convert to spherical coordinates according to the following relationships:

$$r = \sqrt{x^2 + y^2 + z^2} \quad (4.1)$$

$$\theta = \arccos \frac{z}{r} \quad (4.2)$$

$$\phi = \arctan \frac{y}{x} \quad (4.3)$$

Table 4.1 below lists all the cartesian and spherical coordinates of the electrode and ROI locations.

This table thus provides the angular distances between the various electrode coordinates, thus for example the θ angle between the center vertex CZ and the adjacent electrode site of C1 is 12.22°.

Name	Cartesian Coordinates(x,y,z)	Spherical Coordinates (r, θ , ϕ)
GM ROI	(-2.92, 0.32, 141.30)	(141.33, 1.19, -6.25)
WM ROI	(-2.92, 0.32, 134.54)	(134.57, 1.25, -6.25)
CZ	(0, 0, 171.29)	(171.29, 0.00, 0)
C4	(-70.05, -1.02, 137.51)	(154.33, 27.00, 0.83)
C1	(34.9, 2.09, 161.49)	(165.23, 12.22, 3.42)
C3	(65.93, 1.08, 138.05)	(152.99, 25.53, 0.93)
T8	(-89.81, -3.11, 60.92)	(108.57, 55.87, 1.98)
C2	(-44.37, 1.92, 159.25)	(165.33, 15.58, -2.47)
T7	(85.95, -2.44, 62.80,)	(106.48, 53.86, -1.62)

Table 4.1: List of ROI and electrode Cartesian and spherical coordinates

4.4 Boundary conditions

We imposed the following boundary conditions; the current density normal component was set to be continuous across all inner boundaries and electric insulation was applied to all outer boundaries [139]. We simulate the potential difference on the current electrode pair by setting Dirichlet boundary conditions of $\Phi = \Phi_0$ to the electrodes [139]. In addition we follow FEM convention by setting the derivative of the potential normal to the head model to 0 (Neumann boundary conditions are $\sigma \nabla \phi \cdot n = 0$). This condition forces the electric current not to cross the exterior boundary of the model, this represents experimental conditions where the injected current pathway is restricted to the biological tissue under test. For each current electrode pair (see section 4.1.1 and 4.1.2 we adjusted $+\Phi$ to one electrode and $-\Phi$ to the other in order that 1 milliamp is driven into the tissue [139]. We chose a unity quantity of current to enable easy scaling and comparison of simulated stimulation (typically in the mA range) and measurement (μ A range). The Laplace equation $\nabla \cdot (\sigma \nabla V) = 0$ was then solved on the finite element mesh [140, 141]. In section 4.8 we describe variables and parameters calculated for simulation.

4.5 Material Properties and Frequency Range

Tissue impedance is frequency dependent, thus at each frequency point a separate conductivity and permittivity value was required as a material property input for each tissue type.

Reliable data regarding the dielectric frequency of human tissues are scarce. In general we relied heavily on a literature review and series of data collection experiments described by Gabriel et al. in [53–55,142]. The motivation of the work described in these papers was to provide reliable tissue dielectric spectra for models used in the study of electromagnetic dosimetry. The development of anatomically accurate models from medical imaging data, for example see [143], enabled researchers to study the interaction of EM fields with exposed tissues in great resolution and detail. Technology advances have enabled segmentation of many (over 30 [53]) tissue types, thus necessitating the compilation of an accurate record of the dielectric spectra of these tissues.

In general, biological dielectric response results from the interaction of an em field at a cellular and molecular level of a tissue [53]. The mechanisms of interaction have been extensively studied and reviewed and the typical features of a biological dielectric spectrum have been elucidated [144–149]. In summary:

- The relative permittivity of a tissue is very high at low frequencies (10^6 or $10^7 < 100$ Hz)
- Permittivity decreases over frequency in 3 major dispersions referred to as α , β and γ .
- The α low frequency dispersion is related to ionic diffusion through cellular membranes
- The β dispersion (100's of KHz) can be attributed to polarization of cellular membranes, protein and organic macromolecules.

- The γ dispersion (GHz range) is caused by water molecule polarization

In [53], dielectric properties of tissues are derived from the complex relative permittivity

$$\vec{\epsilon} = \epsilon' - j\epsilon'' \quad (4.4)$$

where ϵ' is the relative permittivity and ϵ'' is the out of phase loss factor which is defined as

$$\epsilon'' = \sigma / \epsilon_0 \omega \quad (4.5)$$

where σ is conductivity (SI units Siemens/M), ϵ_0 is the permittivity of a vacuum ($8.854187817 * 10^{-12}$ Farads/M) and ω is the angular frequency (radians/sec).

Literature review results are displayed in a graphical format as ϵ' vs ϵ'' or ϵ' vs σ . In our modelling work we use the ϵ' and σ to define the frequency dependence of the head tissues.

In [54] it was noted that a review of published dielectric spectra revealed data gaps for certain frequencies ranges and tissues. In addition dielectric values measured by different authors for a single tissue are often inconsistent. In order to address these shortcoming, Gabriel et al. [54] measured the dielectric properties of a variety of biological tissues using 3 different impedance analyzers to cover a wide frequency range (10 Hz - 20 GHz). Sources of tissues were excised animal tissue (ovine and porcine), human cadavers and human tongue and skin in-vivo. In order to address remaining gaps in dielectric data for some materials, Gabriel et al. [55] used a 4 parameter Cole model for interpolation and data fitting.

Experimental data from [53–55, 142] of over 100 tissue types was compiled in a database by The Foundation for Research on Information Technologies in Society (IT'IS) [150]. We exported tissue conductivity and frequency from this database for use in our simulation work.

Scalp tissue was not included in the database, thus we had to consider the constituent scalp tissues - fat and muscle. In our modelling work scalp tissue assignment is of critical importance since scalp impedance greatly influences the BIS measurement due to high

current densities in the boundary layer (see section 2.5.2 in [151]). In order to simplify our model we relied on [151] which modeled scalp tissue as a homogeneous layer of skeletal muscle.

For the remaining head tissues we extracted conductivity and permittivity of the following tissues: cortical skull, CSF (cerebrospinal fluid), GM (grey matter), WM (white matter), and the eye (vitreous humor). Data was extracted in the frequency range 1 Hz to 1 GHz, logarithmically spaced at 5 points per decade. We selected this wide range in order to cover the frequency response of the tissues over the α , β and γ dispersion zones.

Material properties are defined in Comsol across space (assuming there is no change in time). In our case our model is defined in a 3D space defined by Cartesian coordinates. A 3*3 matrix (representing the x, y and z conductivity components along the x, y z coordinates) is used to define the material properties. In our case we use isotropic material properties, this is represented as a single scalar which is identical along the x, y and z directions [152]. ¹

We assigned the electrodes the conductivity of 2 S/m to represent the high conductivity of saline soaked sponges or gel [112]. It was shown in [154] that a simulated frequency measurement is sufficiently accurate without modelling the frequency dependence of the electrode material. Following this approach we approximated the relative electrode permittivity as $\epsilon_r = 1$.

4.6 Probe setup and Simulated Noise

Parameters described below in section 4.8 are calculated by integration over volume domains representing the electrodes and head tissue layers (scalp, skull, CSF, GM, WM and eye tissue). Voltage is calculated across boundary domains (electrode and tissues). For

¹The influence of tissue anisotropy on intra-cranial current distribution has recently been studied [96,102,153]. In order to simplify our analysis however we limit our investigation to head tissue materials assumed to be isotropic [71,112]. Study of anisotropic material properties may be considered in future work.

each solved frequency point, parameters all calculated for each domain.

4.7 Simulated noise

In order to account for experimental noise (see for example [155, 156]) and to allow meaningful comparison of model results to experimental data (see chapter 10), we add random normally distributed Gaussian noise. Gaussian noise is used as a method of mimicking natural sources of noise that occur during experimental measurements [56, 157, 158]. In the context of our work experimental noise is assumed to have a normal distribution.

In order to generate noise we use the built-in random function in Comsol which is written as **rn**. **rn** was set to return random Gaussian noise normally distributed with a mean of 0 and a standard deviation of 1. The probability density function (PDF) of **rn** is written as

$$f(x) = \frac{1}{\sigma_n \sqrt{2 * \pi}} * \exp\left(\frac{-(x - \mu_n)^2}{2\sigma_n^2}\right) \quad (4.6)$$

where σ is the standard deviation and μ is the mean. For a calculated element we then simulate noise by multiplying **rn** by 5% of the amplitude of the element. For instance we can write scalp impedance as $scalp_{imp}$. Then noise is added according to $scalp_{imp} + .05 * scalp_{imp} * \mathbf{rn}$. For each simulation run over the our frequency range (see section 4.5, 6 probes are added to each tissue/electrode domain or boundary. If the integrand is a complex quantity (for instance sensitivity or impedance) then noise is also added to imaginary phase. The effect of this noise can be seen in the y offset of the error bars in Nyquist plots of simulated impedance in chapter 8. This level of noise is chosen as a conservative estimate of experimental noise resulting Solatron measurements (see section describing calibration in chapter 9 for more detail of measurement error). In order to simulate random noise, we use a different seed to initialize a pseudo-random generator for each probe measurement (for a detailed discussion of pseudo-random generators see [159]).

Each probe then mimicked the output of a single measurement or sample with random noise added. For a single simulation we then had 6 samples or measurements for each head tissue.

We then calculated the mean value of the probe measurements, the standard deviation and the standard error of the mean (standard deviation divided by number of samples).

Generally results (see chapters 6- 10) are shown as mean values, added error bars are the standard error of the mean.

4.8 Calculated Dose and Measurement Parameters

We describe the fundamental parameters of interest (related to dose and measurement) that will be calculated. All parameters solved for the range of the frequency sweep.

Equations are provided and described for each parameter.

4.8.1 Electric Field

The intra-cranial electric field can be considered a fundamental dose quantity for neuro-stimulation applications such as tDCS [35]. Lasting physiological effects have been attributed to electric fields changing membrane polarization coupled with long term neuroplastic changes (long term potentiation and depression) [160, 161].

Numerous studies [92, 95, 108, 112, 137, 162] have therefore been devoted to determining electric field dose during neurostimulation. Studies have shown the effect of parameters such as electrode dimension and position [84, 163, 164], and tissue anatomical and electrical properties [96, 101, 165] on shaping the intra-cranial distribution of the electric field.

In line with previous research we therefore simulate the electric field in the brain and throughout the head tissues. We specifically investigate the effect of frequency and electrode position on the electric field distribution. We calculate the norm or magnitude of

the electric field which is given by

$$E_{norm} = \sqrt{e_x^2 + e_y^2 + e_z^2} \quad (4.7)$$

where e_x^2 , e_y^2 , and e_z^2 are the x, y and z components of the electric field respectively.

This variable in the Comsol environment is defined as `ec.normE`. SI units are given as V/m.

The Laplace equation, given by

$$\nabla \cdot (\sigma \nabla \varphi) = 0 \quad (4.8)$$

is solved to find the distribution of the potential field φ . This quantity is related to the electric field according to

$$E = -\nabla \varphi \quad (4.9)$$

In Comsol this was defined as `V` (`V` is also given as the unit).

4.8.2 Current Density

Current density is also a fundamental dose parameter which is related to the electric field by the relationship

$$J = \sigma E \quad (4.10)$$

Current density distribution during neurostimulation has been investigated primarily using FEM head models [92, 95, 166, 167]

We also simulate the current density in the head tissues and the electrodes. We solve for current density magnitude or norm which like the electric field norm is given by

$$\|J\| = \sqrt{ec.Jx^2 + ec.Jy^2 + ec.Jz^2} \quad (4.11)$$

where $ec.Jx$, $ec.Jy$ and $ec.Jz$ are the x, y, z current density components respectively. Units of this quantity are given as A/m^2 .

4.8.3 Sensitivity and Impedance

The concept of a sensitivity field can be applied to linear systems that are reciprocal [168]. Helmholtz described the principal of reciprocity in a volume conductor as

$$I_l/V_d = i_r/V_d \quad (4.12)$$

where I_l is current measured in an ammeter connected to a volume conductor, induced by a dipole in the volume whose voltage is V_d , and i_r is current induced in the same volume conductor if the ammeter were replaced by a voltage source of the same magnitude V_d [169].

McFee and Johnston [170] later defined the concept of a lead vector- \vec{J} - as the magnitude and direction of current at a volume element caused by injecting a unit current through the lead (electrode). The current, comprised of all the lead vectors, is formed into a vector field in the volume conductor.

Geselowitz [58] used the reciprocity theorem to show that the sensitivity of a tetrapolar impedance measurement is defined as the scalar product of the vector current densities (the lead fields) for unit current injection between the two pairs of current and voltage electrodes. In his paper this is written in the form of

$$\Delta Z = -\Delta g \int \frac{\nabla(\phi + \Delta\phi)}{I_\phi} \cdot \frac{\nabla\psi}{I_\psi} dv \quad (4.13)$$

where Δg is a change in conductivity, I_ϕ and I_ψ are current injected into a volume between two different pairs of ports (or electrodes). $\nabla\psi$ and $\nabla\phi$ are the divergences of the electric scalar potentials that are associated with I_ϕ and I_ψ . Finally $\Delta\phi$ is a change in potential ϕ that causes a change in conductivity g .

The term for impedance in a material with non-uniform conductivity is derived from the reciprocity theorem by Lehr [171]. This is further developed in Larson et. al. [172] for the complex AC impedance measurement.

We reproduce here the derivation in [172]. We consider a finite region defined by electrical properties σ and ϵ . Four electrodes are placed on the material in 2 pairs. One pair is defined as AB and the second pair is CD. Current injected through AB results in a electric potential distribution of $\phi(r)$, conversely current inject through the CD pair causes an electric potential distribution of $\psi(r)$.

According to the reciprocity theorem we have

$$Z = \frac{\phi_{AB}}{I} = \frac{\psi_{CD}}{I} \quad (4.14)$$

Now we use the properties of the divergence theorem along with the complex part of conductivity (representing displacement current) to write the following relationship

$$\iiint_v \psi(\nabla \cdot [(\sigma + j\omega\epsilon)E_\phi]) + (\sigma + j\omega\epsilon)E_\phi \cdot \nabla\psi \, dv = \oint_s \psi(\sigma + j\omega\epsilon)E_\phi \cdot ds \quad (4.15)$$

Since there are no sources within the medium, $\nabla \cdot [(\sigma + j\omega\epsilon)E_\phi] = 0$. Then eq. 4.15 can be rewritten as

$$\iiint_v \psi(\sigma + j\omega\epsilon)E_\phi \cdot \nabla\psi \, dv = \oint_s \psi(\sigma + j\omega\epsilon)E_\phi \cdot ds \quad (4.16)$$

We can neglect the normal component of the electric field at all points besides the current electrodes. We can then rewrite eq. 4.18 as

$$\iiint_v \psi(\sigma + j\omega\epsilon)E_\phi \cdot \nabla\psi \, dv = \phi_A I - \phi_B I = \phi_{AB} I \quad (4.17)$$

If we divide both sides of eq. 4.18 by I^2 and replace $\nabla\psi$ with E_ψ we can write

$$\iiint_v \frac{\psi(\sigma + j\omega\epsilon)E_\phi \cdot E_\psi}{I^2} \, dv = \frac{\phi_{AB}}{I} \quad (4.18)$$

Using the relationship of $J = \sigma E$ accounting for the complex part of conductivity and using eq. 4.14 we can write

$$Z = \int \frac{J_\phi \cdot J_\psi}{(\sigma + j\omega\epsilon)I^2} dv \quad (4.19)$$

then the sensitivity is

$$S = \int \frac{J_\phi \cdot J_\psi}{I^2} dv \quad (4.20)$$

where σ is the specific conductivity of each tissue given in units of S/M, ω is the angular frequency and ϵ is the relative permittivity (see also [172, 173]).

We calculate the transfer impedance and sensitivity of tissues in a head FEM for various electrode montages as will be discussed in detail in later chapters.

4.8.4 Focality

In the context of neurostimulation electric field focality is described as the distribution of the field in a sphere of defined radius around the target. A useful metric is the half max radius which is defined as the radius that contains half of the electric field magnitude [59]. A small half max radius can be understood as a focal electric field since the field is highly concentrated in a small spherical region.

Here however we define focality using a similar definition in terms of magnitude of electric field delivered to the desired ROI.

We have defined 3 ROIs, a grey matter ROI, a white matter ROI and the whole brain (see section 4.2)

Focality of the grey matter ROI is the ratio of the electric field in the grey matter ROI to the electric field in the whole brain (here we include the CSF)

$$GM \text{ ROI focality} = \frac{EF_{GM \text{ ROI}}}{EF_{Brain}}$$

where EF is the magnitude of the electric field. Similarly focality of the white matter ROI is

$$WM\ ROI\ focality = \frac{EF\ WM\ ROI}{EF\ Brain}.$$

Finally we define focality of the brain as the ratio of the electric field in the brain (CSF, grey matter, white matter, eye tissue) to the total electric field injected into the head tissues. This can be written as:

$$Brain\ focality = \frac{EF\ Brain}{EF\ Total}.$$

4.9 Summary

In this chapter we described many aspects related to simulating and solving our FEM model. Included in this discussion is a description of the type of montages used (four bipolar and three tetrapolar). We discuss how we selected the coordinates of various (ROIs') regions of interest (cortical, white matter and all the neural tissue). We also convert the cartesian coordinates describing electrode montage and ROI position to spherical coordinates. Thus electrode gap can be described in terms of change to the θ angle. We describe in detail our selection and rationale for the boundary conditions imposed on the surface of the head model and on the electrodes. We then describe in detail our methodology for selecting material properties (conductivity and permittivity) as well as the simulated frequency range. We then describe our use of virtual probes for measurement, the number of samples measured for simulation and how we add 5% random Gaussian noise to simulation probes. This chapter concludes with a discussion and definition of dose parameters that we calculate (electric field, current density, sensitivity, impedance and focality).

Chapter 5

Solver configuration

In order to approximate the continuum behavior of real life physics problems FEM models are discretized into many discrete nodes. The number of unknown variables per node are referred to as node degrees of freedom (DOF). Typical high resolution FEM models, such as the head model used in this thesis, have millions of DOF. The size of the matrices, representing the applied physics problem in the model space are expensive to solve both in terms of required computational resources and solution time duration. Appropriate solver selection is thus critical to ensuring that problems are solved efficiently as possible without excessive demands on memory and processing power.

The nature of our modelling problem (solving many frequency points over millions of DOF see section 4.5 and table 3.1) required a fast and efficient solver configuration that would not overwhelm available memory and computational resources of our processing platform.

In this section, we therefore discuss the common FEM solver methods to provide some background context. We describe results achieved with different solvers and the set of considerations that led us to our choice of an appropriate solver configuration.

5.1 Solver Types

5.1.1 Linear Solvers

A simple linear static problem can commonly be generalized in the compact form of

$$AX = b \tag{5.1}$$

where X is a matrix representing the unknown variable/s and b and A are matrices representing material properties and boundary conditions respectively [174].

In general, the fastest method to solve matrix systems in the form of equation 5.1 involves the use of direct solvers such as MUMPS (MULTifrontal Massively Parallel sparse direct Solver) [175–177], Pardiso (PARallel sparse Direct and multi-recursive Iterative Linear SOLvers) [178–180], and Spooles (SParse Object Oriented Linear Equations Solver) [181].

For a small set of equations, direct solvers are generally based on LU (Lower Upper) factorization which is performed prior to direct matrix manipulation operations using the standard Gaussian Elimination Method [182].

LU factorization [182] is a technique whereby a matrix is factored or decomposed into the product of a lower and upper triangular matrix. If A is an invertible square matrix, then appropriate row and column orderings can be used to factorize A in the form of

$$A = LU \tag{5.2}$$

where L and U are a lower and triangular matrix. Thus if A is a 2-by-2 matrix then the factorization of equation 5.2 can be written in the form of

$$\begin{bmatrix} A_{11} & A_{12} \\ A_{21} & A_{22} \end{bmatrix} = \begin{bmatrix} L_{11} & 0 \\ L_{21} & L_{22} \end{bmatrix} \begin{bmatrix} U_{11} & U_{12} \\ 0 & U_{22} \end{bmatrix} \tag{5.3}$$

Factorization allows direct solvers to break up the problem matrix to a more manageable size. Despite this reordering, some models with a very large number of DOF's cannot be

solved in a reasonable time with the standard computing power and resources of an average PC. In addition large sparse matrices require a huge amount of time and memory using a direct solver approach.

Due to the large number of elements and DOF's of our model (see description in section 3.1) our FEM required a very large time to converge using direct solvers. Due to the limits of processing power and memory resources of our computing platform we found the use of direct solvers to be impractical. We thus needed the use an iterative solver method as a core approach in solving our FEM problem.

5.1.2 Jacobi and Gauss-Seidel Iterative Solvers

Iterative solvers are not designed to directly solve the solution of the form of Eq. 5.1.

Instead an initial guess , u_0 , is made as to the solution of the equation. This results in a new solution u_1 . The residual error resulting from this guess is calculated and then a new approximation is provided.

The simplest iterative solvers use the Jacobi Method [183]. For a square system of equations in the form of

$$AX = b \tag{5.4}$$

A can be decomposed in D and R, where D is the diagonal component (non-zero values on the diagonal) and R is the remainder (zero-diagonal values). The solution of equation 5.4 is in the form of

$$X = A^{-1}b \tag{5.5}$$

Rewriting this in terms of D and R for k iterations we have

$$x^{k+1} = D^{-1}(b - Rx^k) \tag{5.6}$$

where x^k and x^{k+1} is the k^{th} and $k^{th} + 1$ iteration over x respectively.

Convergence is achieved, when for a given approximation X_0 of X , the residual of a system of equations (such as $A^{-1}b - X_0$ as based on Eq. 5.4, 5.5), is minimized below a predefined tolerance.

Matrices of a linear system that are diagonally dominant or symmetric and positively definite can be converged using the Gauss-Seidel method [183].

A can be decomposed into a lower and upper triangular matrix so that $A = L + U$. Then Eq. 5.4 can be written as

$$(L + U)X = b \tag{5.7}$$

This can be rewritten in the form of

$$X = L^{-1}(b - UX) \tag{5.8}$$

Iteration of Eq. 5.8 leads to an expression in the form

$$x^{k+1} = L^{-1}(b - Ux^k) \tag{5.9}$$

where the k^{th} iteration of the right hand of equation 5.9 leads to a $k^{th} + 1$ expression for x.

In practice, neither of these solvers successfully converged any of our FEM models. We thus required a more robust iterative method.

5.1.3 Biconjugate Gradient Solvers

In general convergence is achieved by finding the local minimum (or solution) of equations defining a problem. For certain function gradient shapes, it has been shown that following conjugate (or orthonormal) directions results in faster convergence than that which can be achieved by simply following the steepest gradient [184].

The conjugate gradient method is the standard iterative technique used in symmetric systems where the coefficient matrix is positive definite. This method breaks down for

nonsymmetric systems since the residual vectors can not be orthogonalized with short recurrences (recursive expressions) [185].

The Biconjugate gradient method was thus introduced in order to retain the advantages of short recurrences, which are critical for ensuring low storage requirements. Here 2 sequences of residuals are calculated for A and its transpose A^T . The recursive relation for the i^{th} iteration can be written in the form of

$$r^{(i)} = r^{(i-1)} - \alpha_i A p^{(i)} \quad (5.10)$$

$$\bar{r}^{(i)} = \bar{r}^{(i-1)} - \alpha_i A p^{(i)} \quad (5.11)$$

with the p search directions defined as

$$p^{(i)} = r^{(i-1)} + \beta_i A p^{(i)} \quad (5.12)$$

$$\bar{p}^{(i)} = \bar{r}^{(i-1)} + \beta_i A p^{(i)} \quad (5.13)$$

.

The coefficients α_i and β_i are defined as

$$\alpha_i = \frac{\bar{r}^{(i-1)T} r^{(i-1)}}{\bar{p}^{(i)T} A p^{(i)}} \quad (5.14)$$

$$\beta_i = \frac{\bar{r}^{(i)T} r^{(i)}}{\bar{r}^{(i-1)T} r^{(i-1)}} \quad (5.15)$$

which ensures the orthogonality of the residual vectors and the search directions. In other words for $i \neq j$

$$\bar{r}^{(i)T} r^{(j)} = \bar{p}^{(i)T} A p^{(j)} = 0 \quad (5.16)$$

We initially attempted the use of the Biconjugate Gradient Stabilized Method Solver or

(BiCSTAB). BiCSTAB is a variation of Biconjugate Method. For each iteration i , BiCSTAB computes $Q_i * A * P_i * A * r^{(0)}$ where for i iterations Q_i is an i^{th} degree polynomial which is a description of an update of the steepest descent towards the solution [186].

The solver did not however prove suitable for our modelling work. In many instances the solver did not converge to a solution, or a solution was reached only after a very lengthy processing time.

5.2 Solver configuration used for FEM Simulations

5.2.1 Generalized Minimal Residual Method Solver

The Generalized Minimal Residual Method Solver (GMRES) is designed for use in solving nonsymmetric linear systems [187]. GMRES operates by constructing an orthogonal basis spanning the space $A^{(k)}r^{(0)}$. This is referred to as the Krylov subspace which for k terms can be written as

$$K_k(A, r) = span\{r, Ar, A^2r, \dots, A^{(k-1)}r\} \quad (5.17)$$

Orthogonal inner product coefficients $w^{(i)}, v^{(k)}$ are derived from the relation

$$w^{(i)} = Av^{(i)} \quad (5.18)$$

The core of the algorithm is then based on iterating on a term

$$x^{(i)} = x^{(0)} + y_1v^{(1)} + \dots + y_iv^{(i)} \quad (5.19)$$

where the y coefficients are selected to minimize the absolute value of the residual $|b - Ax^{(i)}|$ [188, 189].

Some drawbacks of the GMRES method is the large memory and processing resources required for many iterations. To deal with this issue, GMRES is designed after some m iterations to clear accumulated calculations and to restart with an intermediary value. The

challenge of this approach is selection of the appropriate number of m iterations for restart. A too small m may not result in convergence to a solution, conversely a large m may be unnecessarily expensive in terms of memory and computing power. In general no fixed rule applies as to which m is appropriate as this depends on the nature of the problem being solved (i.e. number of tetrahedral elements or degrees of freedom) [189].

For our modelling work we found that the GMRES solver provided the best results in terms of stability and time required for convergence. The GMRES method was however quite expensive in terms of memory requirements. Our strategy therefore was to combine the GMRES with the Multigrid solver configuration as described in the next section.

5.2.2 Nested Generalized Minimal Residual Method and Multigrid Solver Configuration

The Multigrid method is among the fastest solvers developed to date [190]. This algorithm is based on the principle of iteratively using a direct solver on successively coarser grids until convergence is reached [191]. This can be usually be accomplished at a fraction of the cost of directly solving the problem on the original (finest) grid [192]. The transfer of information between grids is controlled by the prolongation function (from a coarse grid to a fine grid) and restriction function (from a fine grid to a coarse grid).

In general the Multigrid cycle involves the following steps: calculating an estimate to the solution in the form of equation

$$Av = f \tag{5.20}$$

calculating the residual which can be written in the form of

$$r = Av - f \tag{5.21}$$

using the restriction function to transfer the problem to a coarser grid and iterating to

minimize the residual equation which is written as

$$Ae = r \tag{5.22}$$

where e is the error of the solution estimate. If convergence on the residual equation begins to stall, the operation can be transferred to successively coarser grids until convergence has been achieved. Following this step, the solution estimate is transferred to the original grid through a succession of prolongation operations [192].

We selected the V cycle Multigrid algorithm for our modelling work. The name V cycle is a description of the pattern of transfer of the problem from a fine grid to successively coarser grids until an apex is reached (approximating the tip of the V), the residual equation is minimized to within a specified tolerance (convergence) and the converged solution is then returned to the original grid.

We used SOR (Successive Overrelaxation Method) as pre and post smoother for the Multigrid solver. Written in matrix form the k^{th} iteration of the SOR algorithm is

$$x^k = (D - \omega L)^{-1}(\omega U + (1 - \omega)D)x^{k-1} + \omega(D - \omega L)^{-1}b \tag{5.23}$$

where D , L and U are the diagonal, upper and lower triangular matrices. In general SOR is an advanced adaptation of the Gauss-Seidel method whereby the additional weighted term ω is used as a means of accelerating convergence whereby ω is given a value in the range of $(0,2)$ ($\omega = 1$ is the ordinary case of Gauss-Seidel decomposition) [188]. Through trial and error we found that SOR as a pre and post smoother enabled faster convergence to the desired solution.

The final solver configuration we used was V cycle Multigrid algorithm nested within GMRES (the general iterative solver). We used the algebraic multigrid since this method requires no explicit knowledge of the problem geometry [193]. Tolerance was set to error below 10^{-3} . We used 3 levels of grid coarseness whereby the coarsest level was set to only 1 degree of freedom. We used MUMPS (MULTifrontal Massively Parallel Sparse direct

Solver) as the direct solver to be used on coarse grids.

Figures 5.1a and 5.1b below show an illustration of a convergence graph for a single frequency point (1 Hz) and for a frequency sweep (48 points from 1 Hz - 1 GHz) for a $CZ - C1$ montage. The smoothness and speed of descent of the convergence show that this solver configuration performance was adequate for our computational work.

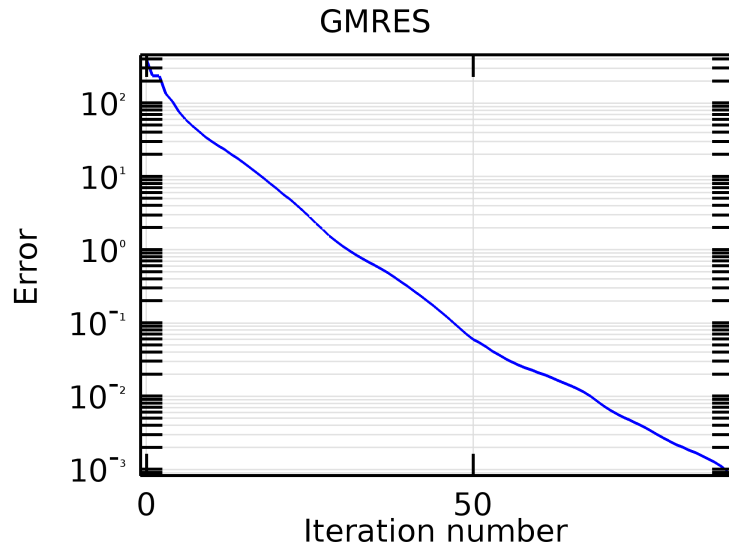
Table 5.1 provides information concerning the processing requirements of the converged solution (including memory use and speed).

Solver Type	DOF	Dependent Variables	Solver Time	Memory
Linear, Parametric	3013088	Voltage	32832 s	Physical 8.29 GB
		Floating boundary 1		Virtual 8.46 GB
		Floating boundary 2		

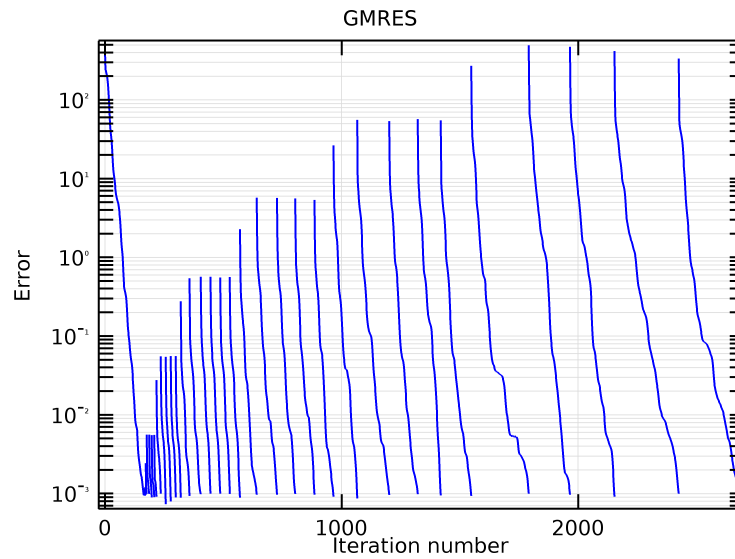
Table 5.1: Solver performance details

5.3 Summary

This chapter provided some background on common solver types as well as as a description of the considerations that led to the solver configuration used in our modelling work. In general the fastest method to solve a FEM is to use direct solvers (MUMPS, Pardiso, Spooles). For very large equations sets (generated from a large number of degrees of freedom) iterative solvers are used (Jacobi, Gauss-Seidel, Biconjugate, and GMRES). The solver configuration that resulted in the fastest convergence time involved the use of GMRES nested in a multigrid solver. We used an algebraic (no explicit knowledge required of the problem geometry) V grid multi-solver (V describes the pattern of transfer of the equations between grids of various degrees of coarseness). Finally we used SOR (Successive Overrelaxation Method) as a pre and post smoother.



(a) Convergence graph of the V Multigrid solver nested with GMRES for a single frequency point (1 Hz) with a CZ-C1 electrode configuration. Error is shown vs iteration number. Convergence is reached when the error is less than 10^{-3} .



(b) Convergence graphs shown a frequency sweep for the CZ-C1 configuration. Frequency sweep is 48 points logarithmically spaced (5 points per decade) from 1 Hz to 1 GHz.

Figure 5.1: Convergence graphs of the V Multigrid algorithm nested in the GMRES iterative solver.

Chapter 6

Multi-frequency Sensitivity Field Simulations

The goals of this thesis include inferring dose parameters related to neuro-stimulation and measurement (such as current density and electric field) by analyzing the multi-frequency bioimpedance spectrum of the human head for various electrode montages.

In order to relate the output measurement (transfer impedance) to the intrinsic or endogenous dose related parameter (i.e. current density, electric field), we introduce the concept of a vector field quantity referred to as the sensitivity field [194]

The link between the sensitivity field and current density is shown by the following equations:

First, based on the definition of sensitivity (4.8.3) for a 2 electrode system we have

$$S = \int_v \frac{|J|^2}{I^2} \quad (6.1)$$

we then can write that

$$S \propto \int_v |J|^2 \quad (6.2)$$

The relation of impedance to sensitivity is given by Eq. 4.19. Combining this equation with Eq. 6.2 we have [195]

$$Z = \int_v \frac{|J|^2}{(\sigma + j\omega\epsilon)} dv \quad (6.3)$$

Thus for a given tissue with electric properties σ (conductivity) and ϵ (permittivity) we can write

$$Z \propto |J|^2 \quad (6.4)$$

Thus we see for a 2 electrode system that impedance is directly proportional to the square of the absolute value of the current density [195]. We mention here that the 2 electrode configuration is a case whereby current injection and voltage measurement are shared between the same pair of electrodes. Thus the sensitivity field in this case will always be positive and easily related to physical properties of the measured or stimulated tissues.

Conversely, the four electrode configuration is separated into (current injection) drive electrodes and (voltage) measurement electrodes. The advantage of this setup is that measurement of the typically high impedance of the electrode - tissue interface is avoided. This setup is more sensitive to potential drop across internal tissue structures.

The sensitivity field is derived from the dot product of the lead (current) and voltage (field) (see eq. 4.20). The relative locations of the drive and voltage electrodes affect the sign and magnitude of the lead and vector fields, depending on the relative orientations of these fields to each other the resulting sensitivity field may be negative.

We will show that the distribution of the negative field affects the magnitude of the transfer impedance. This provides an important way of relating the sensitivity field distribution to the measured transfer impedance.

We also aim to relate the change of the sensitivity over frequency to the dependence of dose to frequency of current injection. The frequency dependence of the sensitivity fields provides another dimension for analysis of the impedance spectrum.

We also show the distribution of the sensitivity field through a realistic MRI derived FEM of the human head. We look in detail at the integration of sensitivity in each of the main head tissues (scalp, skull, CSF, GM, WM and eye matter). In addition we examine the sensitivity distribution in predefined neural targets (shallow target (GM ROI), deeper target (WM ROI), and the whole brain. We analyze the idea of focality (for definition see section 4.8.4) for these defined ROIs. Finally we relate sensitivity to dose (current density and electric field) by examining the correlation between these quantities over the simulated frequency range.

In order to simulate experimental error we add random noise to the probe measurement (see section 4.7). Each sensitivity plot is the mean of 6 samples with error-bars shown as the standard error of the mean (SEM). The addition of noise allows us to make meaningful comparisons to experimental data (see chapter 9)

Overall in this chapter we investigate the following for simulated 2 electrode and four electrode configurations:

- sensitivity distribution in each of the head tissues and predefined ROIs
- dependence of sensitivity distribution on frequency and electrode configuration
- dependence of dose (current density and electric field) on frequency and electrode configuration
- correlation of sensitivity and dose
- dependence of focality of predefined ROIs on frequency and electrode configuration

Frequency range of the simulations are from 1 Hz to 1 GHz, logarithmically spaced with 5 points per decade (see section 4.5). We show the magnitude of the tissue sensitivities which was derived from the complex (real and imaginary) sensitivity values.

6.1 Two electrode configuration

6.1.1 Head Tissue Sensitivity

We show results of the sensitivity field distribution for four 2 electrode montages CZ-C1, CZ-C3, CZ-T7 and T7-T8 (see Fig. 4.1). Electrode position are systemically separated (gap between electrodes are increased) from CZ-C1 (close spacing) to T7-T8 where the electrodes are placed on opposite sides of the head.

We first show graphs of sensitivity field distribution of the four electrode montages. For each montage we show results for 1 Hz, 1 Khz, 100 Khz and 1 Mhz respectively. We chose these frequencies to represent α dispersion (low frequency) and β dispersion (mid frequency) zones. These frequency zones represent ranges of interest for neuro-stimulation and electrical impedance measurements [49].

Fig. 6.1 shows the distribution of the sensitivity field resulting from the montage CZ-C1. The field is shown in a sagittal plane view (through CZ) as scalar values in a colour value where red is the maximum and blue is the minimum of the scale. The threshold and range for the scale was chosen to ensure good visibility of the contrast of the sensitivity field through the simulated medium.

Results show a high concentration of the field around the CZ-C1 electrode pair. Specifically the field has a high density through the scalp tissues in a region under the electrodes bounded by C3 on the left and C2 on the right. A small low density zone is shown in the skull tissue domain - this zone is bounded by high field density. The high density field extends inwards through the skull into the CSF. This field concentration appears to end at the CSF-GM boundary with a further extension of high field laterally through the CSF (light turquoise colour). Thus we see that the CSF acts as a high conductivity shunting layer which bypasses the brain. In general the sensitivity distribution in the neural tissues (GM, WM and eye matter) is quite low on the simulation scale.

Changes of the sensitivity distribution across the frequencies shown are relatively minor.

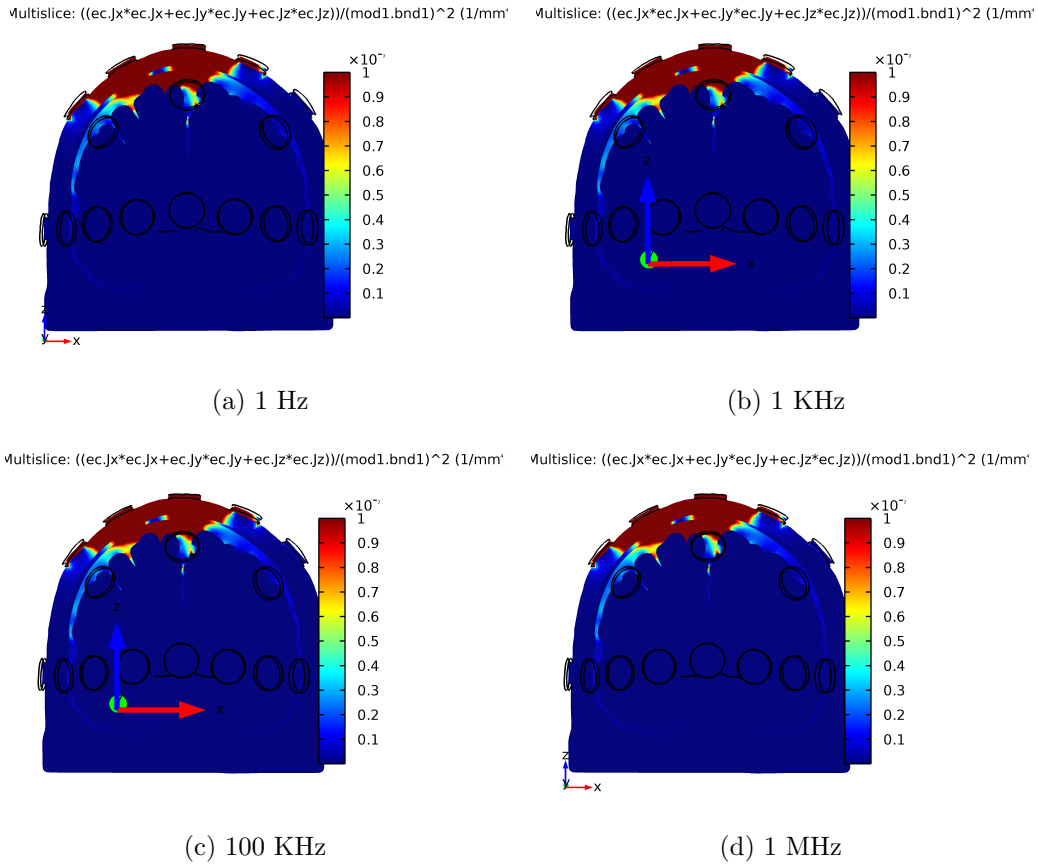
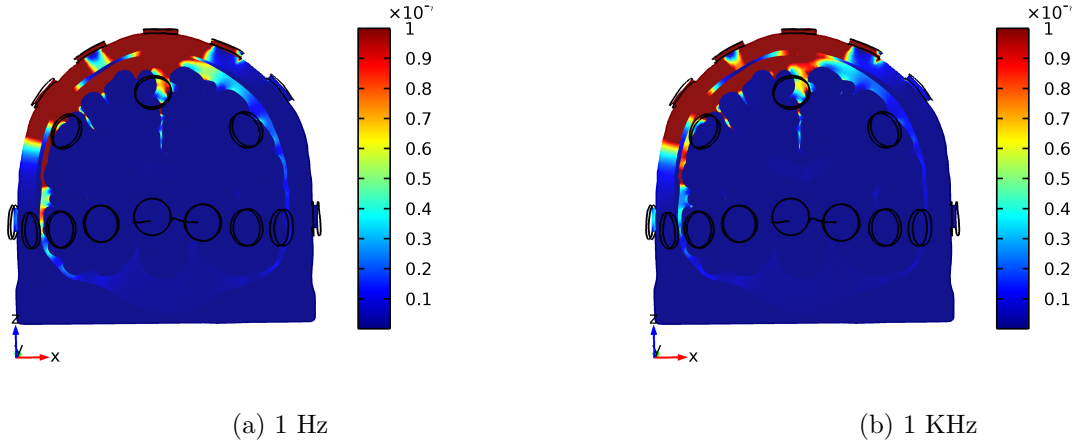


Figure 6.1: Sagittal plane view of sensitivity field from the CZ-C1 montage. Model is oriented such that the face is facing forward. Plots are shown in the mm scale with units as $[1/mm^4]$. Sensitivity is shown with a maximum scale of 10^{-7} . Sensitivity distributions are shown for 4 frequencies (a) 1 Hz, (b) 1 KHz, (c) 100 KHz, (d) 1 MHz.

We see a reduction of sensitivity in the CSF layer as frequency is increased - this is represented by the colour scale changing slightly from red-yellow to turquoise-blue. No perceptible change is seen in the brain tissue for the different frequencies at the shown scale. Numerical results of the integrated sensitivity field are shown in the following sections.

$$\sqrt{\text{Multislice: } ((ec.jx*ec.jx+ec.jy*ec.jy+ec.jz*ec.jz))/(\text{mod1.bnd1})^2} \text{ (1/mm)} \quad \sqrt{\text{Multislice: } ((ec.jx*ec.jx+ec.jy*ec.jy+ec.jz*ec.jz))/(\text{mod1.bnd1})^2} \text{ (1/mm)}$$



$$\sqrt{\text{Multislice: } ((ec.jx*ec.jx+ec.jy*ec.jy+ec.jz*ec.jz))/(\text{mod1.bnd1})^2} \text{ (1/mm)} \quad \sqrt{\text{Multislice: } ((ec.jx*ec.jx+ec.jy*ec.jy+ec.jz*ec.jz))/(\text{mod1.bnd1})^2} \text{ (1/mm)}$$

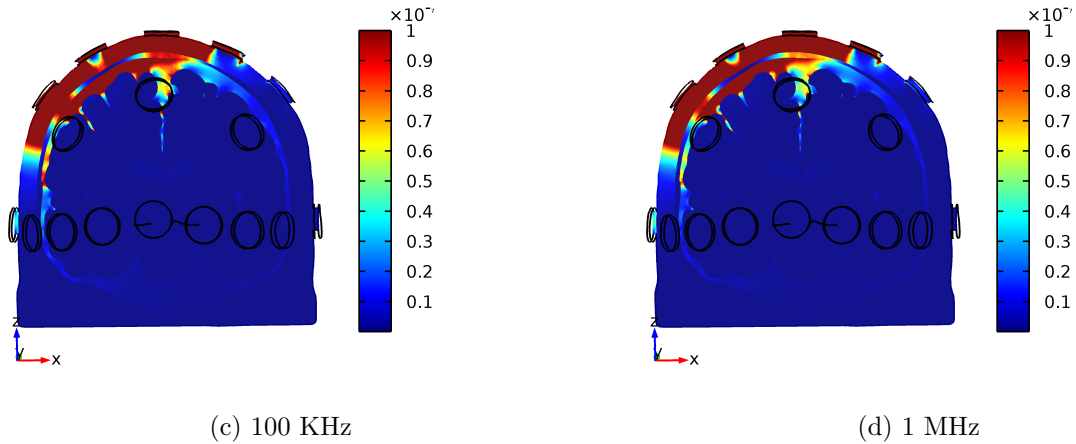


Figure 6.2: Sagittal plane view of sensitivity field from the CZ-C3 montage. Model is oriented such that the face is facing forward. Plots are shown in the mm scale with units as $[1/mm^4]$. Sensitivity is shown with a maximum scale of 10^{-7} . Sensitivity distributions are shown for 4 frequencies (a) 1 Hz, (b) 1 KHz, (c) 100 KHz, (d) 1 MHz.

The sensitivity field distribution is shown the CZ-C3 montage (see Fig. 6.2) where the angle and separation gap between the electrode pair is increased. Here we see that spatial distribution of the high field is increased corresponding to the position of the current

injecting electrodes. A low sensitivity region is shown under the region of the C1 electrode in the scalp and skull tissue. Similar to the field distribution shown in Fig. 6.1, the sensitivity field is highly concentrated in the scalp tissue and CSF between and around the active electrode pair.

Here we notice differences in the sensitivity field for the different simulated frequencies represented by slight changes in the colours of the scalar values. As frequency is increased the sensitivity field in the CSF is decreased - shown by a reduction of the redness of the field. In addition the low sensitivity zone in the skull tissue appears to increase. Conversely the sensitivity field of the scalp appears to increase for higher frequencies as shown by the diminishment of the low field zone between CZ-C3.

In Fig. 6.3 we show results for the CZ-T7 montage whereby the electrode pair are approximately perpendicular to each other. High sensitivity zones are bands in the scalp under and close to the current injecting electrodes. The high sensitivity region in the CSF layer extends past the electrode pair. A low sensitivity region is shown in the scalp tissue between the electrode pair. The brain tissues are shown with low sensitivity as visualized on the colour scale.

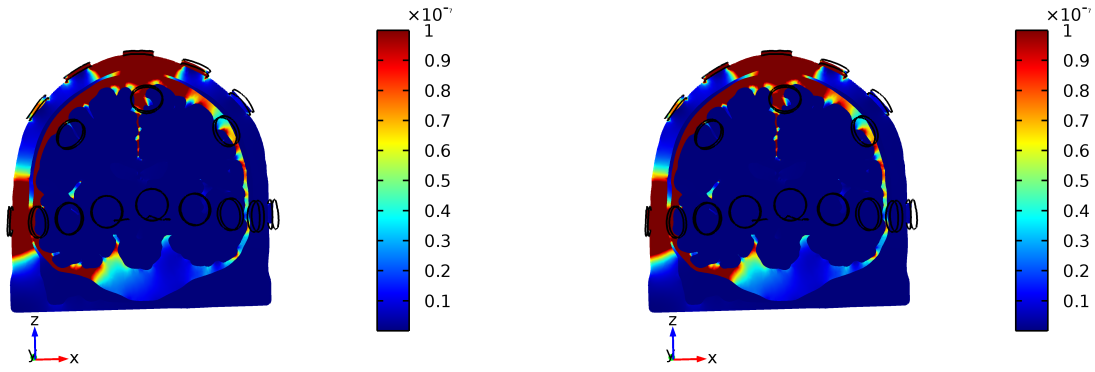
Like prior simulations, as frequency is increased from 1 Hz to 1 MHz the sensitivity field density decreases in the CSF layer and increases in the scalp tissue.

The final 2 electrode simulation is the T7-T8 configuration shown in Fig. 6.4. Here the high sensitivity zones are located in the scalp on diametrically opposed sides of the head near the T7 and T8 electrodes. The high sensitivity zones extend in the CSF layer past the current injection sites.

As frequency is increased, the sensitivity of the CSF layer enveloping the brain is reduced. We see however that the sensitivity field in the CSF ventricle is increased for higher frequencies.

In this section we showed the sensitivity distribution of various 2 electrode montages. We

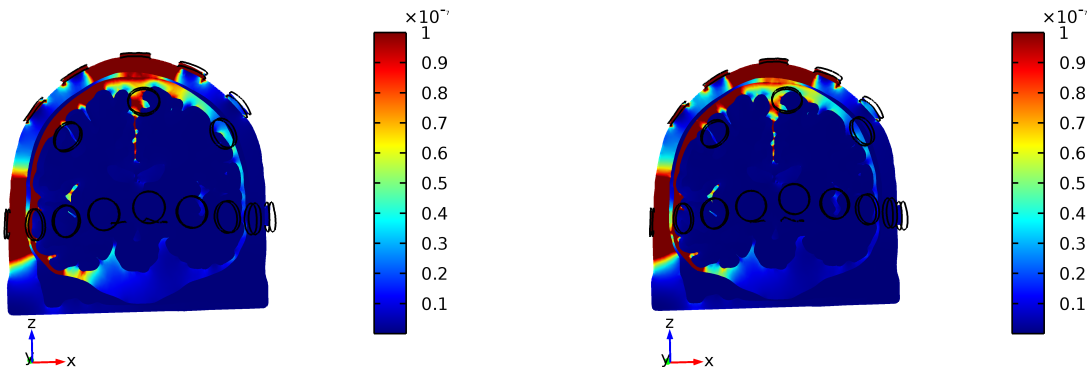
Multislice: ((ec.Jx*ec.Jx+ec.Jy*ec.Jy+ec.Jz*ec.Jz))/(mod1.bnd1)^2 (1/mm⁴) Multislice: ((ec.Jx*ec.Jx+ec.Jy*ec.Jy+ec.Jz*ec.Jz))/(mod1.bnd1)^2 (1/mm⁴)



(a) 1 Hz

(b) 1 KHz

Multislice: ((ec.Jx*ec.Jx+ec.Jy*ec.Jy+ec.Jz*ec.Jz))/(mod1.bnd1)^2 (1/mm⁴) Multislice: ((ec.Jx*ec.Jx+ec.Jy*ec.Jy+ec.Jz*ec.Jz))/(mod1.bnd1)^2 (1/mm⁴)

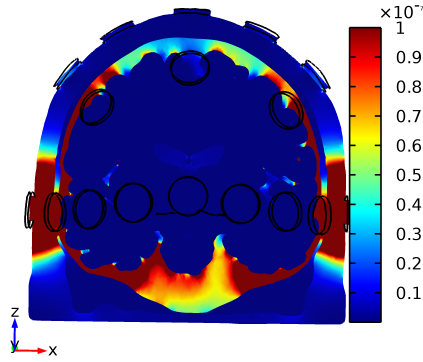


(c) 100 KHz

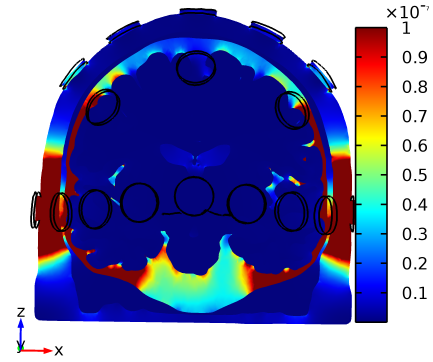
(d) 1 MHz

Figure 6.3: Sagittal plane view of sensitivity field from the CZ-T7 montage. Model is oriented such that the face is facing forward. Plots are shown in the mm scale with units as $[1/mm^4]$. Sensitivity is shown with a maximum scale of 10^{-7} . Sensitivity distributions are shown for 4 frequencies (a) 1 Hz, (b) 1 KHz, (c) 100 KHz, (d) 1 MHz.

Multislice: ((ec.Jx*ec.Jx+ec.Jy*ec.Jy+ec.Jz*ec.Jz))/(mod1.bnd1)^2 (1/mm⁴) Multislice: ((ec.Jx*ec.Jx+ec.Jy*ec.Jy+ec.Jz*ec.Jz))/(mod1.bnd1)^2 (1/mm⁴)

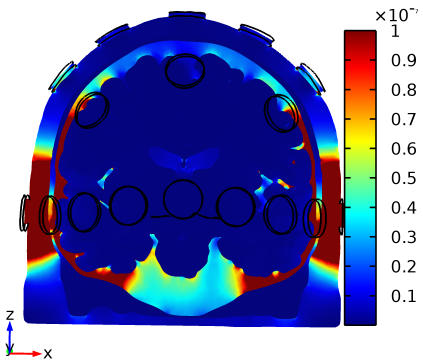


(a) 1 Hz

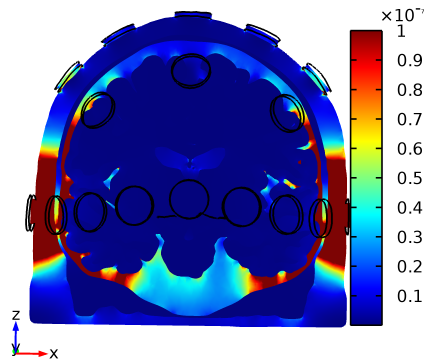


(b) 1 KHz

Multislice: ((ec.Jx*ec.Jx+ec.Jy*ec.Jy+ec.Jz*ec.Jz))/(mod1.bnd1)^2 (1/mm⁴) Multislice: ((ec.Jx*ec.Jx+ec.Jy*ec.Jy+ec.Jz*ec.Jz))/(mod1.bnd1)^2 (1/mm⁴)



(c) 100 KHz



(d) 1 MHz

Figure 6.4: Sagittal plane view of sensitivity field from the T7-T8 montage. Model is oriented such that the face is facing forward. Plots are shown in the mm scale with units as $[1/mm^4]$. Sensitivity is shown with a maximum scale of 10^{-7} . Sensitivity distributions are shown for 4 frequencies (a) 1 Hz, (b) 1 KHz, (c) 100 KHz, (d) 1 MHz.

demonstrated that for the 2 electrode montage the sensitivity field is concentrated in the scalp tissue near the electrodes and in the CSF layer. We also showed that for increasing frequency sensitivity of the scalp increased and the CSF sensitivity decreased.

In the following section we describe in detail numerical results of the multi-frequency sensitivity simulations for all the head tissues. Each tissue is represented in the modelling space as a domain, sensitivity is integrated across each domain volume resulting in a scalar value for each frequency point. Sensitivity is plotted as a function of frequency. The Log_{10} of frequency is shown in the x-axis.

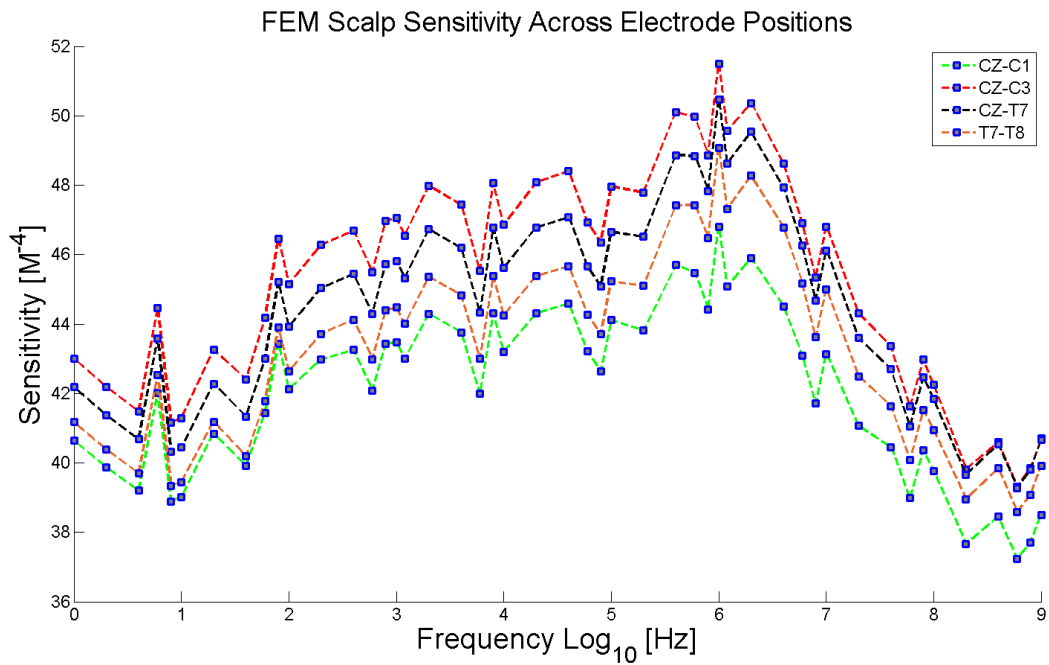
As described in section 4.7, we simulate 6 bioimpedance spectroscopy measurements of each tissue with 5% of normally distributed Gaussian noise. Each measurement can be referred to as a sample. Each data point in the following graphs is the mean of all the samples. Error bars on the graphs are the standard error of the mean (SEM) which is calculated as the std/\sqrt{n} or as the standard deviation divided by the square root of the sample number.

6.1.1.1 Scalp

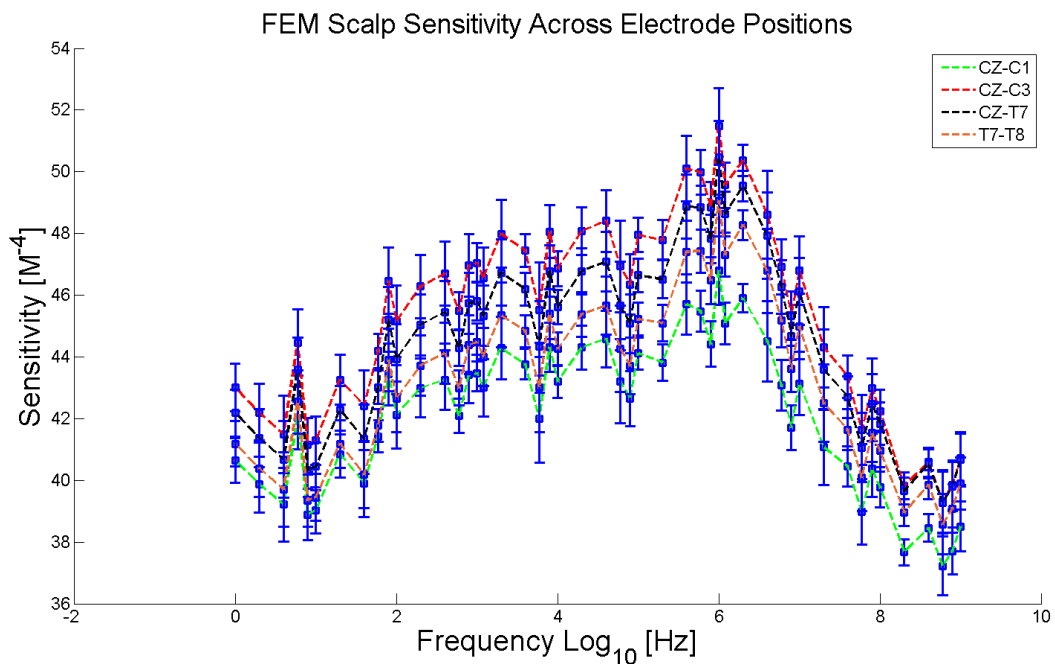
We first show in Fig. 6.5 plots of scalp sensitivity for all 2 electrode montages. Each data point is represented by a blue square marker. Each graph line represents a different electrode montage as shown in the legend of the plot. In order to illustrate the differences between the plots clearly we show both the sensitivity plots without error bars (Fig. 6.5 (a)) and with error bars added (Fig. 6.5 (b)).

We note that the mean sensitivity values of the different montages track very closely together. We see no overlap with the mean values. CZ-C1 has the lowest sensitivity curve followed by T7-T8, CZ-T7 and CZ-C3.

The noise level of the scalp sensitivity is relatively high – as shown in Fig. 6.5 (b) the error bars of many of the sensitivity plots overlap. (In Chapter 7 we determine if there is



(a) Mean scalp sensitivity



(b) Mean scalp sensitivity with error bars (SEM)

Figure 6.5: Mean sensitivity integrated across the scalp domain for all electrode montages, (a) without error bars and (b) with error bars (SEM).

statistical significance (by disproof of the null hypothesis) for the different Cole parameters extracted for the 2 electrode montages. ¹

We note that the sensitivity of the scalp tissue increases as a function of frequency until about 1 MHz. Above this frequency, the scalp sensitivity decreases reaching a minima close to 1 GHz. The increase of scalp sensitivity up until 1 MHz is consistent with the visual graphs shown above in 6.1.1.

6.1.1.2 Skull

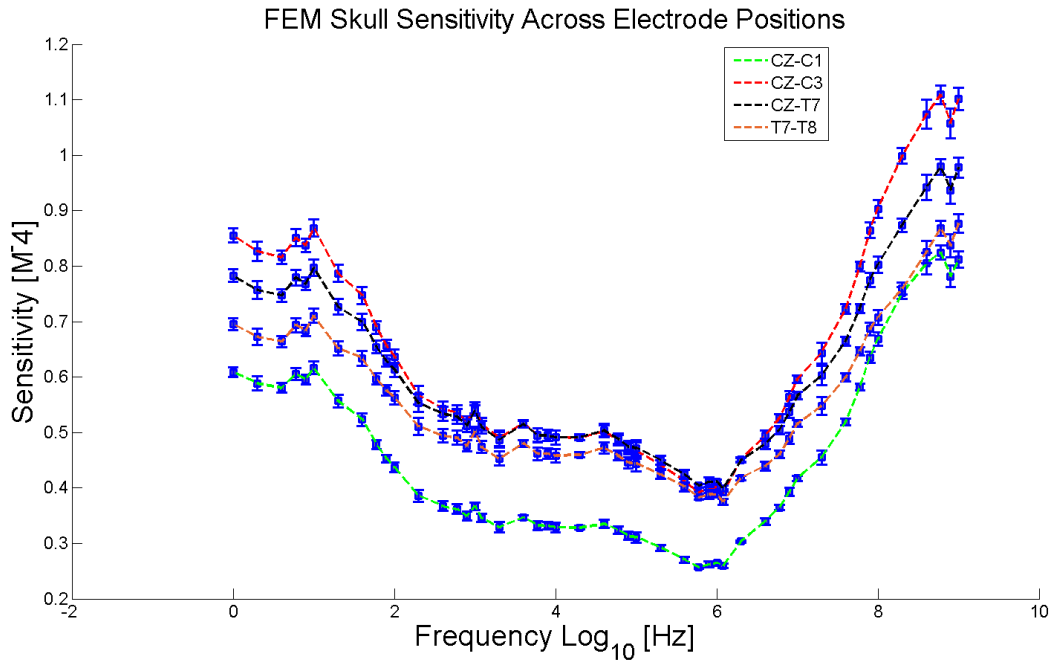


Figure 6.6: Mean sensitivity integrated across the skull domain for all electrode montages.

Fig. 6.6 shows the mean integrated sensitivity of the skull tissue layer for all electrode montages. Error bars show the SEM at each frequency point.

We note that the skull sensitivity follows an inverse pattern to the scalp sensitivity. Here the skull sensitivity decreases to a minimum at 1 MHz before beginning to increase again.

¹The sensitivity field is generally not measured and thus has no noise. Here however since we use virtual probes to "measure" sensitivity we add noise to the figures. Noise is also shown for impedance measurements which can be compared to experimental data

The skull sensitivity graphs from lowest to highest are from montages CZ-C1, T7-T8 , CZ-T7 and then finally T7-T8. These results match the pattern shown for the scalp sensitivity plots. Here we note that the track of the CZ-C1 plot is removed from the plots of the 3 other montages which appear closer together and converge at around 1 MHz.

Results show that the skull sensitivity (ranging from .3 to 1.1 see Fig. 6.6 is much lower than the scalp of sensitivity (ranging from 36 to 51). In Chapter 7 we determine if the skull transfer impedance is a significant contributor to the total impedance.

6.1.1.3 CSF

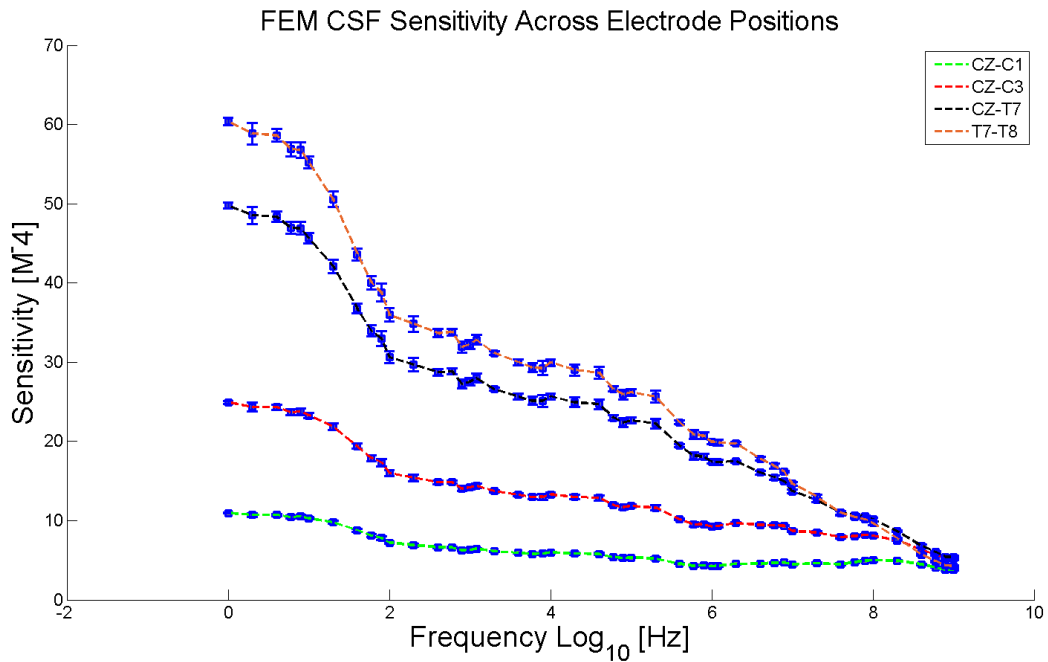


Figure 6.7: Mean sensitivity integrated across the CSF domain for all electrode montages.

Fig. 6.7 shows the mean integrated sensitivity of the CSF tissue layer. The magnitude of the error bars show a relatively small error.

We see that the CSF sensitivity has a strong frequency and electrode montage dependence. In general we note that the greater the gap between the electrodes, the higher the initial sensitivity and the steeper the descent of the sensitivity curve. For instance CZ-C1 is the

electrode pair with smallest gap, the lowest initial sensitivity and the smallest gradient of descent. This is followed by CZ-C3 which has a higher initial sensitivity and a greater rate of descent as frequency is increased. This pattern is continued for CZ-T7. Finally T7-T8, the electrode pair placed on opposing sides of the head, has the highest initial sensitivity and the greatest overall rate of descent.

Fig 6.7 shows the large range of sensitivity values. Over the simulated frequency range sensitivity ranges from over 60 (T7-T8 1 Hz) to under 10 (all montages 1 GHz). The fall of CSF sensitivity as a function of frequency has implications for increasing dose in the brain by bypassing the CSF shunting effect.

6.1.1.4 GM

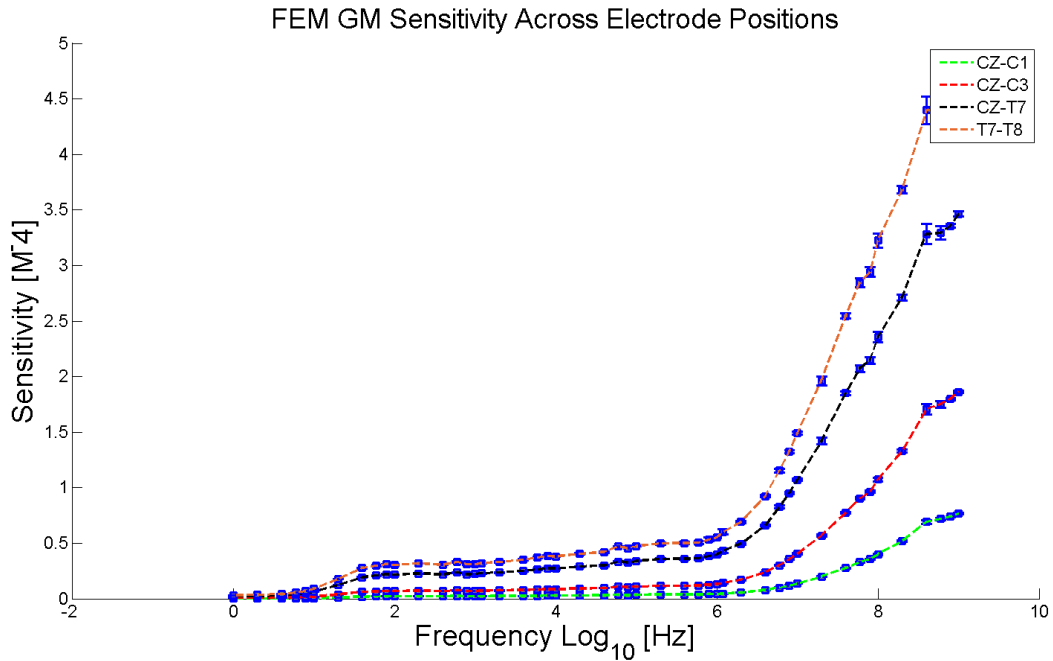


Figure 6.8: Mean sensitivity integrated across the GM domain for all electrode montages.

Fig. 6.8 shows mean GM (grey matter) sensitivity as a function of electrode montage and frequency. The plots show relatively small error like CSF.

GM sensitivity appears to follow an inverse pattern when compared to CSF. Here

sensitivity increases as a function of rising frequency. We note that there are 3 frequency bounded ranges of increasing sensitivity. Up until close to 100 Hz there is an approximately linear increase in sensitivity across all electrode positions. From 100 Hz until 1 MHz the rate of sensitivity growth is decreased. For frequencies higher than 1 MHz sensitivity increases sharply in a non-linear fashion.

Like CSF, GM sensitivity increases as a function of increasing separation between electrodes. Thus CZ-C1 has the lowest sensitivity, followed by CZ-C3, CZ-T7 and finally T7-T8.

Sensitivity magnitude of the GM is relatively low (>1) for frequencies below 1 MHz. Above 1 MHz, sensitivity rapidly increases rapidly (≈ 4.5 for T7-T8).

6.1.1.5 GM ROI

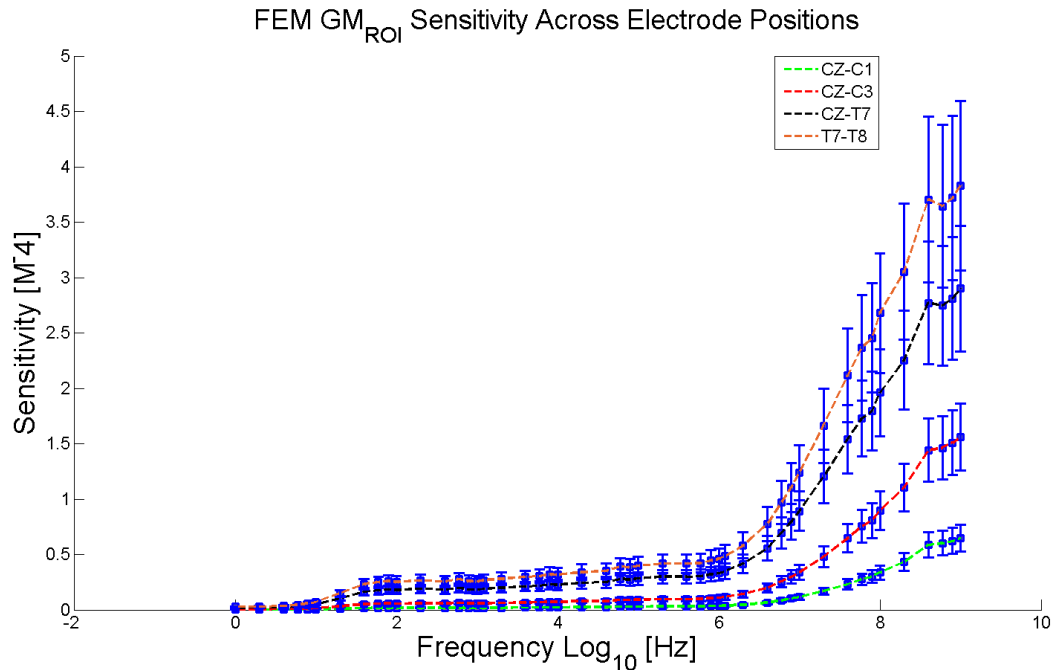


Figure 6.9: Mean sensitivity integrated across the GM ROI domain for all electrode montages.

The mean grey matter region of interest (ROI) (see section 4.2) for all electrode positions is shown in Fig. 6.9

We note that the grey matter ROI sensitivity spectrum follows a similar pattern to that of the the entire grey matter. Some differences are that the grey matter ROI has slightly lower sensitivity values and that the spectrum noise greatly increases for frequencies greater than 1 MHz.

It is apparent that the sensitivity distribution of the grey matter is highly concentrated in the ROI. As described in section 4.1.1 the cathodal electrode (sink) is placed on CZ. We thus see that the placement of the cathodal electrode directly above the ROI appears to a critical component of targeting shallow cortical neural regions.

6.1.1.6 WM

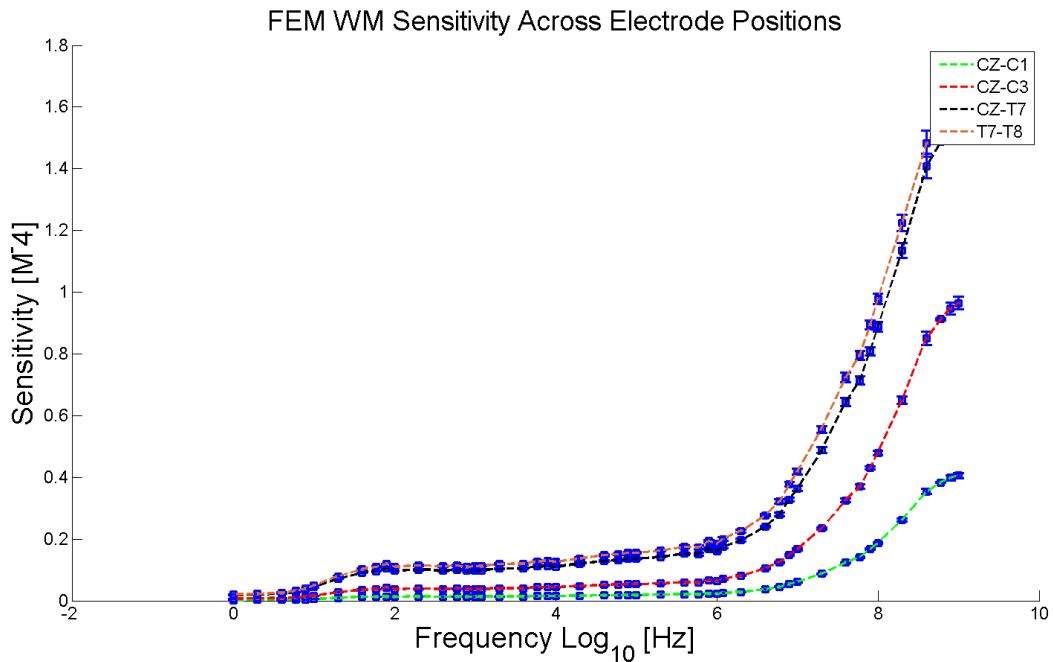


Figure 6.10: Mean sensitivity integrated across the WM domain for all electrode montages.

Fig. 6.10 shows the mean white matter sensitivity for all electrode montages. The white matter sensitivity shows the same pattern as that of the grey matter with however lower absolute sensitivity values. The sensitivity level of each graph from lowest to highest is from electrode montages CZ-C1 followed by CZ-C3, CZ-T7 and T7-T8.

6.1.1.7 WM ROI

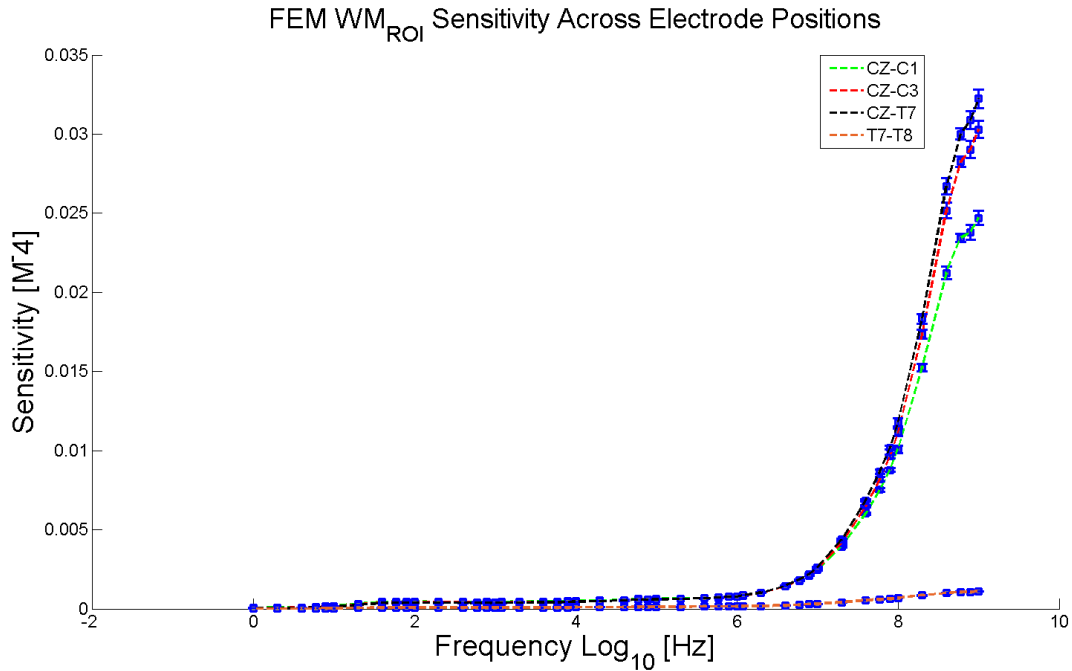


Figure 6.11: Mean sensitivity integrated across the WM ROI domain for all electrode montages.

We show the sensitivity of the white matter region of interest (ROI) (see section) in Fig. 6.11

The white ROI shows increasing sensitivity as a function of increasing frequency. We note here that unlike the white matter sensitivity (Fig. 6.10 here the T7-T8 electrode configuration has the lowest sensitivity values. We also note that sensitivity values are much lower here than for the white matter. The 3 other electrode montages simulated (CZ-C1, CZ-C3 and CZ-T7) track closely together suggesting that changing the electrodes among these positions do not improve focality significantly at the white matter ROI.

6.1.1.8 Eye Matter

We also show the sensitivity plot of deeper internal structures i.e. the optical nerves and eye sockets in Fig. 6.12. As described in section 3.1 the eye matter is not contiguous as the other tissue domains.

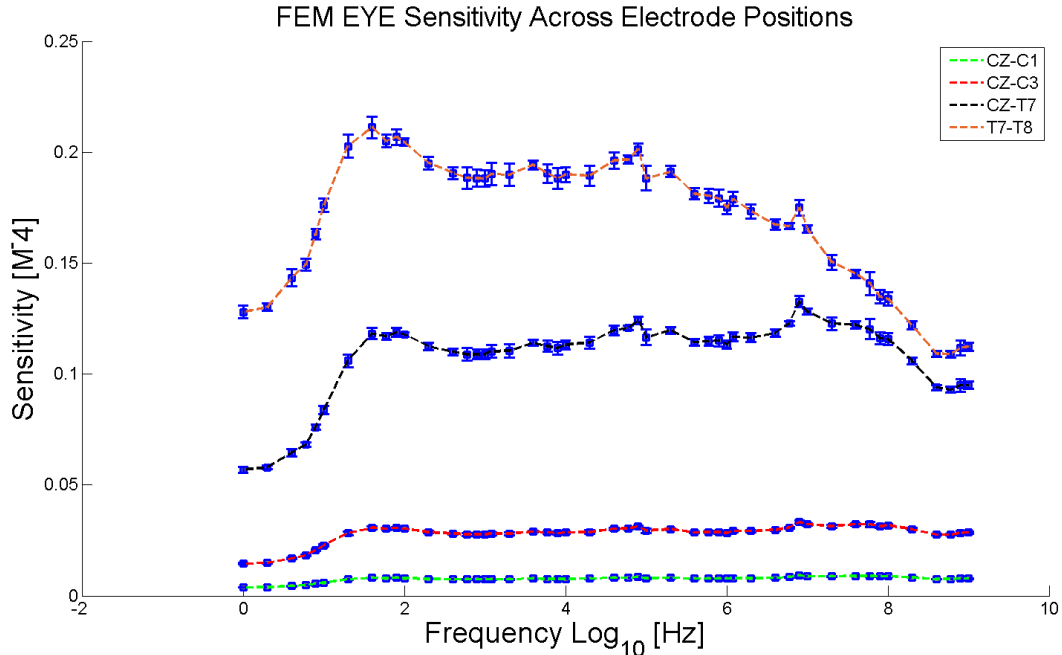


Figure 6.12: Mean sensitivity integrated across the eye domain (optical nerves and eye sockets) for all electrode montages.

We note that sensitivity increases up until about 100 Hz, followed by a declining or flat descent trajectory. We see the clear dependence of sensitivity on separation between electrodes. Sensitivity is lowest for a closely spaced configuration (CZ-C1) and is greatest for electrodes placed on either side of the head (T7-T8). The sensitivity field absolute values are lower than the sensitivity of the WM.

6.1.1.9 Log-Log Plots of Head Tissue Sensitivity

In this section we show the sensitivity spectra of all the tissues plotted on a single graph for each electrode montage. This enables us to compare how the sensitivity field magnitude changes for each tissue type over the simulated frequency range. Sensitivity units are plotted vs frequency on a log-log base 10 scale to enable visualization of a wide range of sensitivity values on a single chart.

As in the previous section we show the mean sensitivity values of 6 samples with random noise added. Here the relative error is shown on the logarithmic scale. Using the

assumption that $\Delta x \ll x$ we calculate the logarithmic error as $\Delta \log_b x \approx \frac{\Delta x}{x \ln b}$ [196]. This simplifies in our case of $b = 10$ to $\Delta \log_{10} x \approx .434 * \frac{\Delta x}{x}$.

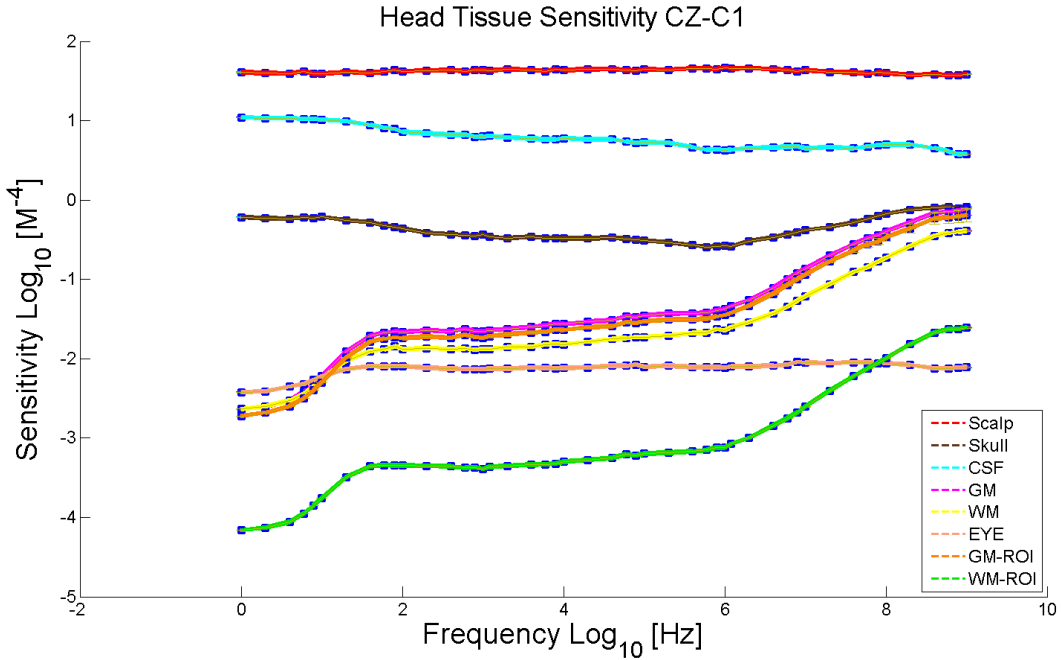


Figure 6.13: Log-Log graph of CZ-C1 head tissues sensitivity vs frequency with error bars (SEM).

Fig. 6.13 shows a log-log plot of head tissue sensitivity vs frequency for CZ-C1. We see that that scalp tissue has the highest sensitivity followed by CSF and the skull.

The GM, GM ROI and WM ROI have the next highest sensitivities. These domains track upwards together as a function of frequency. The relatively flat sensitivity of the eye tissue is shown below this group starting from ≈ 10 Hz. The lowest sensitivity curve is the WM ROI which follows the same track of the GM, GM ROI and WM ROI group albeit at a large offset in sensitivity values.

In Fig. 6.14 we show the sensitivity-frequency log-log graph of tissues for a CZ-C3 montage. Here the main effect of electrode separation is shown as a general increase in CSF sensitivity. Furthermore the high frequency end of the GM and GM ROI intercepts and goes higher than the skull sensitivity.

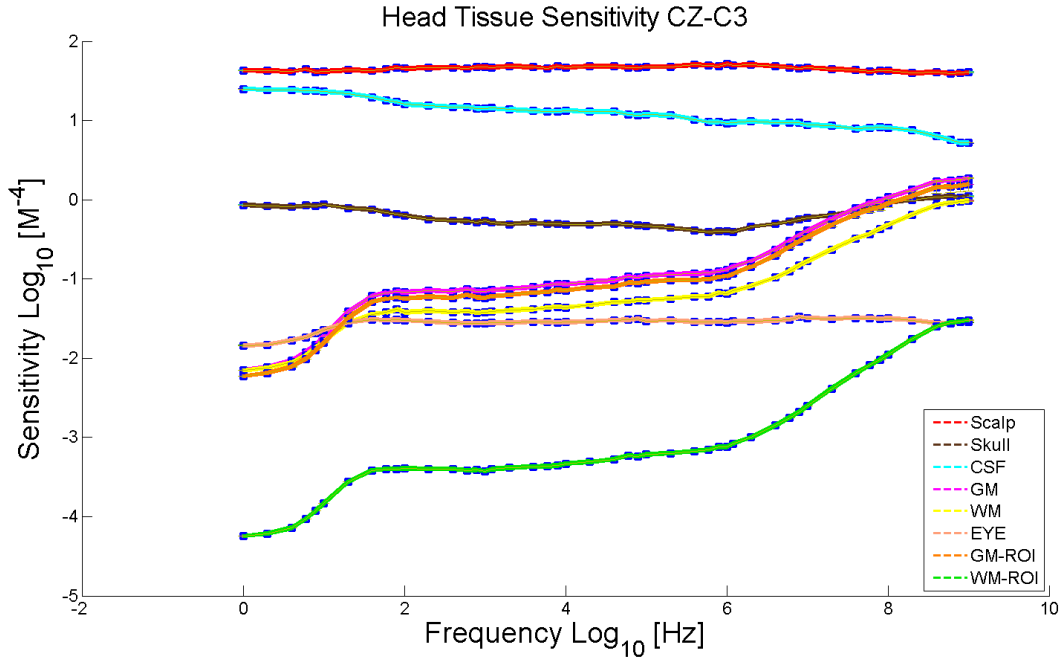


Figure 6.14: Log-Log graph of CZ-C3 head tissues sensitivity vs frequency with error bars

The general profile is of the WM and eye tissue sensitivity curves is relatively unchanged.

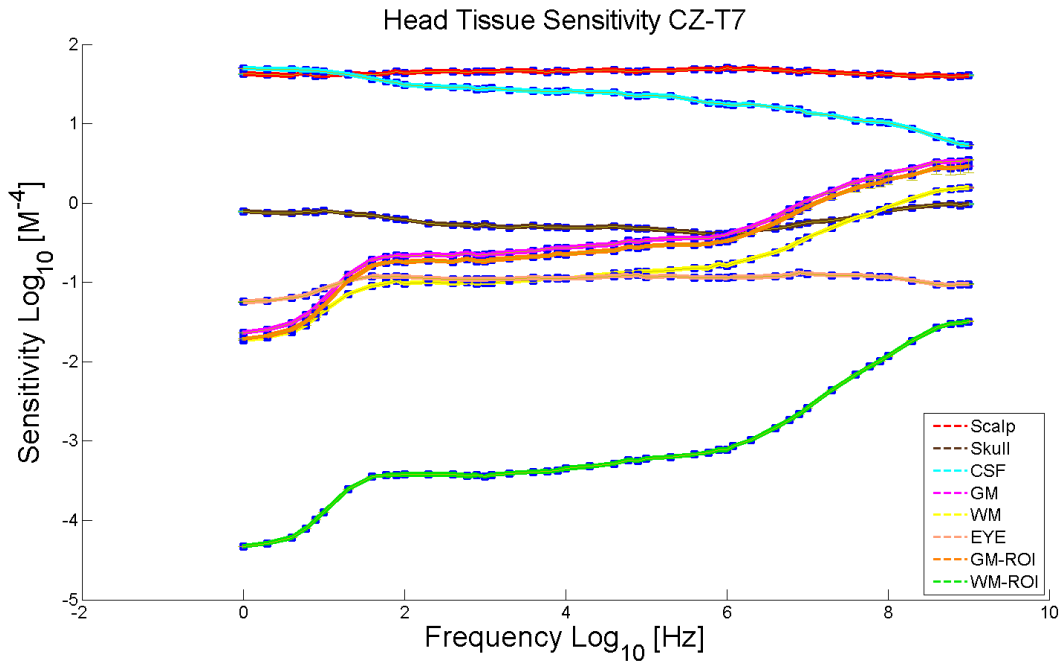


Figure 6.15: Log-Log graph of CZ-T7 head tissues sensitivity vs frequency with error bars.

Fig. 6.15 shows the log-log sensitivity-frequency for CZ-T7. Here we see that at low

frequencies (< 100 Hz) the CSF sensitivity is higher than the sensitivity of the scalp. Like in Fig. 6.14 the high frequency GM and GM ROI is higher than the sensitivity of the skull. The WM sensitivity also overlaps the high end of the skull sensitivity. The eye and WM ROI curves are shown with a higher offset in absolute values but follow a similar track as to that shown in earlier figures.

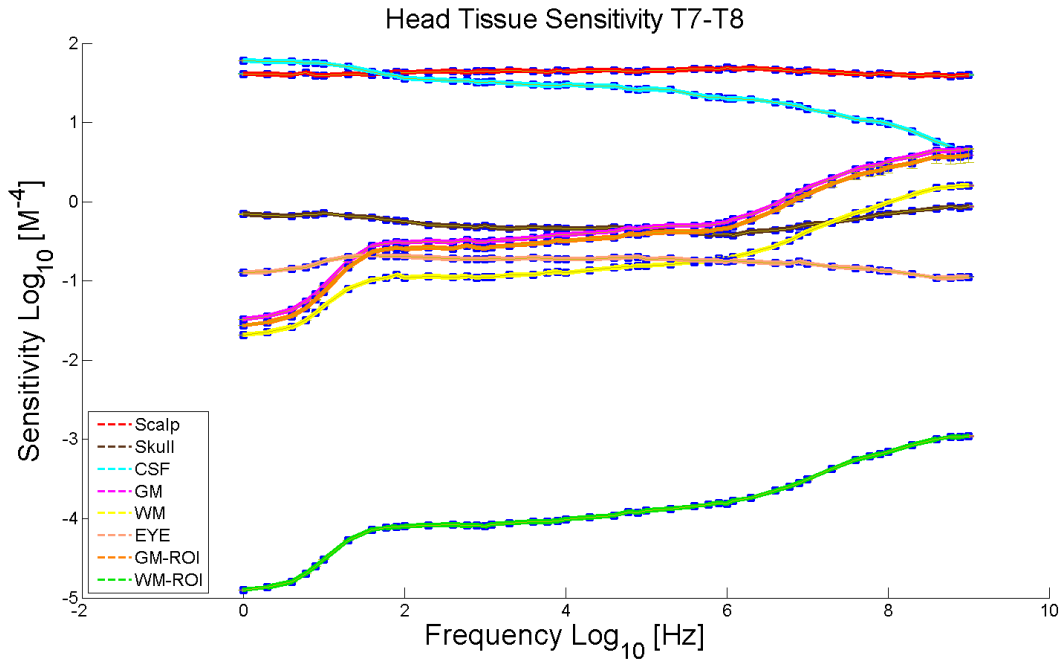


Figure 6.16: Log-Log graph of T7-T8 head tissues sensitivity vs frequency with error bars.

Fig. 6.16 shows the log-log sensitivity frequency curves for the final montage - T7-T8. Here again the CSF sensitivity is higher than the sensitivity of the scalp at low frequencies. The GM, GM ROI and WM all intercept and pass the skull sensitivity at high frequencies. Here the GM and the GM ROI also converges with the CSF sensitivity at the end of the frequency range.

These series of figures show comparison of the sensitivities of the various head tissues over frequency on a log-log graph. We note that the scalp tissue has overall the highest sensitivity followed by CSF. This is consistent with results shown in the visual graphs in section 6.1.1. At the end of this chapter and in chapter 7 we discuss the implications of the

sensitivity simulations in terms of the contribution of each tissue towards the total transfer impedance.

6.1.2 Sensitivity vs. Dose and Measurement Parameters

In this section we investigate the relationship between sensitivity and primary dose parameters (current density and electric field - see section 4.8.2 and 4.8.1). As described in the beginning of Chapter 6 for the 2 electrode montage, sensitivity is proportional to the square of the absolute value of current density.

Here we show the numerical results of simulations of current density and electric field of the head tissues for the CZ-C1 montage. Plots are shown in log-log graphs as in the previous section. We then compare how these results are correlated with the sensitivity plots for the CZ-C1 montage.

We test for correlation using the Matlab syntax of $[r, p] = \text{corrcoef}(A, B)$ where A and B are vectors that are assumed to be normally distributed, r is the correlation coefficient of the linear dependence of A and B and p are significant levels - the lower the P value the higher the probability of significant correlation.

Correlation of A and B can be written as

$$\rho(A, B) = \frac{\text{cov}(A, B)}{\sigma_a \sigma_b} \quad (6.5)$$

where the correlation of A and B is the covariance between A and B divided by the product of the standard deviation of A and B [197, 198].

The correlation matrix is

$$R = \begin{bmatrix} \rho(A, A) & \rho(A, B) \\ \rho(B, A) & \rho(B, B) \end{bmatrix}$$

Since A and B are perfectly correlated with themselves we can write

$$R = \begin{bmatrix} 1 & \rho(A, B) \\ \rho(B, A) & 1 \end{bmatrix}$$

Significance ($\alpha = 0.05$) of correlation is given by the test statistic where r has a t distribution with n-2 (n here is the number of frequencies) degrees of freedom [197]. This is written as

$$t = r \sqrt{\frac{n-2}{1-r^2}} \quad (6.6)$$

In the following section we only extract $\rho(A, B)$ in order to exclude redundant information. We do a pairwise correlation check between each tissue where A is the sensitivity and B is the current density.

6.1.2.1 Sensitivity vs Current Density

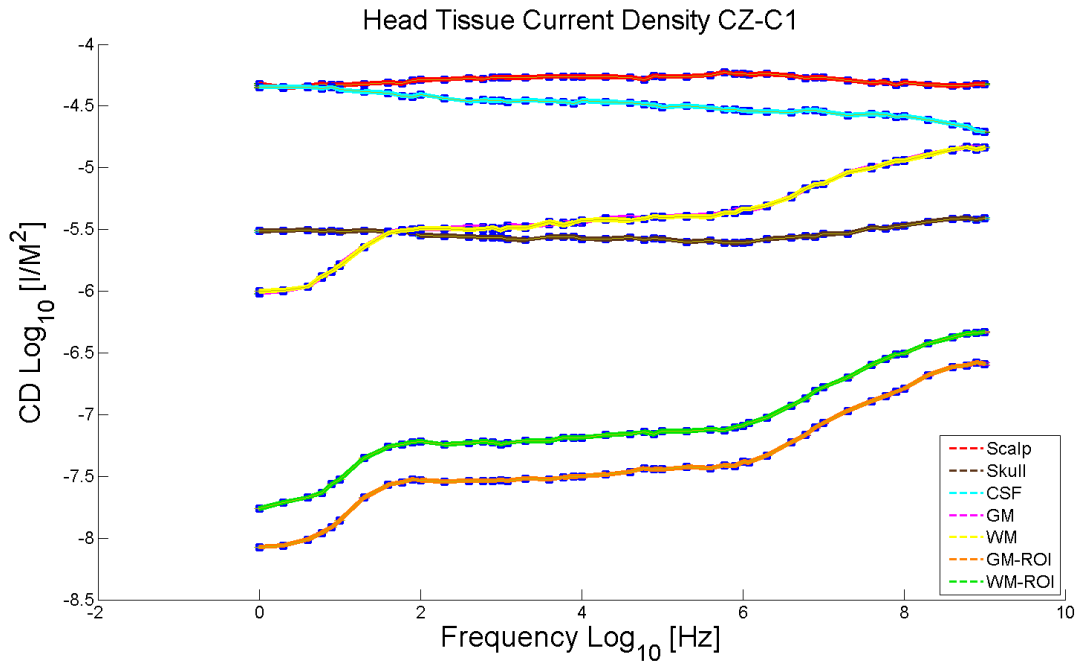


Figure 6.17: Log-Log graph of CZ-C1 head tissues current density vs frequency with error bars (SEM).

Fig. 6.17 shows a log-log graph of current density vs frequency for the montage CZ-C1. The units of the y-axis are $\frac{I}{M^2}$. Error bars are plotted on the graphs according to the method described in section 6.1.1.9. (Eye matter current density is not shown since the calculated current density curve shows many discontinuities unlike the sensitivity profile. This may be due to the fact that eye domains are not contiguous see section 3.1.)

Here we can note that overall profile of the current density curves are quite similar to the sensitivity graphs in the previous section.

There are however significant differences in the absolute values and the magnitude of each tissue current density when compared to sensitivity. This is because the magnitude relationship between sensitivity and current density is (non-linear) quadratic (see eq. 6.2.

Some differences between the sensitivity vs current density graphs include:

- the current density curves have lower absolute values as can be seen by examination of the y-axis values
- the GM and WM current density graphs are superimposed unlike the sensitivity graphs which show that the WM is lower (with a significant offset) to the GM
- the current density of the GM and WM are higher than the skull current density for frequencies around 100 Hz and higher
- the current density of the GM ROI is much lower than its sensitivity

While there are some differences between the two plotted quantities, we also note the similarity of the overall shapes of the curves.

In order to meaningfully compare current density to sensitivity we calculate their correlation as described in section 6.1.2.

In Table 6.1 we show the correlation coefficient of each tissue's sensitivity and current density. The second row in Table 6.1 shows the P values on a logarithmic scale showing the significance of the level of correlation.

Tissue Type	R coefficient	P value
Scalp	0.895	9.039×10^{-18}
Skull	0.970	5.613×10^{-30}
CSF	0.928	2.130×10^{-21}
GM	0.951	4.266×10^{-25}
WM	0.930	1.100×10^{-21}
GM ROI	0.992	2.623×10^{-43}
WM ROI	0.961	2.026×10^{-27}

Table 6.1: Coefficient and p-values of correlation of head tissue sensitivity and current density

We can note the high degree of correlation for each tissue. In all cases the correlation is approximately 0.9 or higher with very low P values. This indicates the close relationship between sensitivity and current density generated in head tissues by a 2 electrode montage. Thus despite the non-linearity of the magnitude relationship we show that there is a strong linear correlation between changes of current density and sensitivity over frequency.

6.1.2.2 Sensitivity vs Electric Field

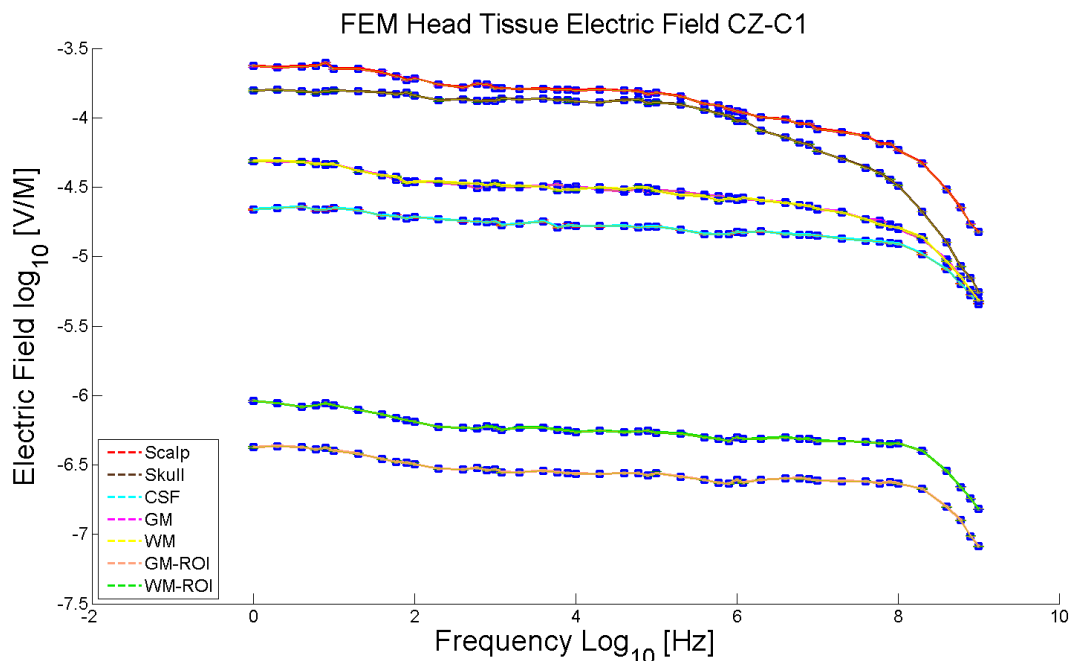


Figure 6.18: Log-Log graph of CZ-C1 head tissues electric field vs. frequency.

As described in section 4.8.1 another fundamental dose-related parameter is the electric

field. In a sense the electric field (given by units $\frac{V}{M}$) is more critical parameter than current density since changes in synaptic firing rates that are hypothesized to cause lasting physiological changes can be attributed to driving strength of the electric field. [160, 161].

Upon analysis of Fig. 6.18 we see important differences between the profile of electric field and sensitivity curves of the head tissues.

- In all cases the electric field magnitude of each tissue trends downwards unlike for sensitivity and current density graphs
- The electric field of the skull , WM and GM is higher than CSF

We thus note that a high current density and sensitivity does not necessarily translate into a high electric field. Although intra-cranial sensitivity may be raised by increasing the inject current frequency this may result in a decreased electric field magnitude.

Tissue Type	R coefficient	P value
Scalp	0.1823	0.2149
Skull	-0.4854	0.0005
CSF	0.8353	1.5586×10^{-13}
GM	-0.8305	2.8231×10^{-13}
WM	-0.8139	2.0140×10^{-12}
GM ROI	-0.7505	8.1816×10^{-10}
WM ROI	-0.7380	2.169×10^{-09}

Table 6.2: Coefficient and p-values of correlation of head tissue sensitivity and electric field.

In table 6.2 we show the coefficient and P-value resulting from the correlation of electric field and sensitivity. Interestingly we note that there is a high linear correlation between many of the tissues. The scalp tissue has a low correlation with a relatively high P-value. The skull has a higher correlation albeit the correlation is negative. Other tissues with a high but negative correlation (and low P-value) are the GM, WM, GM ROI and WM ROI. We have shown here that 2 electrode sensitivity is highly correlated to current density and is also correlated for many head tissues to electric field (albeit for most tissues this is a

negative correlation). This shows an important relationship between sensitivity and dose and has important implications for connecting the measured transfer impedance to dose as will be described in Chapter 7.

6.1.3 Focality

In this section we describe the effect of frequency and electrode montage on focality. We show a fundamental tradeoff between achieving high focality and intensity or magnitude of dose-related parameters.

As described in section 4.8.4 we define focality as the ratio of electric field magnitude in the desired ROI to the total electric field magnitude.

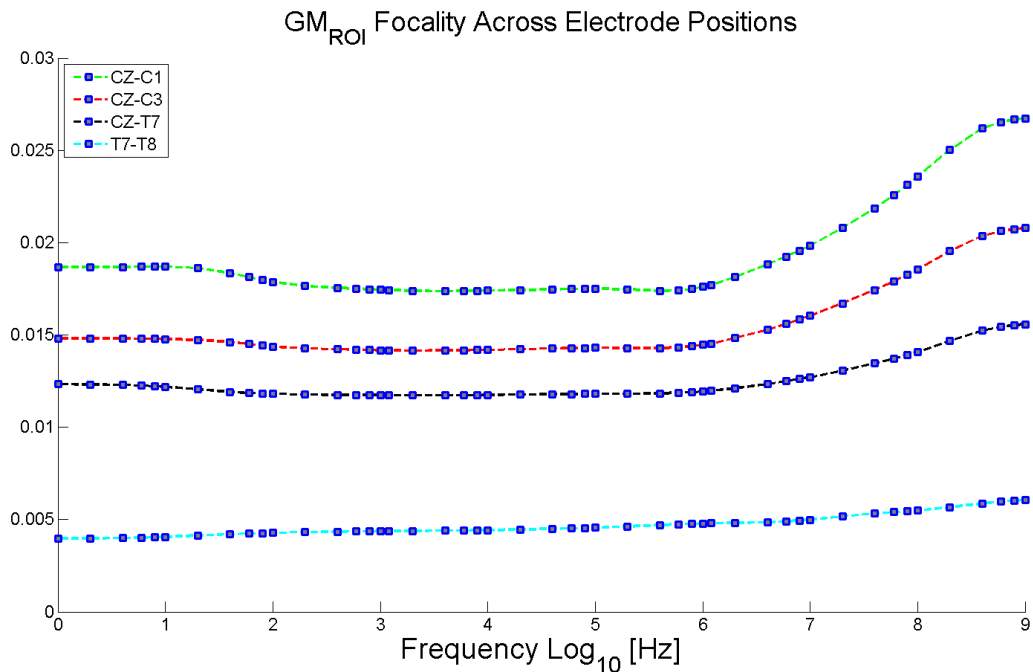


Figure 6.19: GM_{ROI} focality of all electrode montages vs. frequency.

Fig. 6.19 shows the GM ROI focality of all the bipolar montages across the simulated frequency range.

We note that the absolute focality values are relatively low. We see that until 1 Mhz, focality is relatively constant. For frequencies higher than 1 MHz, focality increases for all

montages.

The dependence of focality on electrode configuration is clear. CZ-C1, the electrodes with the smallest and θ angle, show the highest focality. In this montage, the electric field is highly concentrated in a local region including the cortical GM ROI. As the θ angle is increased, focality decreases. Thus CZ-C3 has a lower focality than the previous pair followed by CZ-T7 and finally T7-T8 has the lowest focality.

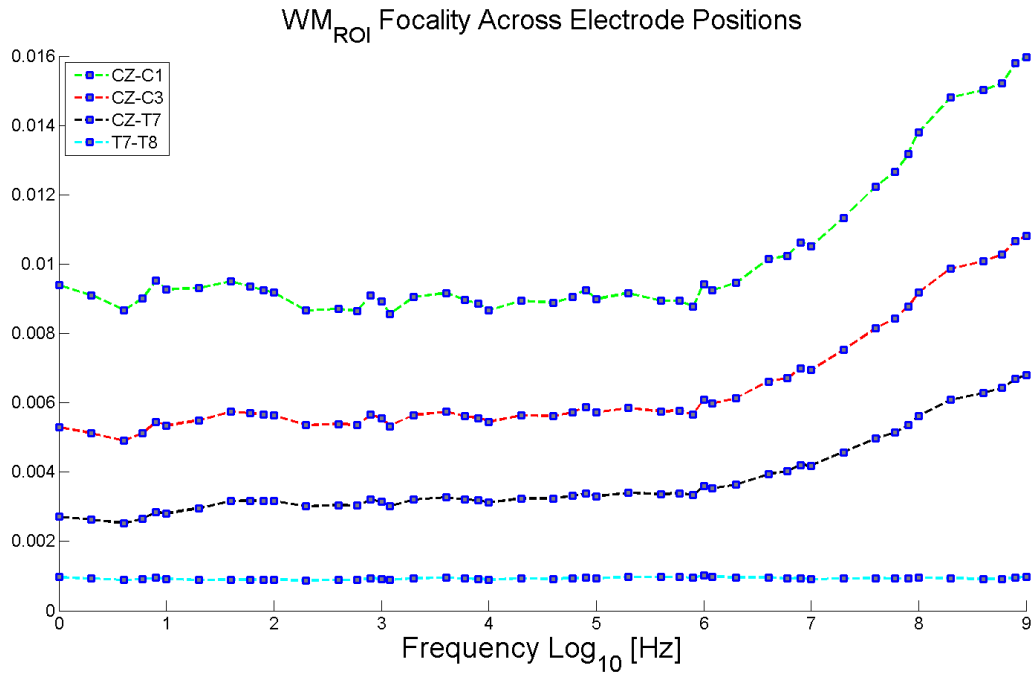


Figure 6.20: WM_{ROI} focality of all electrode montages vs. frequency.

In Fig. 6.20 we show the focality spectra of the bipolar montages. The pattern here follows the same as that of the GM ROI. Overall focality is significantly lower for the WM ROI.

Fig. 6.21 illustrates the focality of the whole brain. Here we see that the electrode montage with widest gap or θ angle (T7-T8) also has the highest focality. We do see however that the focality gain of T7-T8 over the CZ-T7 is minimal. Here the montage that generates the lowest whole brain focality is CZ-C1 where the electrodes are closely spaced.

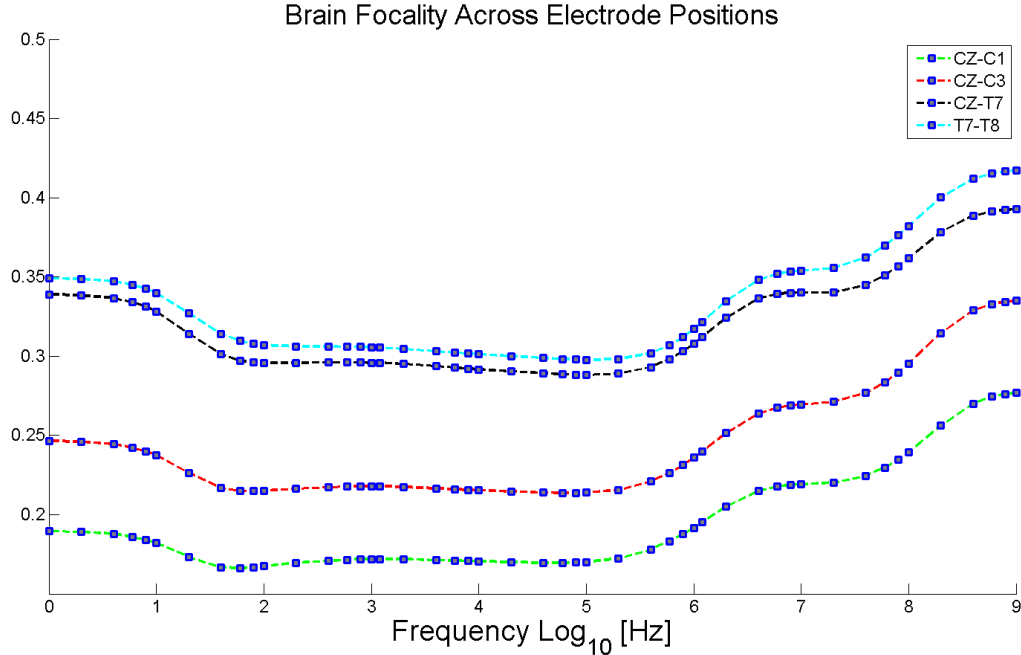


Figure 6.21: Brain focality of all electrode montages vs. frequency.

6.1.4 Discussion

The bipolar or 2 electrode montage is widely used for measurement and stimulation such as time series recording of EEG [199,200] and for application of tDCS [59,201]. Traditionally, bipolar montages are used in neurostimulation applications for DC or low frequencies [202].

We wished however to consider the sensitivity field over a wide frequency range for the following reasons:

Firstly we are interested in a unique impedance spectra that can be related to a particular montage/dose configuration. The DC or low end frequency applications can be thought of as occupying the beginning of the spectra. By analyzing a wide frequency range we hope to gain knowledge of the head tissue frequency response over the α , β and γ relaxation zones (see section 4.5). In chapter 8 we describe how biological tissue frequency response can be modelled as a configuration of circuit elements referred to as the Cole model. By simulation of a wide range of frequency points we gain insight of how each tissue can be fitted to multiple Cole models over the 3 principal dispersion regions.

Secondly, many applications of bipolar montages are using frequencies well above DC.

Examples include studies of neuro plasticity using transcranial alternating current stimulation (tACS) that include stimulation up until 5 KHz [50] and the use of alternating electric fields at 200 KHz for the treatment of brain tumors [51]. In addition transcranial random noise stimulation (tRNS), has been used between 0.1 and 640 HZ [52]. Furthermore bioimpedance studies are generally in the high KHz range due the generally high frequencies needed to measure the dielectric properties of common biological tissue [53–56].

Thus in order to relate the bioimpedance spectroscopy measurement to neural dose in the context of stimulation or measurement we analyzed the sensitivity field distributions resulting from several bipolar montages over a wide frequency range.

As described in [195] the sensitivity field of a bipolar configuration is always positive. Here the current density fields entirely overlap as the current and voltage electrode pair are the same. Since there is field cancellation effect sensitivity values are very high around the electrode sites. We note that for all montages, the scalp tissue and CSF have the highest sensitivity values, this is consistent with the findings of [203,204]. The high sensitivity in the scalp and CSF is also in accord with studies that show that these tissues act as shunt pathways during neuro-stimulation resulting in a decrease of current delivered towards the intended neural ROI [105,167]. A relative comparison of the sensitivity magnitude of each tissue over frequency is shown with a series of Log-Log plots (see Fig. 6.13 - Fig. 6.16)

We show here that the sensitivity distribution in the scalp (modelled with the dielectric and conductivity properties of a muscle see section 4.5 actually increases until about 1 Mhz. Thus increasing stimulation frequency is not effective strategy for bypassing the scalp tissue.

In consideration of the CSF, we do however note a sharp dropoff in sensitivity as a function of increasing frequency. This decrease of sensitivity does not represent however a great increase of current in the neural regions as much of this drop is offset by the increase of

scalp sensitivity. It is only past 1 MHz where we begin to see a relatively large increase in grey matter and white matter sensitivity (see Fig. 6.8 and Fig 6.10) due to decline of both scalp and CSF conductivity. This pattern is mirrored at the GM and WM ROIs' albeit at lower absolute values. We thus see the dielectric properties of the scalp and CSF are critical in influencing sensitivity in the brain.

The sensitivity pattern of the skull tissue is generally inverse to the scalp, however the skull sensitivity is overall much lower than the scalp.

The addition of noise shows some of the challenges of using the bipolar for measurement application. In Fig. 6.5 (b) we see that many of the error bars overlap indicating the potential difficulty of distinguishing measurements derived from close montages. The FEM model idealizes the scalp domain as a material with isotropic conductivity at each frequency, in practice the scalp electrode boundary is the region that produces a significant source of error due to a high impedance contact layer comprised of stratum corneum and hair [205].

Simulation results show the results of spatial separation or increasing the θ angle of the electrodes. We note that the sensitivity graphs of the scalp and skull tissues have a unique order when compared to the other tissues. For scalp and skull, CZ-C1 results in the lowest sensitivity, the CZ-C3 montage however results in the highest sensitivity although the inter-electrode θ angle is not the largest of the all the bipolar montages (see Fig 6.5 and Fig. 6.6). The next montage CZ-T7 results in a lower sensitivity profile. Finally T7-T8 generates a sensitivity graph below that of CZ-T7 but greater than that of CZ-C1.

All other tissues show a clear dependence on inter-electrode θ angle. Thus the sensitivity increases from CZ-C1, CZ-C3, CZ-T7 and finally T7-T8 results in the greatest sensitivity values.

We showed here that the sensitivity response of the head tissues has a strong linear correlation to current density (see table 6.1). In addition this correlation exists for the

electric field distribution as well (see table 6.18) (although there is negative correlation between most tissues with the exception of CSF and scalp is weakly correlated).

Although in the general we show there is a linear relationship between sensitivity and dose (current density and electric field), this is true for variation of these parameters as a function of frequency. However the relationship of the magnitude of these parameters is non-linear (quadratic see for example eq. 6.2. Thus by analyzing the frequency response of the sensitivity and transfer impedance we can gain insight into the frequency response but not necessarily into the magnitude of dose-related parameters. The non-linearity of these relationships can explain the scalp and skull sensitivity pattern as a function of inter-electrode θ angle as described in earlier paragraphs.

We note that for both the GM and WM ROI focality is maximized by decreasing the inter-electrode θ angle, thus CZ-C1 achieves the highest focality and T7-T8 results in the lowest focality. We note that the montage that produces the highest focality also results in the lowest sensitivity magnitude. This shows the fundamental tradeoff between intensity and focality (for further discussion see [59,206]. Furthermore an increase of focality at the high end of the frequency range may come at the penalty of decreased electric field intensity. Results of the whole brain ROI shows as intuitively expected that montages with the highest inter-electrode θ generated the highest focality.

The high sensitivity field concentration in proximity to the electrode pair suggest that this setup is most suitable for targeting shallow cortical ROIs. Indeed transcranial stimulation optimization schemes generally involve the use of multiple electrodes [59,109].

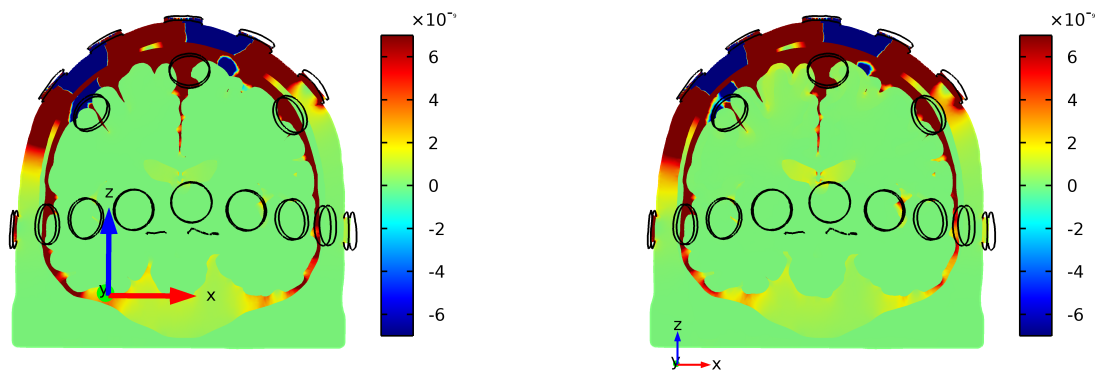
We have analyzed the sensitivity distribution across frequency and electrode montages for a range of bipolar montages. We have shown that sensitivity is related to dose and that focality is dependent on electrode montage configuration. We will explore how to link these parameters to impedance and impedance-derived parameters as these can be measured directly.

6.2 Four electrode configuration

In this part of the chapter we repeat our analysis for a number of tetrapolar montages. See section 4.1.2 for a description of these montages.

6.2.1 Head Tissue Sensitivity

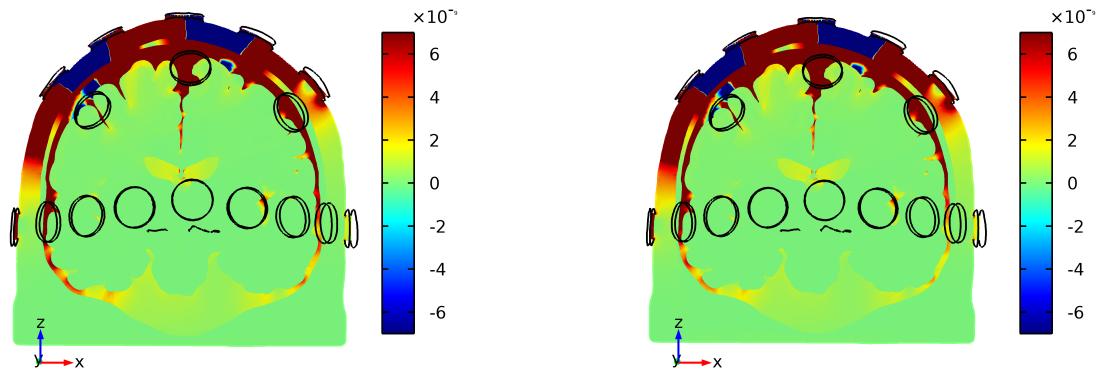
ultislice: $(ec.jx*ec2.jx+ec.jy*ec2.jy+ec.jz*ec2.jz)/(mod1.bnd1)^2 (1/mr$ ultislice: $(ec.jx*ec2.jx+ec.jy*ec2.jy+ec.jz*ec2.jz)/(mod1.bnd1)^2 (1/mr$



(a) 1 Hz

(b) 1 KHz

ultislice: $(ec.jx*ec2.jx+ec.jy*ec2.jy+ec.jz*ec2.jz)/(mod1.bnd1)^2 (1/mr$ ultislice: $(ec.jx*ec2.jx+ec.jy*ec2.jy+ec.jz*ec2.jz)/(mod1.bnd1)^2 (1/mr$



(c) 100 KHz

(d) 1 MHz

Figure 6.22: Sagittal plane view of sensitivity field from the C3-C1-CZ-C2 montage. Model is oriented such that the face is facing forward. Plots are shown in the mm scale with units as $[1/mm^4]$. Sensitivity is shown with a maximum scale of 10^{-7} . Sensitivity distributions are shown for 4 frequencies (a) 1 Hz, (b) 1 KHz, (c) 100 KHz, (d) 1 MHz.

Fig. 6.22 shows the sensitivity field distribution for the montage C3-C1-CZ-C2. Like for

results shown for the bipolar montages, we can note high density of the sensitivity field in the scalp and CSF. Here however we see for the first time a sensitivity field with negative values. The negative field is highly concentrated in the scalp between the current-voltage pairs of C3-C1 and CZ-C2. A small negative field zone is also found in the CSF in this area. The positive field region in the scalp is concentrated between the voltage pair C1-C2 and is also found extending the current electrodes C3 and C2.

The graphs show little change for the plotted frequencies (1 Hz, 1 KHz, 100 KHz and 1 MHz) except for decrease of CSF as represented by a lightening of the CSF colour from red to yellow.

In Fig. 6.23 we see the T7-C3-CZ-C2 sensitivity distribution. Here again the negative sensitivity field is concentrated in the scalp and CSF between the current-voltage pairs of T7-C3 and CZ-C2. The increased gap of T7-C3 results in a larger negative sensitivity zone. We note that the high density positive sensitivity fields are found between in the scalp between C3-CZ as well as past T7 and C3. The CSF also shows a high sensitivity field which diminishes in intensity as frequency is increased.

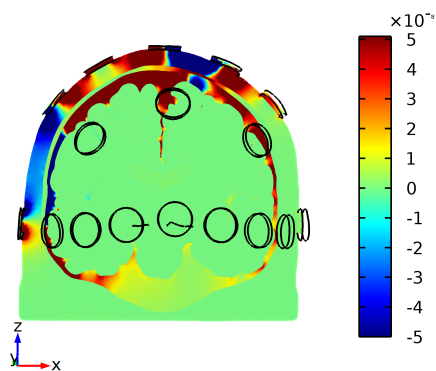
Finally in Fig.6.24 we show the sensitivity field distribution resulting from the montage T7-C3-C4-T8. Here the negative sensitivity field zone extends along the side of head in the scalp and CSF between the current-voltage pairs of T7-C3 and C4-T8.

This section has shown that the tetrapolar montage results in a negative field between the current and voltage electrodes in the scalp and CSF tissues. We now show numerical results of the simulated sensitivity fields. As mentioned for results of the bipolar montages, mean results of 6 measurements (samples) are shown. Error bars in the plots are the standard error of the mean.

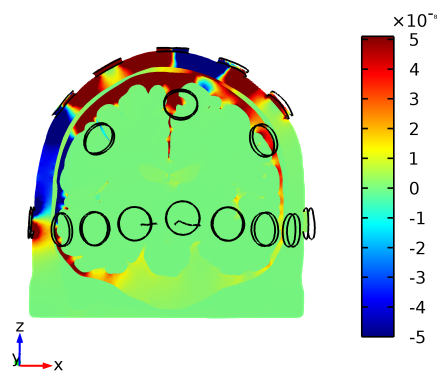
6.2.1.1 Scalp

Fig.6.25 shows the profile of the scalp sensitivity. Here we note that compared to the bipolar montage, the scalp sensitivity is greatly reduced. The scalp sensitivity rises to a

Multislice: (ec.Jx*ec2.Jx+ec.Jy*ec2.Jy+ec.Jz*ec2.Jz)/mod1.bnd1^2 (1/mm⁴) Multislice: (ec.Jx*ec2.Jx+ec.Jy*ec2.Jy+ec.Jz*ec2.Jz)/mod1.bnd1^2 (1/mm⁴)



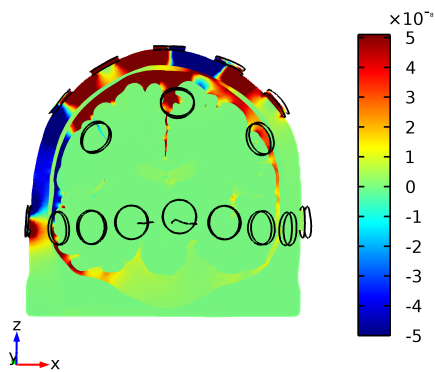
(a) 1 Hz



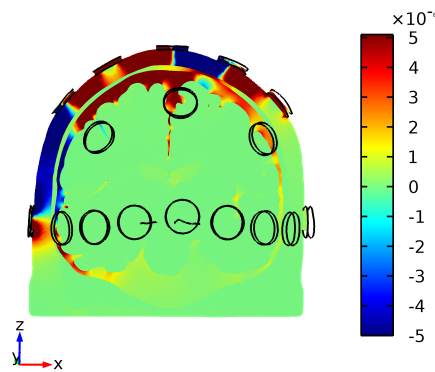
(b) 1 KHz

Multislice: (ec.Jx*ec2.Jx+ec.Jy*ec2.Jy+ec.Jz*ec2.Jz)/mod1.bnd1^2 (1/mm⁴)

Multislice: (ec.Jx*ec2.Jx+ec.Jy*ec2.Jy+ec.Jz*ec2.Jz)/mod1.bnd1^2 (1/mm⁴)



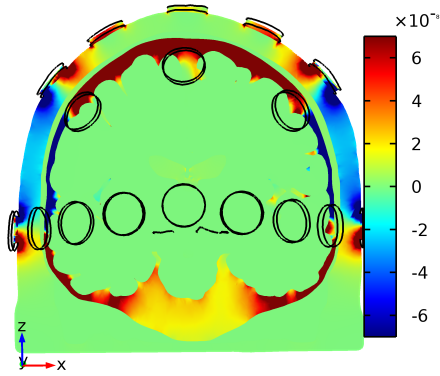
(c) 100 KHz



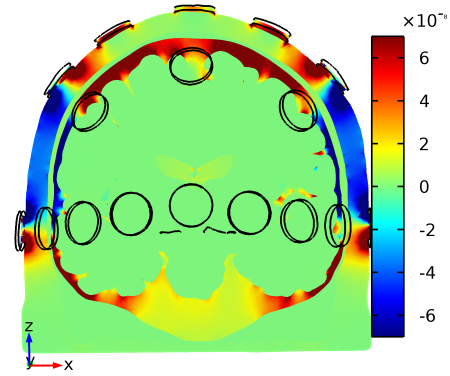
(d) 1 MHz

Figure 6.23: Sagittal plane view of sensitivity field from the T7-C3-CZ-C2 montage. Model is oriented such that the face is facing forward. Plots are shown in the mm scale with units as $[1/mm^4]$. Sensitivity is shown with a maximum scale of 10^{-7} . Sensitivity distributions are shown for 4 frequencies (a) 1 Hz, (b) 1 KHz, (c) 100 KHz, (d) 1 MHz.

Multislice: (ec.Jx*ec2.Jx+ec.Jy*ec2.Jy+ec2.Jz*ec.Jz)/mod1.bnd1^2 (1/mm⁴) Multislice: (ec.Jx*ec2.Jx+ec.Jy*ec2.Jy+ec2.Jz*ec.Jz)/mod1.bnd1^2 (1/mm⁴)



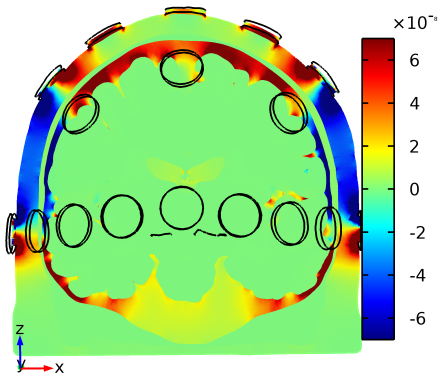
(a) 1 Hz



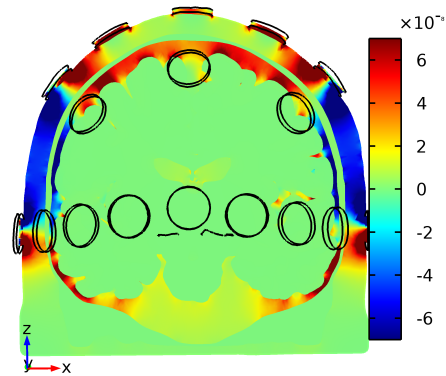
(b) 1 KHz

Multislice: (ec.Jx*ec2.Jx+ec.Jy*ec2.Jy+ec2.Jz*ec.Jz)/mod1.bnd1^2 (1/mm⁴)

Multislice: (ec.Jx*ec2.Jx+ec.Jy*ec2.Jy+ec2.Jz*ec.Jz)/mod1.bnd1^2 (1/mm⁴)



(c) 100 KHz



(d) 1 MHz

Figure 6.24: Sagittal plane view of sensitivity field from the T7-C3-C4-T8 montage. Model is oriented such that the face is facing forward. Plots are shown in the mm scale with units as $[1/mm^4]$. Sensitivity is shown with a maximum scale of 10^{-7} . Sensitivity distributions are shown for 4 frequencies (a) 1 Hz, (b) 1 KHz, (c) 100 KHz, (d) 1 MHz.

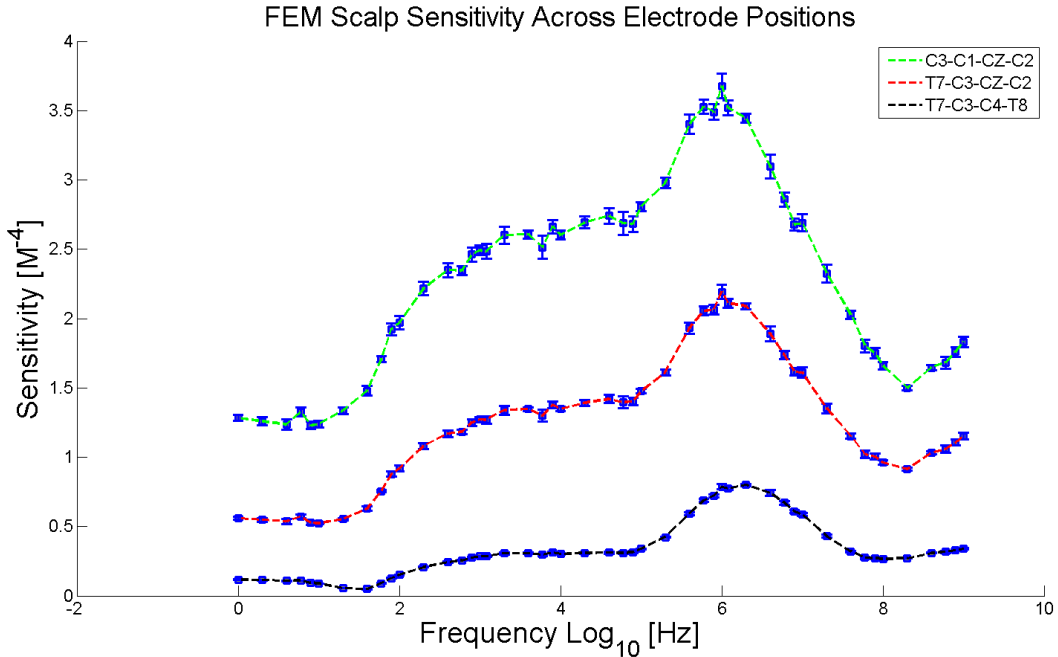


Figure 6.25: Mean scalp sensitivity vs. frequency for all electrode montages.

peak slightly past 1 MHz as shown earlier for the bipolar montage plots.

For the 3 montages shown we see a clear effect of increasing inter-electrode θ angle. The C3-C1-CZ-C2 montage, where all the electrodes are sited in adjacent positions, results in the highest sensitivity. T7-C3-CZ-C2 generates a lower sensitivity graph. Finally T7-C3-C4-T8 shows the lowest sensitivity profile. We note that at frequencies lower than 100 Hz the scalp sensitivity of T7-C3-C4-T8 is almost 0.

6.2.1.2 Skull

In Fig. 6.26 we show the sensitivity of the skull tissue. Like the bipolar montage, the skull sensitivity pattern across frequency appears to be the inversion of the scalp sensitivity.

Overall the tetrapolar skull sensitivity is lower than that of the bipolar montages.

Here again we see the effect of inter-electrode gap or θ . The montage with the smallest gap, C3-C1-CZ-C2, has the highest skull sensitivity. The T7-C3-CZ-C2 montage results in a lower sensitivity profile followed by T7-C3-C4-T8 which shows the lowest sensitivity of all.

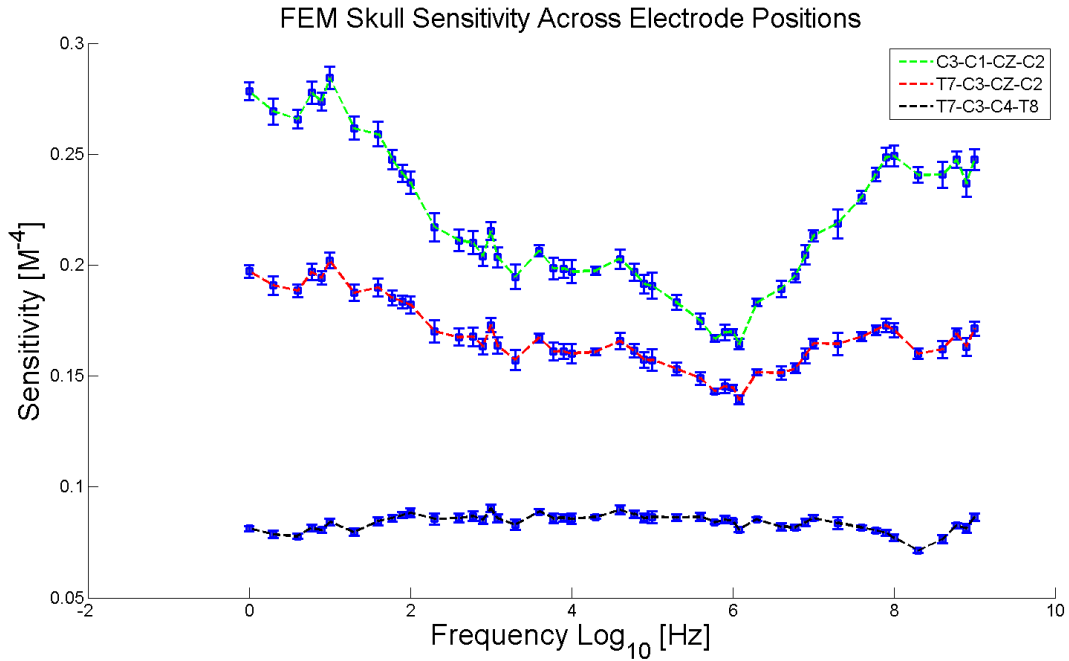


Figure 6.26: Mean skull sensitivity vs. frequency for all electrode montages

6.2.1.3 CSF

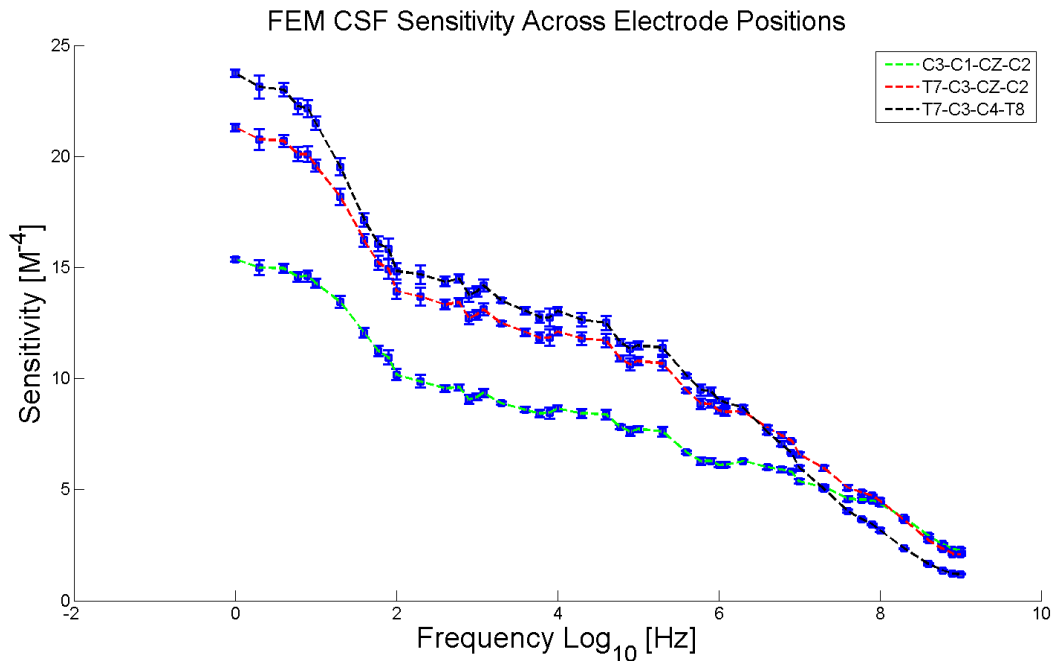


Figure 6.27: Mean CSF sensitivity vs. frequency for all electrode montages.

Fig. 6.27 illustrates the sensitivity profiles of the CSF tissue. Here we see a rapid drop of

sensitivity as a function of increasing sensitivity. The order of sensitivity magnitude from greatest to least is from montages T7-C3-C4-T8, T7-C3-CZ-C2 and C3-C1-CZ-C2 (The high frequency end of the T7-C3-C4-T8 CSF sensitivity intercepts and descends lower than that of the other montages). We note that the profile of the CSF sensitivity curves is similar to those generated from the bipolar montages albeit with lower absolute values.

6.2.1.4 GM

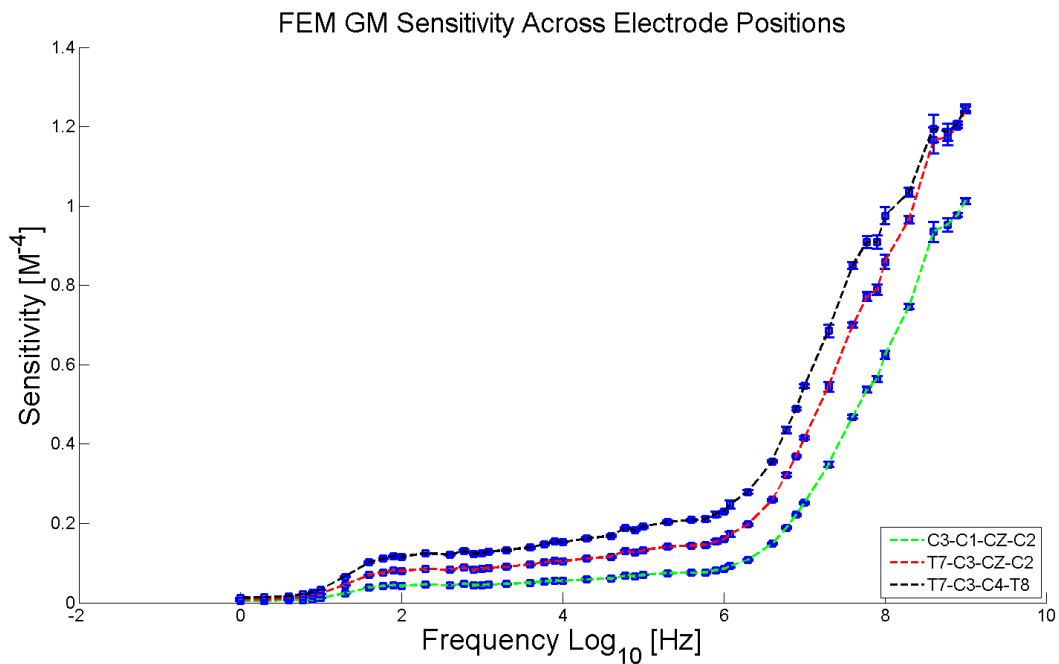


Figure 6.28: Mean grey matter sensitivity vs. frequency for all electrode montages.

Fig. 6.28 shows the sensitivity graphs of the GM.

Again we can see a clear separation between the GM sensitivities generated by the different montages. The arrangement with electrodes the closest together, C3-C1-CZ-C2, results in the lowest sensitivity values. This is followed by T7-C3-CZ-C2.

The overall pattern of the sensitivity over frequency approximates the inverse of the CSF and is similar to the GM sensitivity generated by the bipolar montages except that the absolute sensitivity values are lower.

6.2.1.5 GM ROI

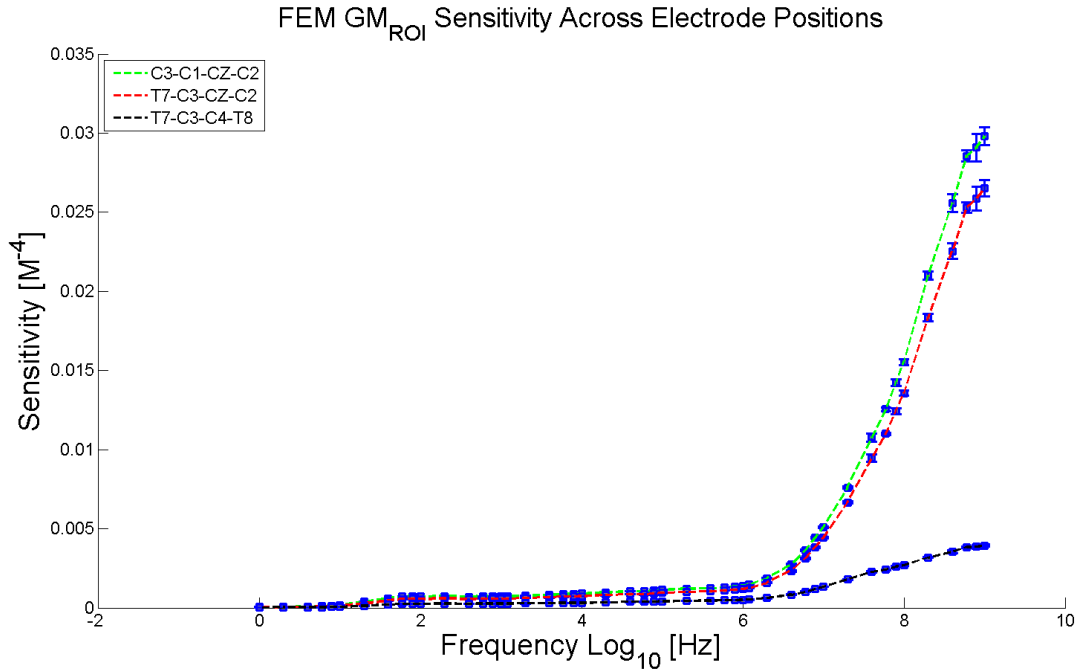


Figure 6.29: Mean grey matter ROI sensitivity vs. frequency for all electrode montages.

In Fig. 6.29 we show the sensitivity of the GM ROI.

There are main two differences here compared to the GM sensitivity:

- First the GM ROI sensitivity of T7-C3-C4-T8 diverges lower at the high frequency end as compared to the sensitivity of other montages
- Secondly the absolute values of the GM ROI sensitivity are significantly lower than that of the GM sensitivity itself (unlike results from the bipolar montage).

6.2.1.6 WM

Fig. 6.30 shows the white matter sensitivity profiles.

The shape of the sensitivity graphs is similar to that of the grey matter. The values of the WM sensitivity are slightly lower than that of the WM sensitivity generated by the bipolar montages.

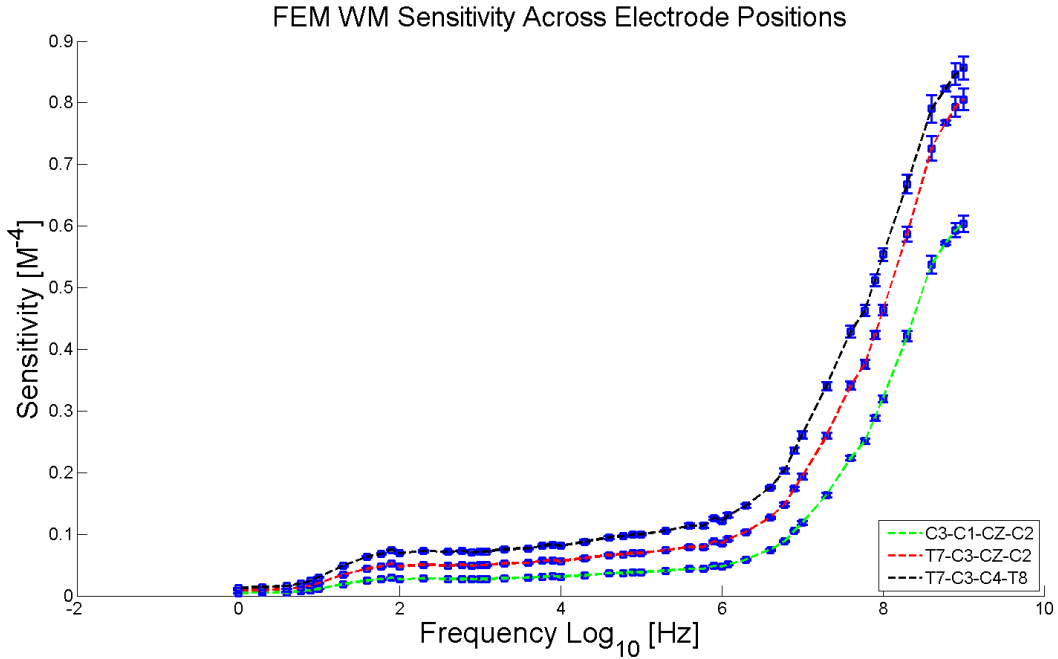


Figure 6.30: Mean white matter sensitivity vs. frequency for all electrode montages

6.2.1.7 WM ROI

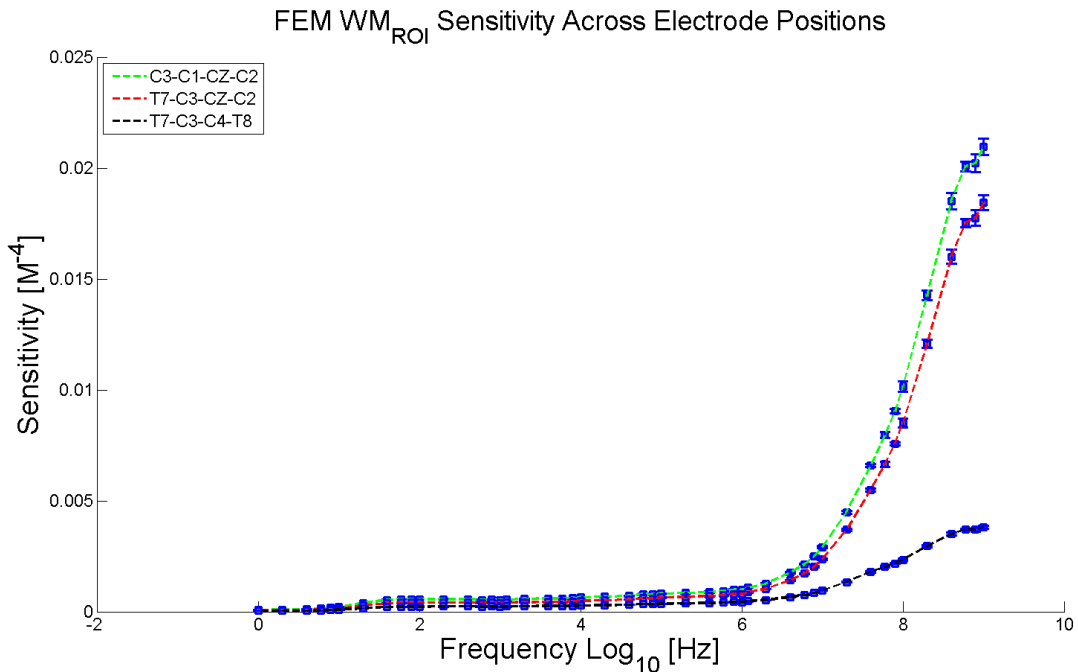


Figure 6.31: Mean white matter ROI sensitivity vs. frequency for all electrode montages.

In Fig. 6.31 we show the sensitivity graphs of the WM ROI. The profiles here are similar to

the graphs of the GM ROI. Thus the sensitivity of T7-C3-C3-T8 diverges lower at high frequencies from the sensitivities of the other montages.

6.2.1.8 Eye Matter

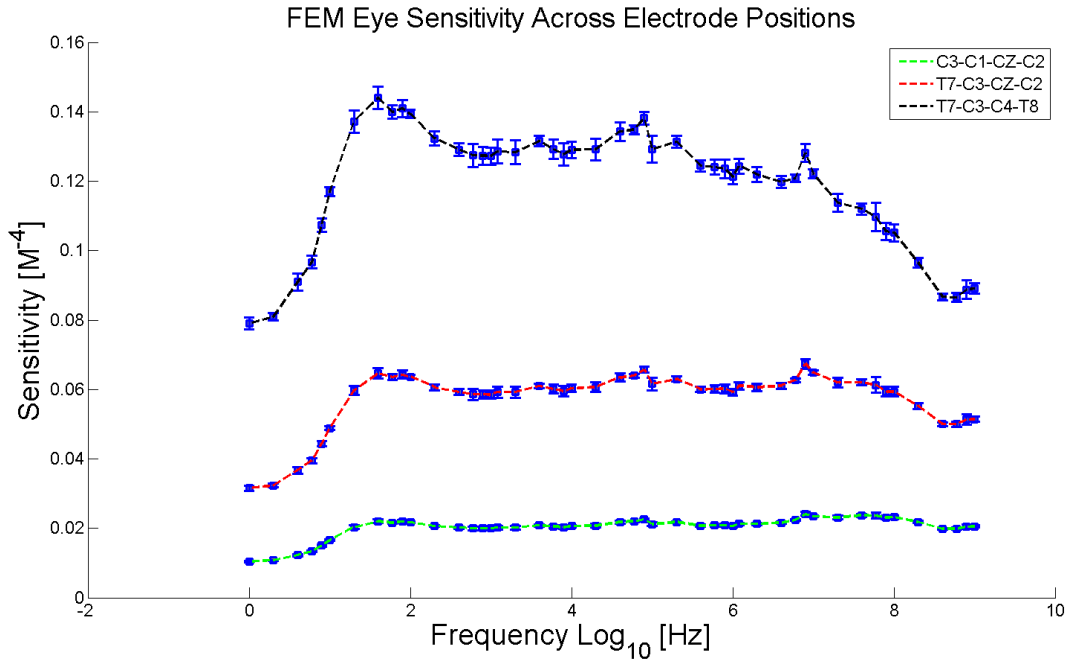


Figure 6.32: Mean eye sensitivity vs. frequency for all electrode montages.

The sensitivity of the eye matter tissue is shown in Fig. 6.32. We note the sensitivity pattern here is similar to eye sensitivity generated from bipolar montages.

Here we see the effect of electrode separation. C3-C1-CZ-C2 generates the lowest sensitivity, this is followed by the sensitivity generated T7-C3-CZ-C2. Finally T7-C3-C4-T8 is shown to result in the highest eye tissue sensitivity.

6.2.1.9 All Head Tissues

In order to visualize the relative magnitude of each tissue sensitivity, we show a series of Log-Log plots that show each tissue sensitivity across frequency for every montage. Error bars are added to the plots as described in section 6.1.1.9.

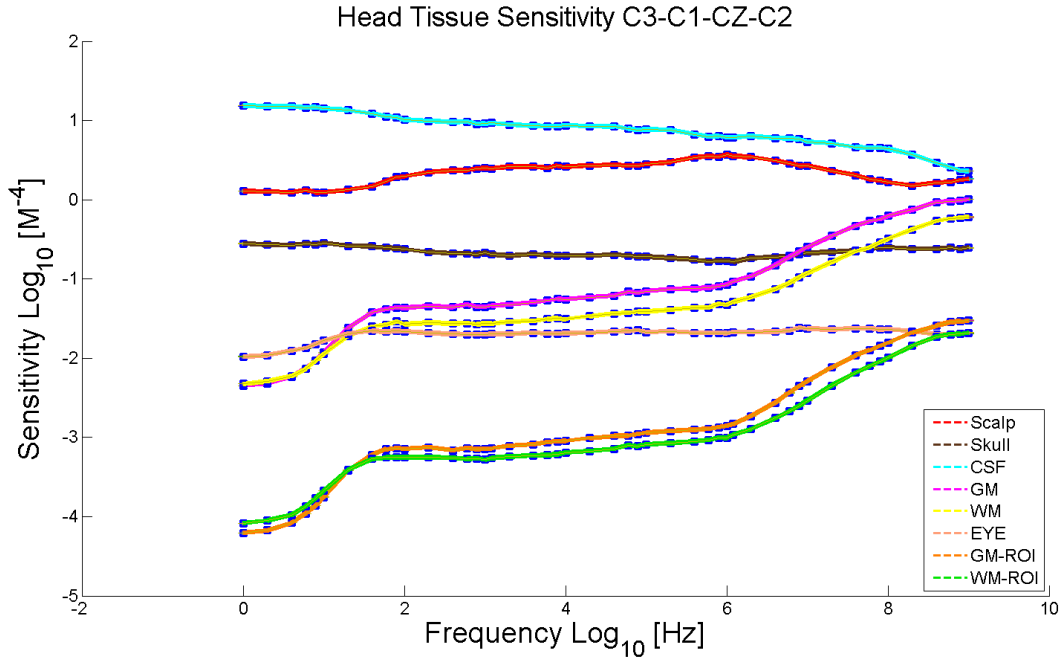


Figure 6.33: Log-Log graph of C3-C1-CZ-C2 head tissues sensitivity vs frequency with error bars (SEM).

In Fig. 6.33 we show the sensitivity of all the head tissues for the montage C3-C1-CZ-C2.

We see that the CSF has the largest sensitivity until the end of the frequency range. This is followed by the scalp tissue and skull. GM and WM sensitivity intercept and climb past the skull at around 10 Mhz. The eye sensitivity is relatively flat across the frequency range. Finally the GM ROI and WM ROI follow the same sensitivity profile over frequency as the GM and WM except with a large sensitivity magnitude offset downwards.

Fig. 6.34 shows the sensitivity graphs of the head tissues for the T7-C3-CZ-C2 montage.

Here we note 2 major changes. First the scalp sensitivity is lower than that of the previous montage. This is shown by the larger offset between the scalp and CSF. Secondly the GM and WM sensitivities are increased, here they intercept the skull sensitivity at a lower frequency - around 1 MHz. The eye sensitivity magnitude is also shown increased.

In Fig. 6.35 we show the sensitivity graphs of the head tissues for the final montage - T7-C3-C4-T8.

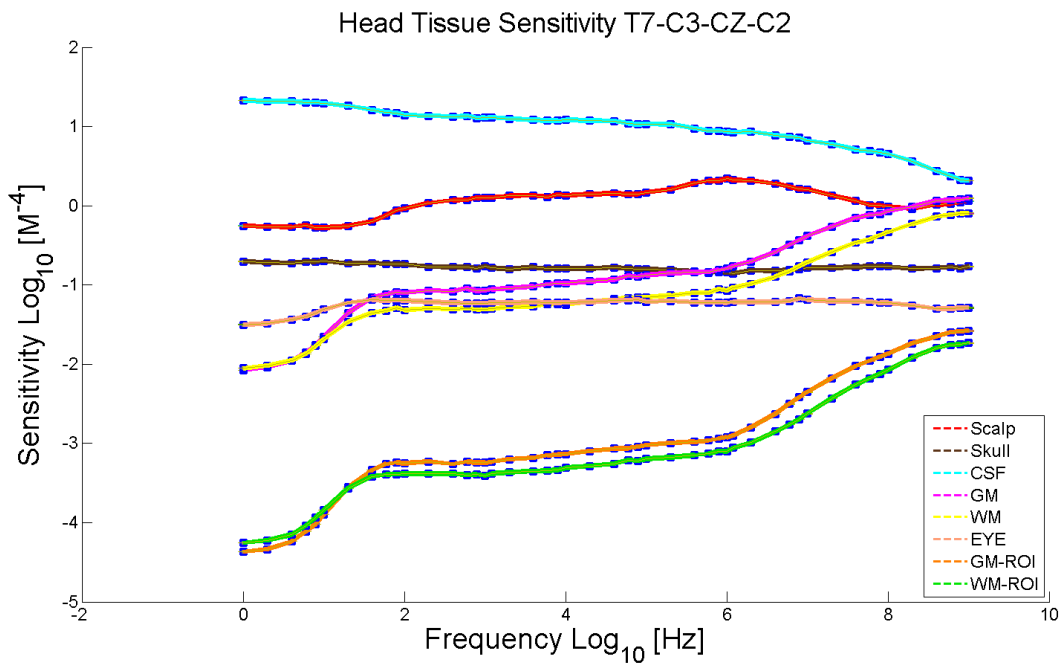


Figure 6.34: Log-Log graph of T7-C3-CZ-C2 head tissues sensitivity vs frequency with error bars (SEM)

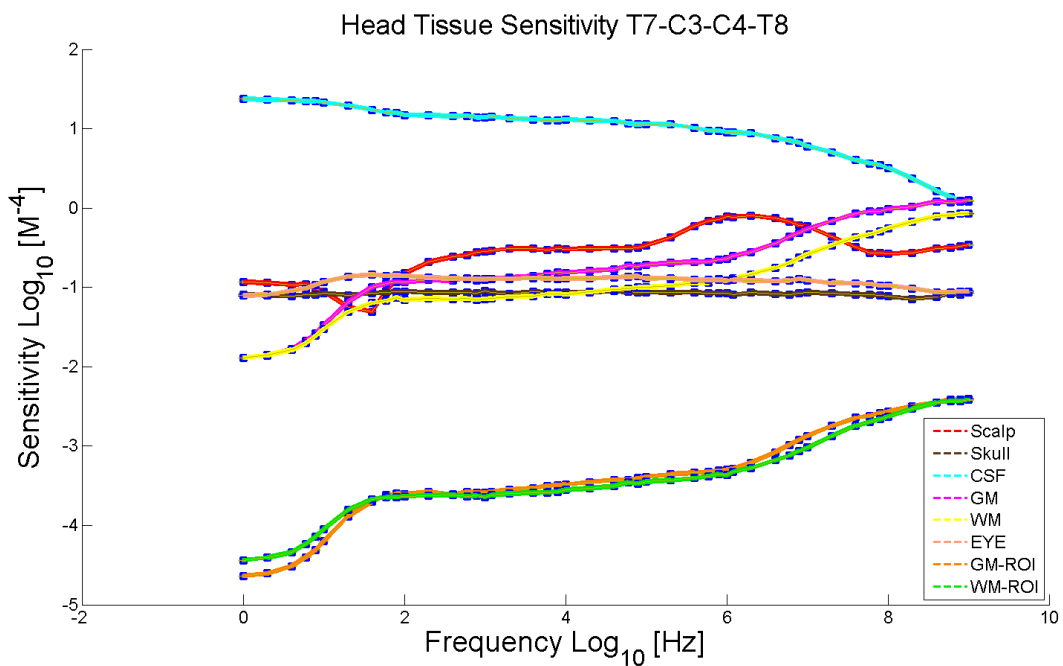


Figure 6.35: Log-Log graph of T7-C3-C4-T8 head tissues sensitivity vs frequency with error bars (SEM).

We mention here some striking changes. Here we see that the scalp sensitivity has greatly decreased at low frequencies. At close to 100 Hz the scalp sensitivity sharply decreases, this is followed by an abrupt increase. The GM, WM and eye tissue sensitivity all track closely to the scalp sensitivity. At some frequencies (≈ 100 Hz and 10 Mhz) we see that these tissues overlap and have a higher sensitivity than the scalp tissue.

6.2.2 Sensitivity vs. Dose and Measurement Parameters

In this section we compare the sensitivity graphs to parameters related to dose, i.e. current density and electric field. We also calculate the level of correlation between these variables.

6.2.2.1 Sensitivity vs Current Density

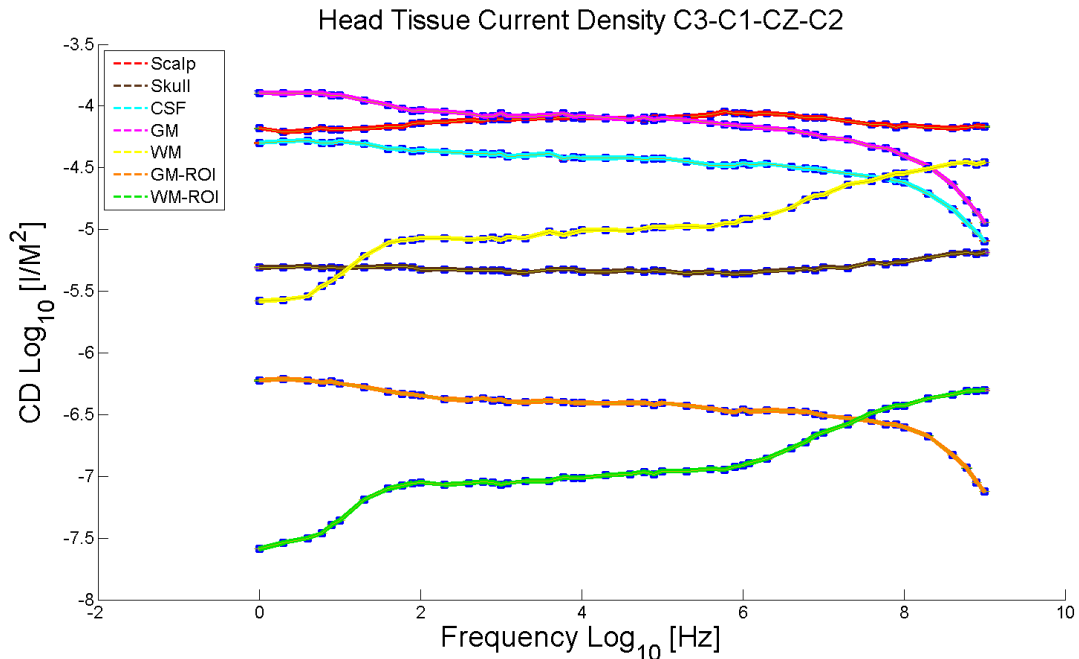


Figure 6.36: Log-Log graph of C3-C1-CZ-C2 head tissue current density vs frequency with error bars (SEM).

In Fig. 6.36 we show the current density profile of all the head tissues (with the exception of the eye tissue due to the high noise and discontinuous nature of the graph) for the C3-C1-CZ-C2 montage.

Some of the differences between the sensitivity and the current density graphs are:

- the grey matter has the highest current density whereas the CSf has the highest sensitivity
- the grey matter and grey matter ROI current density both increase as a function of increasing frequency
- the white matter current density is greater than the skull current density at around frequencies greater than 100 Hz

Tissue Type	R coefficient	P value
Scalp	0.980	3.286×10^{-34}
Skull	0.547	5.815×10^{-05}
CSF	0.945	6.246×10^{-24}
GM	-0.857	7.647×10^{-15}
WM	0.940	4.313×10^{-23}
GM ROI	-0.828	3.653×10^{-13}
WM ROI	0.953	1.452×10^{-25}

Table 6.3: Coefficient and p-values of correlation of head tissue sensitivity and current density for the C3-C1-CZ-C2 montage.

Next we show the correlation between sensitivity and current density in table 6.3.

We see that for most tissues there is a high linear correlation coefficient and a low p-value. The skull tissue has the lowest coefficient of 0.547. We note here that there is a negative correlation between the GM and GM ROi sensitivity and current density.

6.2.2.2 Sensitivity vs Electric Field

Fig. 6.37 shows the electric field graphs of all the head tissues for the C3-C1-CZ-C2 montage. Here we the following major differences between the electric field and sensitivity profiles:

- the scalp and CSF have the highest electric field magnitude

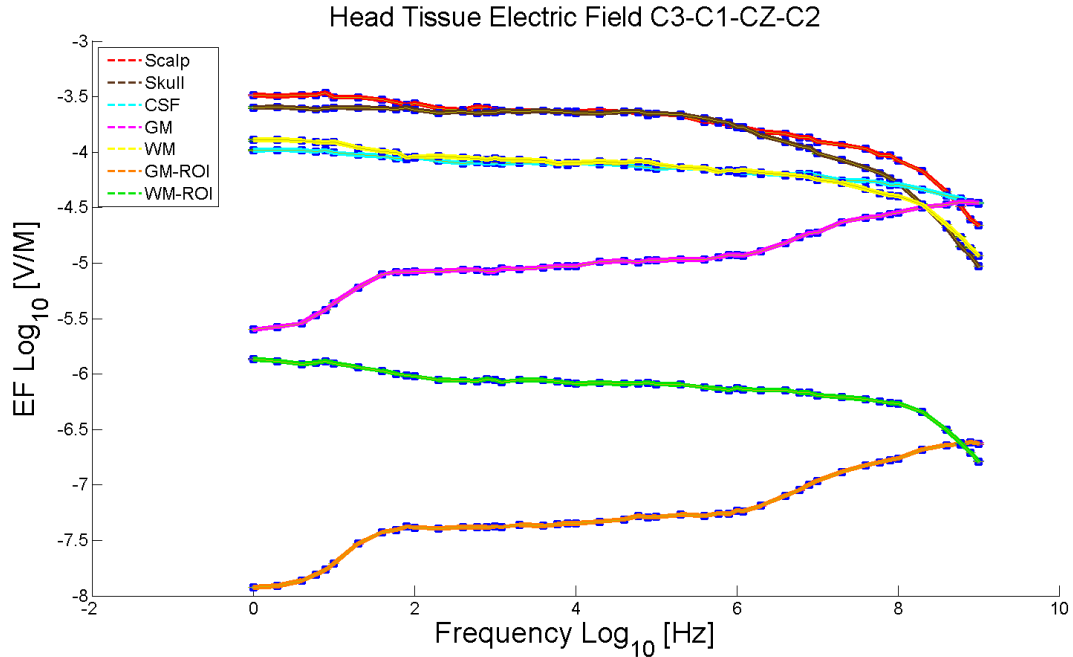


Figure 6.37: Log-Log graph of C3-C1-CZ-C2 head tissue current density vs frequency with error bars (SEM).

- the WM and WM ROI electric field magnitude are higher than their corresponding sensitivity fields
- all the tissues electric field magnitude decrease as a function of increasing frequency except for the GM and GM ROI.

Tissue Type	R coefficient	P value
Scalp	-0.133	0.366
Skull	-0.737	2.274×10^{-09}
CSF	0.982	3.392×10^{-35}
GM	-0.943	1.099×10^{-23}
WM	-0.941	2.232×10^{-23}
GM ROI	-0.903	1.566×10^{-18}
WM ROI	-0.892	1.701×10^{-17}

Table 6.4: Coefficient and p-values of correlation of head tissue sensitivity and electric field for the C3-C1-CZ-C2 montage.

In table 6.4 we see the correlation coefficients and p-values of the electric field and sensitivity. We note that there is a strong correlation between most of the head tissues.

Scalp has the weakest correlation of -.133. The CSF has a high positive correlation of .982. All the other tissue have a high negative correlation coefficient.

6.2.3 Focality

Like the previous section 4.1.1 we show the results of GM ROI, WM ROI and whole brain focality.

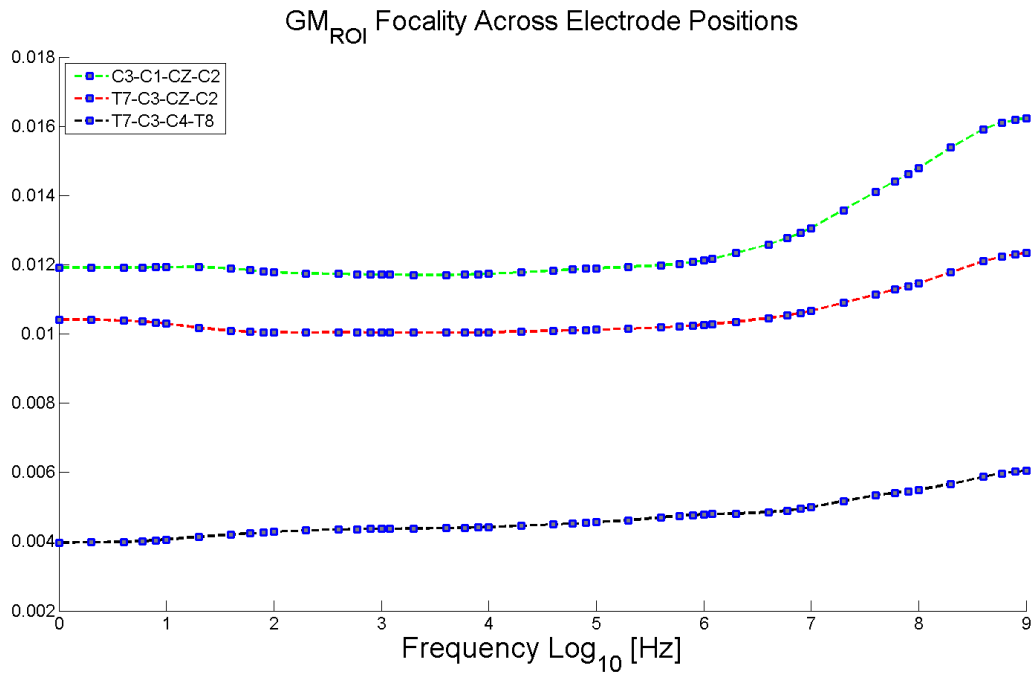


Figure 6.38: GM_{ROI} focality of all electrode montages vs. frequency.

In Fig. 6.38 we see that the highest focality is achieved with the C3-C1-CZ-C2 montage. This is followed by a lower focality for the T7-C3-CZ-C2. Finally T7-C3-C4-T8 has the lowest focality. Thus we see that that increasing the inter electrode gap or θ angle has the effect of decreasing focality.

Fig. 6.39 shows the same pattern as that illustrated in Fig. 6.38. Here we see however that the absolute values are lower - i.e. lower focality can be achieved.

Finally we show in Fig.6.40 the whole brain focality. T7-C3-CZ-C2 has the highest focality until about 10 MHz. T7-C3-C4-T8 focality overlaps and attains a higher focality for

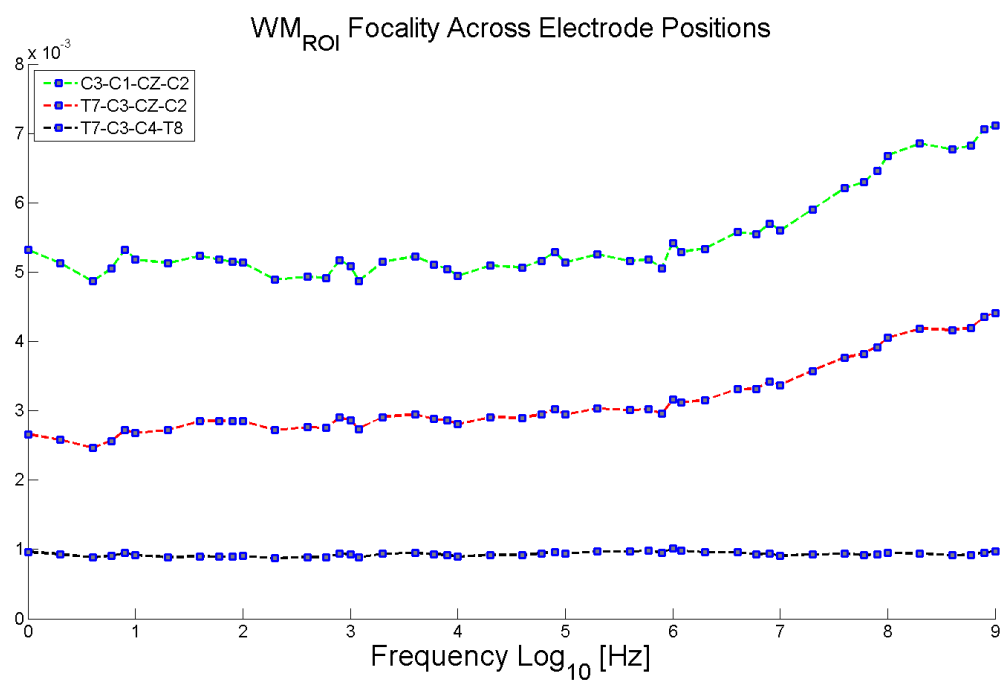


Figure 6.39: WM_{ROI} focality of all electrode montages vs. frequency

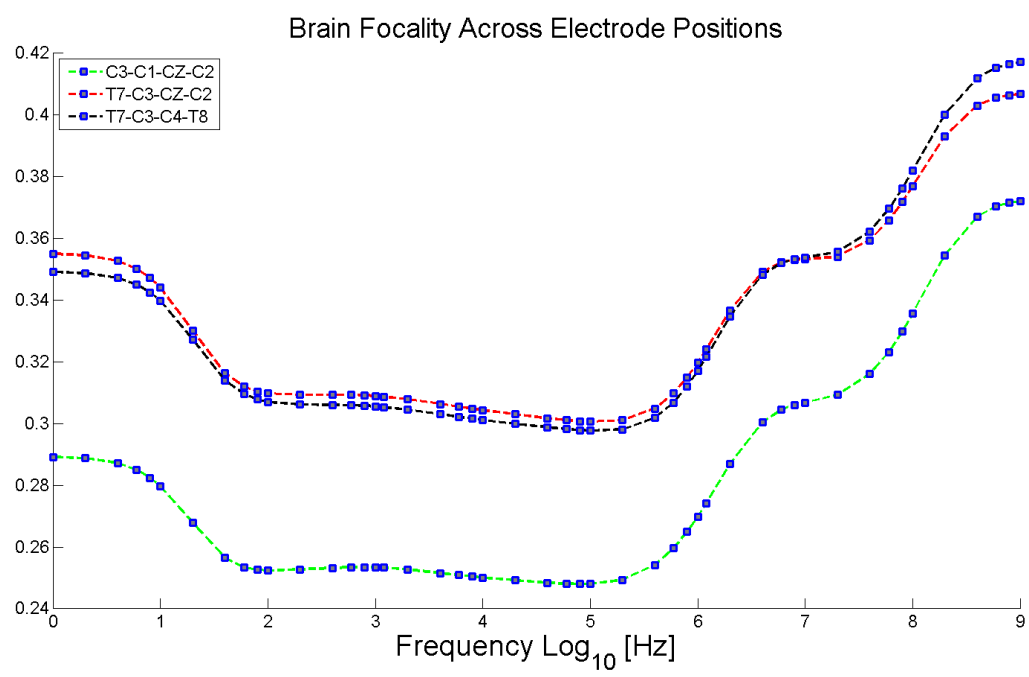


Figure 6.40: Brain focality of all electrode montages vs. frequency.

frequencies higher than 10 MHz. The montage with the lowest focality by a significant margin is C3-C1-CZ-C2.

6.2.4 Discussion

In this section, we described results of sensitivity simulations of 3 tetrapolar montages. The advantage of separating the voltage (pick up) electrodes from the current carrying electrodes is that measurement of the high impedance contact layer is avoided [207].

There are however challenges of using separate current and voltage electrodes. Since the voltage and current lead fields may be at different orientations, the resulting sensitivity field may be negative in parts of the volume (see for example [195]).

We show that the sensitivity distribution in the scalp and CSF include high density negative regions (see Fig. 6.22 - Fig. 6.24).

The greatest effect of the negative sensitivity is a very large reduction of the scalp sensitivity (see Fig. 6.25) and to lesser extent a reduction of CSF sensitivity (see Fig. 6.27). The reduction of sensitivity in the more superficial layers of the head tissues is consistent with the findings of Brown et al. [208] that showed that mean sensitivity of a tetrapolar arrangement is found to be zero on the surface plane.

We show that this large field cancellation effect in the scalp tissue is dependent on the gap or θ angle between the voltage and current electrodes. As shown in Fig.6.22 - Fig. 6.24 the positive sensitivity zone is concentrated between the inner current electrodes whereas the negative sensitivity zone is located mainly between the voltage and current electrodes.

Additionally we show that the larger the angle between the current and voltage electrodes, the greater the negative sensitivity zone and the resulting field cancellation effect. Thus the montage T7-C3-C4-T8 with a large angle between the voltage and current electrode pairs T7-C3 and T8-C4 results in the greatest reduction of scalp sensitivity (see Fig. 6.25). This pattern is true for the skull (Fig. 6.26), the GM ROI (Fig. 6.29) and the WM ROI

(Fig. 6.31).

For all the other tissues we note an opposite effect, as the angle between the current electrodes is increased, the sensitivity also increases in deeper tissues. Thus the highest CSF sensitivity is generated by the T7-C3-C4-T8 montage (see Fig. 6.26). The increased angle between the current electrodes thus balances out and may cancel the effect of the negative sensitivity field.

We also show in a series of Log-Log plots the magnitude of the sensitivity of all the head tissues over our tetrapolar montages (see Fig.6.34 - Fig.6.35). Here we can visualize the decreased scalp sensitivity relative to other head tissues. We note for the montage with the largest negative sensitivity regions - T7-C3-C4-T8, the GM and WM sensitivities track closely to the sensitivity of the scalp.

The implications of the negative sensitivity field cancellation affect are interesting for bioimpedance measurements and neurostimulation. See for instance [209] for a discussion of the importance of reducing scalp impedance. We see that the sensitivity of the scalp can be greatly reduced by careful positioning of the current and voltage electrode pairs. This has the net affect of increasing the SNR and the impedance contribution of the neural tissues such as GM and WM.

Recent advances in neurostimulation suggest using arrays of small electrodes to focus and optimize the stimulation current [59,210]. New approaches in focused neurostimulation suggest that interfering waveforms [211] and pulse stimulation [212] can be used to reach deep targets in the brain. In [206] it is however argued that conventional DC stimulation from multiple electrode sources can achieve results comparable or better to the novel waveforms.

Results of the our simulations support this argument as we have shown that a dramatic reduction of scalp sensitivity at DC can be accomplished by appropriate positioning of current and voltage electrode pairs. In the context of current or electric field, this could

conceivably be accomplished by 2 sets of current electrode positioned appropriately so the field orientations cancel in the scalp tissue.

To further support the link between sensitivity and dose, we show that there is generally a high correlation between the sensitivity and dose parameters (current density and electric field) of all tissues. (Some tissues have a weak correlation such as skull and scalp, others have a strong negative correlation see tables 6.3 and 6.4).

Finally we show that for a relatively close current pair configuration (C3-C1-CZ-C2) maximum focality is achieved at the GM ROI and WM ROI. Results here are obviously dependent on the placement of the ROI. Thus for instance when the entire brain was designated as an ROI, the C3-C1-CZ-C2 had the lowest focality and T7-C3-CZ-T8 and T7-C3-CZ-C2 achieved similar results.

Now that we have shown that sensitivity profile of each tissue is dependent on parameters such as frequency and electric montage, we wish to show how this can related to a measurable output - the transfer impedance. Our goal is then to relate transfer impedance characteristics to the sensitivity and dose parameters of each montage.

6.3 Summary

In this chapter we describe and analyze in detail results of simulations of sensitivity of the head tissues. Results are graphed as the mean values of 6 samples with error bars (standard error of the mean) plotted. First results of the bipolar configurations (CZ-C1, CZ-C3, CZ-T7, T7-T8) are described in detail. We show that for all bipolar configurations the scalp and CSF have the greatest sensitivity distribution. As the angle between the electrodes are increased the intra-cranial sensitivity distribution also increases.

Our analysis of sensitivity distributions resulting from the tetrapolar electrode configurations (C3-C1-CZ-C2, T7-C3-CZ-C2 and T7-C3-C4-T8) show that 3 tissue types (scalp, CSF, GM) have the highest sensitivity concentration. We also show that the

sensitivity field of the four electrode configurations has a negative component that increases as the angle between the current and voltage electrodes are increased. Here we also show that intra-cranial sensitivity increases as inter-electrode angle is increased. We also showed that the sensitivity distribution in the head tissues is highly correlated to dose parameters (current density and electric field) for both the bipolar and tetrapolar configurations.

Chapter 7

Multi-frequency Transfer Impedance Simulations

7.1 Relationship between Transfer Impedance, and Sensitivity

In chapter 6 we analyzed in detail the sensitivity spectra of the head tissues for various bipolar and tetrapolar montages. We showed that the sensitivity magnitude of certain tissues was much larger than that of others (for example the bipolar measurements all generated very high sensitivity).

We now wish to connect the sensitivity simulations to transfer impedance. The relationship between sensitivity and impedance (see the beginning of chapter 6) is:

$$Z = \int S \frac{1}{(\sigma + j\omega\epsilon)} dv \quad (7.1)$$

.

We see that the impedance of each tissue is dependent on its sensitivity and electrical properties (conductivity and permittivity).

When considering the total impedance of the head tissues, it is important to determine the contributing weight of each tissue type.

We can write that the total impedance of the measured head volume is the sum of of its constituent volumes or tissues or:

$$Z_{Volume} = Z_{Vol_1} + Z_{Vol_2} + \dots Z_{Vol_n} \quad (7.2)$$

Thus the the total head impedance is the sum of the impedance of all its components or tissues. For n tissues we then have

$$\sum_1^n Z_{Head\ Tissue(n)} = Z_{Head} \quad (7.3)$$

Impedance is a product of the sensitivity and specific impedance of each tissue. We can then write that

$$\sum_1^n S_{Head\ Tissue(n)} * \sum_1^n \rho_{Head\ Tissue(n)} = Z_{Head} \quad (7.4)$$

We can think of the sensitivity as weight by which the specific impedance of each tissue is multiplied. For each frequency point the sensitivity weight and specific impedance of each tissue may change thus we can write for the total impedance spectra over j frequency points with n head tissue types

$$\begin{aligned} \sum_1^j \sum_1^n S_{Head\ Tissue(n)}(freq(j)) * \sum_1^n \rho_{Head\ Tissue(n)}(freq(j)) \\ = Z_{Head}(freq(j)) \end{aligned} \quad (7.5)$$

Here we analyze the results of simulating the impedance spectra of all the head tissues for our designated bipolar and tetrapolar montages. This will enable us to determine which tissues have the greatest contribution to the total head impedance. These results will show that the impedance spectra of the human head can be approximated as a sum of the impedances of only 3 tissues (scalp, skull and CSF). we thus aim to show how impedance

contribution of several head tissues are negligible and thus eq. 7.6 can be written in fewer terms. This reduces the complexity of decomposing the total impedance measurement to its constituent parts.

Graph results show mean values with relative error on the logarithmic scale as described in section 6.1.1.9.

7.2 Head Tissue Impedance

7.2.1 Two Electrode Configuration

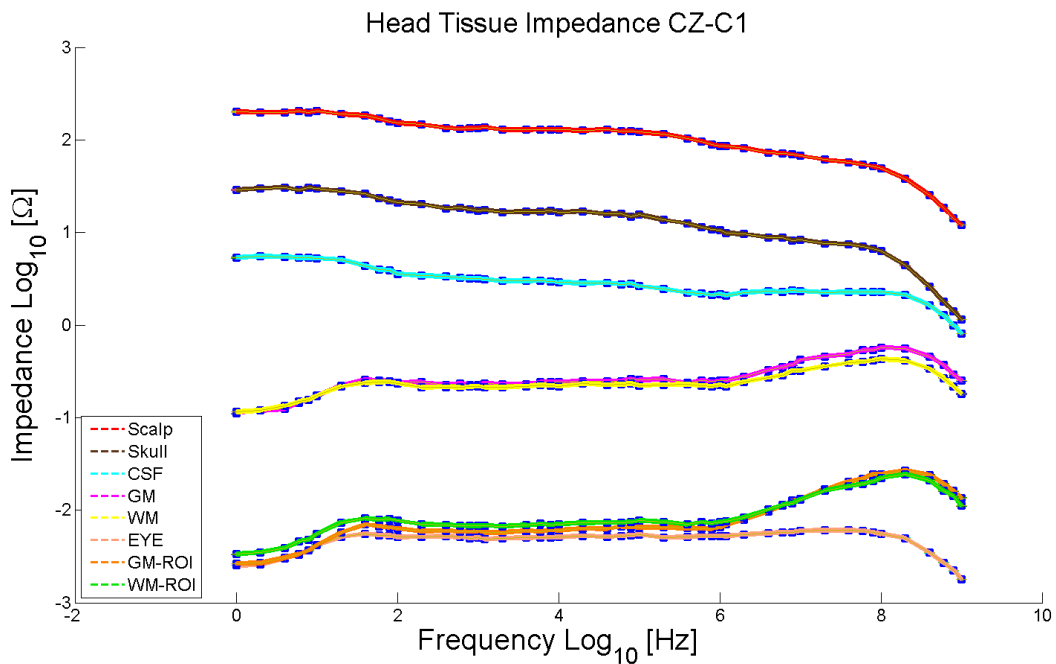


Figure 7.1: Log-Log graph of CZ-C1 head tissue impedance vs. frequency.

Fig. 7.1 shows a log-log graph of head tissue impedance magnitude spectra for the CZ-C1 montage. We see that that the scalp tissue has by the far the largest impedance magnitude. The skull tissue has the next largest impedance followed by the CSF. Other tissues in order of impedance magnitude from greatest to lest are the GM, WM, GM ROI, WM ROI and eye tissue.

Many of the tissue impedance spectra decline as a function of increasing frequency with the exception of the GM, WM (including ROIs). In addition the eye tissue impedance increases in magnitude as for frequencies up until approximately 100 Hz.

We can see that according to eq. 7.1 impedance magnitude is directly proportional to sensitivity and inversely proportional to conductivity. Thus we note that all tissues with a high sensitivity have the greatest contribution to the total impedance. The skull tissue has low sensitivity, it has however a large contribution to impedance due to its low conductivity. Other tissues, such as the GM, WM and eye tissue have a small impedance spectra magnitude since they have low sensitivity and high conductivity.

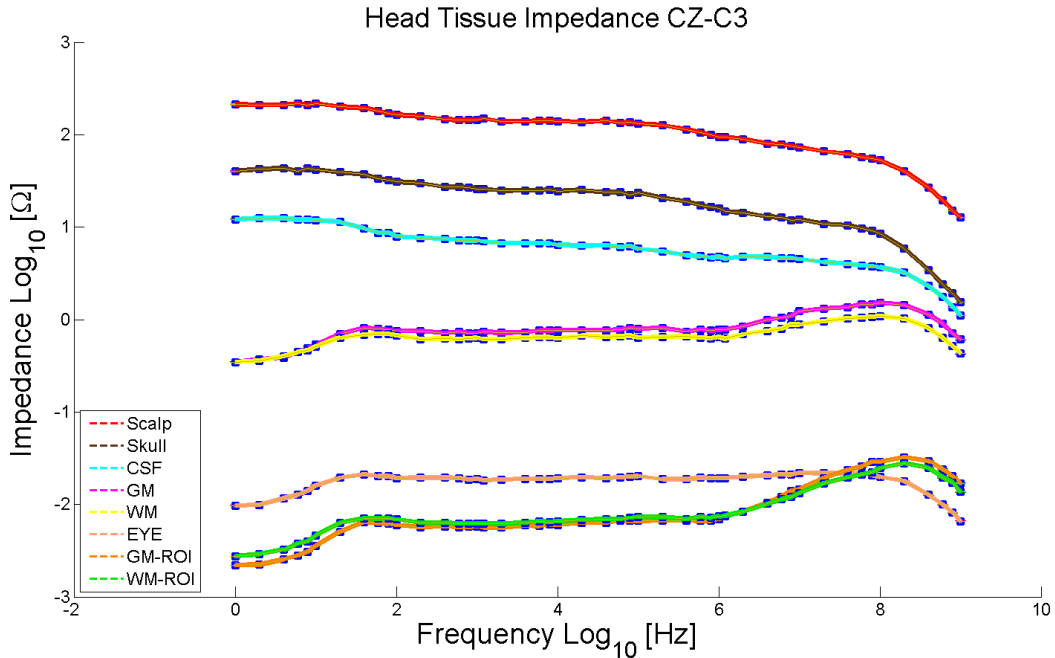


Figure 7.2: Log-Log graph of CZ-C3 head tissue impedance vs. frequency.

In Fig. 7.2 we see the head impedance spectra of the CZ-C3 montage where the inter electrode θ has been increased.

In general the spectra profiles are similar to the impedances shown in Fig. 7.1. We note however some differences: the CSF, GM, WM and eye tissue impedance magnitude have all increased. This is consistent with sensitivity simulation results that show that the

sensitivity of these tissues increase as the electrodes are moved apart. The 3 tissues with a dominant contribution to the total impedance are still (in order of magnitude from greatest to least) the scalp, skull and CSF.

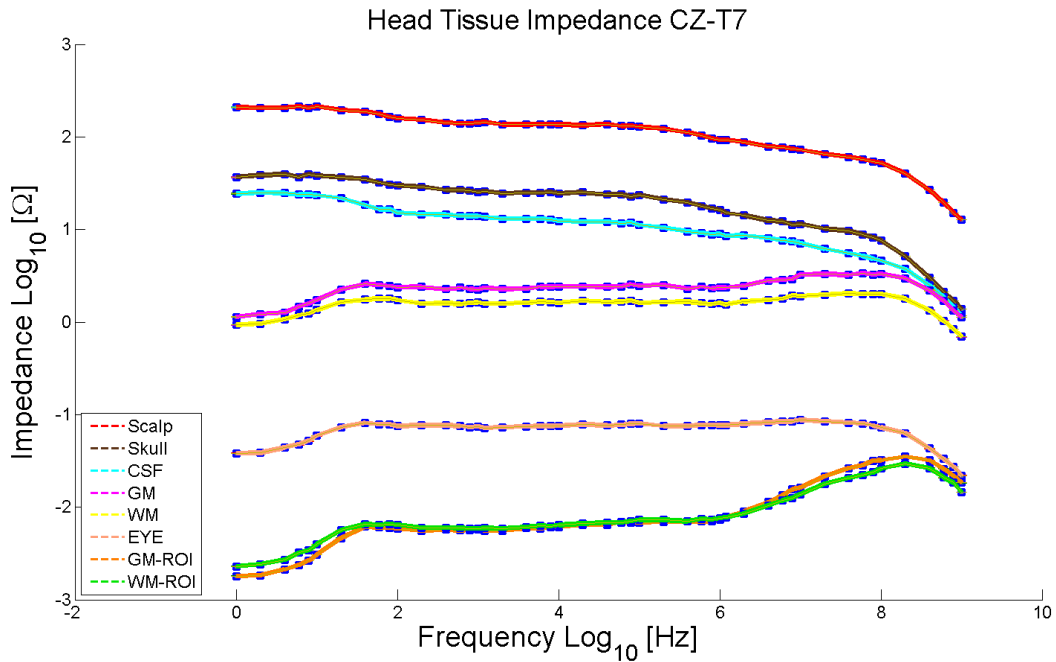


Figure 7.3: Log-Log graph of CZ-T7 head tissue impedance vs. frequency.

Fig. 7.3 shows the head tissue impedance spectra from the CZ-T7 montage. We see a higher impedance for the CSF, GM, WM and eye tissue. This can be attributed to the increased sensitivity of these tissues due to a greater inter-electrode gap as compared to the previous montage.

Finally we see in Fig. 7.4 the impedance spectra resulting from placing the electrodes on opposing sides of the head in the T7-T8 montage.

We note an increase in the CSF and GM impedance. We also see a decrease in the impedance of the GM ROI and WM ROI. The increase of the CSF impedance is due to the increase of CSF sensitivity caused by the electrode positioning. The orientation of the electrodes on the sides of the head however cause a decrease in sensitivity in the ROI which are situated under the central vertex, this then results in a lower impedance contribution of

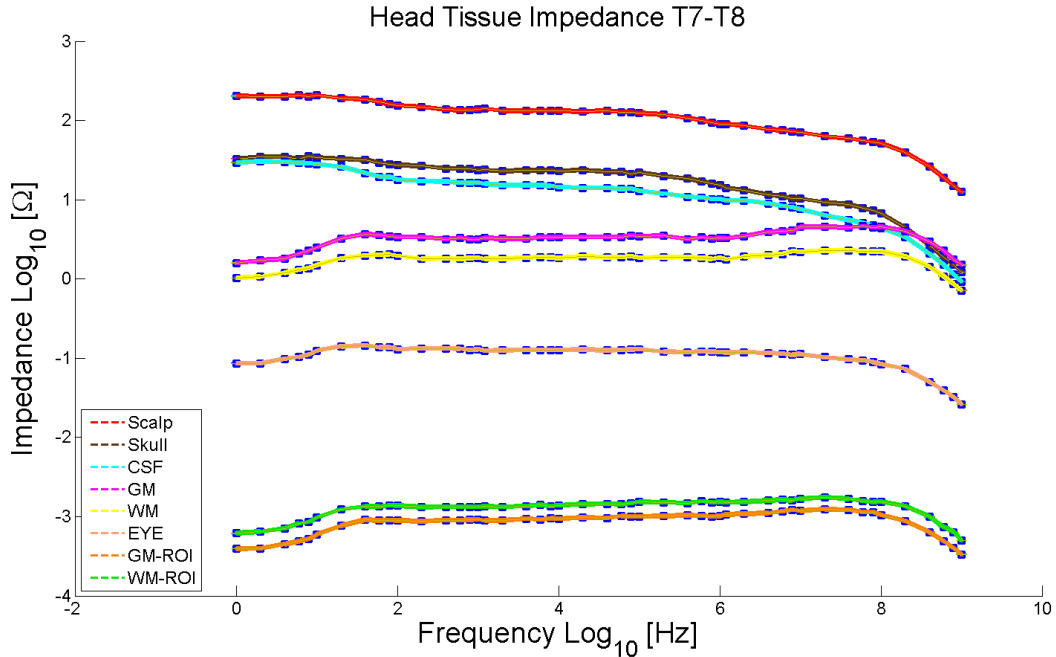


Figure 7.4: Log-Log graph of T7-T8 head tissue impedance vs. frequency.

the ROIs.

For most of the frequency range (until about 100 MHz) the 3 main contributors to the total impedance are first the scalp, then the skull and the CSF.

7.2.1.1 Discussion

Results of this section show that for our bipolar montages, the scalp has the highest impedance followed by the skull and the CSF. It is clear however that the impedance spectra is dominated by the dielectric properties of the scalp. Changing the angle between the electrode pair results in shifts to the magnitude of the tissues - for instance increasing the inter-electrode angle causes an increase in the CSF impedance. This is consistent with [208] who showed that sensitivity of a bipolar montage is always positive and decreases with depth.

Thus we show that analysis of impedance spectra of the bipolar montage can be simplified by generally only considering the impedance contribution of three tissues with the scalp

impedance being the most dominant factor. The implications here are that eq. 7.6 can be simplified to only three terms (scalp, skull, CSF) as

$$\begin{aligned}
 & \sum_1^j (S_{scalp}(freq(j)) * \rho_{scalp}(freq(j)) + \\
 & S_{skull}(freq(j)) * \rho_{skull}(freq(j)) + \\
 & S_{CSF}(freq(j)) * \rho_{CSF}(freq(j))) \\
 & \approx Z_{Head}(freq(j))
 \end{aligned} \tag{7.6}$$

It is interesting to note that tissues that provide the greatest impedance contribution are also potentially the least interesting to observe. In the context of neuro-stimulation and measurement we are interested in measuring or altering the electrical properties of the neural areas rather than the surrounding tissues (see for instance [130, 133, 213]).

We also see the difficulty of directly measuring a small ROI of the brain with the bipolar montage as the GM ROI and WM ROI magnitude is very small compared to other tissues. For instance the DLPFC (Dorso Prefrontal Lateral Cortex) and the M1 cortex (common targets in the context of neurostimulation [213–215]) impedance would very difficult to separate from the total head and brain tissue impedance.

In some contexts however, the bipolar montage could be useful. For instance a paper explored the use of bioimpedance spectroscopy to monitor changes to the scalp impedance during tDCS as a method of monitoring changes to dose during tDCS [41]. Other potential uses include preventing overvoltage during tDCS by ensuring low electrode-scalp interface impedance [216].

Another approach is to consider changes in the impedance of the scalp, skull and CSF as a proxy method of examining changes in dose (electric field and current density) in the brain or a desired ROI. We will discuss in chapter 8 is spectral impedance parameters can be used to analyze the sensitivity and dose distribution resulting from the bipolar configurations.

7.2.2 Four Electrode Configuration

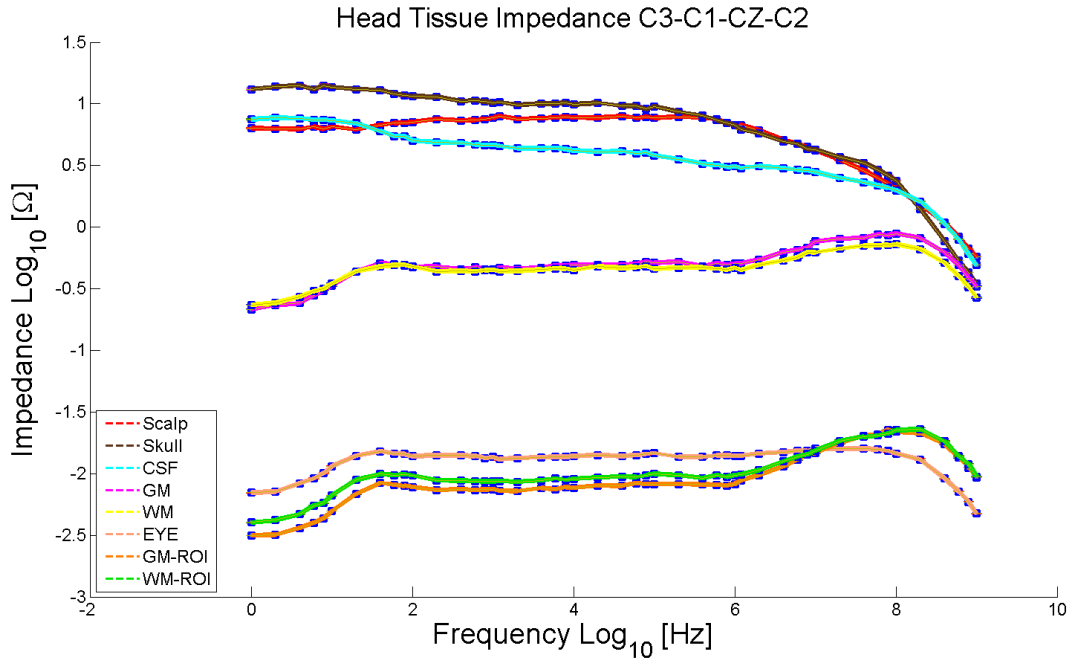


Figure 7.5: Log-Log graph of C3-C1-CZ-C2 head tissue impedance vs. frequency.

Fig. 7.5 shows the head impedance spectra resulting from the C3-C1-CZ-C2 montage. Here we can clearly see the effect of the negative sensitivity field (see Fig. 6.22). The skull has the largest magnitude impedance whereas the scalp and CSF impedance is reduced.

The GM and WM impedance spectra track together at a significantly lower magnitude. This is followed by the eye tissue, WM ROI and GM ROI.

We see in Fig. 7.6 the impedance spectra of the T7-C3-CZ-C2 montage. Here the negativity sensitivity zone in the scalp is increased (as shown in Fig. 6.23) resulting in a lower scalp impedance. Here again the dominant contributors to the total transfer impedance are skull, CSF and scalp. The impedance of the GM, WM and eye tissue has increased, whereas the impedance of the GM ROI and WM ROI appears relatively unchanged.

Fig. 7.7 illustrates the head impedance spectra for the final montage - T7-C3-C4-T8. Here we see a dramatic change in the impedance spectrum of the scalp. First the scalp spectra

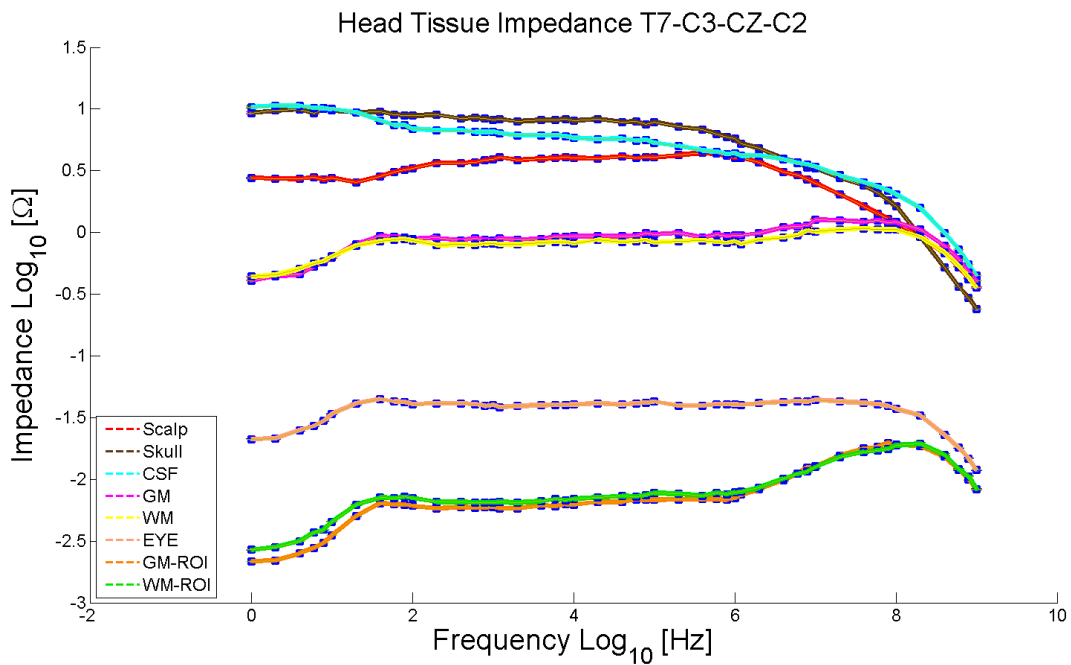


Figure 7.6: Log-Log graph of T7-C3-CZ-C2 head tissue impedance vs. frequency.

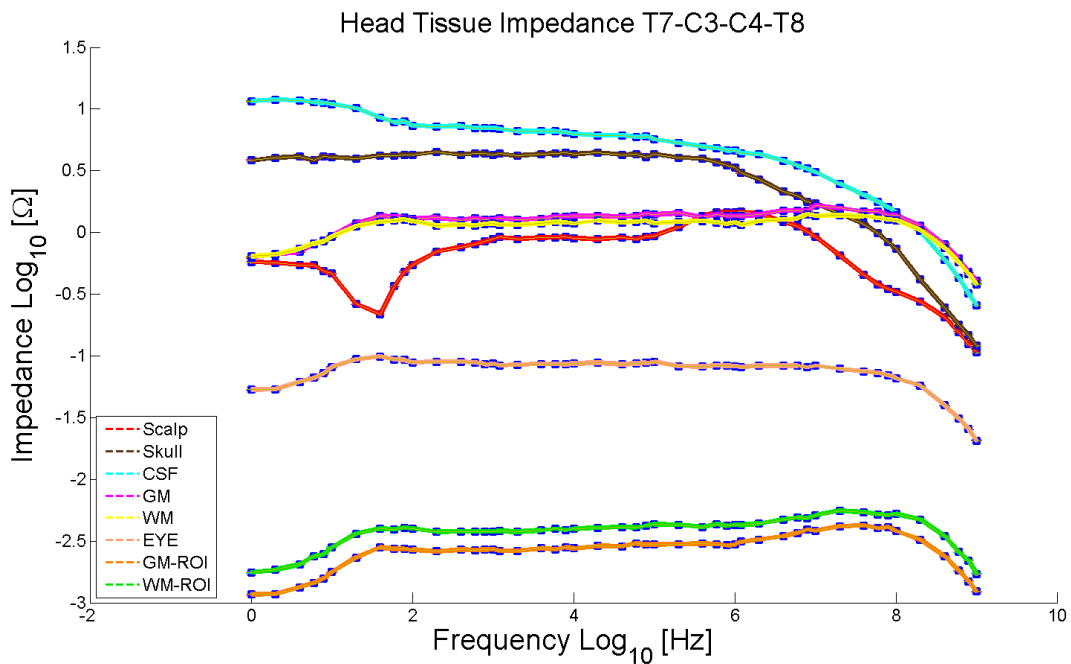


Figure 7.7: Log-Log graph of T7-C3-C4-T8 head tissue impedance vs. frequency.

magnitude is decreased below that of GM and WM for a narrow low frequency band with a minima situated close to 100 Hz. The scalp impedance then increases but generally remains below the GM and WM magnitude. Scalp impedance reaches a maxima at around 1 MHz before beginning to decline.

The great decrease in scalp impedance can be attribute to a sensitivity field cancellation effect caused by integration of the negative and positive field (see 6.24 for an illustration of the negative and positive sensitivity zones).

Here the total impedance is dominated by the CSF and the skull with smaller contributions from the GM and WM. We also see that the skull impedance is reduced whereas the CSF impedance is relatively unchanged. Other tissue impedances (eye tissue, GM ROI and WM ROI) remain negligibly small.

7.2.2.1 Discussion

Previous simulation studies have shown that the tetrapolar measurement generates negative sensitivity zones between the current and voltage electrodes [195]. Our results confirm this and show that the negativity zones act to largely reduce the scalp impedance as well as the CSF and skull in a smaller measure.

We saw earlier in this chapter that the scalp impedance dominated the bipolar montage measurement although contributions from the skull and CSF were also significant. The main effect of using a tetrapolar montage was to decrease measurement sensitivity of the high impedance scalp. Since we are interested in measuring dose in the brain, a reduction of scalp impedance is beneficial and acts to increase the relative impedance contribution of the other tissues.

We also not the dependence of the scalp impedance reduction on the angle between the voltage and current electrodes. The montage with the smallest gap between these electrodes - C3-C1-CZ-C2- produced the smallest reduction of scalp impedance. Increase of

this angle with the T7-C3-CZ-C1 montage results in a greater reduction of scalp impedance. Finally the montage T7-C3-C4-T8 with the largest current-voltage inter-electrode gap generates the greatest decrease in scalp impedance.

In Fig. 7.7 we note an interesting dip in the scalp impedance reaching a minima at close to 100 HZ before climbing back upwards. Setting an impedance measurement to a small frequency band around this critical point could be useful for applications where scalp properties are considered as signal contaminants. For instance Electrical Impedance Tomography (EIT) has been developed as a tool to record electrical activity in the brain in real time [135]. A concern of EIT image reconstruction is attenuation of the brain activity by impedance tissues until the point that the signal is reduced below the sensitivity of the EIT system [135]. EIT is also concerned with optimization of the sensitivity field in parts of a measured volume. A study has already shown that analysis of the sensitivity lead field using finite element simulations is a useful method of optimizing electrode placement [217].

Our results indicate that careful control of the angle between the current and voltage electrodes can indeed reduce sensitivity in the outer head tissues and thus increase the relative sensitivity to the neural regions.

In the tetrapolar case we also note that the total head impedance spectra can approximated as the weighted sum of 3 (scalp, skull and CSF) or 2 (skull CSF) tissue impedances depending on the montage. This has important implications for the problem of relating the transfer impedance measurement to the sensitivity field and dose as will be described in detail in the next chapter.

7.3 Summary

This chapter describes the relationship between sensitivity and impedance. In general we describe the impedance spectra as a weighted sum of the impedance measured in each head tissue where the weight is provided by the tissue sensitivity. Logarithmic plots of head

tissue impedance vs frequency show the dependence of impedance on electrode montage. Analysis of the bipolar and tetrapolar configurations showed that scalp, skull and CSF have the highest impedance. We show that as the inter-electrode angle is increased the impedance contribution of intra-cranial tissues increases as well.

Chapter 8

Cole model and Principal Component Analysis

8.1 Head Tissue Cole Model

In 1940 Kenneth S. Cole proposed an empirical mathematical equation to model the frequency dependence of tissue impedance [218]. This is written as

$$Z = R_{\infty} + \frac{\Delta R}{1 + (j\omega\tau_z)^{\alpha}} \quad (8.1)$$

where $\Delta R = R_0 - R_{\infty}$, ω is the angular frequency in Hertz, α is a dimensionless phase quantity between 0 and 1 and τ is RC - the characteristic time constant of the tissue.

The equivalent circuit of this equation is based on a Debye circuit. It has an ideal conductance element G in parallel with a non-realizable electric element referred to as a Fricke constant phase element (CPE). The CPE is modelled as a parallel resistor and capacitor; the phase of both these elements can be set to a constant which is independent of frequency [219].

Cole parameter extraction involves the fitting of a semi-circular arc in the complex plane where the horizontal axis is the resistance or the real part of the impedance and the vertical axis is the reactance or the imaginary impedance component. The right and left intersection of the arc with the horizontal axis are R_0 and R_{∞} respectively. The semi-circle

thus has an approximate radius of $\frac{R_0 - R_\infty}{2}$ when α approaches one. α is a dimensionless quantity that assumes values between 0 and 1 and provides a measure of the position of the Cole semi-circle with respect to the horizontal (resistance) axis, and τ is the characteristic time constant which corresponds to characteristic frequency f_c (at which reactance is at a maximum). The resulting extracted parameters can then be defined by the vector $m = [R_0, R_\infty, f_c, \alpha]$.

Many biological tissues have multiple layers thus a single Cole system may not adequately model its frequency dependence. (Our use of the terminology Cole system means a characteristic semi-circle in the Nyquist plane (real component of impedance vs negative imaginary component of impedance) that can be fitted to the Cole model/circuit. A single Cole system in this context can represent multiple dispersions or semi-circles for a single tissue. Multiple systems are separate semi-circles for different tissues. The total Cole system is the semi-circle or series of semi-circles that results from a single measurement of all the head tissues combined i.e. calculating the total by measuring the voltage drop across the active electrode pair.) Thus a number of authors have employed the use of multiple Cole systems to fit the impedance of biological systems with multiple dispersions [157, 220] in series or in parallel [220].

Here we are concerned with the analysis of the complex multi-layered head FEM. We propose that this system may be analyzed by fitting each tissue impedance to a separate Cole system after plotting the real impedance vs negative reactance. Adding in series the real and imaginary impedance of all the tissues results in a total or global Cole system. The Cole parameters extracted from the total Cole system then represents the contribution of the Cole system of all the tissues.

8.2 Two electrode configuration

We first consider the impedance derived from our bipolar montages (see section (4.1.1)).

8.2.1 Nyquist plots

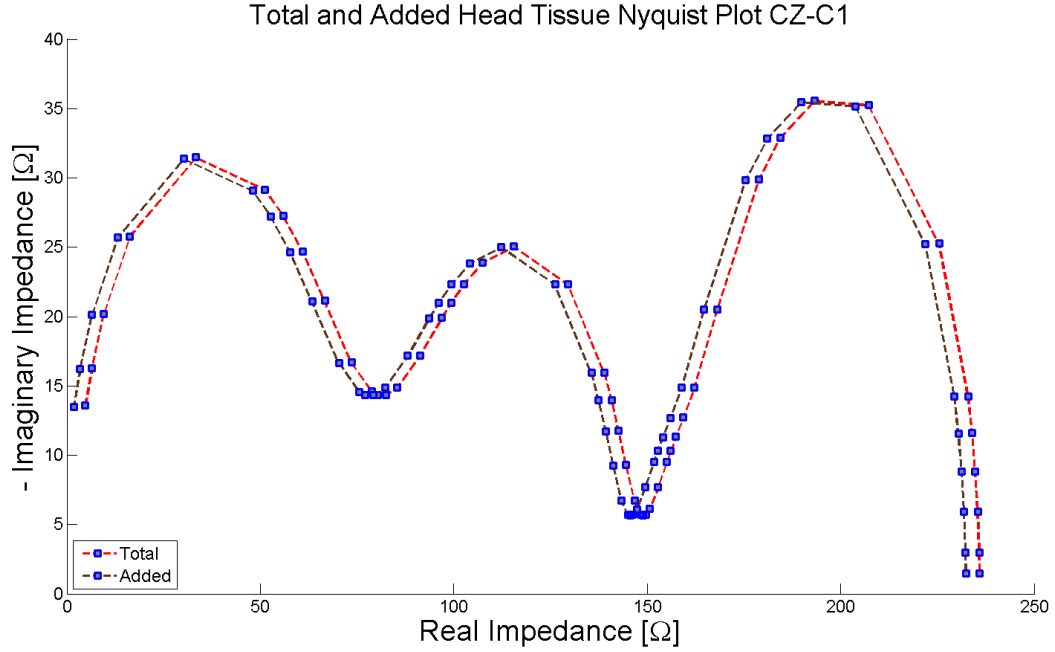


Figure 8.1: Nyquist plot of total and added real and imaginary impedance.

We show in Fig. 8.1 two Nyquist plots of the CZ-C1 montage. The first plot, labeled Total, represents the Cole system of three dispersion (α , β and γ) measured across the electrodes on CZ-C1. We set a boundary condition so that 1 milliamp would be injected between the electrode pair (see section 4.4) and then we calculated the total resulting impedance across the frequency range according to the equation:

$$Z = V/I \quad (8.2)$$

We first removed the impedance contribution of the electrodes. We then extracted the real and imaginary parts of the complex impedance and plotted the results as shown in Fig. 8.1.

The impedance labeled Added was derived by calculating the impedance of each tissue separately using probes (see section 4.6) according to eq. 4.19. We then extracted the real and imaginary components of each tissue and then summed all the real and imaginary components separately before plotting the real vs -imaginary as shown in Fig. 8.1.

We show the two data sets with an offset of 3Ω . In reality the error between the plots $> .1 \Omega$.

We thus show for a bipolar montage that the total Cole system is the sum in series of each tissues' separate Cole system.

We now show the plots of the Cole system across all the electrode montages for the entire head and for each tissue separately. We show mean values of 6 samples, noise bars in the y and x axis show the SEM (see section 4.7).

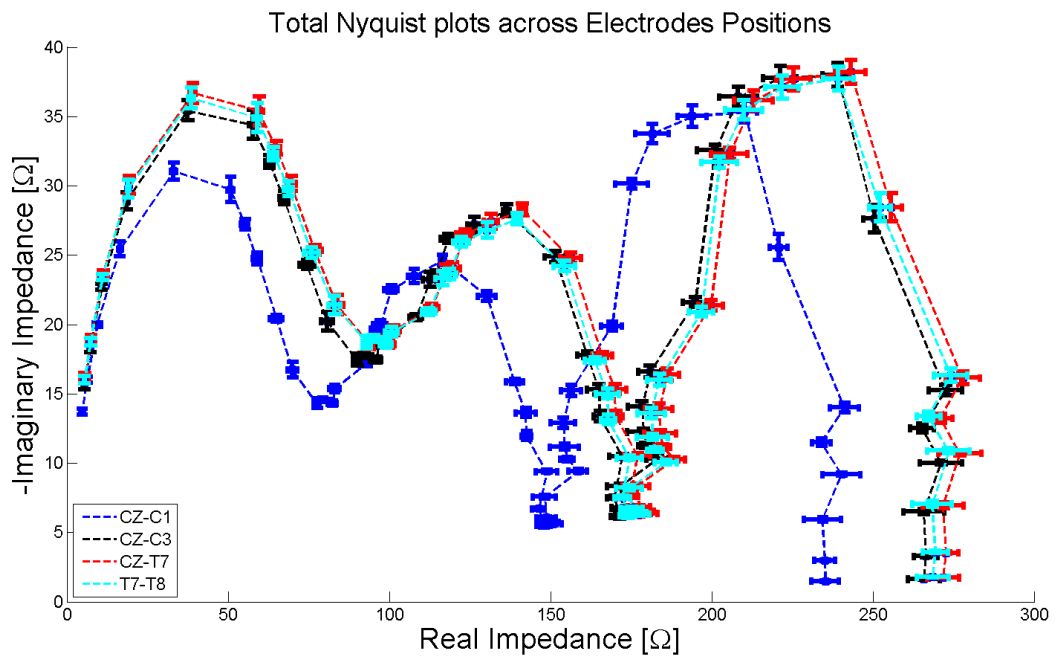


Figure 8.2: Total Nyquist plots for all electrode montages. Mean values with error bars are shown.

Fig. 8.2 shows the Nyquist plots of the entire head of all the bipolar montages. We can see 3 distinct semi-circles representing the α , β and γ dispersions. We also note that the size of the error appears to the greatest for the lowest frequencies, as the frequency is increased we can see a gradual reduction in error.

The Nyquist plots here show a distinct pattern. All the plots have a very similar shape.

The CZ-C1 impedance has a lower magnitude along both the real and imaginary axis. The

other montage plots are tightly grouped together in the following order along the real axis (from least to greatest): CZ-C3, T7-T8 and finally CZ-T7.

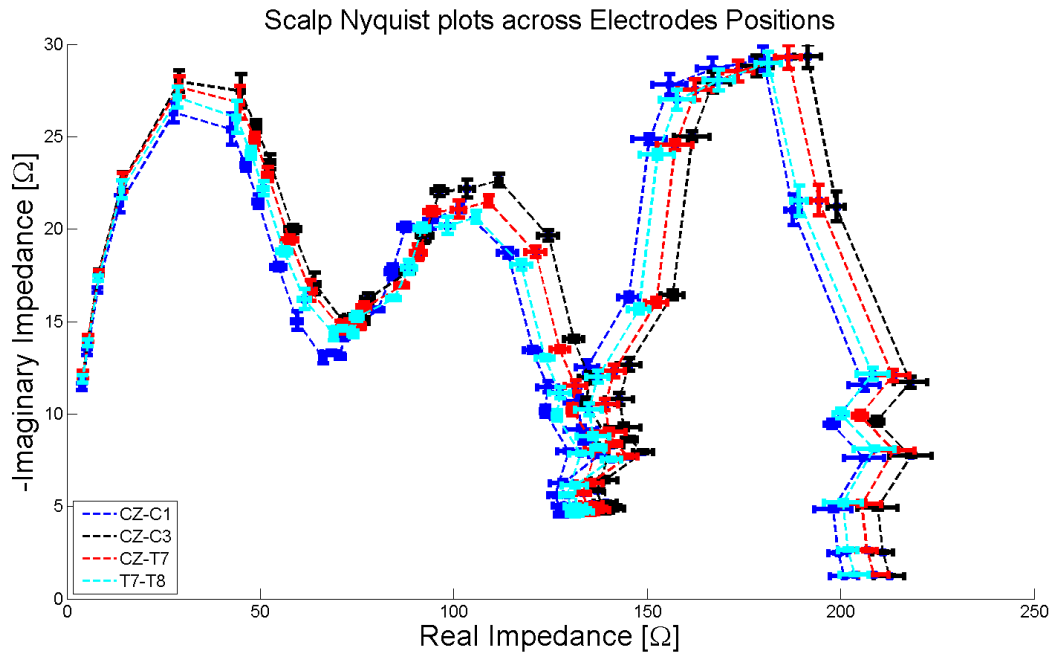


Figure 8.3: Nyquist plot of scalp for all electrode montages. Mean values with error bars are shown.

In Fig. 8.3 we see the scalp Nyquist plots. We can see that that scalp plots are very similar in shape, albeit with a smaller real and imaginary magnitude, than the total Nyquist plots shown in Fig. 8.2. Here we can see that all the graphs are tightly clustered together with a small offset between them. The magnitude order of the plots (from least to greatest) are T7-T8, CZ-T7 and CZ-C3.

Fig. 8.4 shows the Nyquist plots of the skull tissues across all the montages. Here there are significant differences between each spectrum with offsets both along the real and imaginary axis. The CZ-C1 spectrum has the lowest magnitude on the real axis. This is followed (from least to greatest) by T7-T8, CZ-T7 and CZ-C3. We find a different order of magnitude versus the imaginary axis namely (from least to greatest): T7-T8, CZ-C1, CZ-T7 and CZ-C3.

Fig. 8.5 illustrates the spectra of the CSF. Here we see a clear relationship between Cole

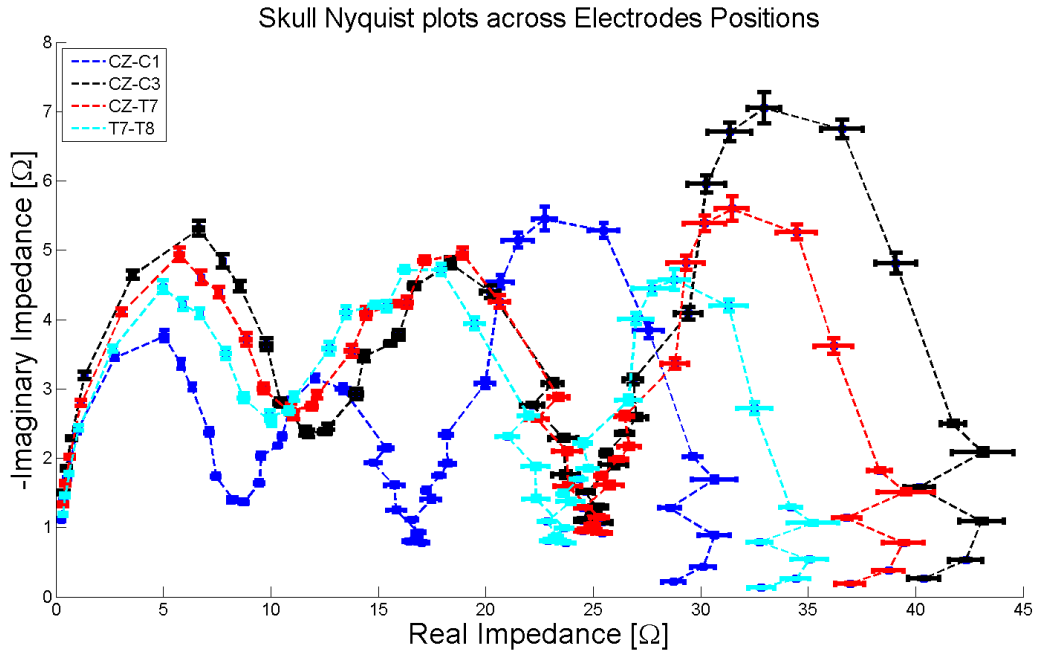


Figure 8.4: Skull Nyquist plots for all electrode montages. Mean values with error bars are shown.

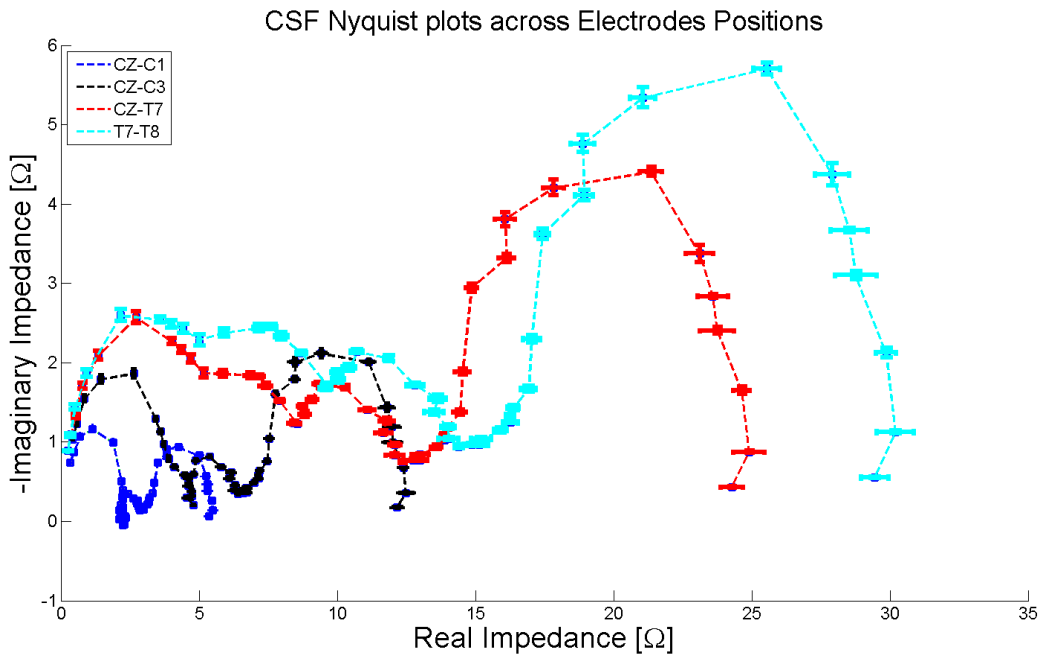


Figure 8.5: CSF Nyquist plots for all electrode montages. Mean values with error bars are shown.

plot magnitude and inter-electrode θ .

The CZ-C1 montage produces an impedance spectrum with a very small magnitude (real and imaginary). In order of magnitude from least to greatest we then have the spectra from the following montages: CZ-C3, CZ-T7 and T7-T8.

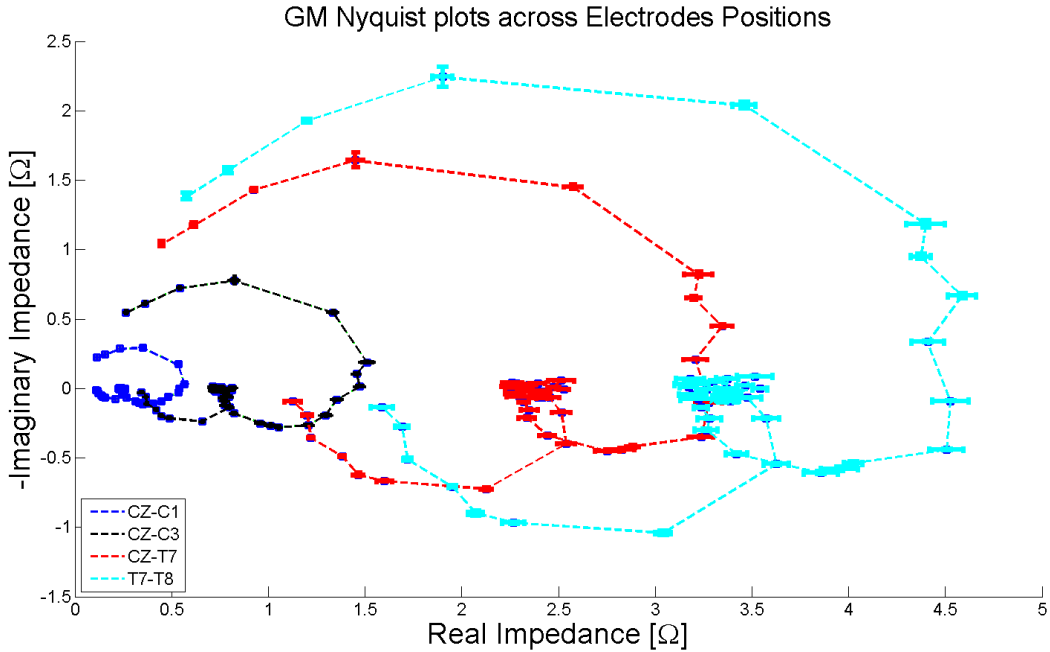


Figure 8.6: GM Nyquist plots for all electrode montages. Mean values with error bars are shown.

We notice an interesting change in the shape of the impedance for tissues deeper than the CSF layer. We note inverted Cole systems for the α and β dispersions followed by a Cole semi-circle for the γ dispersion. There is a clear section of impedance overlap shown between the inverted semi-circles, this can be envisioned as a closed loop. This pattern is clearly seen for the GM tissue as shown in Fig. 8.6. Order of montage generating impedance spectra from least to greatest magnitude is CZ-C1, CZ-C3, CZ-T7 and T7-T8. We can see that the overall impedance range for the GM is quite low (> 5 real Ω and > 2.5 imaginary Ω).

In Fig. 8.7 we see the same pattern for the WM as shown in Fig. 8.6. Here the impedance range is smaller than that of the GM (> 2.5 real Ω and > 1.2 imaginary Ω).

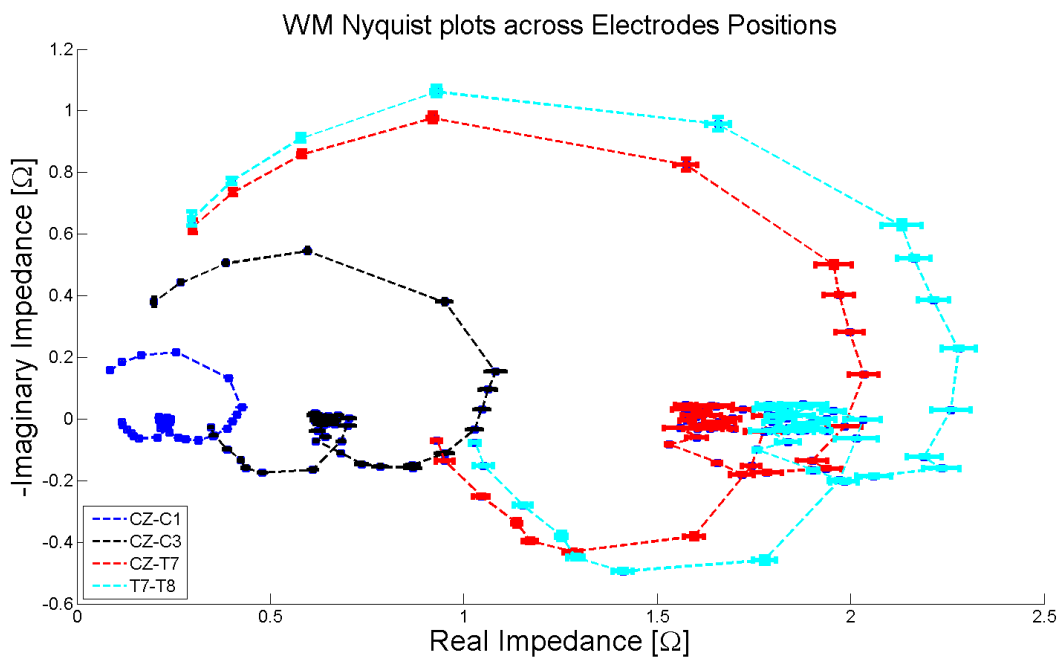


Figure 8.7: WM Nyquist plots for all electrode montages. Mean values with error bars are shown.

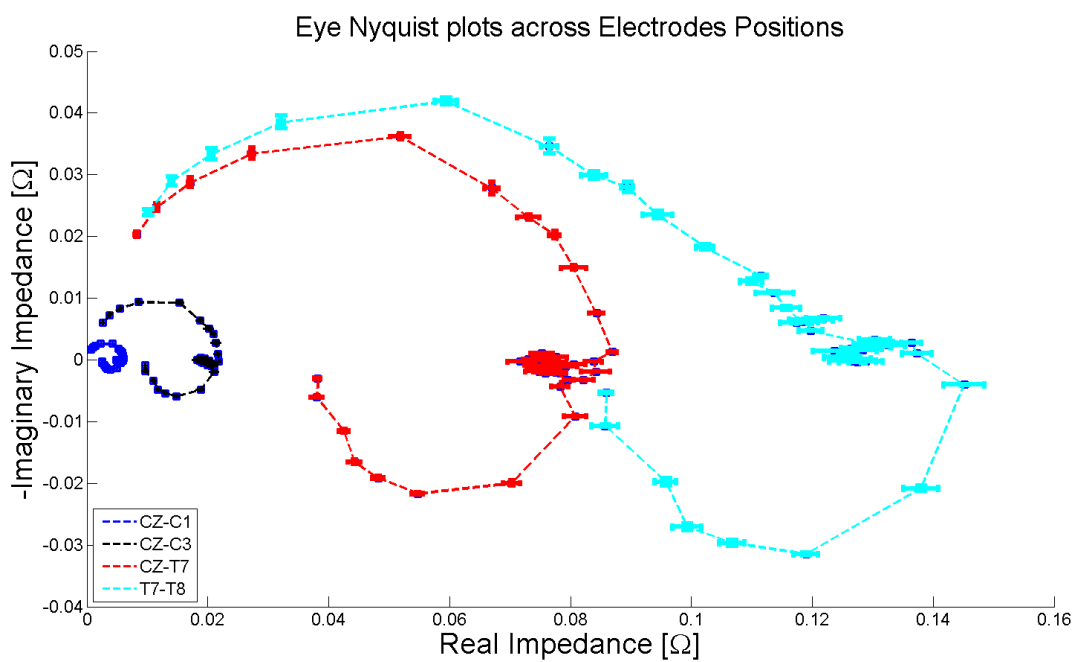


Figure 8.8: Eye tissue Nyquist plots for all electrode montages. Mean values with error bars are shown.

Finally we show in Fig. 8.8 the impedance of the eye tissue. Here the same pattern is repeated except that the β dispersion appears to be contained in the inverted loop between the α and β dispersions. We see that the magnitude of the impedance plots is greatly reduced ($> .16$ real Ω and > 0.05 imaginary Ω).

8.2.2 Cole parameters

8.2.2.1 Cole Parameter fitting and extraction

We now describe our fitting/extraction methodology of Cole parameters.

Our parameter extraction code was written in Matlab 2013a. First we input the frequency points, real and imaginary part of the impedance into a Matlab function called *ColeExtract*. The output of the function is the Cole parameters. In the code this takes the form of $[R_0, R_\infty, f_c, \alpha] = \text{ColeExtract}(f, \text{real}, \text{imaginary})$

The Cole model plots the negative imaginary impedance vs. real impedance along the positive y-axis. Thus the first step is to reverse the sign of the negative imaginary impedance.

We thus assign the following:

$$Z_{IM} = -Z_{IM} \quad (8.3)$$

where IM is imaginary impedance.

The next step is to find the index whereby IM is positive using the command:

$$I = \text{find}(Z_{IM} > 0) \quad (8.4)$$

Using this index we then define a vector v with components v_1, v_2 and v_3 such that

$$v_1 = \text{mean}(\text{real}(I)) \quad (8.5)$$

$$v_2 = \text{mean}(\text{imag}(I)) \quad (8.6)$$

$$v_3 = (\text{max}(\text{real}(I)) - \text{min}(\text{real}(I)))/2 \quad (8.7)$$

whereby v_1 and v_2 are the mean of the real and imaginary impedance respectively and v_3 is half of the Δ of the real impedance. These 3 variables represent the center coordinates and the radius of a Cole semi-circle.

To find the optimal points in our data that satisfies these conditions we use a Matlab program called *fminunc*. This non-linear algorithm finds the minimum of an unconstrained multi-variable function of the form of $\min_x f(x)$ where $f(x)$ is a function that returns a scalar.

We used the default *fminunc* option which is based on a quasi-newton algorithm. This approach, referred to as the BFGS (Broyden, Fletcher, Goldfarb, and Shanno) Quasi-Newton method [221, 222], uses a cubic line search procedure to find the function minima. In general the minimization problem can be stated as

$$\min_x \frac{1}{2} x^T H x + c^T x + b \quad (8.8)$$

where H is the Hessian matrix, c is a constant vector and b is a constant. The optimal solution point x^* can be written as

$$\nabla f(x^*) = H x^* + c = 0 \quad (8.9)$$

or

$$x^* = -H^{-1}c \quad (8.10)$$

The BFGS algorithm updates the Hessian matrix according to

$$H_{k+1} = H_k + \frac{q_k q_k^T}{q_k^T s_k} + \frac{H_k s_k s_k^T H_k^T}{s_k^T H_k s_k} \quad (8.11)$$

where

$$s_k = x_{k+1} - x_k \quad (8.12)$$

and

$$q_k = \nabla f(x_{k+1}) - \nabla f(x_k) \quad (8.13)$$

For each iteration k the search direction is updated according to

$$d = -H_k - 1 \cdot \nabla f(x_k) \quad (8.14)$$

This process is continued until the objective function is minimized below a preset criteria. (for more detail see [223] and [224]).

Maximum iterations was set to 100000. We used a default tolerance of 10^{-6} .

The optimized points are returned as a new vector in the form of

$$[x] = fminunc(fdist, v0) \quad (8.15)$$

and

$$x_1 = x_0 \quad (8.16)$$

$$x_2 = y_0 \quad (8.17)$$

$$x_3 = r_0 \quad (8.18)$$

where x_0 , y_0 , and r_0 are the xy central coordinates and radius respectively of the fitted Cole semi-circle circle.

The characteristic frequency fc is located at the peak of the semi-circle. fc is found through interpolation of the $real(I)$, $f(I)$ and x_0 .

α is found through the relation

$$\alpha = 2 * \arccos(abs(y0)/r0)/pi \quad (8.19)$$

The next step is setting a grid of points for interpolation and plotting of the Cole semi-circle. The interval size of the real impedance and frequency are defined as

$$real_{step} = ((max(real) - min(real))/n); \quad (8.20)$$

and

$$frequency_{step} = ((max(f) - min(f))/n); \quad (8.21)$$

where the magnitude of n is used to determine the size of the step.

A grid along the real impedance is then defined according to

$$Z_{real} = min(Z_{real}) : real_{step} : max(Z_{real}) \quad (8.22)$$

The center-radius form of the circle equation is

$$r^2 = (x - x_0)^2 + (y - y_0)^2 \quad (8.23)$$

where x_0 and y_0 are the circle center coordinates.

Solving for y or the imaginary impedance and inserting Z_{real} for the variable x we can write

$$y = (sqrt(r^2 - (Z_{real} - x_0)^2) + y_0) \quad (8.24)$$

This is the fit to the Cole-semi circle as shown in Fig. 8.9 below.

R_0 and R_∞ are then found as the maximum and minimum intercepts of the fitted Cole-semi circle and the x-axis.

Rearranging eq. 8.23 and substituting 0 for y (x-axis intercept) the 2 solutions are:

$$R_0 = (x_0 + sqrt(r^2 - y_0^2)) \quad (8.25)$$

and

$$R_\infty = (x_0 - \text{sqrt}(r^2 - y_0^2)) \quad (8.26)$$

As described in section 4.7 each simulation generated 6 samples (measurements) of each head tissue. Using the fitting methodology described above we extracted Cole parameters for all samples and then calculated the mean of the extracted values. This was done for each montage over all the dispersion zones over the frequency range of the model.

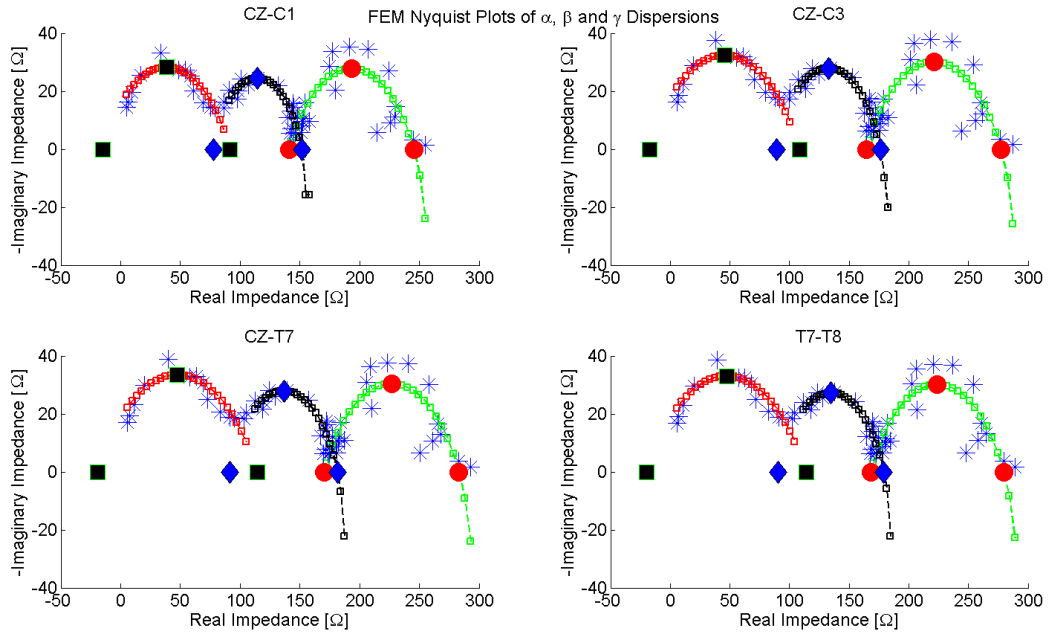


Figure 8.9: Cole plots shown for all bipolar electrode montages. The first, second and third semi circle represent the α , β and γ frequency distributions respectively. Markers show the locations of fitted Cole parameters (R_0 , f_c and R_∞).

Fig. 8.9 shows an example of 3 fitted Cole parameters for the Nyquist plots of all the bipolar montages. Specifically we show the locations of R_0 at the right hand intercept of each semi-circle with the y-axis, f_c at the peak of each semi-circle and R_∞ at the left hand intercept of each semi-circle. The fitted plots here are shown for a single sample.

8.2.2.2 Cole Parameter Comparison

We used a 2 sided paired t-test [225] (for examples of use of the t-test in bioimpedance spectroscopy studies see [226, 227]) to compare results across montages by testing the validity of the null hypothesis (meaning there is no difference between the mean values) ¹. The difference between the mean values is assumed to be normally distributed [225]. Each value represented on the bar chart is the mean of $n = 6$ simulations. The significance level is Bonferroni corrected by dividing α by the number of pairwise comparisons. There are a total of 6 pairwise comparisons for each Cole parameter for the 2 electrode configuration. We calculated the significance or the p-values of the t-tests. In Fig 8.10 comparison between bar graphs is shown by brackets (the end of bracket side rests above the values being compared) and significance level is indicated by the number of stars; i.e. * represents $p \leq 0.05$, ** represents $p \leq .01$ and *** represents $p \leq .001$. Results are assumed to be significant at $p \leq 0.05$.

Fig. 8.10 shows the results of comparing mean Cole parameters across the bipolar montages for the α dispersion. Mean Cole parameters are indicated by the level of the bar charts, error bars are also shown.

Table 8.1 shows the p-values for each pairwise comparison of Cole parameters in the α dispersion. NS stands for not significant.

P-values of Cole parameter comparisons in the β range are shown in table 8.2.

P-values of Cole parameter comparisons in the γ range are shown in table 8.3.

8.2.3 Principal component analysis

In the previous section we discussed the parametrization of the simulated impedance using the parameters of Cole model. Now we wish to analyze the impedance using a multivariate

¹We limited our analysis to Bonferroni corrected t-tests to check for significance between pairwise comparisons of Cole parameters. A more systematic approach would have been to first check for significance using one-way ANOVA testing see for instance [228].

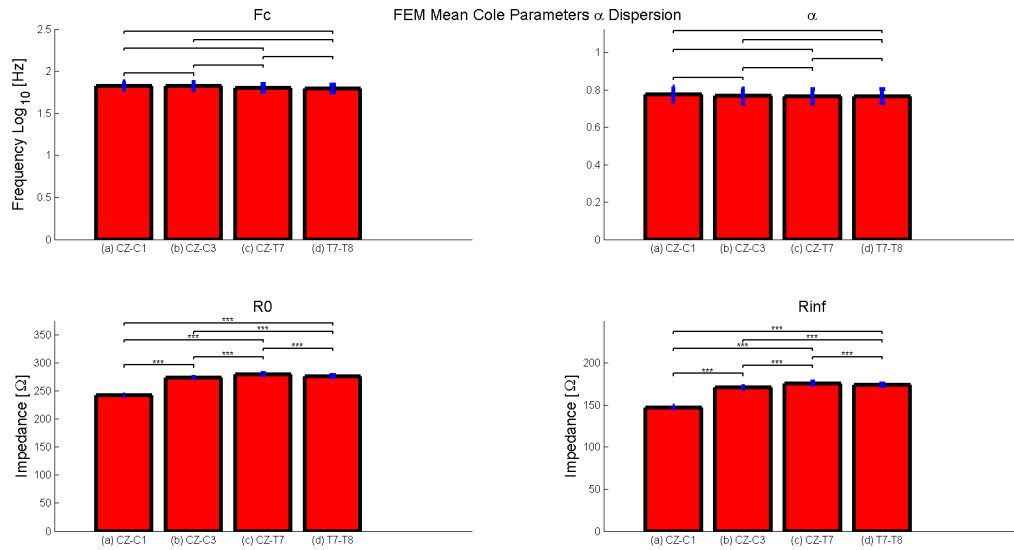


Figure 8.10: Bar graphs showing mean Cole parameters of 2 electrode configurations for the α dispersion. Comparisons between mean values is made with a paired t test. Significance level is shown by number of stars.

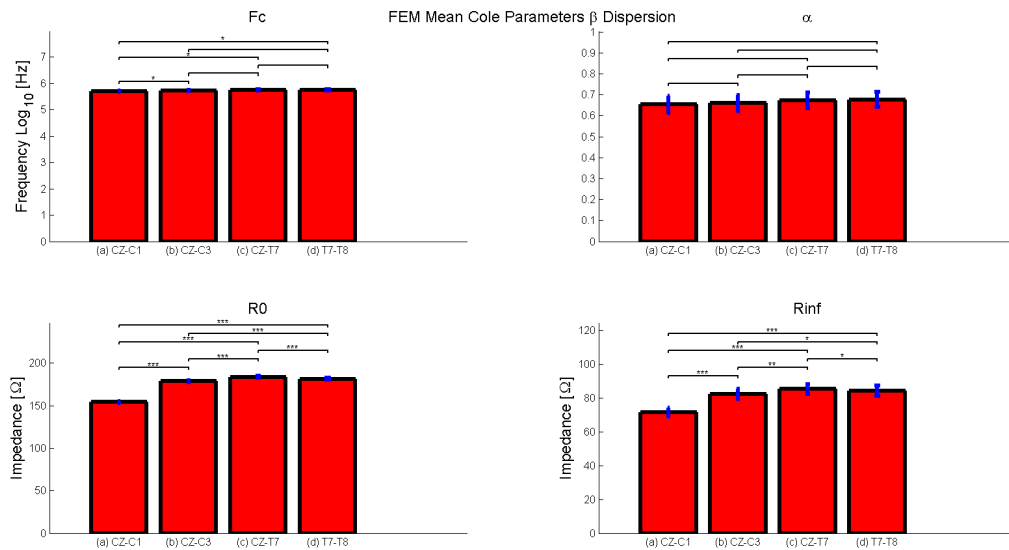


Figure 8.11: Bar graphs showing mean Cole parameters of 2 electrode configurations for the β dispersion. Comparisons between mean values is made with a paired t test. Significance level is shown by number of stars.

α dispersion				
P value for f_c comparisons \leq				
	CZ-C1	CZ-C3	CZ-T7	T7-T8
CZ-C1		NS	NS	NS
CZ-C3			NS	NS
CZ-T7				NS
T7-T8				
P value for α comparisons \leq				
	CZ-C1	CZ-C3	CZ-T7	T7-T8
CZ-C1		NS	NS	NS
CZ-C3			NS	NS
CZ-T7				NS
T7-T8				
P value for R_0 comparisons \leq				
	CZ-C1	CZ-C3	CZ-T7	T7-T8
CZ-C1		.001/6	.001/6	.001/6
CZ-C3			.001/6	.001/6
CZ-T7				.001/6
T7-T8				
P value for R_∞ comparisons \leq				
	CZ-C1	CZ-C3	CZ-T7	T7-T8
CZ-C1		.001/6	.001/6	.001/6
CZ-C3			.001/6	.001/6
CZ-T7				.001/6
T7-T8				

Table 8.1: P-values showing statistical significance for differences between α Cole parameters. α significance level is Bonferroni corrected for $n = 6$ pairwise comparisons.

β dispersion				
P value for f_c comparisons \leq				
	CZ-C1	CZ-C3	CZ-T7	T7-T8
CZ-C1		0.01/6	0.01/6	0.01/6
CZ-C3			NS	NS
CZ-T7				NS
T7-T8				
P value for α comparisons \leq				
	CZ-C1	CZ-C3	CZ-T7	T7-T8
CZ-C1		NS	NS	NS
CZ-C3			NS	NS
CZ-T7				NS
T7-T8				
P value for R_0 comparisons \leq				
	CZ-C1	CZ-C3	CZ-T7	T7-T8
CZ-C1		.001/6	.001/6	.001/6
CZ-C3			.001/6	.001/6
CZ-T7				.001/6
T7-T8				
P value for R_∞ comparisons \leq				
	CZ-C1	CZ-C3	CZ-T7	T7-T8
CZ-C1		.001/6	.001/6	.001/6
CZ-C3			.01/6	.05/6
CZ-T7				.05/6
T7-T8				

Table 8.2: P-values showing statistical significance for differences between β Cole parameters. α significance level is Bonferroni corrected for $n = 6$ pairwise comparisons.

γ dispersion				
P value for f_c comparisons \leq				
	CZ-C1	CZ-C3	CZ-T7	T7-T8
CZ-C1		NS	NS	NS
CZ-C3			.01/6	.01/6
CZ-T7				.05/6
T7-T8				
P value for α comparisons \leq				
	CZ-C1	CZ-C3	CZ-T7	T7-T8
CZ-C1		.01/6	.01/6	.001/6
CZ-C3			.01/6	.01/6
CZ-T7				.01/6
T7-T8				
P value for R_0 comparisons \leq				
	CZ-C1	CZ-C3	CZ-T7	T7-T8
CZ-C1		.001/6	.001/6	.001/6
CZ-C3			.001/6	.001/6
CZ-T7				.001/6
T7-T8				
P value for R_∞ comparisons \leq				
	CZ-C1	CZ-C3	CZ-T7	T7-T8
CZ-C1		.001/6	.001/6	.001/6
CZ-C3			.001/6	.001/6
CZ-T7				.01/6
T7-T8				

Table 8.3: P-values showing statistical significance for differences between γ Cole parameters. α significance level is Bonferroni corrected for $n = 6$ pairwise comparisons.

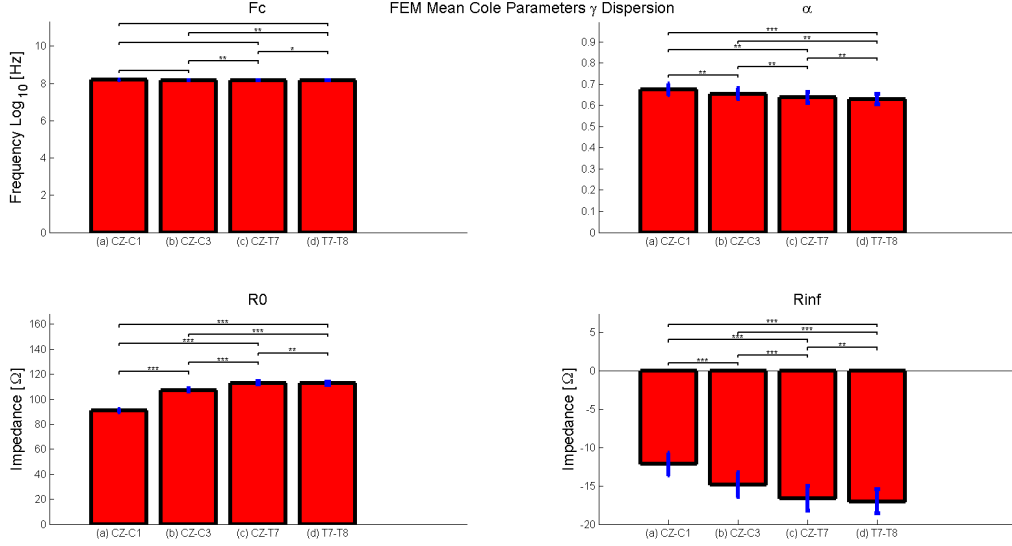


Figure 8.12: Bar graphs showing mean Cole parameters of 2 electrode configurations for the γ dispersion. Comparisons between mean values is made with a paired t test. Significance level is shown by number of stars.

method called Principal Component Analysis or PCA.

Bioimpedance spectroscopy measurement may result in a large series of highly correlated and redundant data [228]. We therefore use PCA, [158, 220, 228–233] as a concise method for dimensionality reduction or reducing the number of variables for analysis [229].

Principal Component Analysis (PCA) is a non-parametric *descriptive* method of modelling and analyzing data where no assumptions are made concerning the physiology or physics of the measured phenomenon. PCA is used to reveal internal structure of the data in a way that best explains the variance in the data [220], [158].

In the context of BIS measurements a data matrix X , can be generated composed of $M \times N$ rows and columns where M is the number of *observations* or measurements and N is the number of frequencies at which the measurements are taken. The data is then mean centered $X - \bar{X}$. The covariance of the mean adjusted data is calculated as

$$C_x = [c_{ij}] = \frac{1}{M-1} X^T X, \quad (8.27)$$

where x_{ij} is the element corresponding to the i^{th} impedance measurement at the j^{th} frequency. C_x can then be expanded according to

$$C_x = \frac{1}{M-1} V \Sigma^2 V^T \quad (8.28)$$

where Σ is $N \times N$ diagonal matrix with $\sigma_1 \geq \sigma_2 \geq \dots \geq \sigma_N \geq 0$ singular values and V is $N \times N$ matrix of eigenvectors of C_x . The expansion of the covariance matrix provides a linear orthogonal basis that represents the directions of variance in the data.

In PCA, principal components indicate the direction and magnitude of data variability; axis orientation is provided by the covariance eigenvectors and magnitude by eigenvalues. Principal components are ranked in order with the largest principal component corresponding with the axis oriented along the largest direction of data variability. Usually most of data variance and meaningful information is contained within the first few principal components, thus PCA provides a useful method of reducing dimensionality of multivariate data, like BIS measurements, without loss of essential information [220], [158]. Feature extraction is generally comprised of PCA scores which are obtained by mapping (by the dot product operation) impedance spectra on the new set of uncorrelated orthogonal vectors V_i . The scores, essentially projections of impedance measurements on the new orthogonal basis, are considered as features of the spectrum and can be fed to a classifier for further analysis [158].

We showed earlier in this chapter that the total Cole system of the head is composed of the sum of the Cole systems of each tissue. The sensitivity can be thought of as weight multiplied to impedance of each tissue. For each montage, the sensitivity and thus the relative weights of each tissue change.

We wish to investigate through PCA the nature of this change of impedance spectra by analyzing the number of significant uncorrelated sources of variability. This is shown by the number of principal components and magnitude of the scores. Analysis of the nature of

variation between the spectra may provide insight into dose-related changes.

8.2.3.1 PCA parameters

First a covariance matrix is generated by

$$V = Z1 * Z2' \tag{8.29}$$

where Z1 is a vector comprised of an impedance spectrum and Z2 is a different impedance spectrum of the same length. The symbol Z2' shows that Z1 is multiplied by the transverse of Z2 (rows are switched with columns).

We then use the matlab function of [COEFF,latent,explained] = pcacov(V) where V is the covariance matrix, COEFF is the principal component coefficients or loading, Latent returns a vector with the principal component variances i.e. the eigenvalues of V. Finally explained outputs a vector which is comprised of the percentage of the total variance of each principal component.

In this section we show the results of PCA on pairs of impedance spectra generated by different bipolar montages. We consider the spectrum generated by CZ-C1 as as reference.

Thus we implement PCA on the following pairs:

- CZ-C1 and CZ-C3
- CZ-C1 and CZ-T7
- CZ-C1 and T7-T8

For each pair, PCA parameters are extracted separately for the real and imaginary part of impedance.

We use the Matlab biplot function in order to visualize the results.The biplot function shows the principal component coefficients. The plot is 2-D if there 2 columns or 3-D if

they are 3 columns. The axes in the plot represent the principal components. The biplot shows the magnitude and sign of each variable's contribution to the first two components. This plot imposes a sign convention, forcing the element with largest magnitude in each column of coefficients to be positive. This has the effect of flipping some of the vectors in the opposing direction (see for example the left side of Fig. 8.13), this does not however change interpretation of the graph.

The PCA scores are scaled by dividing each score by the maximum absolute value of all scores and then by multiplying by the maximum coefficient length of the loadings.

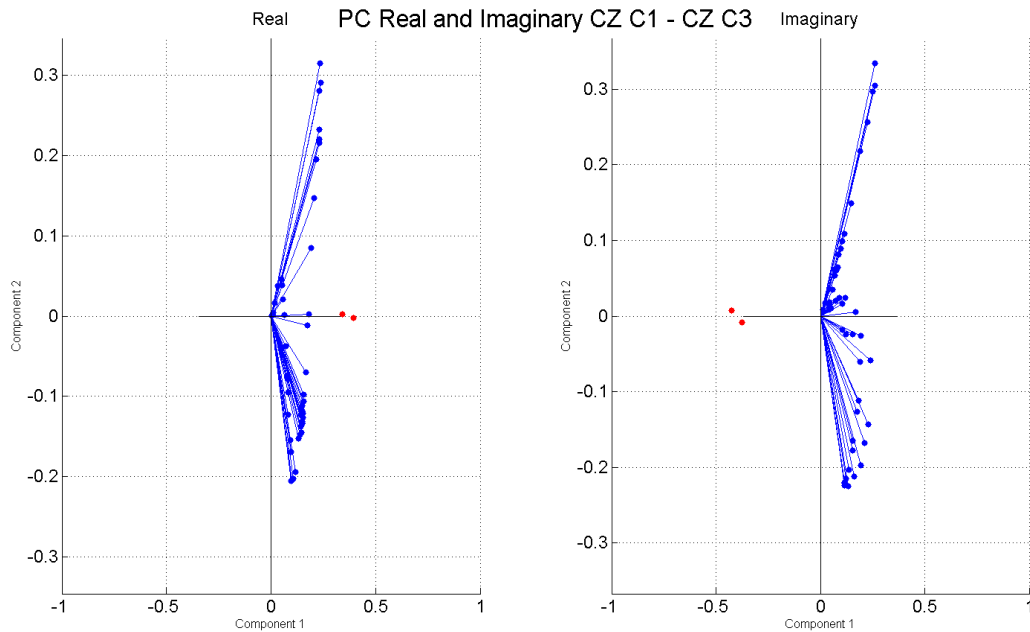


Figure 8.13: Principal components, scores and coefficients shown of real and imaginary components of electrode montages CZ-C1 and CZ-C3.

In Fig. 8.13 we show the biplots for PCA on the real (left plot) and imaginary (right plot) covariance matrices of CZ-C1 and CZ-C3.

We see here the scores represented as two red dots above and slightly below the axis representing the first principal component. The scores of the imaginary component follow the same pattern but are reversed along the negative part of the the first principal component axis. The loadings (coefficients rows) are represented here as blue vectors

(vectors on imaginary components are flipped due to sign convention see above). The loadings shown here correspond to the two scores. It is important to note that the variance of the spectra is represented by the scores along the principal components and not the loadings. Thus the position of the 2 scores indicate a very large variance along the first principal component and a much smaller variance along the second principal component. The percentage of variance described by each principal component is shown in the tables below.

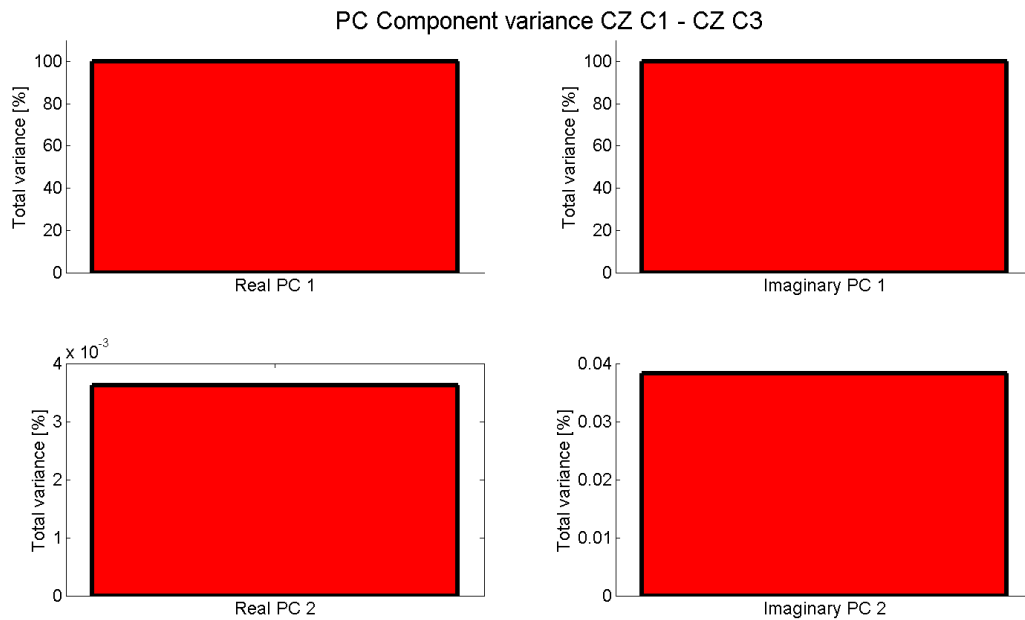


Figure 8.14: Percent of total variance of first and second principal components of real and imaginary components, shown for electrode montages CZ-C1 and CZ-C3.

Fig. 8.14 shows the percentage of the variance between the impedance spectra which is accounted for by each principal component. The left side of the graph shows the percentage of variance for the first and second principal components of the real part of the impedance. The right part of the graph shows the same information for the imaginary component of impedance. We see that almost 100% of the variance is explained by the first principal component with a much smaller percentage of the variance along the second component (real PC2 \approx .0035%, imaginary PC2 \approx .04%)

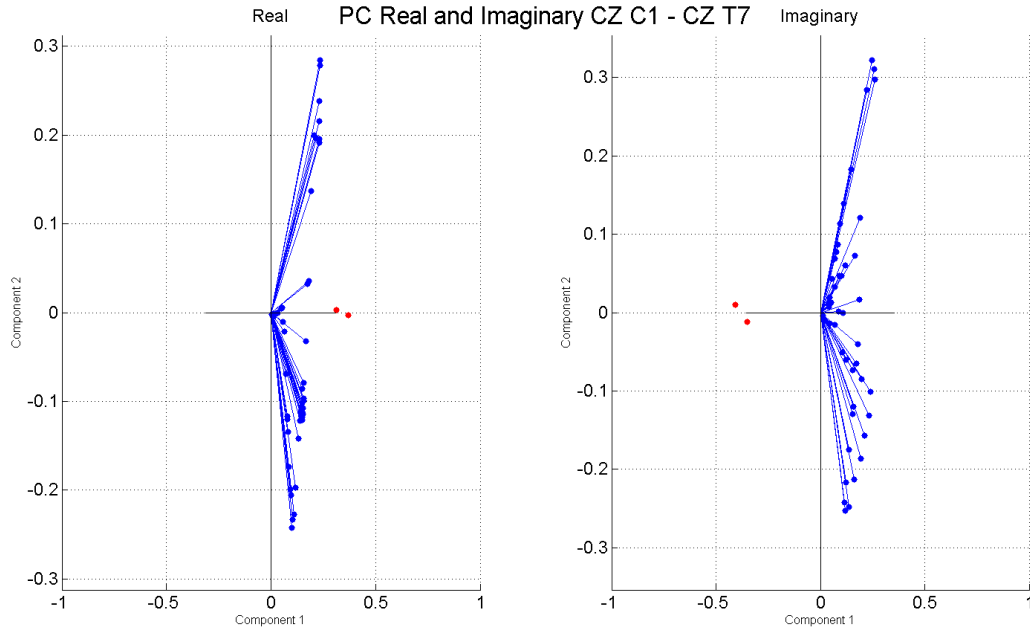


Figure 8.15: Principal components, scores and coefficients shown of real and imaginary components of electrode montages CZ-C1 and CZ-T7.

In Fig. 8.15 biplots are shown for the real and imaginary part of the CZ-C1 and CZ-T7 pair. Again we can see the loading coefficients as well as the first two principal component scores on and near the first principal component axis. The scores position relative to the principal component axis are similar to that shown in 8.15.

Fig 8.16 shows the percentage of variance accounted for by the first 2 principal components. We note that close to 100% of variance can be expressed along the first principal component. The percentage of variance described by the second principal component has approximately doubled (real PC2 \approx .008%, imaginary PC2 \approx .08%).

In Fig. 8.17 we show a biplot of the for the real and imaginary part of the final impedance spectra pair from CZ-C1 and T7-T8 pair. Here again we see a plot of coefficient factors, scores are shown on and slightly below the first principal component axis (negative side for the imaginary scores).

Fig. 8.18 shows the percentage of variance described by the first and second principal

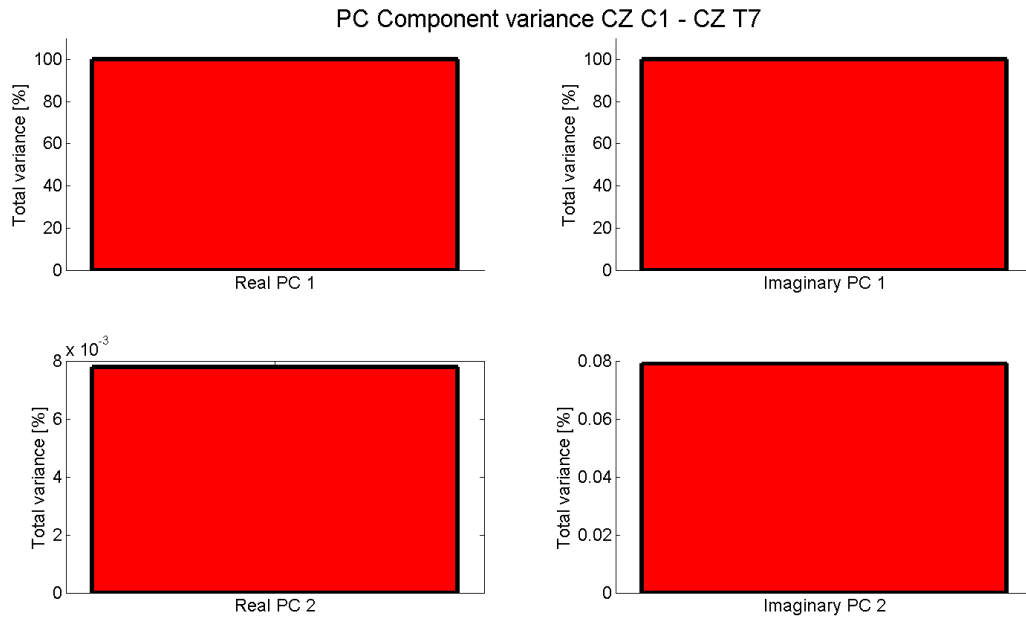


Figure 8.16: Percent of total variance of first and second principal components of real and imaginary components. Shown for electrode montages CZ-C1 and CZ-T7

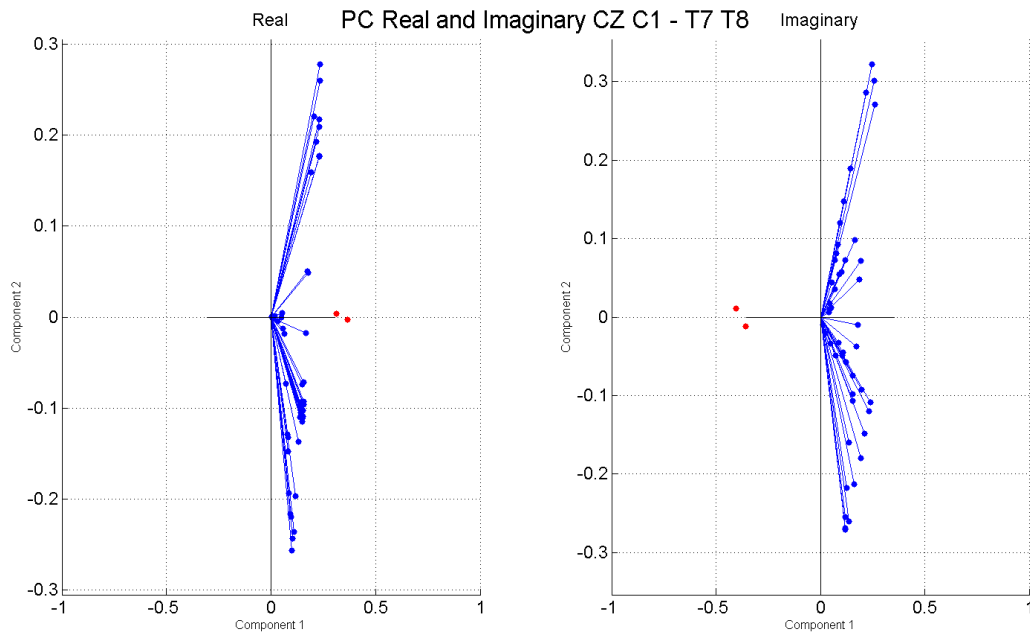


Figure 8.17: Principal components, scores and coefficients shown of real and imaginary components of electrode montages CZ-C1 and T7-T8.

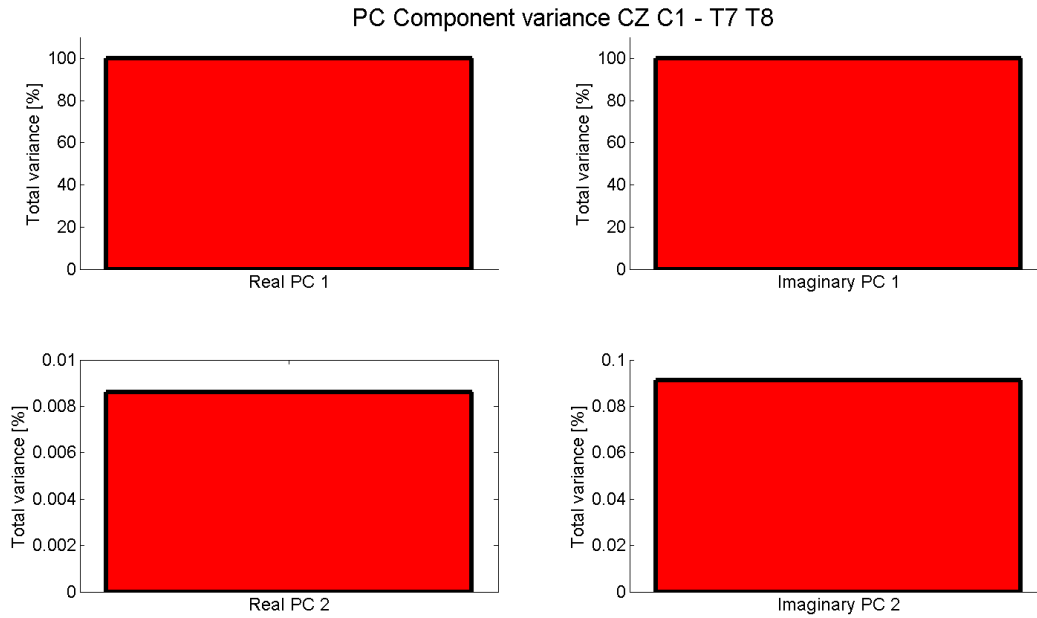


Figure 8.18: Percent of total variance of first and second principal components of real and imaginary components, shown for electrode montages CZ-C1 and T7-T8.

components. Like earlier results most of the variance can be expressed by a single principal component. We see here a further slight increase in the proportion of variance described by the second principal component (real PC2 \approx .009%, imaginary PC2 \approx .09%)

8.2.4 Discussion

The frequency response of the head is a complex non-linear function of the electrical properties of each tissue as well as of boundary conditions and input current type (magnitude and frequency).

Due to the great number of outputs of a bioimpedance spectroscopy sweep (complex impedance for each frequency point) we use both explanatory models to parametrize the data as well as non-parametric descriptive to reduce data dimensionality by removing non-essential or redundant data [49].

The most commonly used explanatory model is based on the Cole equation; fitting impedance to the Cole equation results in a reduction of the data to four Cole

parameters [49]. PCA is a descriptive model which analyzes the data structure without making any assumptions of phenomenological causes [49].

In the first part of this chapter we analyzed impedance spectra generated by a set of bipolar montages using both modelling methods.

Our goal was to investigate if the principle of linear superposition (shown to be valid for combination of electric field from multiple electrodes for a single frequency stimulation [59,234]) could be extended towards analysis of bioimpedance spectra.

Although the frequency response of tissue as modeled by a Cole circuit is highly-non linear, we posited that the frequency response of all the head tissues (the total Cole system) is a simple linear combination (addition in series) of the frequency response or Cole system of each tissue individual. This is hypothesized to be true for the entire range of simulated frequencies (covering the α , β and γ range). We also hypothesized that the principal contributors to the total Cole system would consist of only several head tissues while some tissues contribution could be considered negligible.

If we can apply the linear supposition principle to bioimpedance spectroscopy measurements, then that would simplify our attempts to relate characteristics of impedance spectra to sensitivity and dose distribution in neural regions of interest as well as to relate experimental and finite element bioimpedance measurements.

Results shown in Fig. 8.1 show indeed that the total or global Cole system is a linear combination of the sum of each individual Cole system. We then showed in detail the impedance spectra of each individual head tissue, represented as a separate Cole system.

We then shown that the principal contributors to the total impedance and Cole system are the scalp, skull and CSF (see Figs. 8.3, 8.4 and 8.5). Scalp is shown to be by far the largest contributor to the total Cole system and the shape of the total impedance spectrum most closely resembles the scalp (see 8.5).

It is interesting that tissues below or deeper than the CSF showed a positive phase change

as a function of increasing frequency for some of the dispersions. This mimics the behaviour of a flipped or inverted Cole element. This perhaps can be explained according to the findings of Grimnes and Martinsen [195] who showed that when current has multiple current paths through tissue it is possible to measure positive phase, which indicates voltage leading current, without any actual induction occurring in the tissue. Although they described this phenomenon in the context of tetrapolar electrodes, we posit that a similar effect may occur, even for a bipolar montage, deeper than the CSF-GM interface. This perhaps may be attributed to structure and electrical properties of the CSF which can act as a highly conductive pathway [235] parallel to the brain.

Our findings outline some of the challenges facing attempts to measure global or regional properties of the brain with bioimpedance spectroscopy (see for example [132, 236]). We see the signal may be considered highly contaminated with the impedance of the scalp and other superficial head tissues.

The linearity properties of the head impedance spectrum however suggests that a simple linear operation could be used to decrease the scalp impedance. For instance we see that the CZ-C1 has the greatest proportion of scalp impedance relative to the other head tissues. Subtraction of the impedance spectra generated from this montage from another montage with a greater inter-electrode gap could remove much of the impedance of the superficial layers. Small electrode arrays that are primarily sensitive to the scalp (for example see p.289 in [135]) could be used to measure and then separate the impedance of this tissue layer. Careful calibration of the CZ-C1 may be required before subtraction operations are performed, to account for a greater spread of current in the scalp caused by montages with an increased inter-electrode gap.

Another approach that we consider is to relate characteristics and changes in the bioimpedance spectra to changes in dose (electric field and current) in the brain. As the montage is changed, the sensitivity distribution in the tissues is altered resulting in changes to impedance. Thus we consider changes in the scalp, skull and CSF tissue sensitivity as a

proxy for changes in sensitivity and dose in neural areas of interest. We also considered the effect of error by adding random Gaussian noise to the simulation (see section 4.7.)

It is interesting to note that most of our pairwise comparisons (between Cole parameters extracted from impedance spectra of different montages) showed significant differences. Some exceptions to this included the α and f_c parameter (in the α and β dispersion) which no significant differences for many pairwise comparisons. In general the level of significant difference increased and p-values decreased for higher frequency dispersions. This suggests that increasing frequency may be considered as a method of increasing measurement accuracy. We also saw that the greatest significant differences were found for the R_0 and R_∞ parameters. This is in accord with findings that showed that the ratio of R_0 and R_∞ was successfully used with a classifier sequence to predict arm posture of a selected group of volunteers [237].

Across the 3 dispersion zones analyzed we can make following general observations as the inter-electrode angle θ is increased:

- we see the value of f_c descends slightly
- R_0 and R_∞ increases (a small decrease is shown for the T7-T8 montage)
- A strong decrease in the α angle is shown in the γ dispersion

We see that that in the γ dispersion the negative value of R_∞ increases, this is an artifact of the fitting method and does not represent an actual physical phenomenon. We can still use this parameter as instructive of the general shape of the impedance spectrum.

We have however shown that the Cole parameters can be used to distinguish between electrode montages. This information can be linked to the weights of the separate Cole system of each tissue and ultimately to the dose distribution in the neural tissues. For instance the increase in R_0 can be linked to the increase in the impedance of the scalp,

skull and CSF (see Figs. 8.3-8.4). The change in impedance contribution of these tissues may also be linked to the change in sensitivity (correlated to dose) in neural tissues such as GM and WM (see Figs. 6.8 - 6.10) as well to changes in the focality of these tissues (see Figs. 6.19 - 6.20).

Results of the PCA analysis also support our hypothesis of the application of the principle of linear superposition to the impedance spectra of the head tissues. We showed that almost 100% of the variance between two impedance spectrum (generated by different bipolar montages) can be described by a single principal component. Thus we can think of the translation between 2 impedance spectrum as being approximately linear such as by multiplication by a constant.

Although PCA results are generally difficult to link with physical phenomena (see for example [220,228], here we suggest an interpretation of our findings (in line with other papers that relate physical phenomena to PCA characteristics [230,238] . First, as we showed earlier, the head impedance is dominated by the impedance contribution of only several of the tissues. We can view the impedance spectrum as being approximately the result of a weighted sum of these tissues. Changing the electrode montage has the result of changing the weights or the sensitivities of these tissues. The PCA results suggest that the variance in sensitivity is approximately linear can be described along a single principal component.

We do however see that a small second component does exist (see Figs. 8.14 - 8.18) whereby the variance described by the imaginary component is approximately larger by a factor of 10 than the real component. That shows that the real part of impedance spectra from 2 bipolar montages are more highly correlated than the imaginary part.

We also posit that the proportion of variance explained by the two principal components (as shown by the location of the scores) are a useful measure of describing changes to sensitivity and dose. Thus by example the proportion of variance explained by the second

principal component approximately doubles from the montage pair CZ-C1 - CZ-C3 to CZ-C1 - CZ-T7. The variance proportion then increases much more slowly when comparing CZ-C1 - CZ-T7 to CZ-C1 - T7-T8. This suggests that change in the weights or sensitivity between the first and second montage pairs is much greater than the change in sensitivity weights between the the second and third montage pair.

We can see indeed that increase between the sensitivity of the GM and the WM (see Figs. 6.8-6.10) resulting from changing the montage from CZ-C1 to CZ-C3 is roughly the same as the increase in sensitivity from CZ-C3 to CZ-T7. In other words, the increase in sensitivity resulting from changing the montage from CZ-C1 to CZ-T7 is approximately twice as much as the increase in sensitivity from from CZ-C1 to CZ-C3. This is not the case however for the change in sensitivity from CZ-T7 to T7-T8 which is smaller than the previous sensitivity increases.

Thus we show that PCA analysis is useful as method of showing the high degree of linearity and correlation between two impedance spectra. The small changes in the overall variance between different impedance spectra potentially be used to demonstrate the non-linearity of subtle changes to sensitivity and to dose.

8.3 Four electrode configuration

In this section we repeat the Cole analysis for 3 tetrapolar montages (see section 4.2).

8.3.1 Nyquist Plots

In Fig. 8.19 we show in a Nyquist plot the total and added Cole system for the C3-C1-CZ-C2 montage (see beginning of section 8.2.1).

The total Cole system was derived by calculation of the impedance of the entire head simultaneously. Boundary conditions were set so 1 mA of current was injected between the outer electrode pair C3-C2. Voltage was then calculated across the surface of the inner

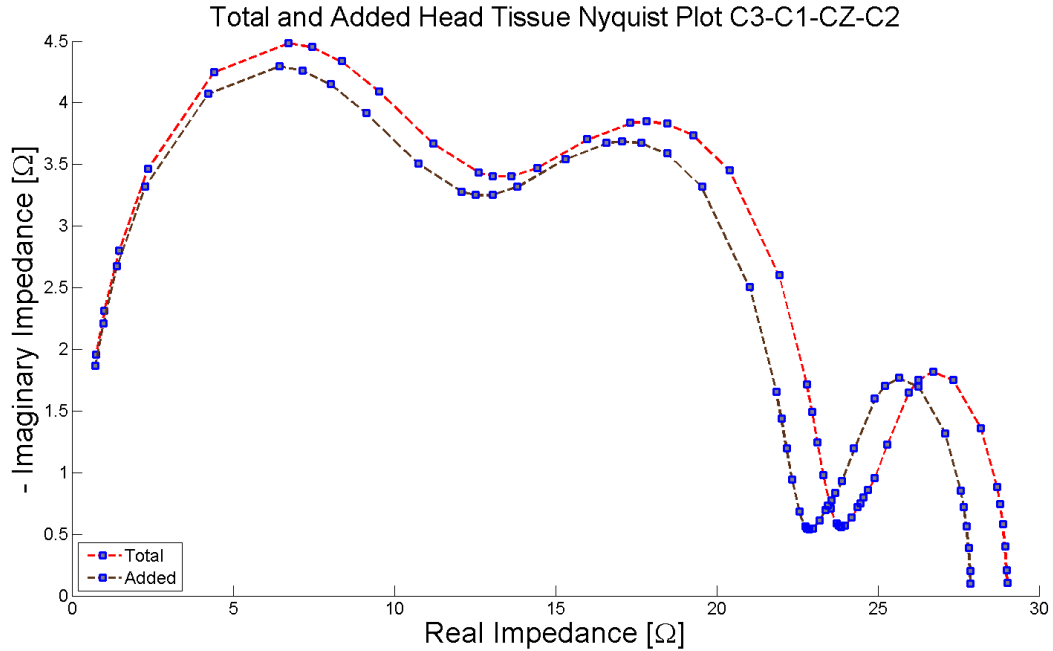


Figure 8.19: Nyquist plot of Total and Added real and imaginary impedance.

electrode pair C1-CZ over the frequency range. Impedance was then calculated according to $Z=V/I$ and then separated into real and imaginary components. The real component was then plotted vs the negative imaginary component as the Total data series.

We also calculated the impedance of each tissue separately by using virtual probes to integrate eq. 4.19 over each domain. The real component of each tissue impedance was then added together, the same operation was then repeated for the imaginary impedance components. The Added data series shows a plot of the real impedance vs negative imaginary.

The offset between the 2 plots in Fig. 8.19 is caused by the additional impedance of the electrodes in the Total data-series. After the electrode impedance is removed the error between the 2 plots is $\approx 1 \Omega$.

We now show Nyquist plots of Cole systems for the total head and for each tissue individually. Impedance values are the mean of the results of 6 separate probes with Gaussian noise added (see section 4.7. Error bars are shown along the x and y-axis (real

and imaginary impedance).

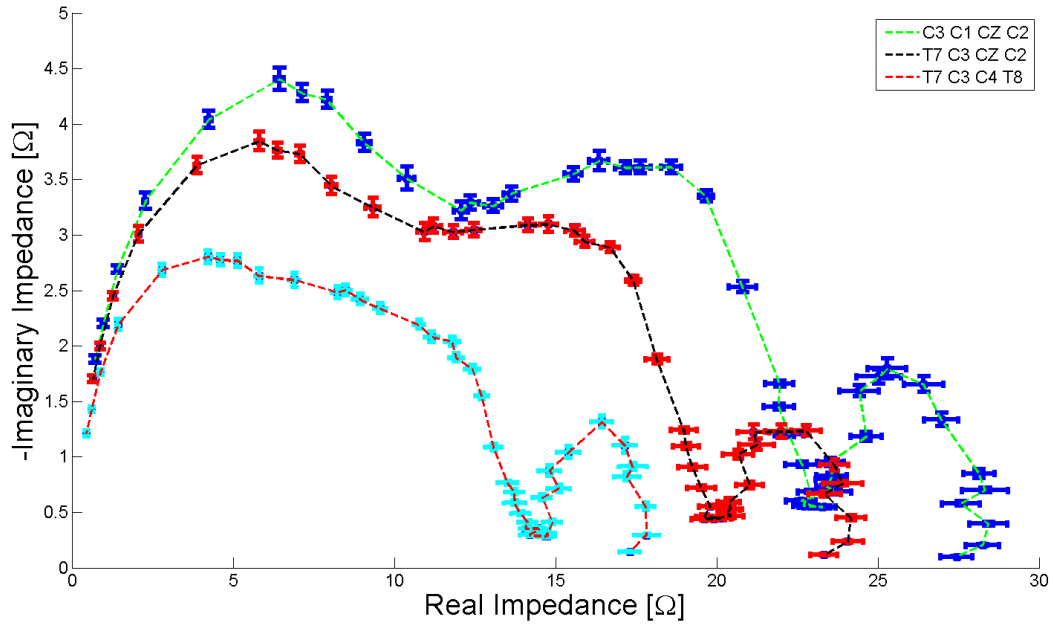


Figure 8.20: Total Nyquist plots for all electrode montages. Mean values with error bars are shown.

Fig. 8.20 shows the Nyquist plots for the total head tissues. We can see a distinct difference in magnitude of the plots both along the x and y axis. C3-C1-CZ-C2 has the greatest impedance, this is followed by a reduction of impedance magnitude for the montage T7-C3-CZ-C2. Finally the lowest impedance magnitude is generated by T7-C3-C4-T8.

We also see for each montage the shape of 3 semi-circles representing the 3 (α , β and γ) frequency dispersions. The α dispersions semi-circles of the 3 montages have a relatively large separation along the x-axis (with some overlap). In the β dispersion in addition to offset along the real x-axis we note a difference in semi-circle shape. C3-C1-CZ-C2 has the semi-circle with the greatest degree of concavity, this is followed by a flatter shape for T7-C3-CZ-C2 and finally the semi-circle shape for T7-C3-C4-T8 is barely discernible. The γ dispersion again shows an offset of the semi-circles along the x-axis.

Fig. 8.21 shows Nyquist plots of the scalp impedance. We see here that all the montages generate reversed semi-circles or Cole systems. We can see 2 reversed Cole systems for the

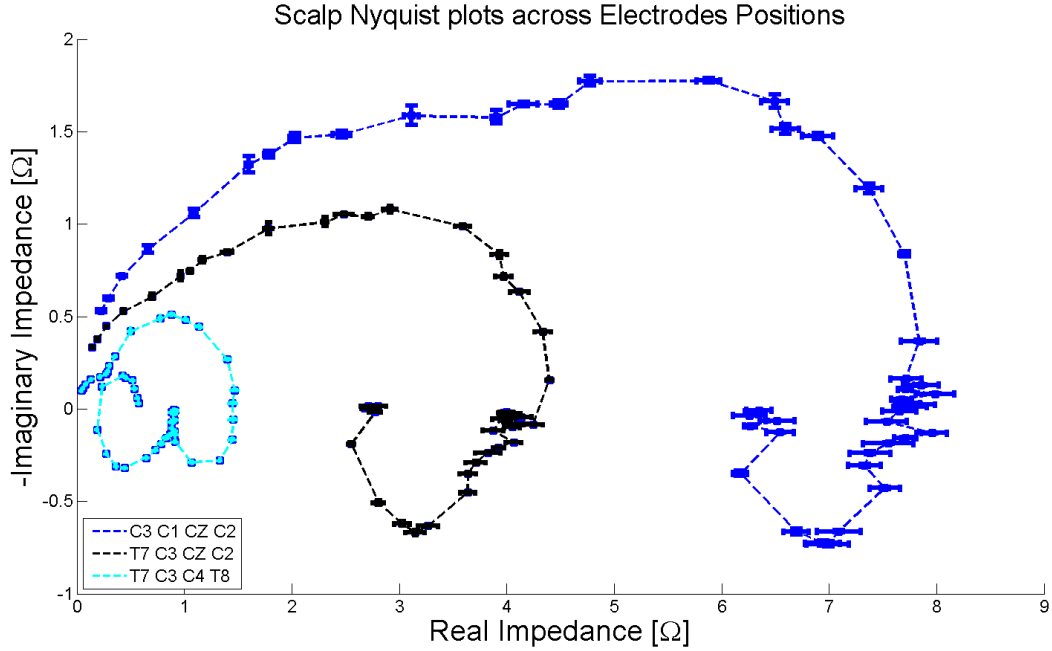


Figure 8.21: Nyquist plot of scalp for all electrode montages. Mean values with error bars are shown.

α and β dispersion of T7-C3-C4-T8. The other montages (T7-C3-CZ-C2 and C3-C1-CZ-C2) show a single reversed Cole system in the α frequency band. The demarcation between the β and γ Cole systems are difficult to find. For C3-C1-CZ-C2 it appears to be at a slight dip in the graph corresponding with 4.5Ω on the real axis. For the T7-C3-CZ-C2 this point appears to correspond to $\approx 2.8 \Omega$ on the real axis.

There is also a large difference between the magnitude of the scalp impedances along the real and imaginary axis. From the order of smallest magnitude to greatest we have scalp impedance of T7-C3-C4-T8, T7-C3-CZ-C2 and C3-C1-CZ-C2.

Fig. 8.22 illustrates the Nyquist plots of the skull Cole systems. Here again we note that there are 3 semi-circles for each montage corresponding to α , β and γ . We see that the T7-C3-C4-T8 has a single inverted α Cole system followed by 2 semi-circle outlines corresponding to the β and γ dispersions. All other montages are comprised of 3 α , β and γ semi-circles or Cole systems.

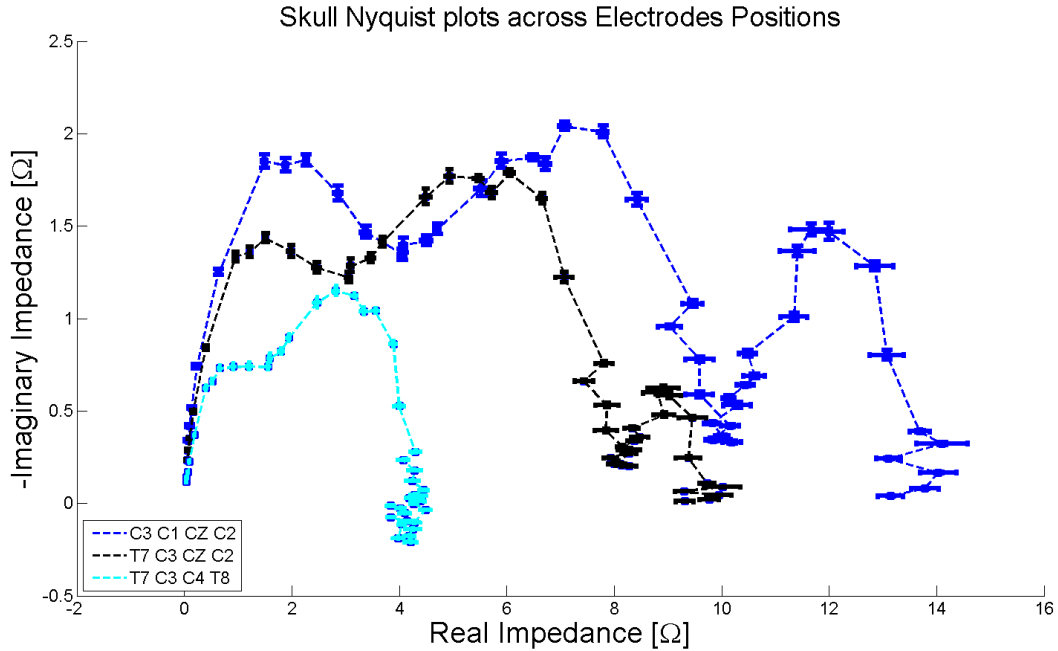


Figure 8.22: Skull Nyquist plots for all electrode montages. Mean values with error bars are shown.

We see here as well the order of impedance magnitude (real and imaginary) from least to greatest is from montages T7-C3-C4-T8, T7-C3-CZ-C2 and C3-C1-CZ-C2.

Fig. 8.23 shows the Nyquist plots of the CSF tissue. We note that there are no inverted Cole systems. Each plot has 3 semi-circles corresponding to the 3 dispersions. Here the magnitude order is reversed: from least to greatest we have CSF impedance from montages C3-C1-CZ-C2, T7-C3-CZ-C2 and T7-C3-C4-T8.

In Fig. 8.24 we see a set of inverted and regular Cole systems similar to what was already shown for the bipolar montages (see Fig. 8.6). For the α and β dispersions we see all montages generate inverted Cole systems. Finally the γ dispersion is comprised of a regular Cole system. The magnitude order of the impedance spectra, from least to greatest, are generated from C3-C1-CZ-C2, T7-C3-CZ-C2 and finally T7-C3-C4-T8.

Fig. 8.25 shows a similar pattern as for that shown in Fig. 8.24. Here we see that magnitude of the WM plots is slightly less than that off the GM.

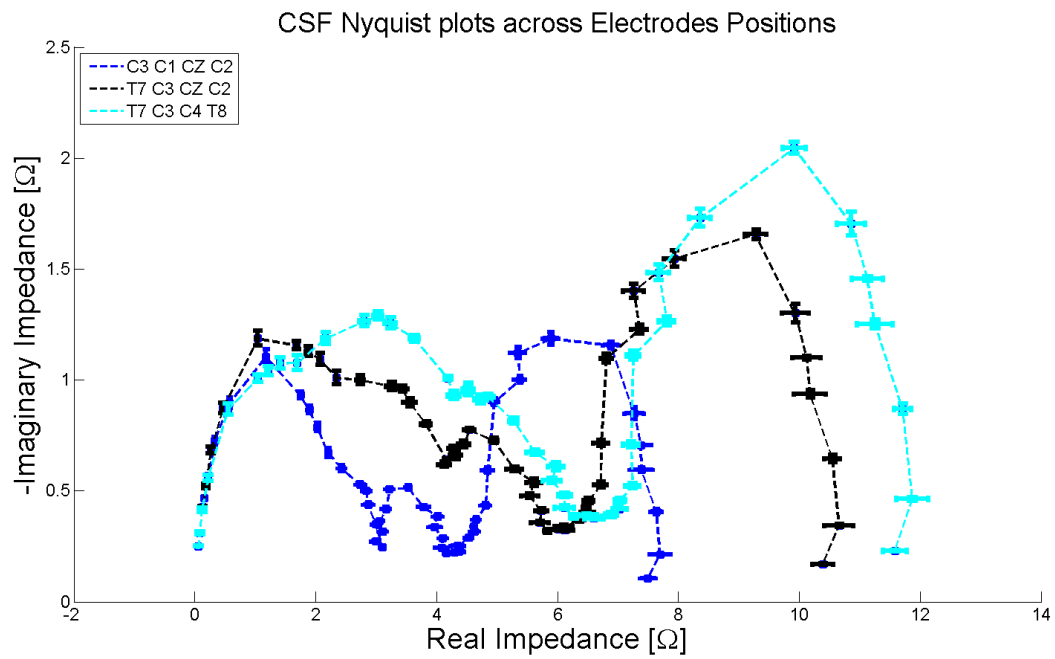


Figure 8.23: CSF Nyquist plots for all electrode montages. Mean values with error bars are shown.

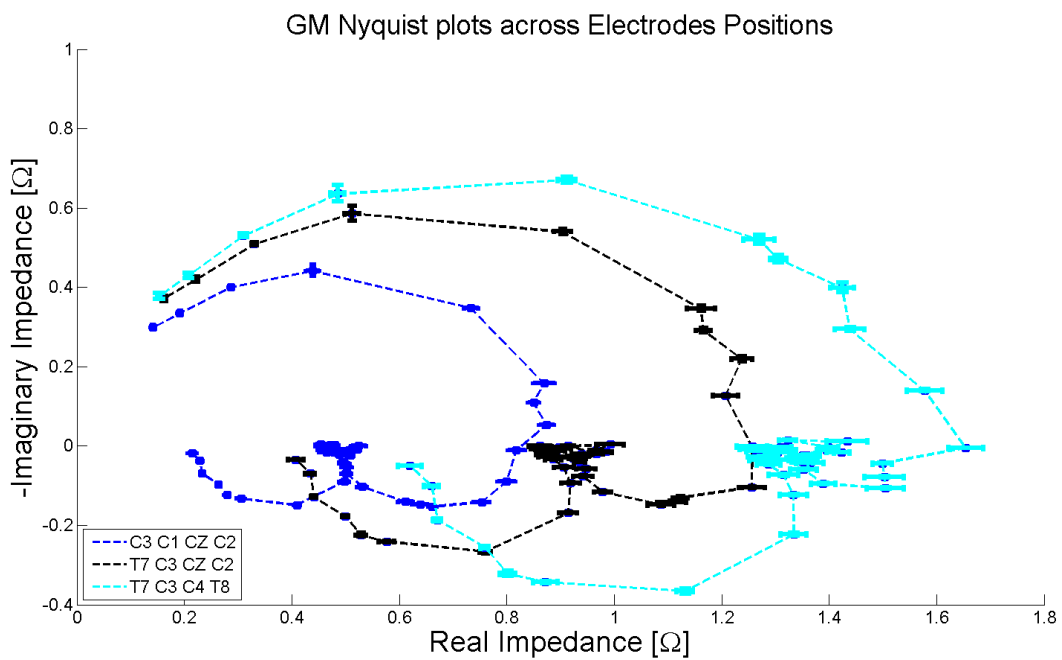


Figure 8.24: GM Nyquist plots for all electrode montages. Mean values with error bars are shown.

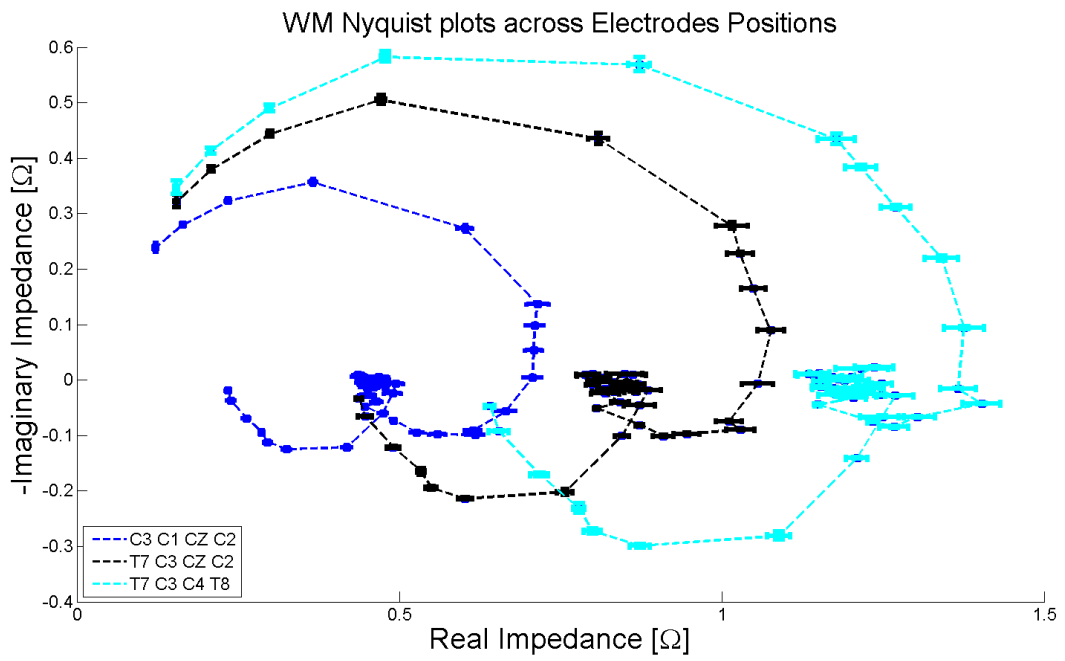


Figure 8.25: WM Nyquist plots for all electrode montages. Mean values with error bars are shown.

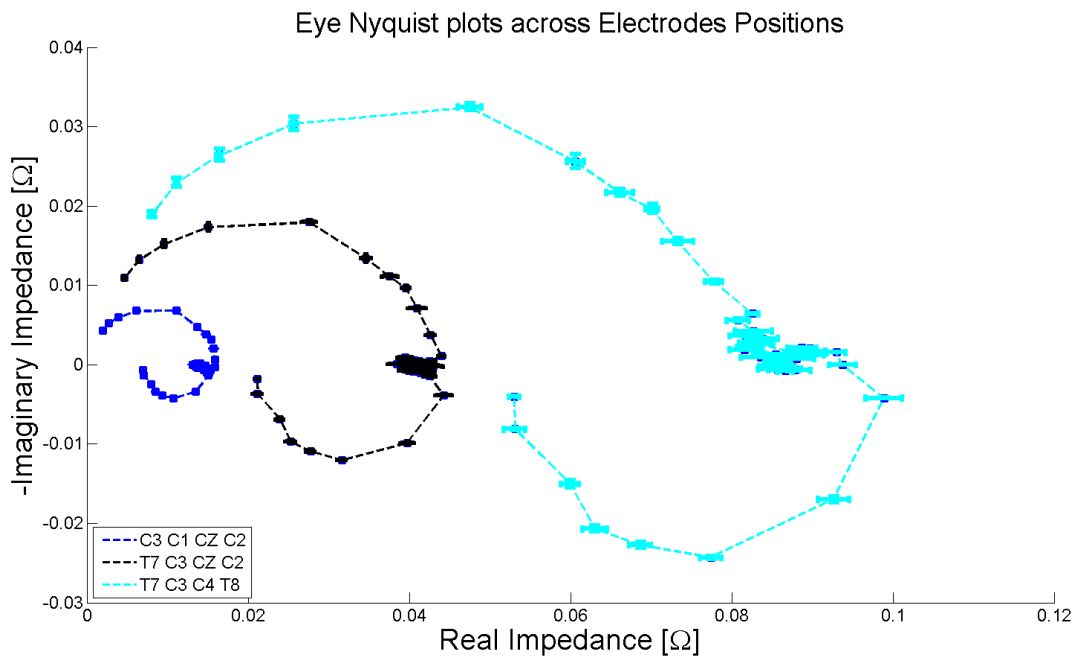


Figure 8.26: Eye tissue Nyquist plots for all electrode montages. Mean values with error bars are shown.

Fig. 8.26 shows the Nyquist plots of the eye tissues. we see a similar pattern to that shown in Fig. 8.26. Here there are 2 inverted semi-circles from each montage corresponding to the α and β dispersion. The inverted semi-circle corresponding to α is clearly visible, the second inverted semi-circle appears to be contained in small closed loop. The 3rd γ semi-circle is shown in the normal orientation.

8.3.1.1 Cole parameters

In this section we show the results of the extraction of the Cole parameters from impedance measurements obtained from C3-C1-CZ-C2, T7-C3-CZ-C2 and T7-C3-C4-T8. Theory on the Cole model as well methodology used for fitting and extraction of Cole parameters is described in sections 8.1 and 8.2.2.1. Significance level α is Bonferroni corrected to the number of pairwise comparisons, for the tetrapolar configuration this is $n=3$.

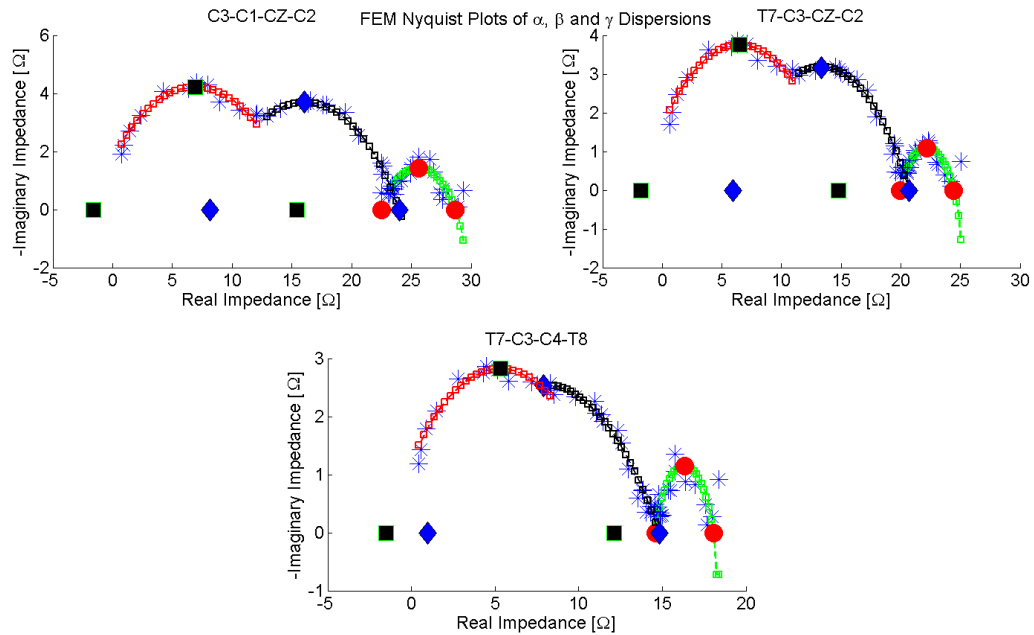


Figure 8.27: Cole plots shown for all 3 tetrapolar electrode montages. The first, second and third semi circle represent the α , β and γ frequency distributions respectively. Markers show the locations of fitted Cole parameters (R_0 , F_c and R_∞).

Fig. 8.27 provides a visualization of the fitting of the impedance spectra to the Cole model.

Data points are represented as blue stars. Green squares, black outlined diamonds and red outlined diamonds represent curves fitted to the α , β and γ dispersion respectively.

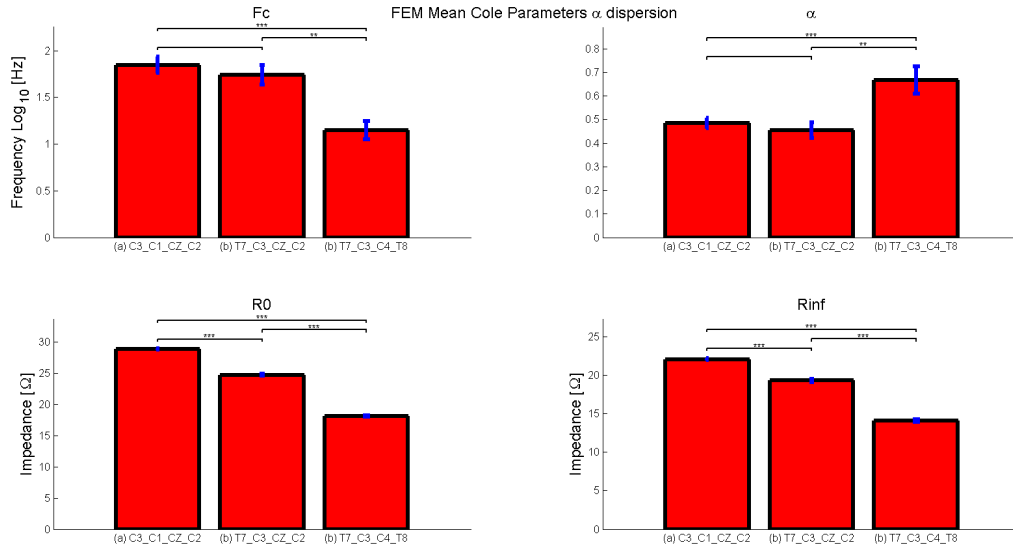


Figure 8.28: FEM 4 electrode alpha dispersion Cole parameter comparison. Stars show significance level of paired t-tests.

In Fig. 8.28 we see a bar chart showing the mean Cole parameters for the α dispersion. Error bars show the SEM. Comparison is made between the different montages using the paired t-test (see section 8.2.2.2).

We note the following observations (from C3-C1-CZ-C2 to T7-C3-C4-T8):

- f_c , R_0 and R_∞ decreases
- α increases

Significance level of pairwise comparisons is shown as number of stars. We assume a significance level of $\alpha = .05$, significance is meant here in terms of difference of means. P-values for the different comparisons are shown in table 8.4 below:

Fig. 8.29 shows a bar chart showing the mean Cole parameters for the β dispersion.

We see the following trends (from left to right on each bar chart):

α dispersion			
P value for f_c comparisons			
	C3-C1-CZ-C2	T7-C3-CZ-C2	T7-C3-C4-T8
C3-C1-CZ-C2		NS	.001/3
T7-C3-CZ-C2			.01/3
T7-C3-C4-T8			
P value for α comparisons			
	C3-C1-CZ-C2	T7-C3-CZ-C2	T7-C3-C4-T8
C3-C1-CZ-C2		NS	.001/3
T7-C3-CZ-C2			.01/3
T7-C3-C4-T8			
P value for R_0 comparisons			
	C3-C1-CZ-C2	T7-C3-CZ-C2	T7-C3-C4-T8
C3-C1-CZ-C2		.001/3	.001/3
T7-C3-CZ-C2			.001/3
T7-C3-C4-T8			
P value for R_∞ comparisons			
	C3-C1-CZ-C2	T7-C3-CZ-C2	T7-C3-C4-T8
C3-C1-CZ-C2		.001/3	.001/3
T7-C3-CZ-C2			.001/3
T7-C3-C4-T8			

Table 8.4: P-values showing statistical significance for differences between α Cole parameters. α significance level is Bonferroni corrected to $n = 3$ pairwise comparisons.

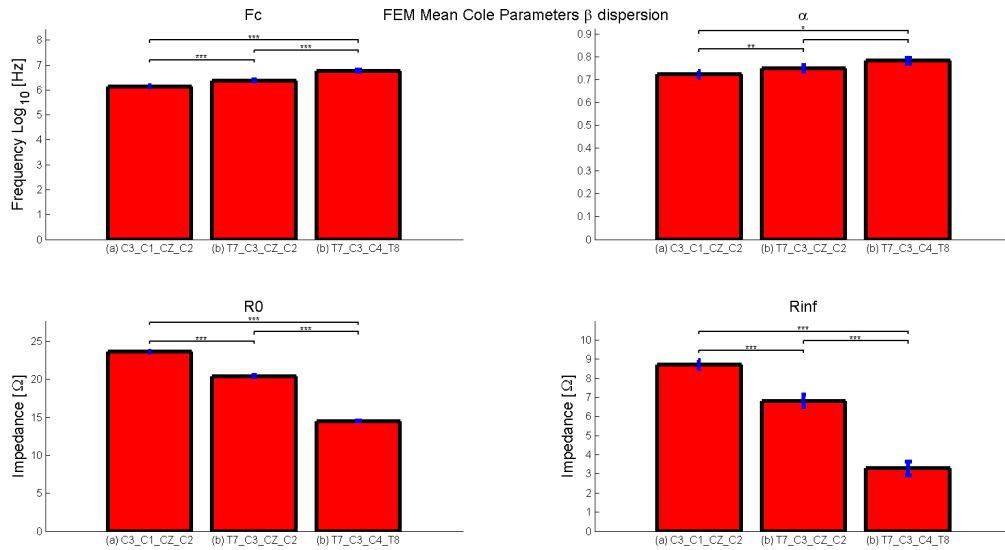


Figure 8.29: FEM 4 electrode beta dispersion Cole parameter comparison. Stars show significance level of paired t-tests.

- f_c and α increase
- R_0 and R_∞ decrease

Table 8.29 shows the P-values for the comparison of the β parameters.

Fig. 8.30 shows a bar chart showing the mean Cole parameters for the β dispersion.

We see the following trends (from left to right on each bar chart):

- f_c and α decreases
- R_0 decrease
- R_∞ reaches a maximum negative value at T7-C3-CZ-C2 and then increase slightly

Table 8.29 shows the P-values for the comparison of the γ parameters.

β dispersion			
P value for f_c comparisons			
	C3-C1-CZ-C2	T7-C3-CZ-C2	T7-C3-C4-T8
C3-C1-CZ-C2		.001/3	.001/3
T7-C3-CZ-C2			.001/3
T7-C3-C4-T8			
P value for α comparisons			
	C3-C1-CZ-C2	T7-C3-CZ-C2	T7-C3-C4-T8
C3-C1-CZ-C2		.01/3	.01/3
T7-C3-CZ-C2			NS
T7-C3-C4-T8			
P value for R_0 comparisons			
	C3-C1-CZ-C2	T7-C3-CZ-C2	T7-C3-C4-T8
C3-C1-CZ-C2		.001/3	.001/3
T7-C3-CZ-C2			.001/3
T7-C3-C4-T8			
P value for R_∞ comparisons			
	C3-C1-CZ-C2	T7-C3-CZ-C2	T7-C3-C4-T8
C3-C1-CZ-C2		.001/3	.001/3
T7-C3-CZ-C2			.001/3
T7-C3-C4-T8			

Table 8.5: P-values showing statistical significance for differences between β Cole parameters. α significance level is Bonferroni corrected to $n = 3$ pairwise comparisons.

γ dispersion			
P value for f_c comparisons			
	C3-C1-CZ-C2	T7-C3-CZ-C2	T7-C3-C4-T8
C3-C1-CZ-C2		.01/3	.001/3
T7-C3-CZ-C2			.001/3
T7-C3-C4-T8			
P value for α comparisons			
	C3-C1-CZ-C2	T7-C3-CZ-C2	T7-C3-C4-T8
C3-C1-CZ-C2		.001/3	.001/3
T7-C3-CZ-C2			.001/3
T7-C3-C4-T8			
P value for R_0 comparisons			
	C3-C1-CZ-C2	T7-C3-CZ-C2	T7-C3-C4-T8
C3-C1-CZ-C2		.001/3	NS
T7-C3-CZ-C2			.01/3
T7-C3-C4-T8			
P value for R_∞ comparisons			
	C3-C1-CZ-C2	T7-C3-CZ-C2	T7-C3-C4-T8
C3-C1-CZ-C2		.001/3	.001/3
T7-C3-CZ-C2			.001/3
T7-C3-C4-T8			

Table 8.6: P-values showing statistical significance for differences between γ Cole parameters. α significance level is Bonferroni corrected to $n = 3$ pairwise comparisons.

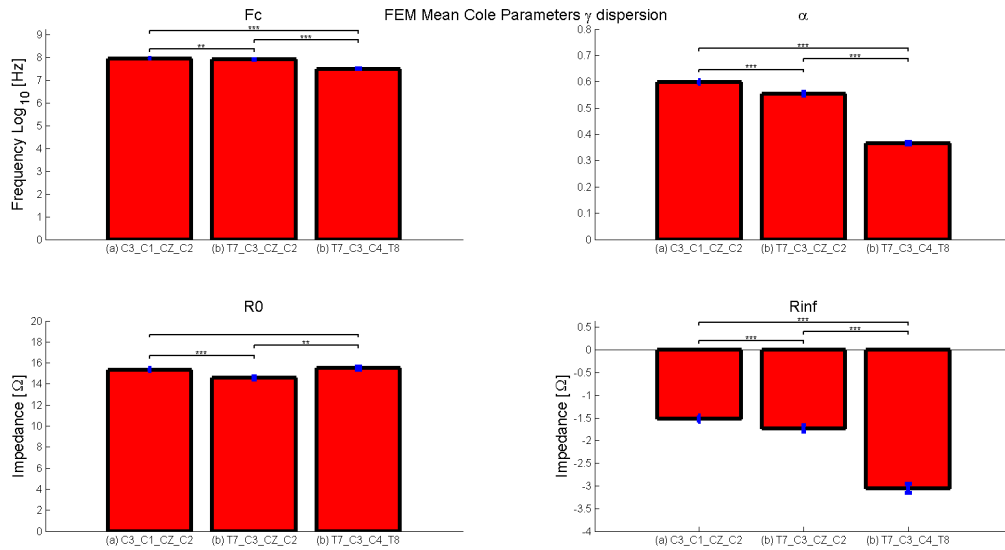


Figure 8.30: FEM 4 electrode beta dispersion Cole parameter comparison. Stars show significance level of paired t-tests.

8.3.2 Principal component analysis

In this section we show the results of PCA on impedance spectra pairs with the first montage set as the reference impedance (C3-CZ-C2-C1 - T7-C3-CZ-C2) and (C3-CZ-C2-C1 - T7-C3-C4-T8). Some background theory on PCA as well as a discussion of our methodology can be found in sections 8.2.3 and 8.2.3.1.

Fig. 10.9 shows a biplot of the coefficients (loadings) and principal scores of generated from the impedance pair C3-C1-CZ-C2 and T7-C1-CZ-C2. The real and imaginary loadings and score are on the left and right side of the graph respectively. We see that the scores for the imaginary component are located along the negative axis of the first principal component. The loading vectors are flipped according to the biplot sign convention as described in section 8.2.3.1.

We see in Fig. 8.32 the percent of variance described by the first two principal components. The left and right side of the graph shows the variance percentage for the real and imaginary components respectively.

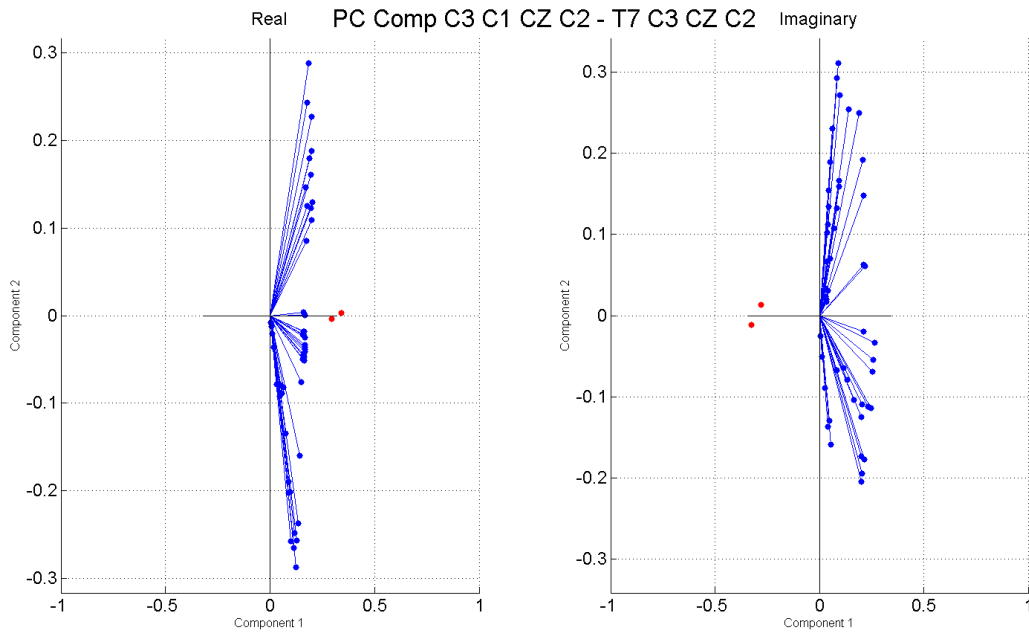


Figure 8.31: Principal components, scores and coefficients shown of real and imaginary components of electrode montages C3-C1-CZ-C2 and T7-C1-CZ-C2

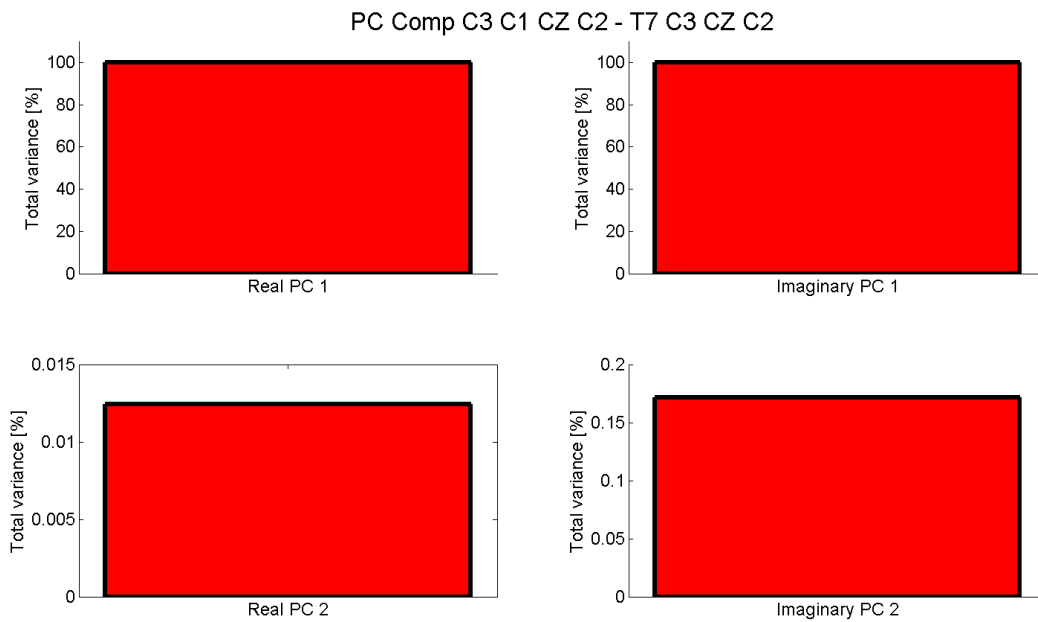


Figure 8.32: Percent of total variance of first and second principal components of real and imaginary components, shown for electrode montages C3-C1-CZ-C2 and T7-C1-CZ-C2.

As shown earlier for the bipolar montages, the first component describes $\approx 100\%$ of the variance. We note here that the percent variance of the second component is approximately greater by a factor of 10 for the real impedance component as compared to the imaginary component (Variance of second principal component real ≈ 0.013 , imaginary ≈ 0.16)

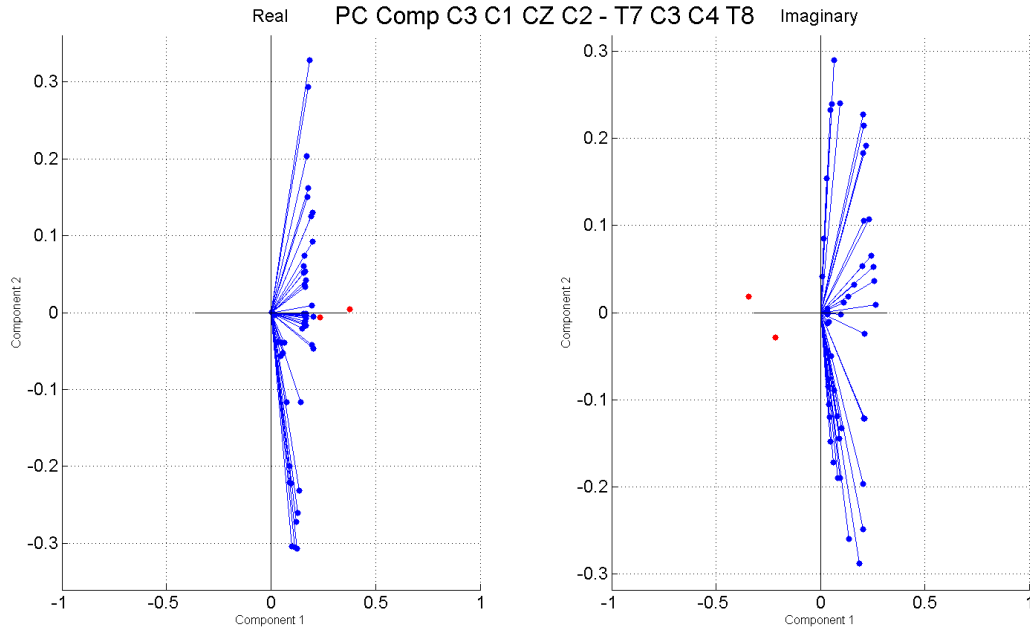


Figure 8.33: Principal components, scores and coefficients shown of real and imaginary components of electrode montages C3-C1-CZ-C2 and T7-C3-C4-T8.

Fig. 10.10 shows the biplot for the impedance spectra pair C3-C1-CZ-C2 and T7-C3-C4-T8. We can see a change in the relative positions of the score points as compared to Fig. 10.9, here the real scores are more widely separated along the first principal component axis whereas the imaginary scores show a greater offset from both the second and first principal component axes.

Fig. 8.32 shows the relative variance described by the first and second principal components of the real and imaginary impedance. We see that the variance for the second component has increased compared to the other impedance pair. Here we have $\approx .03\%$ real variance and $\approx .7\%$ imaginary variance attributed to the second principal component.

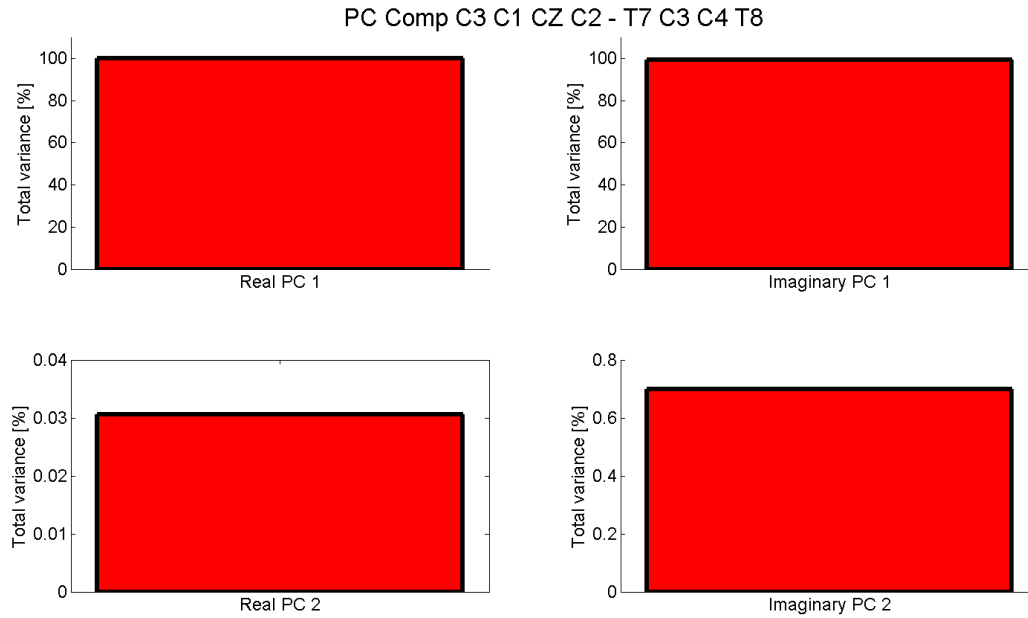


Figure 8.34: Percent of total variance of first and second principal components of real and imaginary components, shown for electrode montages C3-C1-CZ-C2 and T7-C3-C4-T8

8.3.3 Discussion

In this section we analyzed the Cole and PCA parameters from 3 tetrapolar montages. We first wished to investigate if the total Cole system is composed of a linear combination (sum in series) of Cole sub-systems of individual tissues.

We wished to analyze the Cole systems over a large frequency range instead of simply measuring a few frequency points. This allowed us to investigate the linearity properties over the whole spectrum. In addition we are interested in analyzing other macro properties of the spectrum such as the shape of the impedance in the nyquist plane.

We showed in Fig. 8.19 that indeed that measurements of the total Cole system and the addition of the tissue individual Cole elements (plot of real vs negative imaginary impedance) led to approximately the same results (error was shown to be under $< 1\Omega$).

In addition to the non-linearity of the Cole circuit (comprised partly of a Fricke Constant Phase element in parallel with an ideal conductance element) [49], we have an additional

source of non-linearity in the tetrapolar measurement itself. Here the pickup and current sources are separated which result in many sources of measurement artifact. As explained in detail in [195], sources of error include negative sensitivity zones between the voltage and current electrodes, positive phase angles caused by multiple current paths, common mode signal artifacts and surface shunt paths affecting the potential of the voltage electrode.

Due to the complex layered arrangement of the head tissues it is difficult to determine an arrangement of Cole circuits that accurately represents the different layers. In general only single or double dispersion models are suggested as interpretations of the frequency response of biological system [157, 220]. In [220] there is a discussion concerning multiple Cole systems that can be added in series or in parallel, depending on the modeled circuit arrangement. Thus there no is no clear description concerning a Cole circuit arrangement that can adequately model the multiple layers of the human head. In addition the current path through the head can be considered to have multiple current paths in series and in parallel which increases the difficulty of setting up a an accurate circuit model.

We have shown here through numerical simulations that each tissue does indeed generate independent Cole systems which can be visualized as semi-circles in a Nyquist plot. These semi-circles are shown for 3 different dispersion zones. These independent semi-circles, when added together, comprise the total Cole system of the head.

We posited that the total Cole system can be approximated as the weighted sum of only several of the head tissues. By analysis of the Cole plot figures of all the tissues (see Figs. 8.21 - 8.26) we see indeed that the total Cole system is dominated by the skull, CSF and scalp. In order of magnitude from greatest to least we have the skull and CSF impedance (approximately equal) followed by the scalp.

Here we note an interesting phenomena that occurs with the scalp impedance. As the angle between the voltage and current electrodes are increased, the negative sensitivity field concentration in the scalp tissue also grows. This results in a field cancellation effect

whereby the scalp impedance is greatly reduced (see Fig. 8.21). We see however, a clear frequency and spatial (electrode montage) dependence on the magnitude of the negative sensitivity field. For low frequencies (i.e. α dispersion) all the tetrapolar montages generate inverted semi-circles (Cole systems). For 2 of the montages (T7-C3-CZ-C2 and C3-C1-CZ-C2) the β and γ Cole systems have reverted back to normal orientation. For the 3rd montage T7-C3-C4-T8, which has the largest inter voltage current electrode angle, both the α and β Cole systems are inverted and only the high frequency γ system has returned to normal orientation. The inverted Cole element can also be seen for the skull in the α dispersion zone for the montage T7-C3-C4-T8 (Fig. 8.21).

We can see that the CSF impedance is comprised of standard Cole systems (Fig. 8.21). Thus the CSF plays an important role in contributing to the total head impedance. Tissues deeper than the CSF (GM, WM and eye tissue see Figs. 8.24 -8.25) all show inverted Cole elements for the α and β dispersions. These results are similar to that shown for the bipolar montaged (see Figs. 8.6 -8.7). This may be due to a parallel current path effect [195] caused by the highly conductive CSF.

We note that the overall effect of the negative sensitivity fields is to reduce the magnitude of the impedance spectra with the greatest reduction at low frequencies with montages with large angles between the current and voltage angles.

We then examined to see if the changes in the sensitivity distribution and individual tissue Cole systems would be detectable by analysis of global impedance characteristics. We specifically compared Cole parameters and PCA outputs across the tetrapolar montages - thus covering the most common forms of explanatory and descriptive modelling.

The most stable Cole parameters were R_0 and R_∞ which showed significant decreases for increased inter-electrode angle across all dispersion zones (with the exception of the negative values of R_∞ extracted for the γ dispersion which has no physical meaning and is an artifact of the fitting algorithm see earlier discussion in this chapter). All these

differences have very small p-values.

For the α dispersion there was no significant difference between f_c and α for the montages of and C3-C1-CZ-C2 and T7-C3-CZ-C3, however there was a significant difference for these parameters between T7-C3-CZ-C3 and T7-C3-C4-T8. This suggests that the presence of noise (here we have Gaussian noise added to the model as well the error of the Cole fitting algorithm) may present difficulties in extracting significantly different impedance parameters from different but relatively close montages. The author in [158] showed in fact that Cole parameters extracted without data preprocessing, could not be used with a classifier to reliably relate the impedance characteristics measured on the arm with arm posture. In that study it was shown that after the use of SVD (singular value decomposition), the Cole parameters of $\frac{R_0}{R_\infty}$ and f_c were used to accurately classify arm impedance measurements with arm posture. We can confirm in our results that R_0 and R_∞ provide the most stable differences between montages. However we must note that we may have underestimated the noise level of an experimental bioimpedance measurement which may in fact be much higher than our estimated levels (see section 4.7).

In the β dispersion we do see that f_c and α increase (see Fig. 8.29). This appears to be caused mainly by the effect of the shape of scalp Cole system on the total Cole plot. We see for instance that for T7-C3-C4-T8 the scalp is comprised of a double inverted Cole system followed a single Cole system at high frequencies. The effect of addition of the scalp system is thus to increase the curvature radius of the total Cole system at high frequencies- this has the net effect of reducing the demarcation (minima) point between the β and γ dispersions and causing the f_c and α parameters of the β dispersion to increase (see Fig. 8.20) .

The effect of changing montages can also be seen in the PCA results. As shown earlier for the bipolar montage, almost 100% of the variation of impedance spectra of different montages can be attributed to single principal component. Thus the translation or change of impedance caused by changing electrode position is almost linear along the principal component axis. Here we note that the proportion of the variation attributed to the second

principal component (real and imaginary) changes dependent on the electrode montage pair. Thus for the pair C3-C1-CZ-C2 and T7-C3-CZ-C2 the proportion of variance along the second principal component is $\approx .013\%$ for the real impedance and is $\approx .16\%$ for the imaginary impedance. For the pair C3-C1-CZ-C2 and T7-C3-C4-T8 this increases to $\approx .03\%$ for the real impedance and to $\approx .7\%$ for the negative impedance. Thus we can see a non-linear increase in the variation described by the second principal component especially for the imaginary impedance. This is in accord with our analysis of the Cole plots generated by the different montages, we do see that impedance spectrum parameters of T7-C3-C4-T8 has significant differences when compared to other montages. We can then potentially link degree of change in impedance spectra (as characterized by PCA scores and percentage of variation along first and second principal components) to changes in dose in the brain.

8.4 Summary

In this chapter we analyze the impedance spectra generated from the bipolar and tetrapolar configurations using the Cole model and PCA. We show linear properties of the spectra - namely that Cole plots of each head tissue add in series to equal Cole plot resulting from all the tissues and that the variance between impedance spectra is almost 100% represented by a single principal component. We show using Bonferroni corrected paired t tests the significance of differences between Cole parameters of impedance spectra of the bipolar and tetrapolar electrode configurations. We also show that the variance between spectra described by the second principal component increases as the inter-electrode angle is increased.

Part IV

Experimental study

Chapter 9

In-Vivo Experiments

9.1 Study Research Goals

In the previous chapters of this thesis (chapters 6 - 8) we have simulated and analyzed the sensitivity fields, dose (electric field and current density) transfer impedance, Cole parameters and PCA of bipolar and tetrapolar montages. Results from FEM simulations showed the linear properties and characteristics of the relationship of impedance spectra generated from different montages, we also showed that the total impedance of the head is dominated by a few tissues. We showed that different montages produced unique bioimpedance parameters (Cole and PCA) thus providing a potential method of linking characteristics of the transfer impedance to dose.

We now provide the method and results of a pilot study in which we measured impedance spectra of the head from a group of volunteers. Our aim here is two-fold: first we wish to compare the experimental and FEM results to examine the how close our numerical results and assumptions accord with physical reality; secondly we wish to infer dose and impedance parameters by comparison of the experimental results to the ideal FEM model.

Despite the difficulty of perfect validation (see for example [239]), we still find it instructive to compare features of theoretical results to those obtained experimentally. A close agreement between these results can be useful in estimating the utility of the model towards approximating the frequency response of the head tissues. In addition, features of

the experimental data can be used as model inputs - thus potentially increasing the accuracy of the FEM.

We also analyze independently relationships and features of the experimental data set. Specifically we investigate measures such as repeatability and variability of measurements as well as error levels and patterns across and between subjects.

Relationships derived between simulated and experimental spectra can be used towards optimization of both measurement and stimulation of neural tissue. As discussed in the FEM section, the impedance spectra is partly a function of the sensitivity field which is also related to the concept of electrical dose. Analysis of both real and imaginary impedance spectra characteristics can thus provide insight into both the real and reactive components of electrical current in the brain.

9.2 Instrumentation

In this section we describe the instrumentation and calibration procedure used prior to experimental measurements.

9.2.1 Experimental Configuration

The main part of our experimental configuration consisted of the Solartron (1294) FRA (Frequency Response Analyzer) together with the front-end Solatron (1255b) which served as an interface between the subject and the FRA (both modules declare conformity to relevant safety standards including IEC 60601-1). Both Solatron modules were controlled by custom software (SMART) installed on a PC. The SMART software was used to set all the parameters for each experiment including current level, number of frequency points and frequency range.

See Fig.9.1 for a graph of the basic elements of the measurement configuration. The SMART software is installed in the PC which is connected through a GPIB and a parallel

port to the FRA and the 1294 Impedance Interface respectively. The 1294 connects through 4 leads (2 current and 2 voltage) to the sample (subject head).

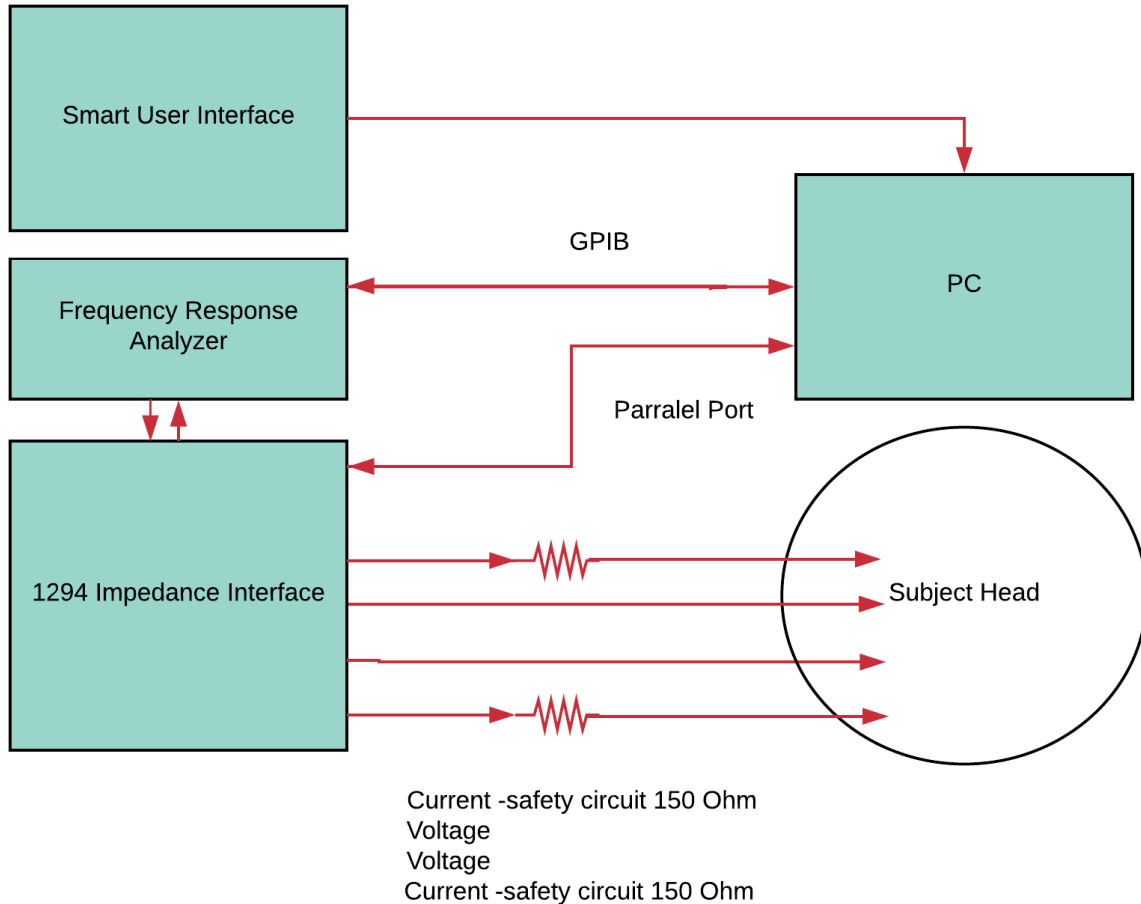


Figure 9.1: Components of the measurement configuration shown, the double head arrows show the communication pathways between the different elements of the frequency sweep experiment.

Drive and voltage were transmitted from the front-end Solatron (1255b) through 4 shielded leads of approximately 1 meter length. The leads were then attached (using alligator clips) to the lead wires of four 9 mm diameter tin electrodes (e21-9s disk electrode Electro Cap International Inc) which were in turn attached to electrode sites on each subjects head. As an additional safety measure in the event of sudden current flow to ground through the subject, we added $150\ \Omega$ resistors in series between the 2 current leads and the copper

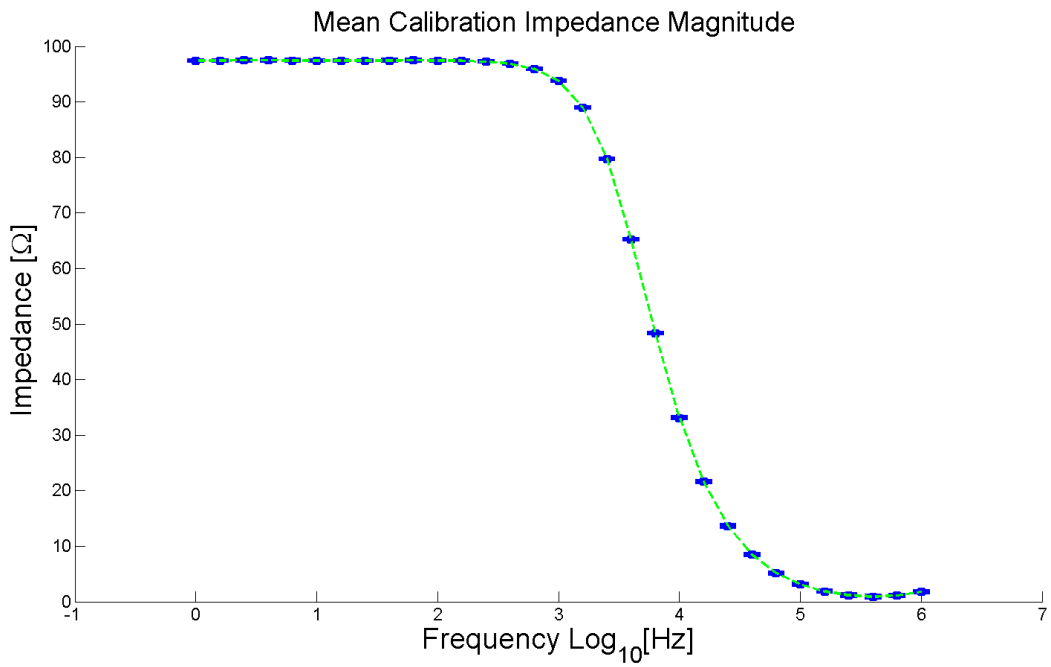
wires (safety circuits are shown as resistors in Fig. 9.1).

Our selection of the resistors values was based on an experiment where we ran a frequency sweep whereby the current electrodes were attached to each other via a $100\ \Omega$ resistor representing a simulated load in series with the current. We set the measurement parameters to current generator ($100\ \mu$ Amps (see experimental procedure in section 9.3.2), frequency range 1 Hz - 1 MHz, with 5 frequency points per decade. The voltage drop across the load resistor was measured via a parallel connection to an oscilloscope (Tektronix). Results showed in this test case a maximum peak to peak voltage of 2.2 volts over the entire frequency range which we considered low enough for our scalp measurements.

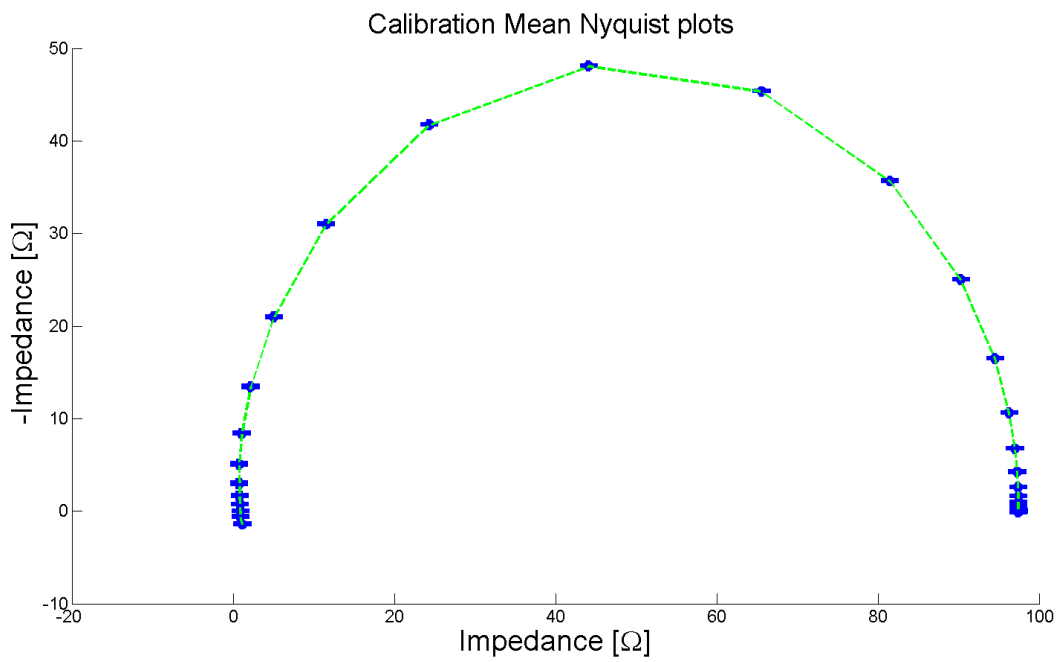
9.2.2 Calibration

In order to verify the accuracy of our instrumentation, we measured a frequency of a provided calibration box. Frequencies were logarithmically spaced at 5 points per decade from 1 Hz until 1 MHz. The calibration box consisted of a network of resistors and capacitors in parallel. Four inputs are provided, 2 outer inputs (labeled as high and low) are designated for current leads and 2 inner outputs (also labeled as high and low) are designated as voltage leads. The calibration circuit consisted of a resistor between the voltage leads inputs in parallel with a capacitor. The resistor has a resistance of $101\ \Omega$ and a tolerance of 5%. The capacitor is 470 nF. Between the high current and high voltage input there is another parallel circuit with a $4700\ \Omega$ resistor (1% tolerance) and a 4.4 nF capacitor. Finally there is another parallel circuit between the low current and low voltage input with a $1000\ \Omega$ resistor (1% tolerance) and a 4.4 nF capacitor.

Figure 9.2 (a) shows the measured impedance of the calibration unit. Plots are the mean of 2 measurements, errors are the standard error of the mean. At DC until 1 KHz we note a flat measured impedance of $97.5\ \Omega$. This represents an error of 3.5% of the stated value of the resistor of $101\ \Omega$ which is however well within the resistor tolerance of 5%. As the frequency is increased, more of the displacement current is shunted through the capacitors



(a)



(b)

Figure 9.2: Bode and Nyquist plot of impedance shown for calibration measurement of the Solatron.

resulting in a drop of impedance in a typical "curve" shape. We see the graph of impedance begin to curve at around 1 KHz as the displacement current starts to dominate the measurement. The impedance curve flattens again at ~ 400 Khz. Afterwards the impedance begins to rise again. This rise is a deviation from expected behavior and may be error due to stray capacitive coupling.

Another representation of the calibration impedance response is shown as a Nyquist plot in Figure 9.2 (b). As expected, R_0 and R_∞ are close to 100 and 0 Ω . The plot is the mean of 2 measurements, standard error of the mean is shown as error bars for both real and imaginary impedance. The error at high frequencies can be visualized as a slight inwards deviation of the semi-circle near R_∞ .

Since the error from calibrated values is relatively small we decided to not apply any correction factor. We expect however that stray capacitive coupling would increase error at the high end of the frequency range.

9.3 Study Description

9.3.1 Study recruitment

Ethics was obtained from the Carleton University Board of Ethics for this study referenced as Protocol #: 102566. The ethics certificate is found in Appendix A.

We recruited 8 healthy subjects for participation in the study. Subjects were all males although females were not excluded from the study. Demographic data such as age was not collected, however each subject confirmed that they were at least 18 years of age. Subjects read the information sheet and signed the informed consent form. The investigator ascertained that the study protocol was understood by each subject and that all concerns and questions had been answered satisfactorily.

9.3.2 Procedure

Participants in the study were asked to be seated upright in a chair facing the control PC (see Fig.9.1) Electrodes were carefully cleaned with a rubbing alcohol solution and soap and water prior to use. Our experiment consisted of measurements of 3 tetrapolar montages: a) C1 C3 CZ C2 closely spaced along the top of the head, b) T7 C3 CZ C2 whereby the gap between the drive electrode T7 on the left side of the head and the voltage electrode at C3 was increased, and c) T7 C3 C4 T8 whereby spacing was increased between the two voltage electrodes (C3 and C4) and the right hand current voltage electrodes (C4 T8) (see Fig. 4.1.2). (We used exclusively tetrapolar measurements (separate drive current and voltage electrodes) in order to remove the effect of contact impedance). Our first step was therefore to locate all the electrode coordinates on the subject scalps. We asked each subject to place a standard 21 channel EEG cap on their heads closing a velcro strap under their chin to ensure a snug fit. Next all electrode points were marked using a water soluble skin marker. At certain coordinates, no electrode channels were found on the cap. In those cases we approximated the location of the coordinate using neighboring channels as landmarks. We found that the marker could penetrate the thin cap material.

After the locations were marked we applied skin preparation methods in order to reduce the contact layer allowing satisfactory skin-electrode coupling. First we applied alcohol swabs to the scalp at the marked locations. Next we used an ex-foliating cream to further reduce skin impedance. Standard EEG cream (1020 conductive neurodiagnostic electrode paste weaver and company) was placed on our electrodes which were then set on the marked coordinates. Tissue swabs were used to apply pressure on the EEG paste coated electrodes to ensure a good coupling occurred between electrodes and scalp tissue. We found that adding saline drops (Life saline solution gentle ph balanced formula) to electrode-skin interface significantly aided in reducing skin impedance. This was done through a trial and error process by analyzing Cole plots measured with the Solartron.

High skin impedance resulted in bad electrode-skin coupling which usually caused out of phase measurements (i.e. positive phase instead of negative). We also noticed very high impedance values for inadequate electrode-skin coupling. Adding saline drops reduced the impedance magnitude and resulted in in-phase measurements. This represented the final step in skin preparation.

After the electrode placement, we then set the experiment parameters using the SMART software interface. The drive electrode were set as a current source so that current injection amplitude would be the same for all frequencies. This methodology was also used when setting up the FEM (see section 4.4). The current magnitude was set to a constant 100 μAmps . We considered this level of current to be below the threshold of human sensation and well below current density levels that could be damaging to human tissue (see an extensive review of safe current density levels in the brain in the context of tDCS [240]).

We set the range of our frequency sweeps from 100 Hz until 1 MHz with 10 logarithmically spaced points per decade resulting in a total of 41 frequency points. This selection was designed to essentially cover the entire range of our instrument (maximum frequency of 1 MHz) while studying the frequency response of the tissues over 2 (α and β) dispersion bands (see section 4.5). We began measurements with electrodes spaced closely together and then gradually increase the spacing between the electrodes. Thus the first measurement montage was C1-C3-CZ-C2, followed by T7-C3-CZ-C2 and finally T7-C3-C4-T8. All measurements were repeated 4 times in order to assess measurement repeatability and in to compare mean measurements across different subjects. After each measurement set of a montage, electrodes were removed and replaced on new coordinates as necessary. Data was initially stored in a dat file configuration and then converted to the csv prior to export and further processing.

Each subject was asked to report if they felt any painful sensation during measurement especially at low frequencies. Some subjects mentioned that they felt a slight "pinching" sensation at the onset of the stimulation. Others had no perceptible sensation. In all cases

the sensation was considered tolerable and there no grounds for interrupting the measurements ¹.

9.4 Data Analysis

After extraction of the impedance measurements, we investigated a number of impedance parameters. We plotted Bode plots (Impedance magnitude vs frequency) of all montages for each subject. We also showed Nyquist plots of the real vs negative imaginary impedance. Error bars in each plot show the standard error of the mean for four measurements. We then fitted each subject data to the Cole model (for a review of the Cole model theory as well as our fitting methodology see sections 8.1 and 8.2.2.1. Comparisons of Cole parameters for the each subject across the different electrode montages was made using a paired t-test with a significance level of $\alpha = 0.05$ [225–227](see section 8.2.2.2).

We then calculated and plotted the mean impedance, phase, and real and imaginary impedance of all subjects for each montage. We fitted the mean impedance to the Cole model. Comparisons of Cole parameters for the subject mean values across the different electrode montages was made using a non-paired t-test with a significance level of $\alpha = 0.05$ (for an example of use of the non-paired t-test for bioimpedance spectroscopy studies of inter-group differences see [241]). Finally we performed PCA on pairs of the mean impedance spectra (i.e. C3-CZ-C1-C2 and T7-C3-CZ-C2 and C3-CZ-C1-C2 and T7-C3-C4-T8) (see section 8.2.3.1).

9.4.0.1 Experimental Cole fitting

The algorithm described in section 8.2.2.1 is suitable for Cole fitting and parameter extraction when the experimental data forms an approximate semi-circle.

Our data however doesn't always conform to this shape as we can see for example C3 C1 CZ C2 and T7 C1 CZ C2. in Fig. 10.4 Past a certain frequency range the plots do not

¹Two out of the eight subjects felt a mild pinching sensation. Other subjects had no perceptible sensation.

assume a rounded peak or shape but rather ascend in sharp positive slope. This may be due to the limited frequency range of our instrument (max 1 MHz) which does not capture the entire frequency dispersion.

In such a case we approximate the experimental graph as part of a semi-circle. This is accomplished by shifting the value of v_0 (see section 8.2.2.1) leftwards along the x-axis. In practice we found that applying *fminunc* to $v_0/1.1$ provides a good fit as shown in the top right and left of Fig. 9.8 in such cases we cannot accurately extract R_∞ since only part of the semi-circle can be fitted. In addition, the characteristic frequency F_c can not be directly calculated in the case where the experimental Nyquist graphs do not have a peak. We use a nearest neighbor optimization algorithm (reference) to determine the data point which is closest to the interpolated value.

9.5 Results

We now show the results acquired from measurements of each individual subject.

9.5.1 Individual Subjects

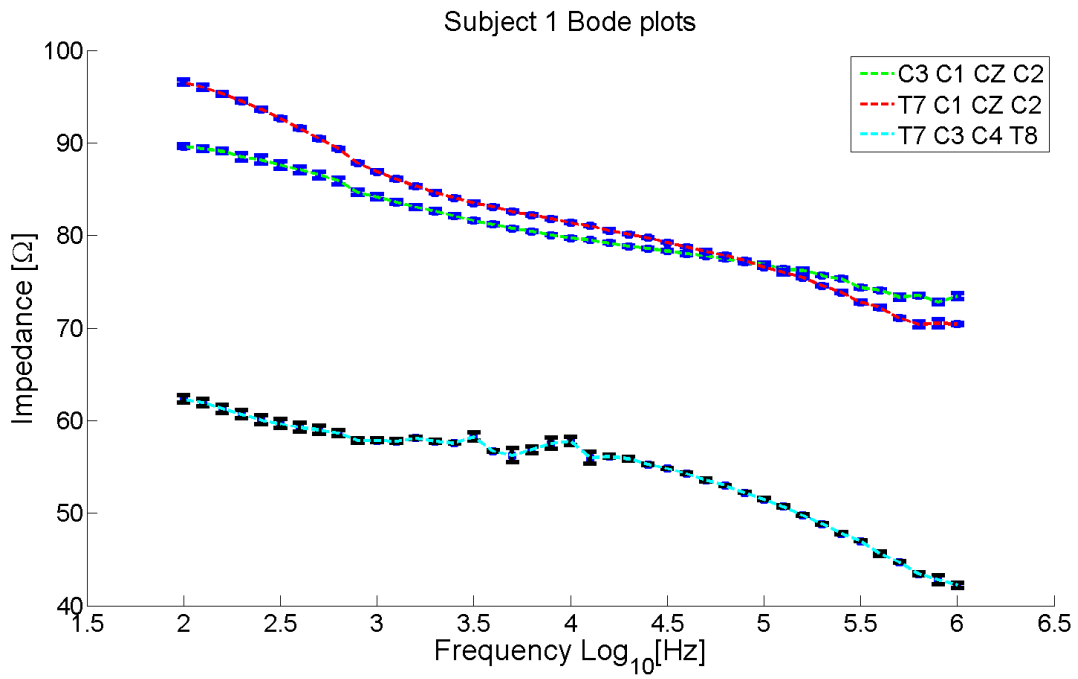
Outputs of the measurements are impedance magnitude vs frequency (Bode plots) and negative imaginary vs real impedance (Cole plots). We plot the mean values, error bars show the standard error of the mean (sem) which is given by:

$$sem = \sigma/n \tag{9.1}$$

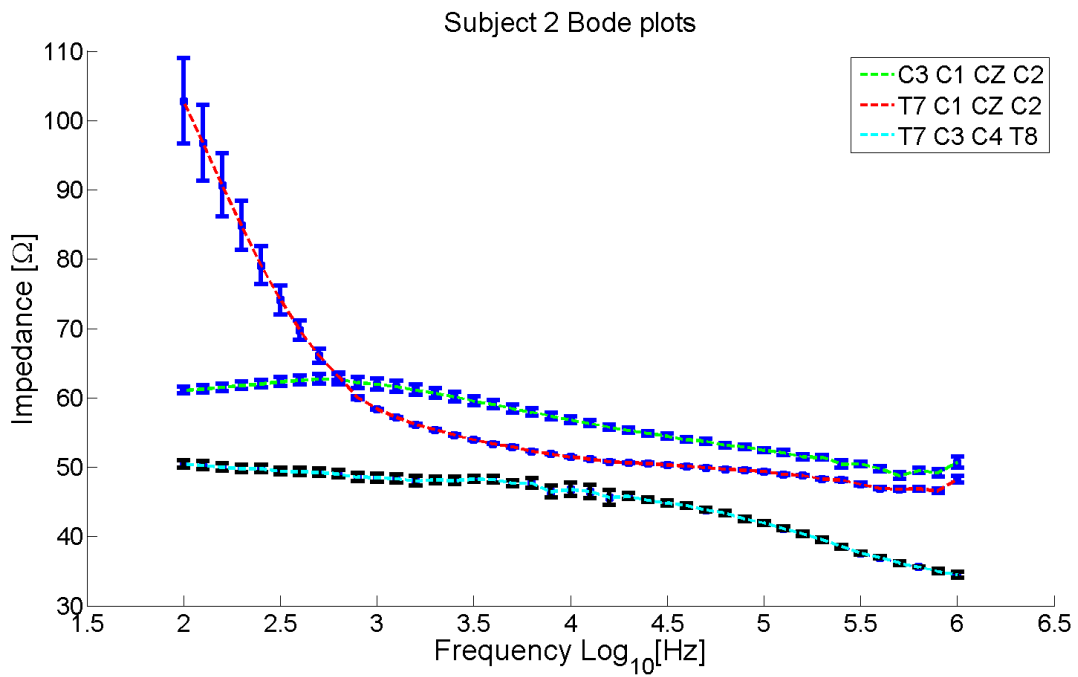
where σ is the standard deviation and n is the number of measurements taken. As mentioned above (see section 9.3.2) we took 4 measurements per subject of each montage.

9.5.1.1 Bode Plots

We first show the Bode plots of all 8 subjects.



(a)



(b)

Figure 9.3: Subject 1 and 2 impedance magnitude vs frequency.

Fig. 9.3 (a) and (b) shows impedance vs frequency measurements for subject 1 and 2. The Log_{10} of the frequency is provided as the x-axis. Both graphs show that each electrode montage results in a distinct spectral response. In general impedance is shown to decline as a function of frequency.

C3 C1 CZ C2 and T7 C1 CZ C2 general track close together. For subject 1 the shape of the curves from these montages show similar trends. First from 100 to 1000 Hz, the graphs follow a convex shape. At 1000 until around 160 KHz, the graphs show a roughly linear descent. From 160 KHz until 1 Mhz, the impedance curves assume a convex shape. At around 100 KHz, the T7 C1 CZ C2 curve intercepts and descends below C3 C1 CZ C2.

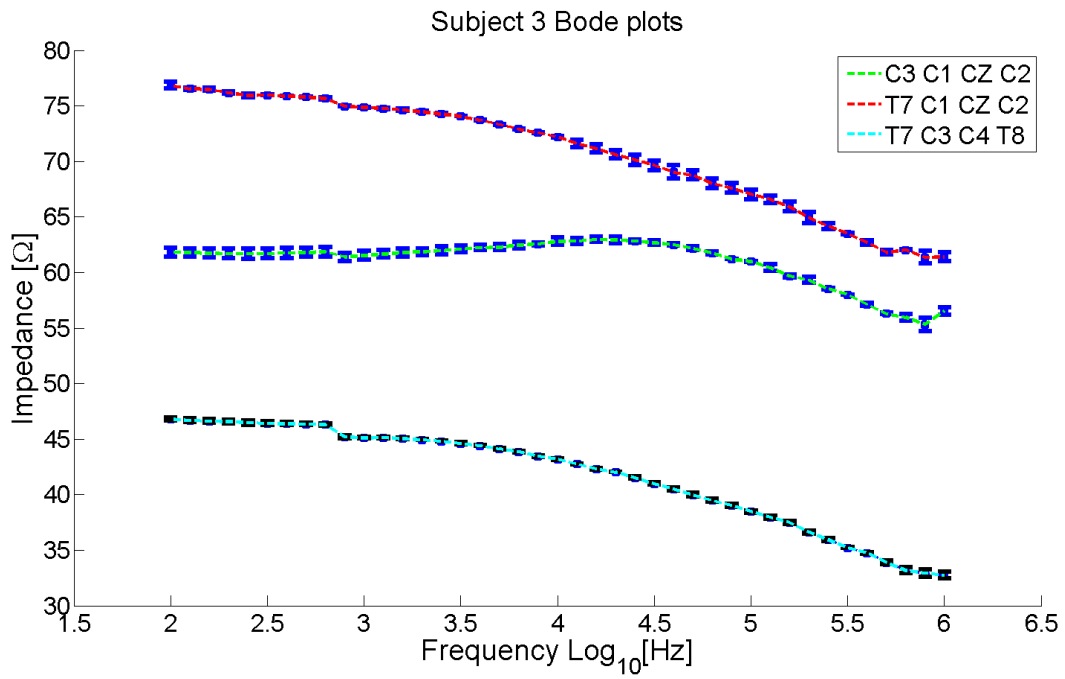
The graph of T7 C3 C4 T8 is different from the prior 2 graphs in both absolute values and shape of descent. First, impedance values are roughly 30Ω less than the other curves along the whole length of the spectral measurement. From 100 Hz until ~ 1 KHz, the descent of the graph is slightly concave. From 1 KHz until the end of the frequency range the shape of graph follows a convex shape.

In Fig. 9.3 b, T7 C1 CZ C2 falls sharply from 100 Hz until about 1 KHz. The relatively large error bars of this part of the frequency spectrum indicate the variance of these measurements. T7 C1 CZ C2 intercepts C3 C1 CZ C2 at ~ 1 KHz. Thereafter the T7 C1 CZ C2 impedance plot continues to track below C3 C1 CZ C2 at slightly concave shape. Both C3 C1 CZ C2 and T7 C3 C4 T8 follow the same pattern as in Fig. 9.3 a.

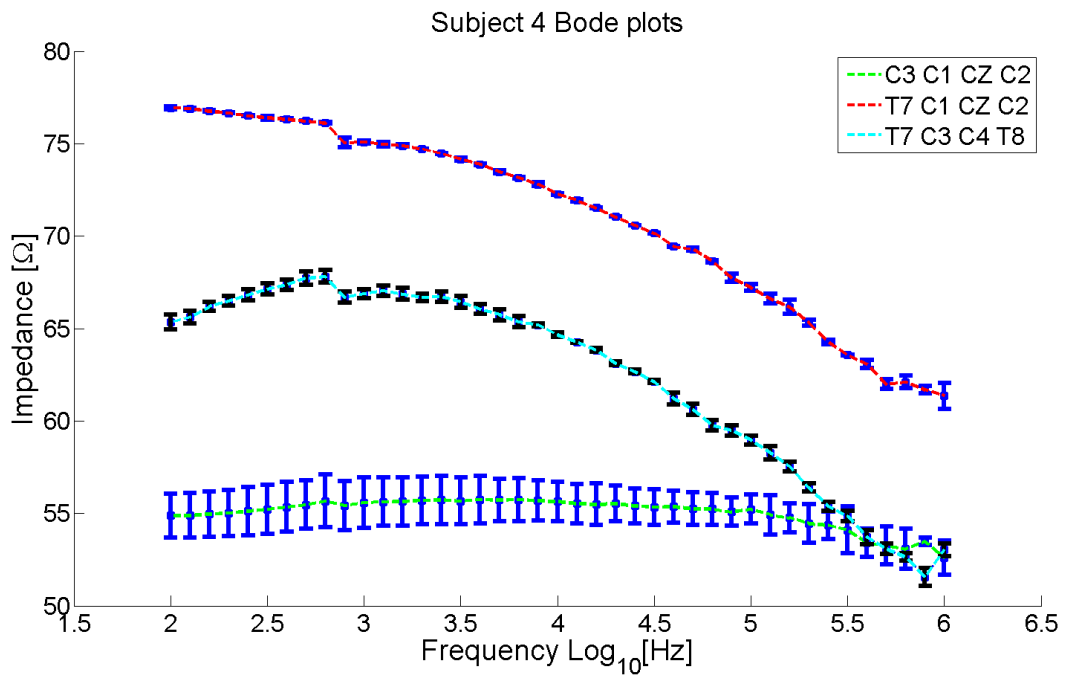
In Fig. 9.4 a, impedance plots of subject 3 show the same pattern as described above. C3 C1 CZ C2 and T7 C1 CZ C2 follow similar paths from around 10 KHz onwards. T7 C3 C4 T8 is the lowest impedance of these set and steadily diverges from the other 2 graphs.

In Fig. 9.4 b, T7 C1 CZ C2 and T7 C3 C4 T8 are similar to graphs of earlier subjects. Here we see that C3 C1 CZ C2 is the lowest and noisiest of the impedance data set.

Fig. 9.5 a. shows that C3 C1 CZ C2 and T7 C1 CZ C2 converge at around 150 KHz. T7 C3 C4 T8 has the lowest impedance and diverges away from the other 2 graphs following a



(a)



(b)

Figure 9.4: Subject 3 and 4 impedance magnitude vs frequency.

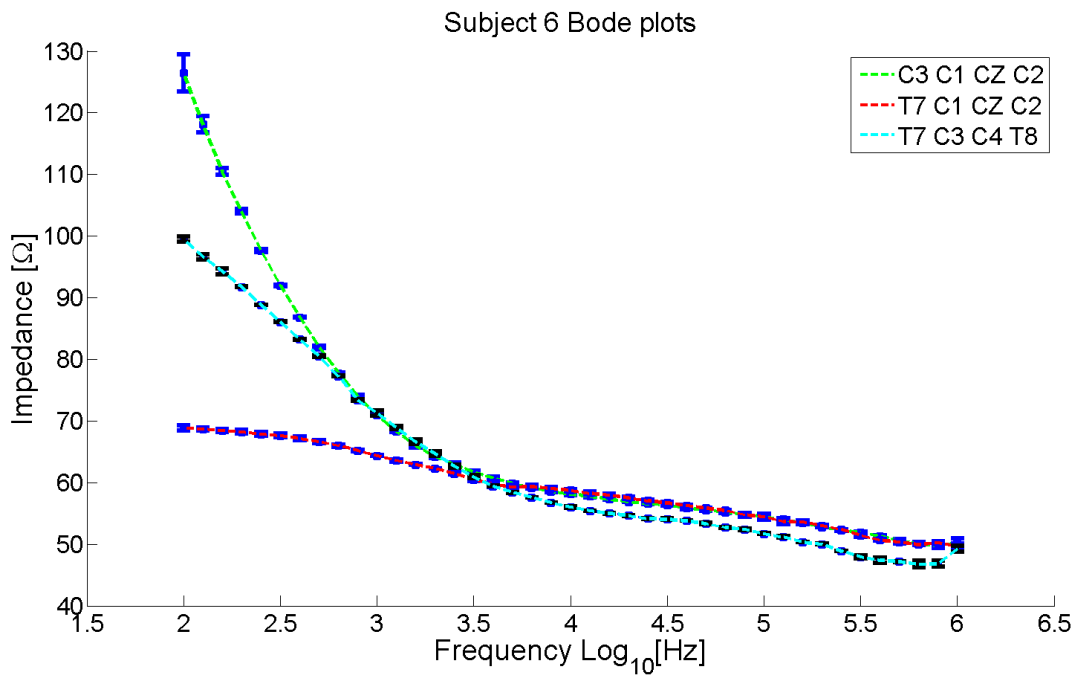
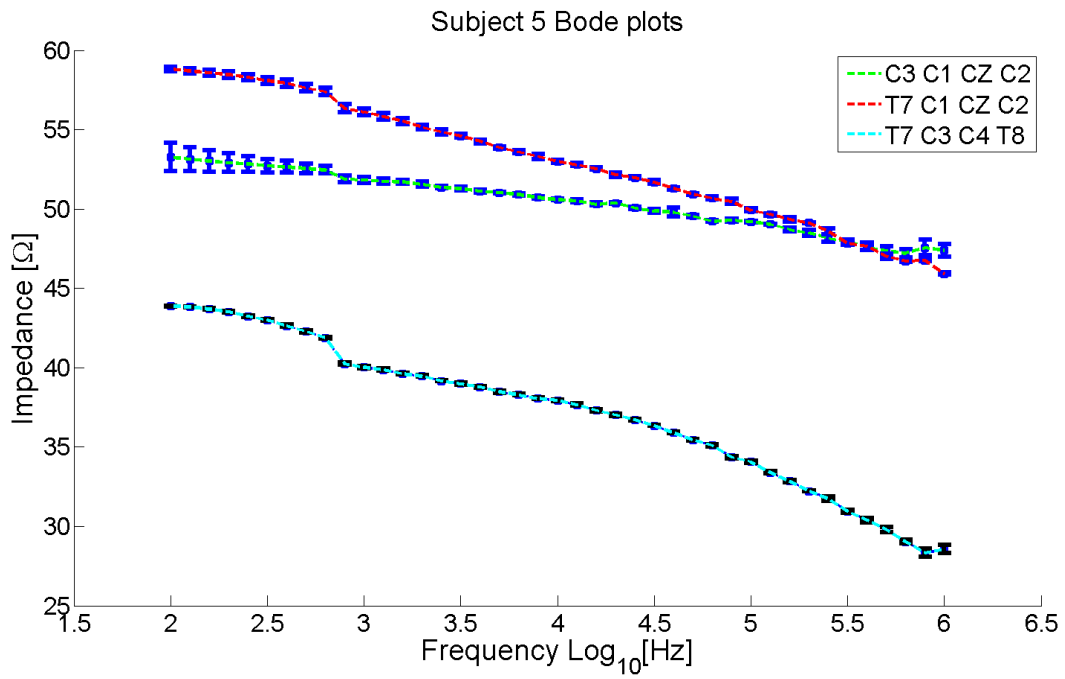


Figure 9.5: Subject 5 and 6 impedance magnitude vs frequency.

concave shape.

Fig. 9.5 b shows a distinct pattern whereby the impedance measurements of the electrode montages converge rapidly in the low frequency range. Here C3 C1 CZ C2 and T7 C3 C4 T8 converge together. T7 C1 CZ C2 intercepts the other 2 graphs at around 3 Khz and continues descending in a roughly linear manner.

Finally in Fig 9.6 T7 C3 C4 T8 is shown to be a relatively noisy measurement compared to the other electrode positions measured.

Fig 9.6 a. shows that T7 C3 C4 T8 follows a distinct convex shape at a much higher impedance than the other 2 impedance sets. In Fig 9.6 b. T7 C3 C4 T8 intercepts C3 C1 CZ C2 and T7 C1 CZ C2 and continues lower in a roughly linear path.

9.5.1.2 Discussion

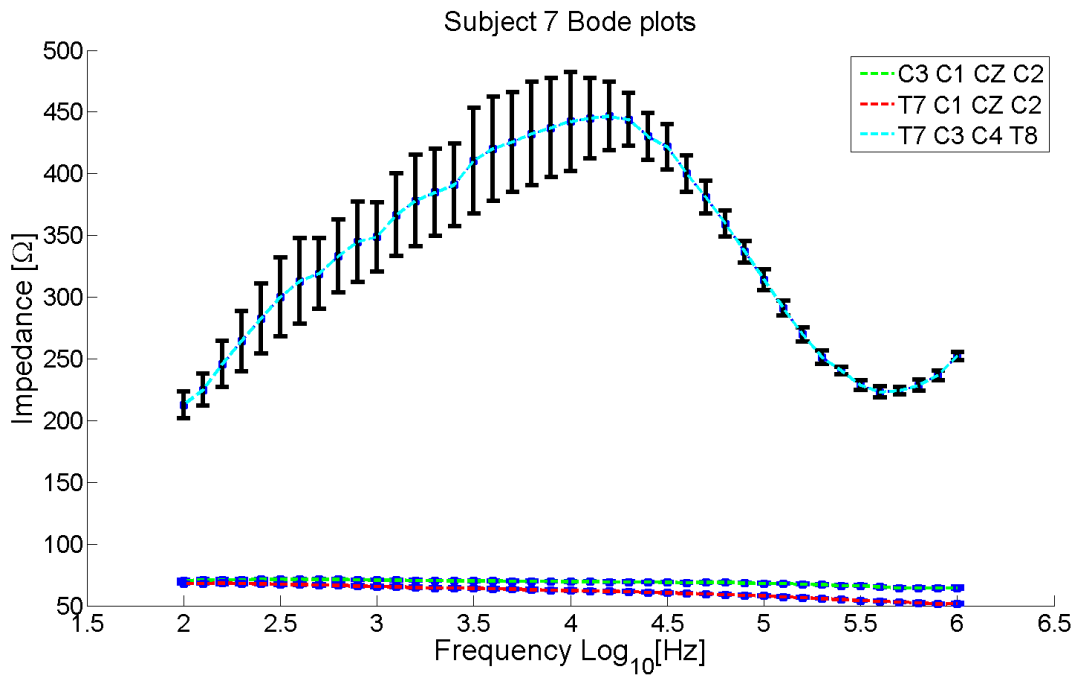
After our preliminary analysis of the results, it is apparent that there are features of the impedance plots that seem to repeat themselves across subjects -i.e. recurring patterns. On the other hand it is also clear that there is a great deal of variability between subjects.

We note the following observations concerning the following topics:

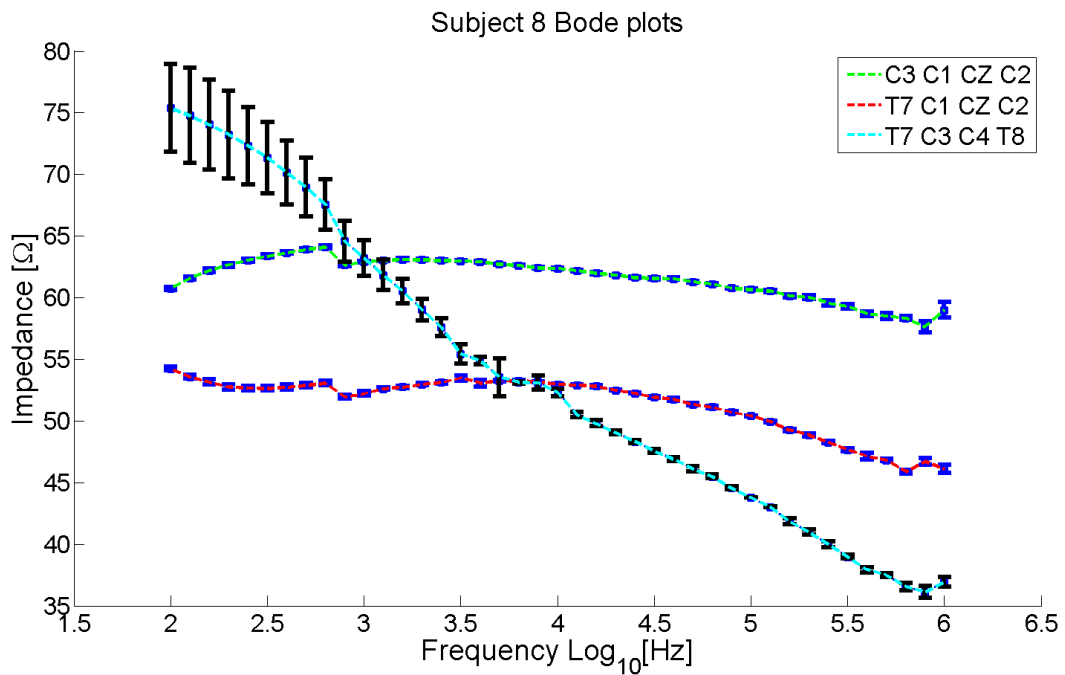
- Error level

In general error from paired or repeating measurements is very low as shown by the magnitude of the error bars relative to the measurement values. In some cases however paired measurements showed a relatively high error. We see this for instance in Fig 9.3 b for the T7 C1 CZ C2 impedance up to 1 Khz, in Fig 9.4 b for C3 C1 CZ C2, and in Fig. 9.6 a. and b. for T7 C3 C4 T8.

The tetrapolar electrode configuration is designed to avoid contact impedance. One common source of error [242] would be excessively high skin impedance especially at the voltage-skin electrode coupling site. Another cause of error is unequal voltage



(a) Scalp



(b)

Figure 9.6: Subject 7 and 8 impedance magnitude vs frequency.

electrode size or impedance mismatch at the measurement points [243]. The difficulty in ensuring standard, equal low impedance at the low voltage sites may be a significant cause of error and noise between the normal variability between subjects.

As discussed in section 9.3.2, we added saline drops to electrode sites. While this may have caused an overall reduction in impedance, this may also have contributed to measurement error by potentially generating a shunt path between closely spaced electrodes as well as introducing variability in skin impedance not related to the measurement.

- Outliers

All impedance measurements were in a band of 100 to 30 Ω with the exception of the results shown in Fig. 9.6 a. for T7 C3 C4 T8 measurement of subject 7 which appears to be an outlier with a maximum impedance magnitude of ≈ 450 .

- Patterns

Despite the variability of these data sets we attempt to show features of that are common between subjects. In general C1 C3 CZ C2 and T7 C3 CZ C2 show a similar pattern with impedance dropping as a function of frequency. T7 C3 C4 T8 is usually at a noticeable offset (lower impedance) from the other measurements. It also can be noted that generally T7 C3 C4 T8 drops in impedance at a greater rate as a function of frequency than the other data sets. This indicates a distinct pattern in phase which is dependent on the electrode configuration.

We also note that in some instances, impedance can be shown to rise as frequency of the measurement is increased. This effect can be seen in the slight concave shapes of impedance curves T7 C3 C4 T8 in Fig. 9.3 a., C3 C1 CZ C2 and T7 C3 C4 T8 in Fig. 9.3 b. and C3 C1 CZ C2 in Fig. 9.4 a. In addition, many of the impedance curves can be seen to rise at end of the spectrum sweep -i.e. over 500 Khz.

This effect can be most clearly seen as a large climbing "hill" at the low end of the impedance frequency spectrum, rising towards a maximum and then descending as a function of increasing frequency. This shape can be seen in T7 C3 C4 T8 graphs in Fig. 9.4 b. and in Fig. 9.6 a.

As discussed previously in section 4.8.3, impedance is related to the concept of sensitivity. Our FEM model showed that a tetrapolar measurement consists of negative sensitivity zones due to cancellation effects of the leads. This translates into an increase of impedance as a function of frequency as well as inverted Cole elements especially in the low frequency dispersion bands (for example see scalp Nyquist plots for tetrapolar montages in Fig. 8.21). We therefore posit that the rise in impedance as a function of increasing frequency is related to changes in the negative sensitivity zones as a function of frequency. As frequency is increased the negative sensitivity field decreases with the net result that the measured impedance increases.

A comparison of FEM results with the experimental data in chapter 10 will demonstrate in greater detail the relationship between the trend of impedance plots and changes in the negative sensitivity zone.

9.5.1.3 Cole Plots and Parameters

In this section, we provide the results of Cole parameter extraction both for each subject. We show the fitted plots for the experimental impedance measurements. Mean Cole parameters of four measurements are provided in bar charts. As described in section 8.2.2.2, significance level is indicated by the number of stars; i.e. * represents $p \leq 0.05$, ** represents $p \leq .01$ and *** represents $p \leq .001$. Results are assumed to be significant at $p \leq 0.05$.

Fig. 9.7 shows the Nyquist (bottom left), fitted plots and location of some Cole parameters. Results are shown for subject across the tetrapolar montages. Data points are shown as blue stars. We fit the data to 2 Cole systems. The fit to the low frequency α

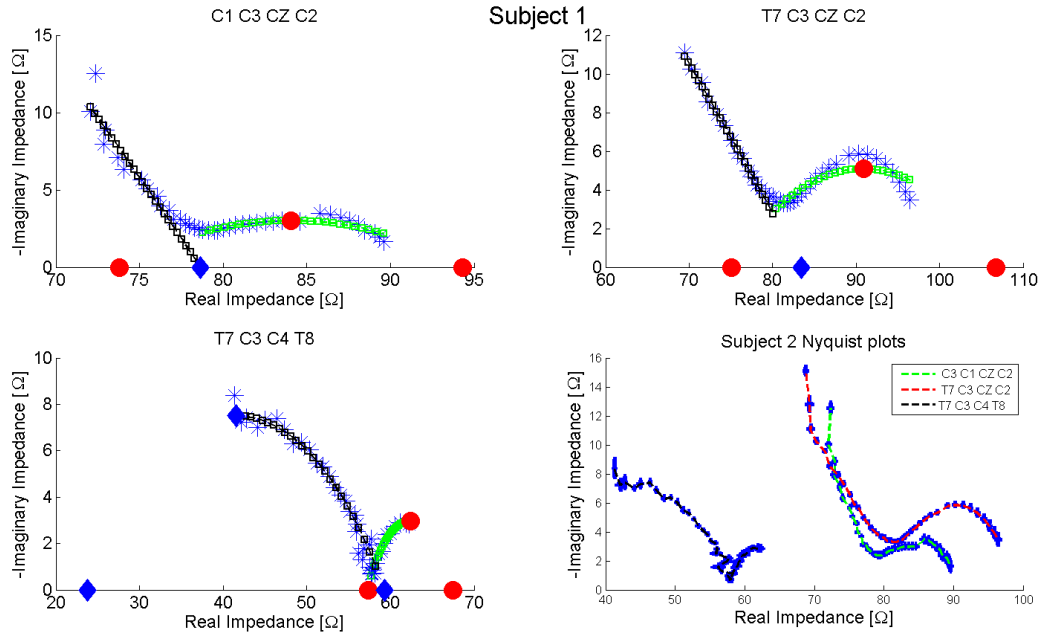


Figure 9.7: Nyquist plots shown of electrode montages. Cole parameter location of R_0, F_c and R_∞ , shown in the α (red circles) and β range (blue diamonds).

dispersion is shown in green. R_0, f_c and R_∞ of the α dispersion is shown from right to left as red dots. The fit to the β dispersion is shown in black. The location of R_0 (and for the montage T7-C3-C4-T 8 f_c and R_∞) is shown as a blue marker.

We see here a large difference in the shape of the spectra of C3-C1-CZ-C2 and T7-C3-CZ-C1 and the impedance of T7-C3-C4-T8. The α dispersions of the first 2 montages are much wider along the real axis than that of T7-C3-C4-T8. In addition the β dispersion of C3-C1-CZ-C2 and T7-C3-CZ-C1 show almost a linear climb as if only part of the Cole semi-circle is within range (hence the need for the modified fitting algorithm as described in section 9.4.0.1) On the other hand the β of T7-C3-C4-T8 is more well rounded and shows the peak of a semi-circle, this allows easier extraction of Cole parameters.

Figs.9.8 and 9.9 shows a comparison between the subject 1 Cole parameters for the α and β dispersions.

We note the following trends.

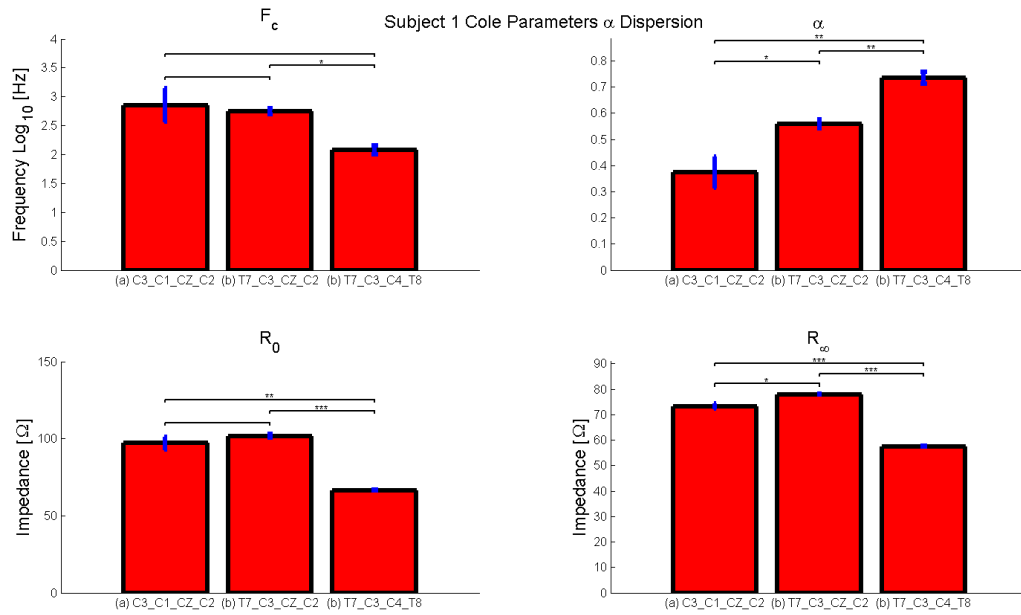


Figure 9.8: Bar graphs showing mean Cole parameters of 4 electrode configuration measurements obtained from subject 1. Comparisons between mean values is made with a paired t test. Significance level is shown by number of stars.

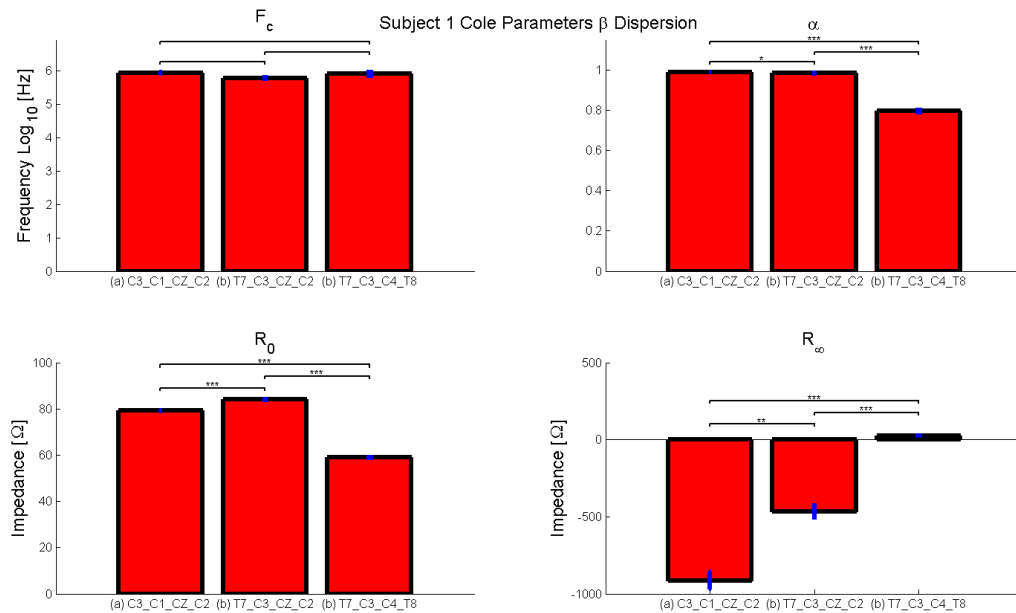


Figure 9.9: Bar graphs showing mean Cole parameters of 4 electrode configuration measurements obtained from subject 1. Comparisons between mean values is made with a paired t test. Significance level is shown by number of stars.

For the α dispersion:

- f_c trends downwards (from left to right) and there is a significant difference ($p = < .05$) between T7-C3-CZ-C2 and T7-C3-C4-T8
- α trends upwards and there is a significant difference for this parameter between all the montages
- The only significant difference in R_0 is between the first two montages and T7-C3-C4-T8 whereby R_0 decreases
- R_∞ increases slightly and then decrease (all changes are significant)

For the β dispersion:

- There is no significant difference between f_c
- α decreases (there is a significant differences between parameters)
- R_0 decreases significantly
- R_∞ significantly increases

Fig. 9.10 shows the Cole plots and fitting for subject 2. Here we note the inverted semi-circle at low frequencies for the the C1-C3-CZ-C2 montage. T7-C3-CZ-C2 shows a very different pattern with a very large half semi-circle (large reactance values) for the α dispersion followed by a small semi-c-circle for the β dispersion. T7-C3-C4-T8 shows a different distinct shape with a small α semi-circle and a large half of semi-circle for the β dispersion.

Figs.9.11 and 9.12 shows a comparison between the subject 2 Cole parameters for the α and β dispersions.

We note the following for the α dispersion:

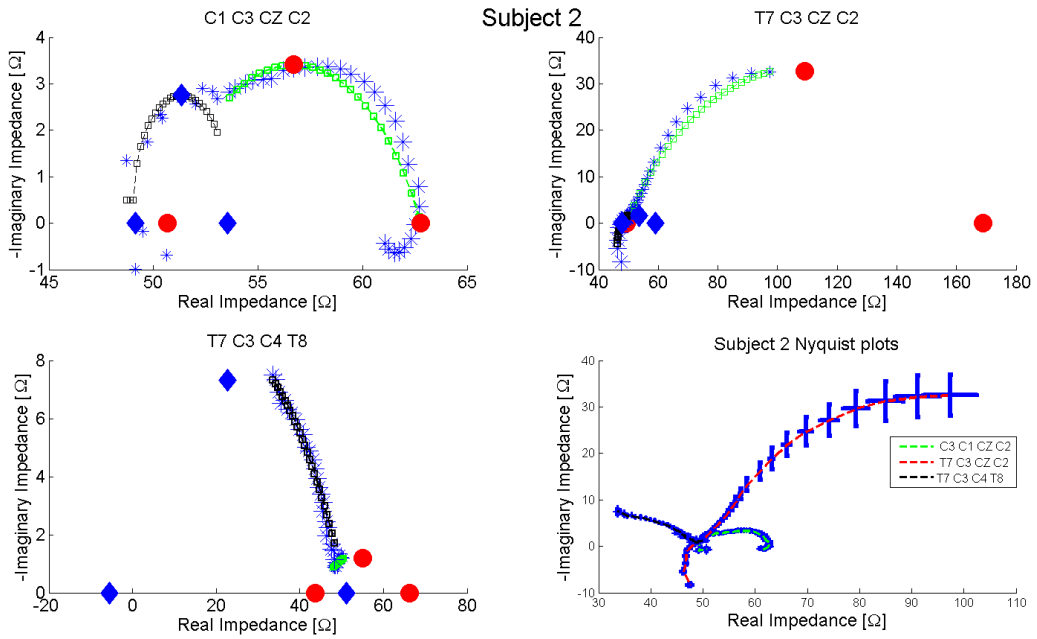


Figure 9.10: Nyquist plots shown of electrode montages. Cole parameter location of R_0, F_c and R_∞ , shown in the α (red circles) and β range (blue diamonds).

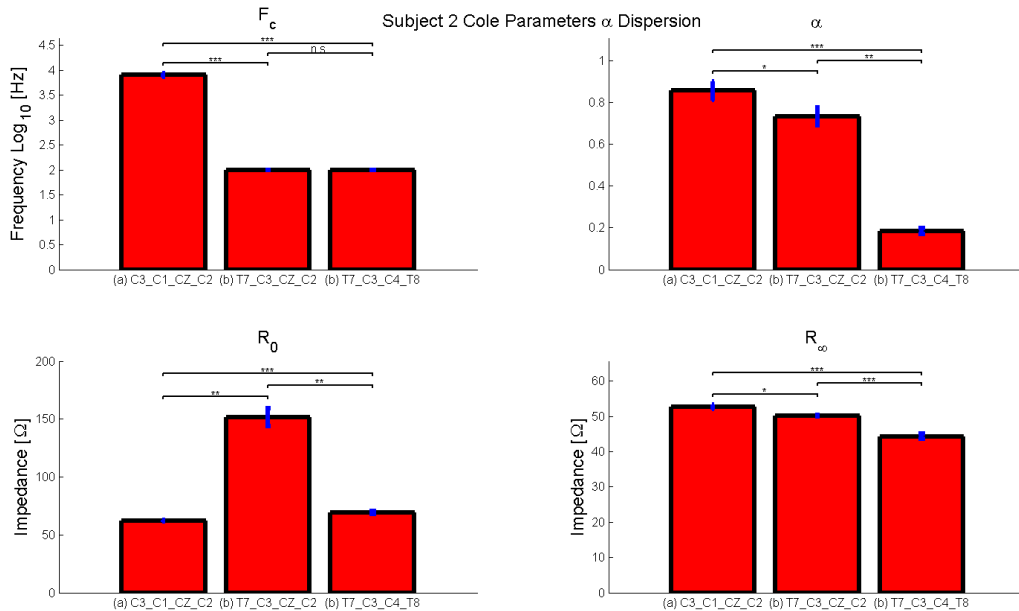


Figure 9.11: Bar graphs showing mean Cole parameters of 4 electrode configuration measurements obtained from subject 2. Comparisons between mean values is made with a paired t test. Significance level is shown by number of stars.

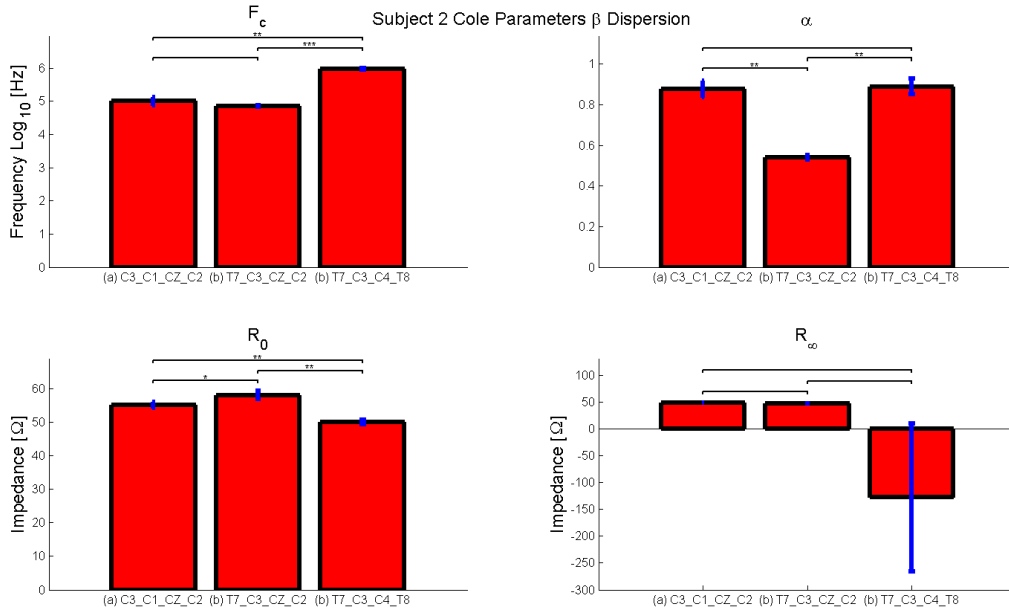


Figure 9.12: Bar graphs showing mean Cole parameters of 4 electrode configuration measurements obtained from subject 2. Comparisons between mean values is made with a paired t test. Significance level is shown by number of stars.

- f_c , α and R_∞ significantly decrease
- R_0 increases from C3-c1-CZ-C2 to T7-C3-CZ-C2 and then decreases for T7-C3-C4-T8 (changes are significant)

The β dispersion has the following features:

- f_c significant increase from the first 2 montage to T7-C3-C4-T8
- α decreases and then increase
- R_0 increase and then decreases
- no changes in R_∞ were significant

Fig. 9.13 shows the Cole plots along with fitted parameters. We can see for the C1-C3-CZ-C2 montage the steep slope of the β dispersion. The α dispersion appears to be

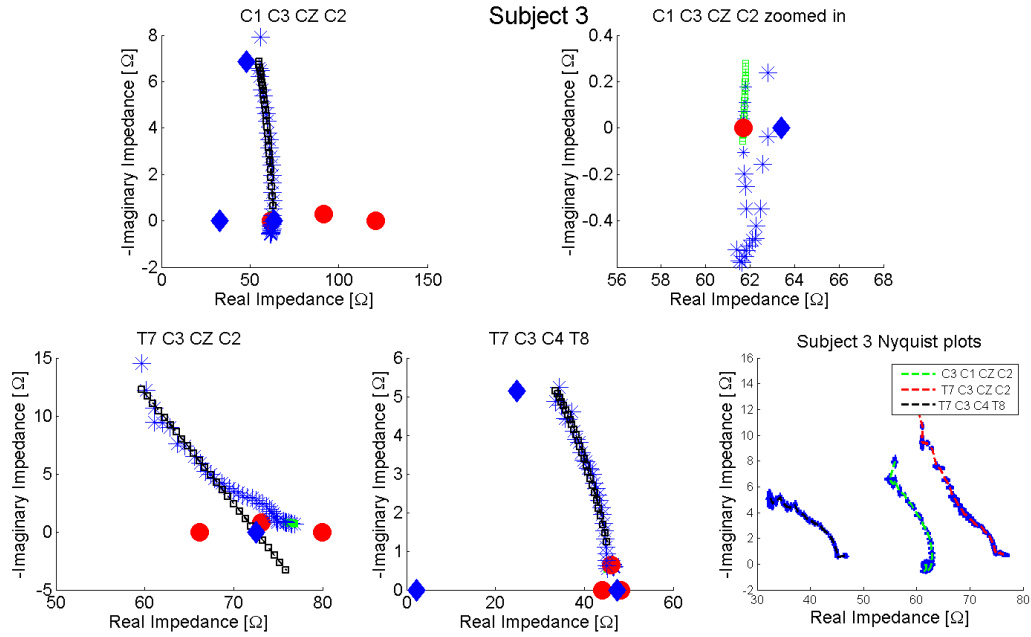


Figure 9.13: Nyquist plots shown of electrode montages. Cole parameter location of R_0, F_c and R_∞ , shown in the α (red circles) and β range (blue diamonds).

largely comprised of an inverted Cole semi-circle (zoomed in plot shown on the top right). The T7-C3-CZ-C2 plot consists of a small α dispersion followed by a large half semi-circle in the β dispersion. Finally the T7-C3-C4-T8 has a small α semi-circle followed by a well defined semi-circle (lower magnitude and smaller curvature radius compared to the other montages).

We can make the following observations for subject 3 Cole parameter comparisons shown in Figs. 9.14 and 9.15.

For α :

- f_c increase significantly (except from C3-C1-CZ-C2 to T7-C3-CZ-C2)
- the mean α value trends downwards although this is not significant
- R_0 trends downwards (not significant from C3-C1-CZ-C2 to T7-C3-CZ-C2)
- the only significant change in R_∞ is a decrease from C3-C1-CZ-C2 to T7-C3-C4-T8

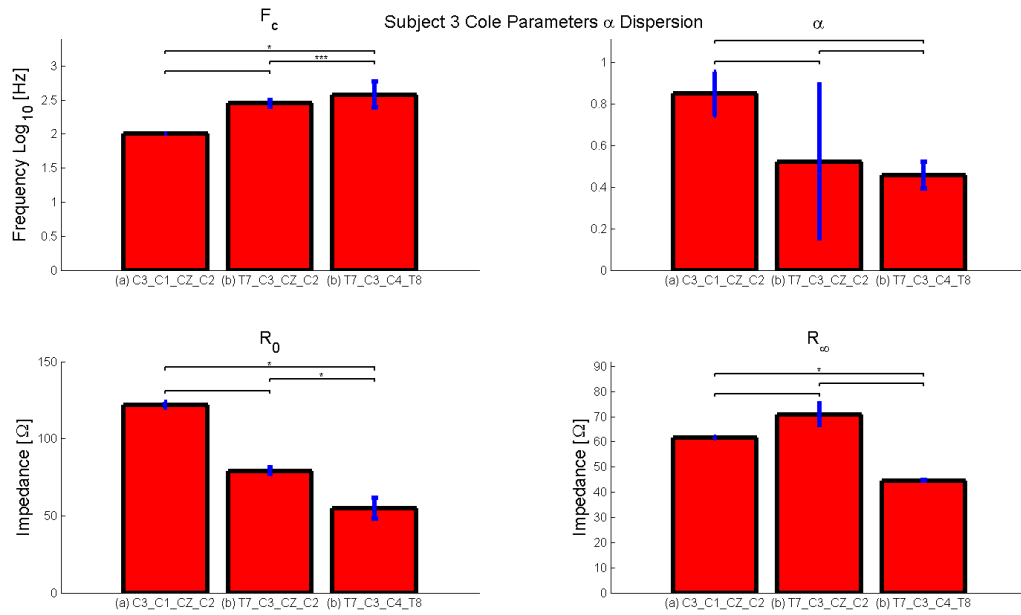


Figure 9.14: Bar graphs showing mean Cole parameters of 4 electrode configuration measurements obtained from subject 3. Comparisons between mean values is made with a paired t test. Significance level is shown by number of stars.

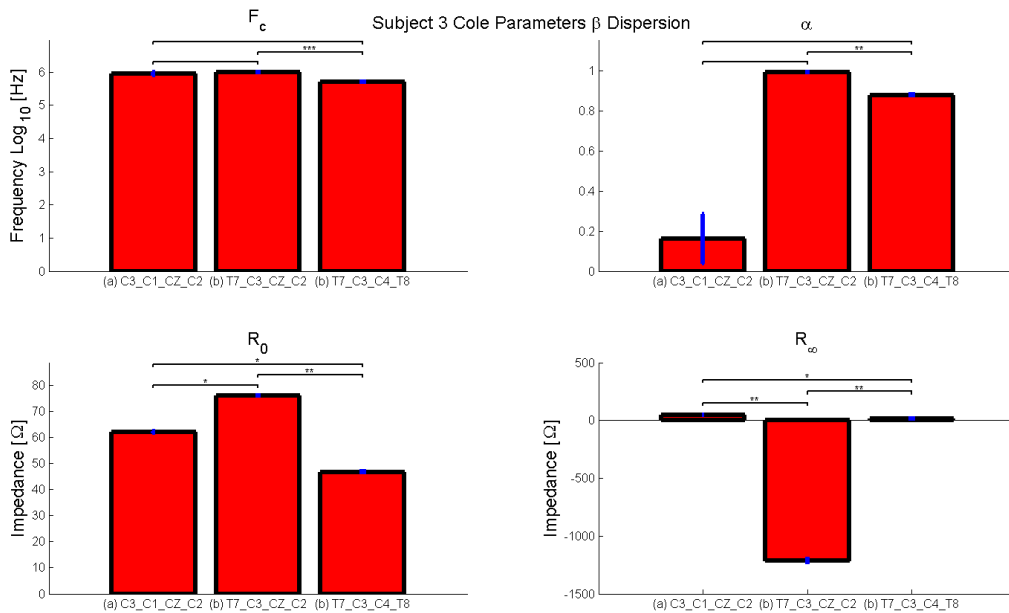


Figure 9.15: Bar graphs showing mean Cole parameters of 4 electrode configuration measurements obtained from subject 3. Comparisons between mean values is made with a paired t test. Significance level is shown by number of stars.

For β :

- f_c and α decreases significantly from T7-C3-CZ-C2 to T7-C3-C4-T8
- R_0 increases from C3-C1-CZ-C2 to T7-C3-CZ-C2 and then decreases (changes are significant)
- R_∞ decreases from C3-C1-CZ-C2 to T7-C3-CZ-C2 and then increases for T7-C3-C4-T8 (changes are significant)

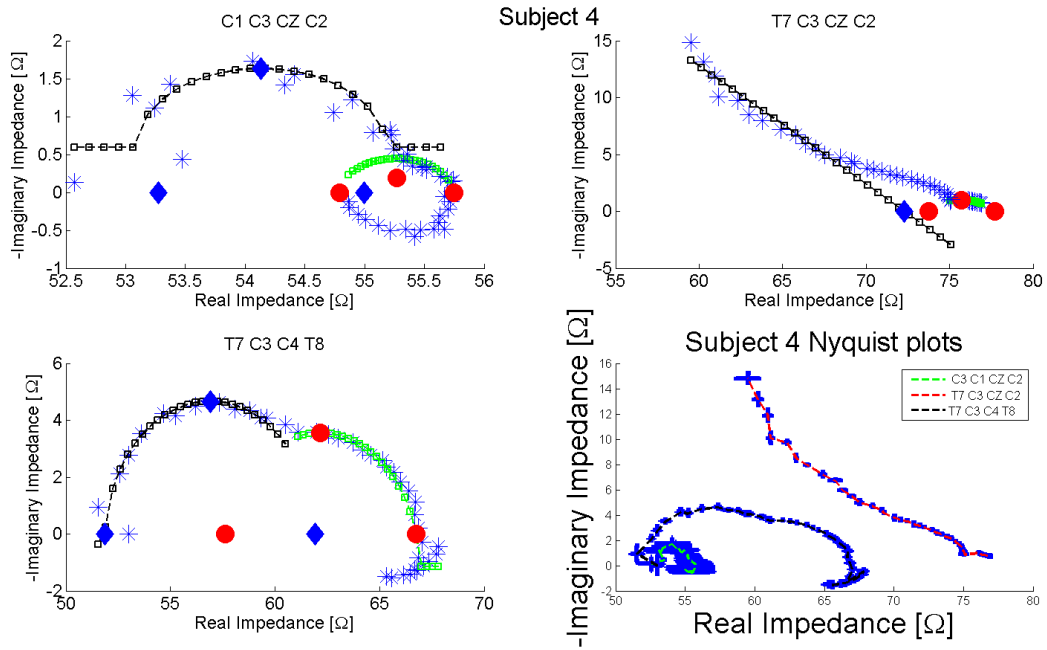


Figure 9.16: Nyquist plots shown of electrode montages. Cole parameter location of R_0, F_c and R_∞ , shown in the α (red circles) and β range (blue diamonds).

Fig. 9.16 shows Cole plots and fitted parameters for subject 4. Here again we note that most of the low frequencies of the α dispersion comprise an inverted semi-circle. The β dispersion covers a very small impedance range of about 2Ω on the real and imaginary axis. T7-C3-CZ-C2 has a small α semi-circle followed by a large rise in the β approximating part of a semi-circle. Finally T7-C3-C4-T8 shows for the α range part of an inverted Cole system followed by another semi-circle. This is followed by another well defined semi-circle in the β range.

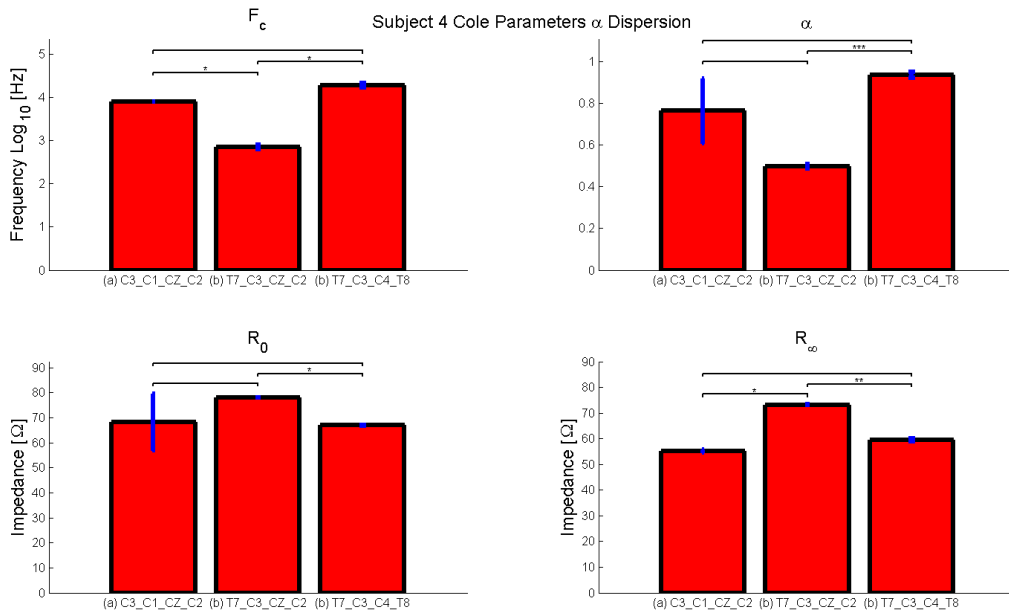


Figure 9.17: Bar graphs showing mean Cole parameters of 4 electrode configuration measurements obtained from subject 4. Comparisons between mean values is made with a paired t test. Significance level is shown by number of stars.

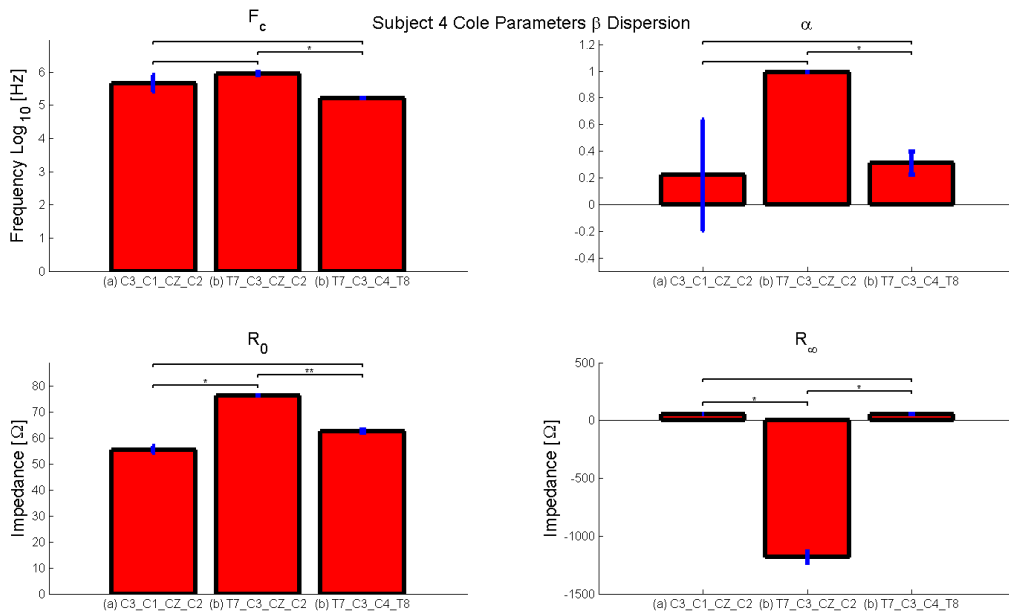


Figure 9.18: Bar graphs showing mean Cole parameters of 4 electrode configuration measurements obtained from subject 4. Comparisons between mean values is made with a paired t test. Significance level is shown by number of stars.

We note the following for Cole parameters in the α and β dispersion as shown in Figs. 9.17 and 9.18:

For α :

- f_c declines and then increases (changes are not significant from C3-CZ-C1-C2 to T7-C3-C4-T8)
- the only significant change in α is an increase from T7-C3-CZ-C2 to T7-C3-C4-T8
- the only significant change in R_0 is a decrease from T7-C3-CZ-C2 to T7-C3-C4-T8
- R_∞ increases from C3-CZ-C1-C2

For β :

- f_c and α decreases significantly from T7-C3-CZ-C2 to T7-C3-C4-T8
- R_0 increases from C3-CZ-C1-C2 to T7-C3-CZ-C2 and then decreases to T7-C3-C4-T8
- R_∞ decreases from C3-CZ-C1-C2 to T7-C3-CZ-C2 and then increases to T7-C3-C4-T8

Fig. 9.19 illustrates Cole plots and fitted parameters of subject 5. Both C1-C3-CZ-C2 and T7-C3-CZ-C2 have similar profiles, a small semi-circle for the α distribution followed by a steep slope representing part of the semi-circle of the β distribution. T7-C3-C4-T8 shows a well defined α circle as well as part of a semi-circle representing the β distribution.

We observe the following for Cole parameters comparisons in Figs. 9.20 and 9.21:

For α :

- f_c tends to increase (but changes are not significant)
- the only significant change in α is an increase from T7-C3-CZ-C2 to T7-C3-C4-T8

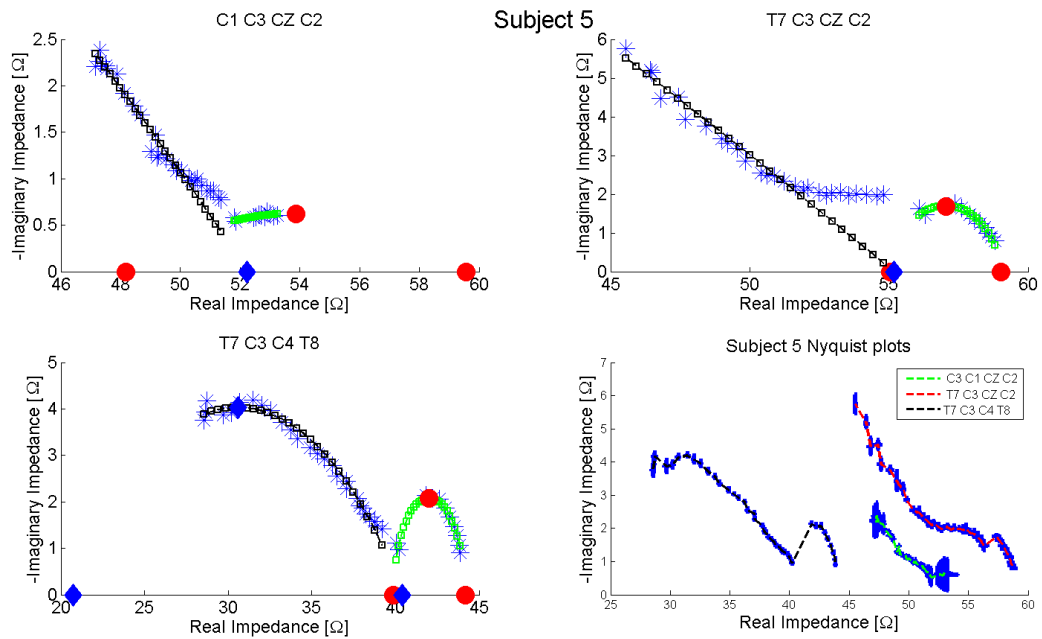


Figure 9.19: Nyquist plots shown of electrode montages. Cole parameter location of R_0, F_c and R_∞ , shown in the α (red circles) and β range (blue diamonds).

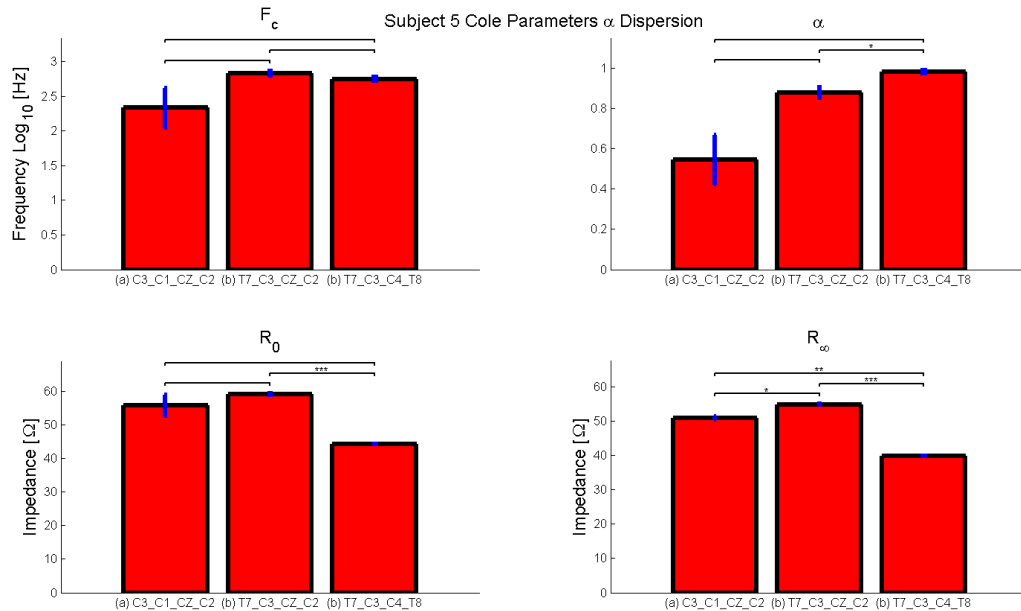


Figure 9.20: Bar graphs showing mean Cole parameters of 4 electrode configuration measurements obtained from subject 5. Comparisons between mean values is made with a paired t test. Significance level is shown by number of stars.

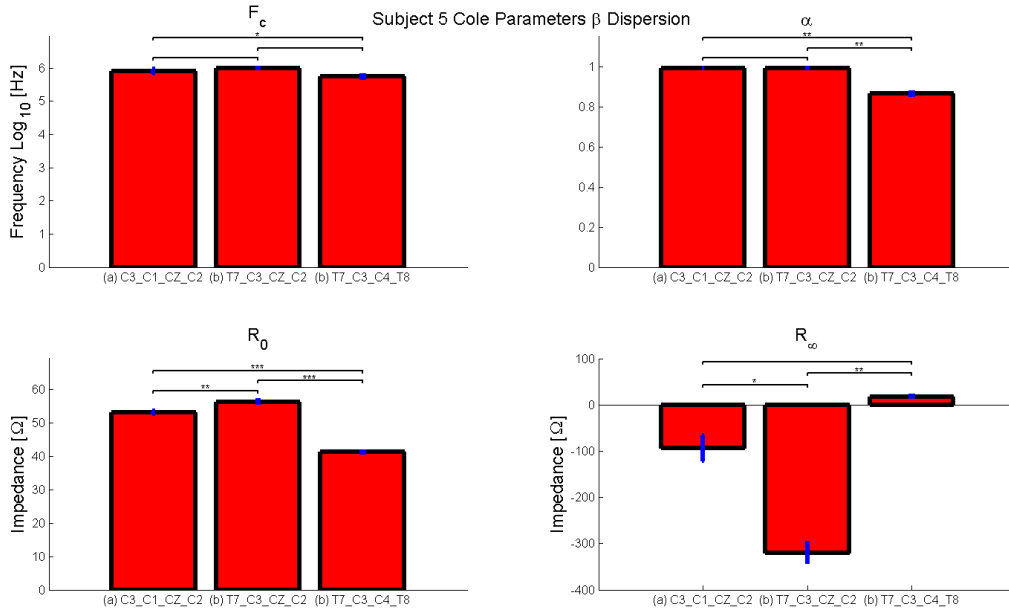


Figure 9.21: Bar graphs showing mean Cole parameters of 4 electrode configuration measurements obtained from subject 5. Comparisons between mean values is made with a paired t test. Significance level is shown by number of stars.

- the only significant change in R_0 is a decrease from T7-C3-CZ-C2 to T7-C3-C4-T8
- R_∞ increases from C3-CZ-C1-C2 to T7-C3-CZ-C2 and then decreases to T7-C3-C4-T8

For β :

- f_c and α decreases significantly from c3-C1-CZ-C2 and T7-C3-CZ-C2 to T7-C3-C4-T8
- R_0 increases from C3-CZ-C1-C2 to T7-C3-CZ-C2 and then decreases to T7-C3-C4-T8
- R_∞ increases from C3-CZ-C1-C2 to T7-C3-CZ-C2 and then decreases to T7-C3-C4-T8

Fig. 9.22 shows Cole fitted parameters and plots for subject 6. (see Fig. 9.22 for similarities). Here C1-C3-CZ-C2 and T7-C3-C4-T8 have large semi-circles for the α

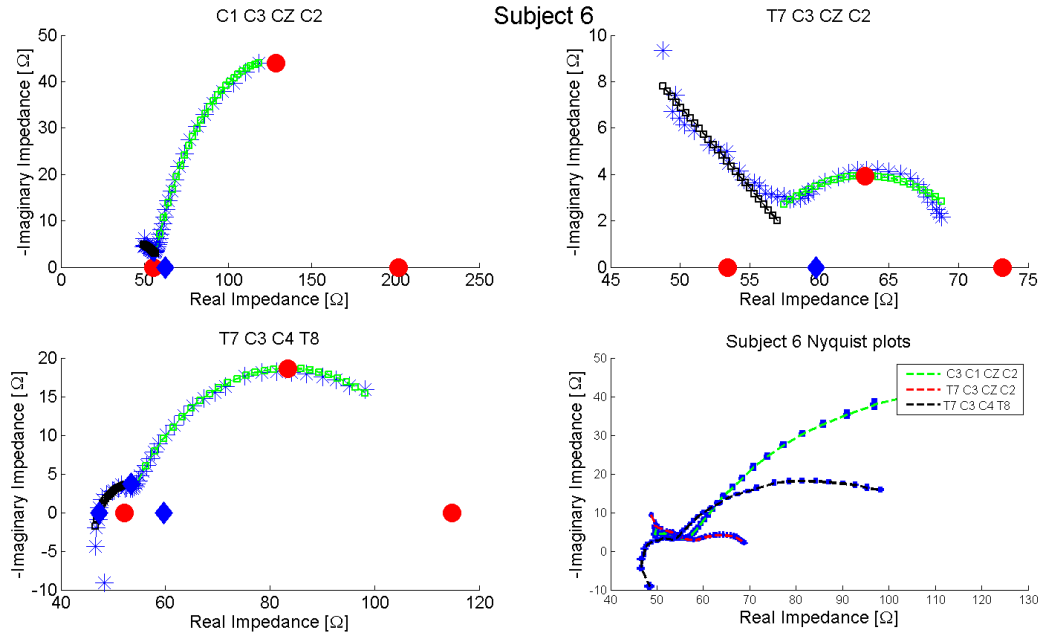


Figure 9.22: Nyquist plots shown of electrode montages. Cole parameter location of R_0 , F_c and R_∞ , shown in the α (red circles) and β range (blue diamonds).

distribution. We see the left end of the Cole semi-circle gradually descends towards the real-axis from C1-C3-CZ-C2 to T7-C3-CZ-C2 until T7-C3-C4-T8.

We note the following for Figs. 9.23 and 9.24.

For α :

- f_c rises and then decreases
- there is no significant change in α
- R_0 decreases from C3-CZ-C1-C2 to T7-C3-CZ-C2 and then increases from T7-C3-CZ-C2 to T7-C3-C4-T8
- R_∞ decreases from C3-CZ-C1-C2 to T7-C3-C4-T8

For β :

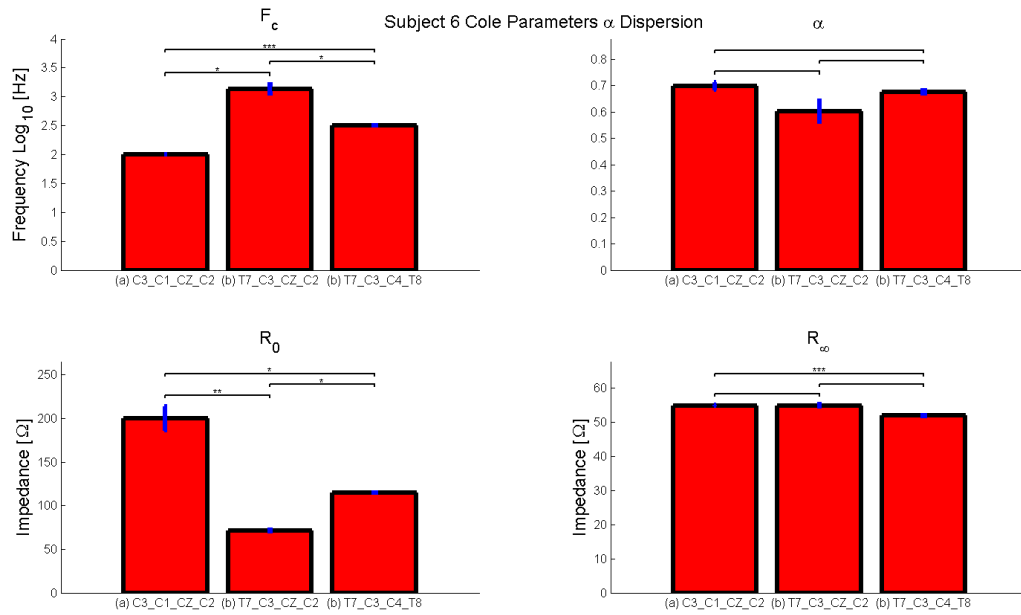


Figure 9.23: Bar graphs showing mean Cole parameters of 4 electrode configuration measurements obtained from subject 6. Comparisons between mean values is made with a paired t test. Significance level is shown by number of stars.

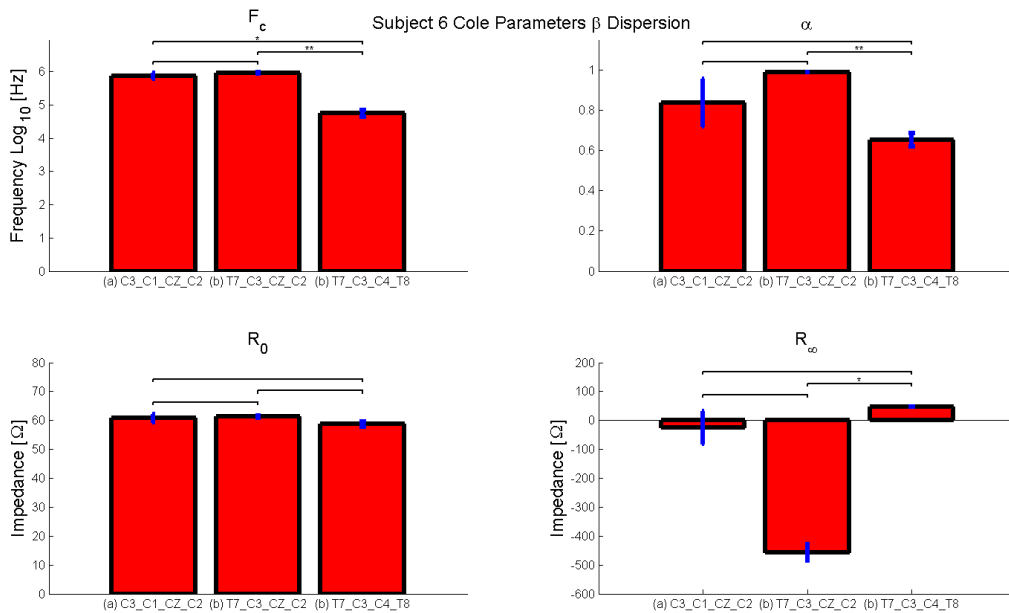


Figure 9.24: Bar graphs showing mean Cole parameters of 4 electrode configuration measurements obtained from subject 6. Comparisons between mean values is made with a paired t test. Significance level is shown by number of stars.

- f_c and α decreases significantly T7-C3-CZ-C2 to T7-C3-C4-T8, f_c also decreases from C3-CZ-C1-C2 to T7-C3-CZ-C2
- There is no significant change see for R_0
- R_∞ increases from T7-C3-CZ-C2 to T7-C3-C4-T8

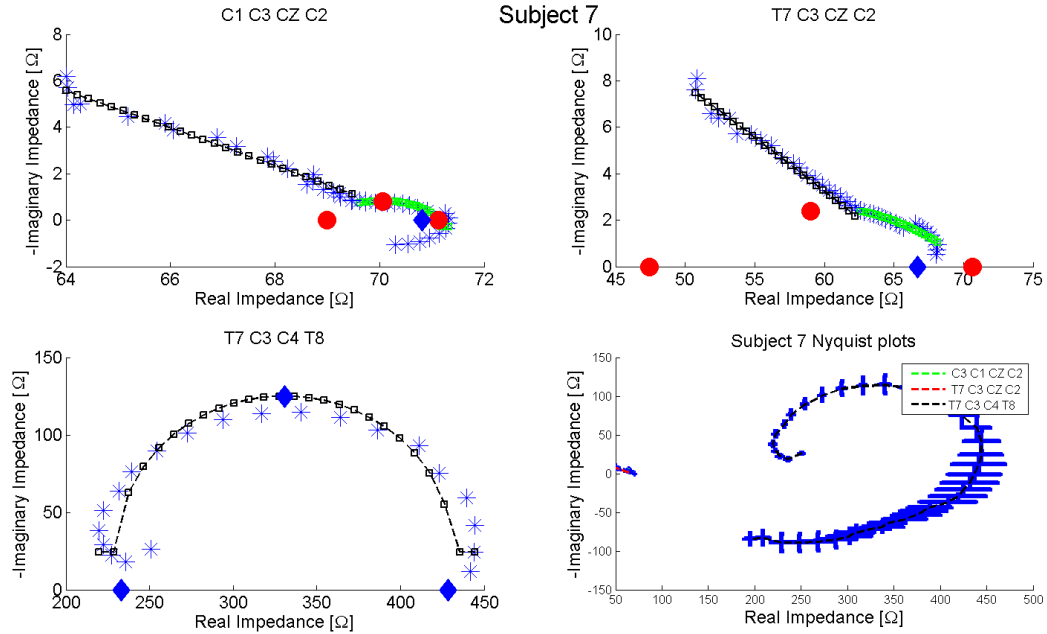


Figure 9.25: Nyquist plots shown of electrode montages. Cole parameter location of R_0 , F_c and R_∞ , shown in the α (red circles) and β range (blue diamonds).

We see in Fig. 9.25 Cole plots and fitted parameters of subject 7. We can see that T7-C3-C4-T8 appears to be an outlier as the magnitude of the plot is much larger than that of the other montages. We see that the low frequency α dispersion part of T7-C3-C4-T8 appears to be comprised of an inverted semi-circle. C3-C1-CZ-C2 and T7-C3-CZ-C2 are have a small α Cole system followed by a steep curve representing part of the β dispersion.

We observe for Figs. 9.26 and 9.27.

For α :

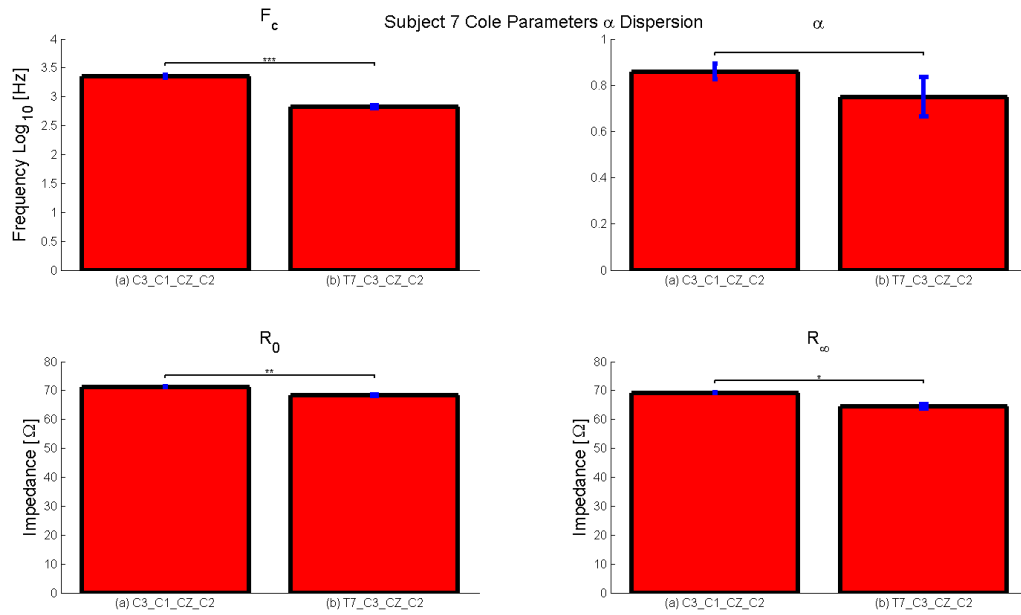


Figure 9.26: Bar graphs showing mean Cole parameters of 4 electrode configuration measurements obtained from subject 7. Comparisons between mean values is made with a paired t test. Significance level is shown by number of stars.

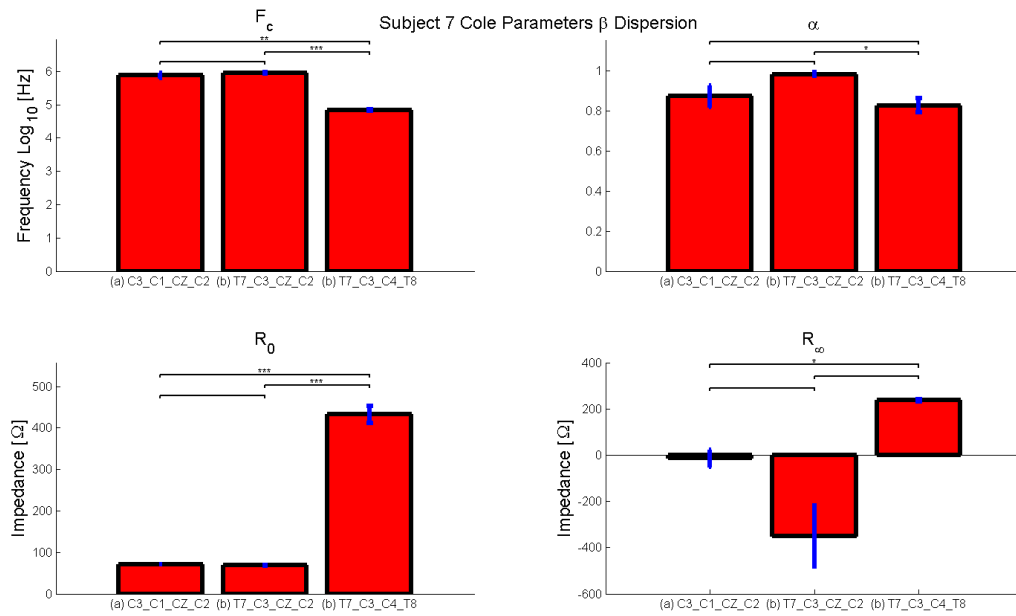


Figure 9.27: Bar graphs showing mean Cole parameters of 4 electrode configuration measurements obtained from subject 7. Comparisons between mean values is made with a paired t test. Significance level is shown by number of stars.

- we have no parameters for T7=C3-C4-T8 as we were unable to extract parameters for this dispersion
- f_c decreases
- there is no significant change in α
- R_0 and R_∞ decreases

For β :

- f_c decreases significantly from C3-CZ-C1-C2 and from T7-C3-CZ-C2 to T7-C3-C4-T8
- α decreases from T7-C3-CZ-C2 to T7-C3-C4-T8
- R_0 increases from C3-CZ-C1-C2 and from T7-C3-CZ-C2 to T7-C3-C4-T8
- R_∞ increases from C3-CZ-C2-C1 to T7-C3-C4-T8

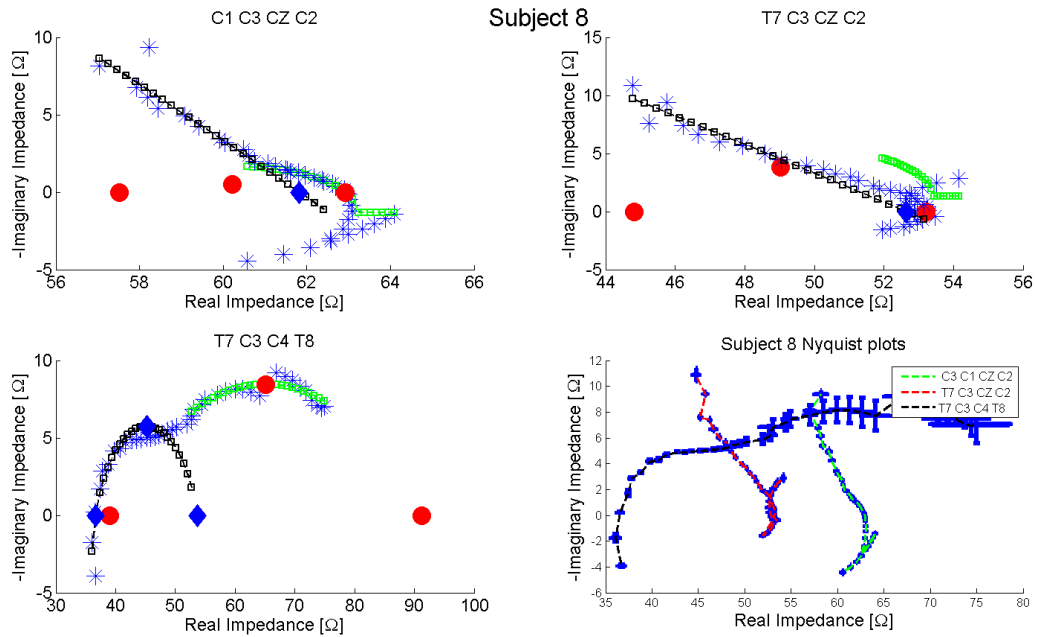


Figure 9.28: Nyquist plots shown of electrode montages. Cole parameter location of R_0 , F_c and R_∞ , shown in the α (red circles) and β range (blue diamonds).

Cole plots and fitted parameters are shown for subject 8 in Fig. 9.28. Both C1-C3-CZ-C2 and T7-C3-CZ-C2 have inverted Cole systems at part of the α dispersion. These montages have a small α Cole system followed by a steep curve representing part of β . T7-C3-C4-T8 has a large α Cole system followed by a well defined semi-circle for the β distribution.

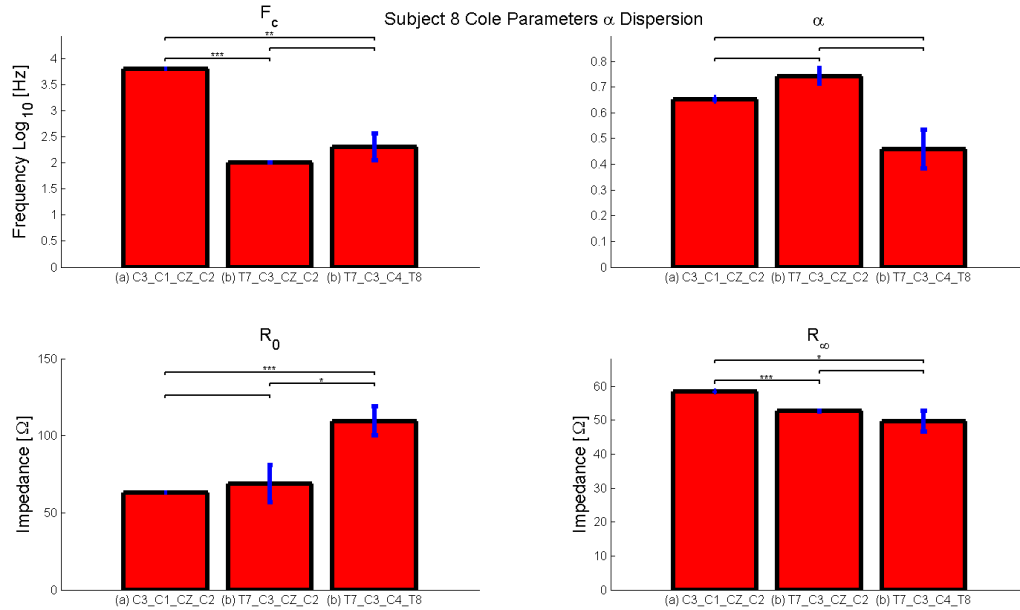


Figure 9.29: Bar graphs showing mean Cole parameters of 4 electrode configuration measurements obtained from subject 8. Comparisons between mean values is made with a paired t test. Significance level is shown by number of stars.

Features of the Cole parameter comparison plots in Figs.9.29 and 9.30 include:

For α :

- f_c decreases and then rise
- there is no significant change in α
- R_0 increases from C3-CZ-C1-C2 to T7-C3-C4-T8 and from from T7-C3-CZ-C2 to T7-C3-C4-T8
- R_∞ decreases from C3-CZ-C1-C2 to T7-C3-CZ-C2 and to T7-C3-C4-T8

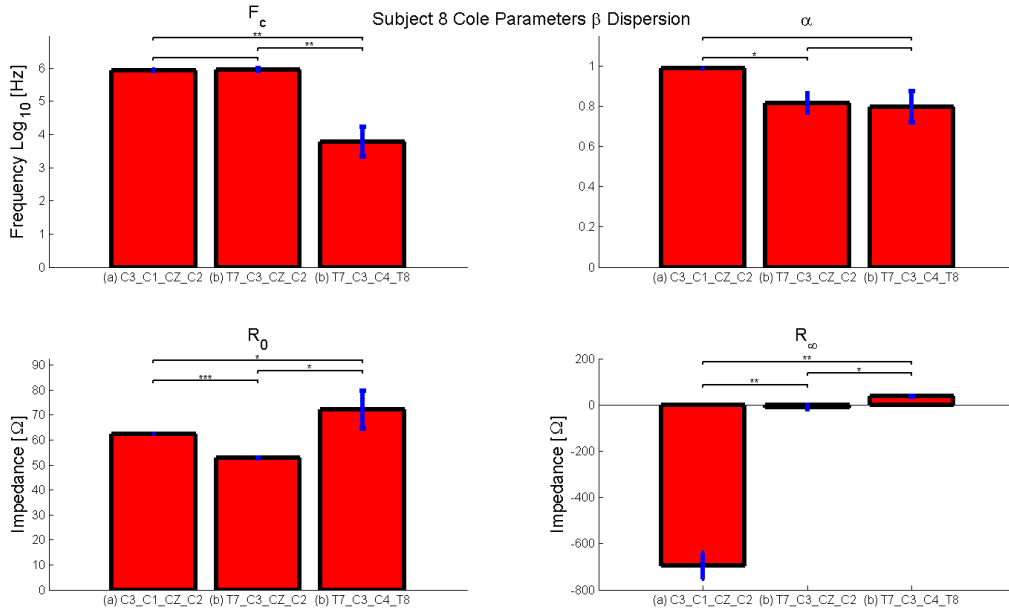


Figure 9.30: Bar graphs showing mean Cole parameters of 4 electrode configuration measurements obtained from subject 8. Comparisons between mean values is made with a paired t test. Significance level is shown by number of stars.

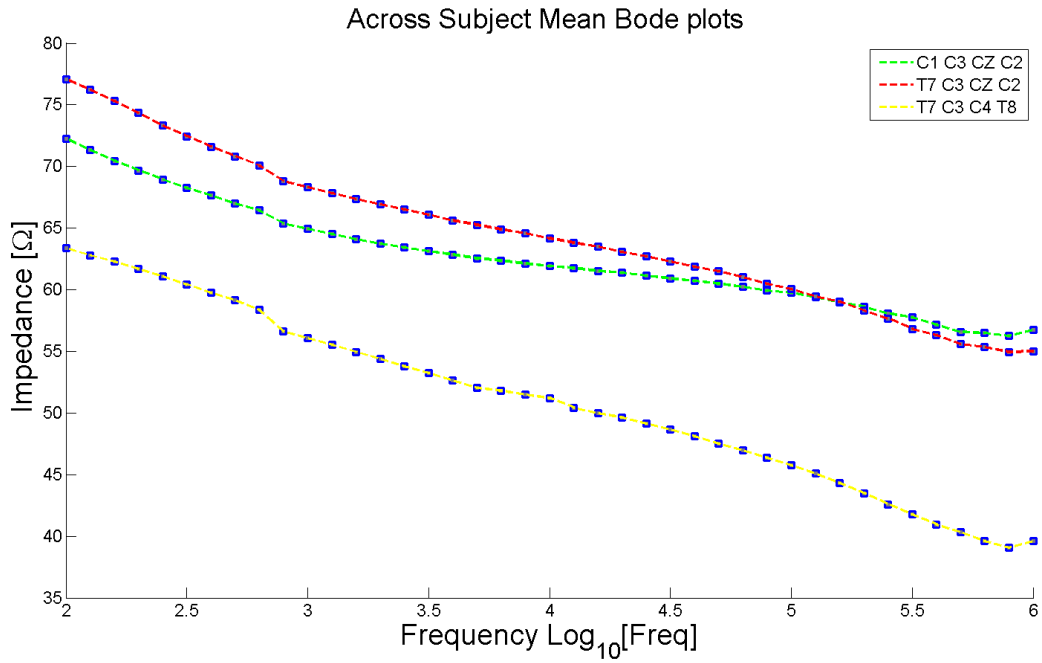
For β :

- f_c decreases from C3-CZ-C1-C2 to T7-C3-CZ-C2 and from T7-C3-CZ-C2 to T7-C3-C4-T8
- α decreases from significantly C3-CZ-C1-C2 to T7-C3-CZ-C2
- R_0 decreases from C3-CZ-C1-C2 to T7-C3-CZ-C2 and increases from T7-C3-CZ-C2 to T7-C3-C4-T8 and from C3-CZ-C1-C2 to T7-C3-C4-T8
- R_{∞} increases

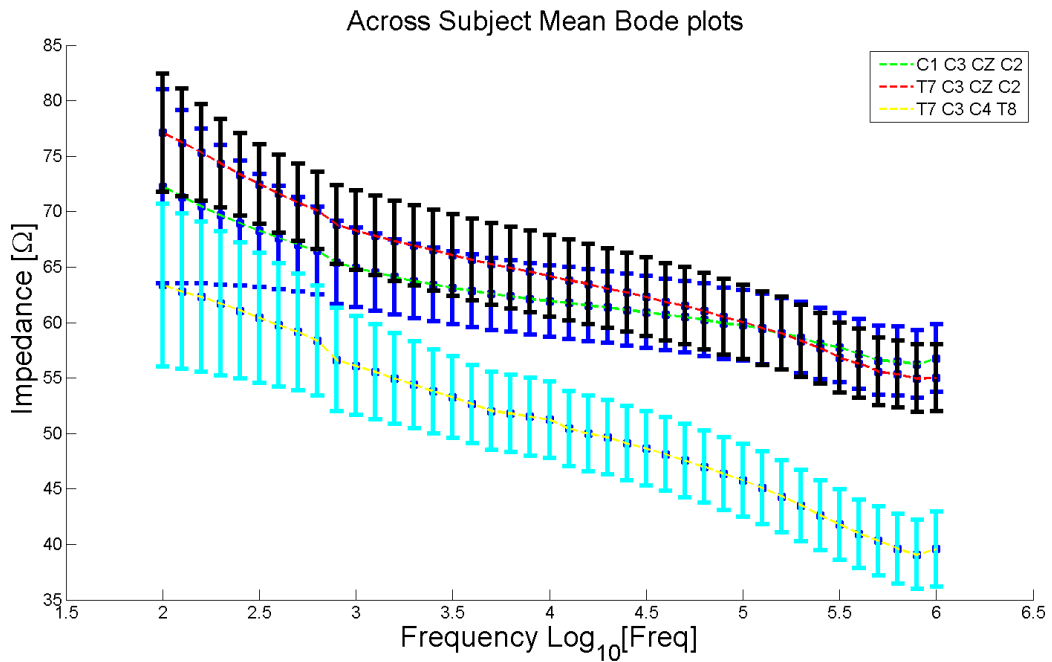
9.5.2 Across Subject Mean

In this section, we present the results of the mean of all the subjects. Error is defined here as the standard error of the mean. In this way we look for trends in impedance and Cole parameters across all subjects.

9.5.2.1 Bode Plots



(a) Mean Bode plot across all subjects with no error bars. Data points are shown as square markers



(b) Mean Bode plot across all subjects with error bars added

Figure 9.31: Across Subject Mean Bode plots shown with and without error bars.

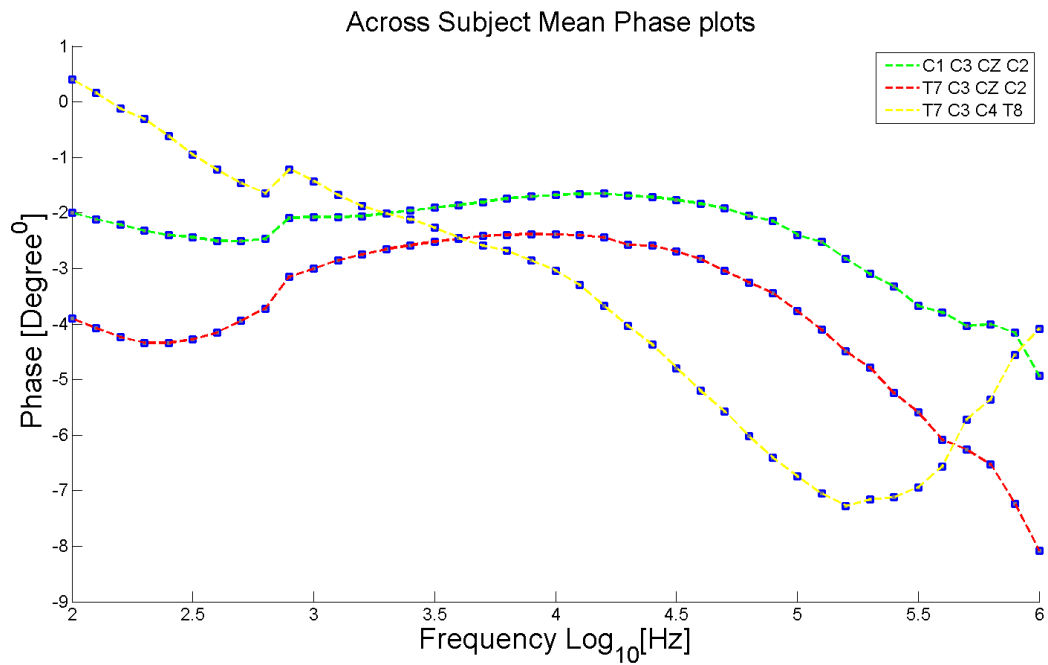
In Figure 9.31 we also show the mean impedance magnitude across all subjects for the 3

electrode measurement configurations (subject 7 is removed from the T7 C3 C4 T8 data set as the measurement appears to be an outlier that would greatly skew the mean values see Fig.9.6). In order to visualize the general track of the impedance curves, we show in Figure 9.31 (a) the mean impedance values of all subjects for each electrode montage without error bars. In Figure 9.31 (b), we add error bars calculated as the standard error of the mean of the data. As can be seen, C1 C3 CZ C2 and T7 C3 CZ C2 closely track a similar path. The overlapping error bars (blue and black) show that across all subjects the 2 measurements appear to be within the error of the measurements. At the level of the individual subject, the graphs show distinct differences between the results of these montages.

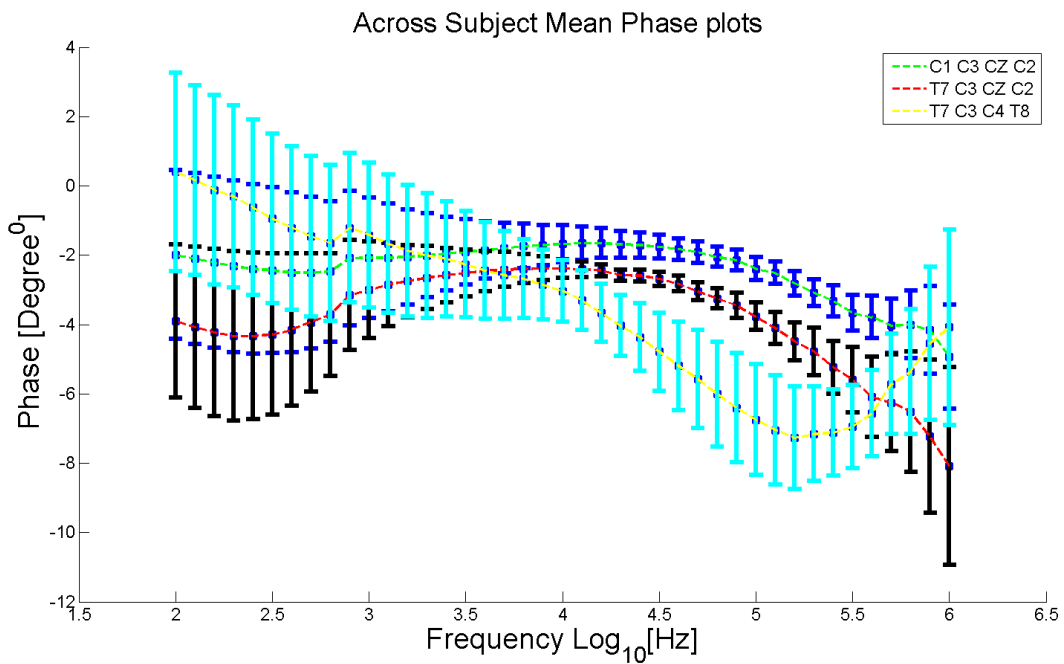
Below 1000 Hz (frequency is given in logarithmic base 10 units) C1 C3 CZ C2 error bars are at their maximum. As frequency is increased, the error bars slowly decrease in a funnel shape. T7 C3 C4 T8 error bars shows a similar shape. This shows that error decreases as frequency rises above 1 Khz. As frequency is increased, C1 C3 CZ C2 and T7 C3 C4 T8 impedance converge towards each other until a crossover point is reached at about 100 Khz; thereafter the two data sets diverge.

Fig. 9.32 a. shows the mean phase plots without errorbars in order to visualize the distinct phase pattern of each electrode configuration. Fig. 9.32 b. shows the mean phase plots with errorbars (standard error of the mean added). We can see that the measurement is largest at the low (>10 Khz) and high (<300 Khz) frequency range of the spectrum. In the frequency band ($10 \text{ Khz} < f < 300 \text{ Khz}$) the 3 spectra show the greatest separation. The phase plots suggest that the electrode montages show greater variability across the different electrode configurations than variability of the same electrode configuration across different subjects.

T7 C3 C4 T8 shows a very distinct pattern whereby impedance drops off more rapidly than impedance curves of other electrode configurations. This drop of impedance is related to the change of phase as a function of frequency. The differences of phase of the electrode configurations can be visualized in Fig. 9.32 a and b. Both the mean phase of C1 C3 CZ



(a) Mean phase plot across all subjects with no error bars



(b) Mean phase plot across all subjects with error bars added

Figure 9.32: Across Subject Mean phase plots shown with and without error bars.

C2 and T7 C3 CZ C2 of all subjects show a similar pattern. Firstly all phase measurements are negative. Phase is approximately concave from 100 Hz until 1 Khz; direction of the phase is then inverted in a convex shape until the end of the frequency range. T7 C3 C4 T8 follows a different pattern. Phase is first positive. As frequency is increased, phase decreases approximately linearly until ~ 10 Khz. After this point phase follows a convex shape reaching a minimum after 100 Khz and then rising until the end of frequency range.

9.5.2.2 Bode Plots Features and Outliers

In section 9.5.1 we presented results for the 8 individual subjects. We showed the high variability between the different impedance spectra pattern and Cole parameters.

We therefore plotted the mean Bode and phase plots across all subjects to determine if there were any patterns emerging from the mean of all the data.

We can note the following:

- Mean Bode plots

We see that the impedance of the 2 montages, C3-C1-CZ-C2 and T7-C3-CZ-C2, track closely together as compared to the very different path of T7-C3-C4-T8.

Although the path of the first 2 montages are not identical, we see (Fig. 9.31 b.) a high overlap of error bars which may imply a difficulty in distinguishing statically significant differences between the 2 spectra. (Indeed we showed that for many Cole parameters there was no statically significant differences between C3-C1-CZ-C2 and T7-C3-CZ-C2 see section 9.5.2.3). On the other hand we see a distinct Bode plot for the 3rd montage, T7-C3-C4-T8, with very little error bar overlap except at low frequencies. In general we also observe that the noise is the highest for all 3 montages at the low frequency end of the spectrum.

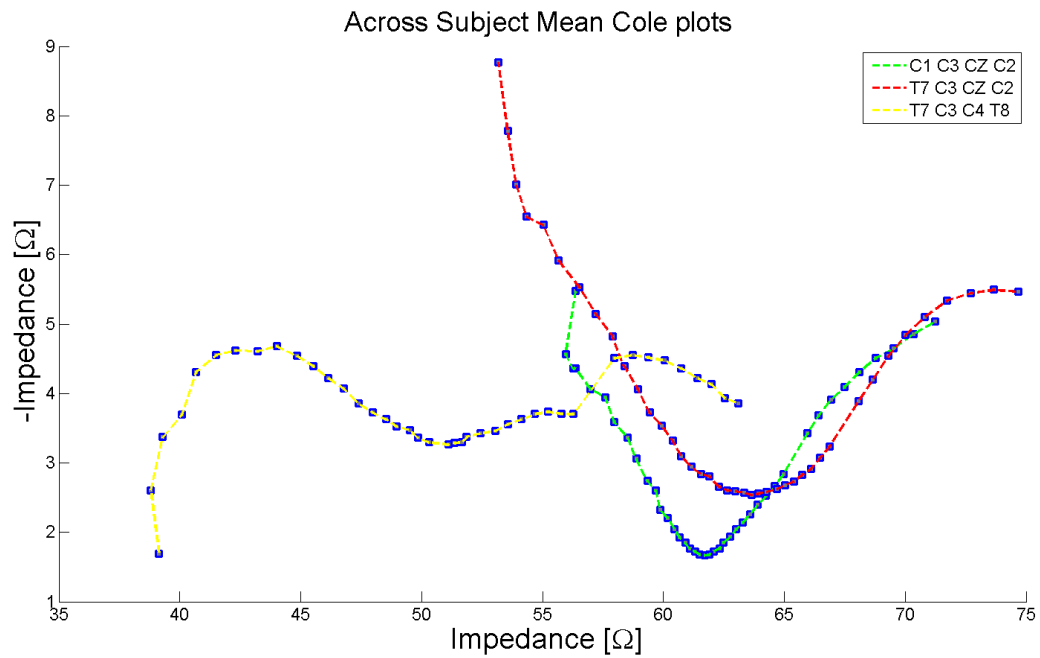
- Mean Phase plots

We see here again that the first two montages (C3-C1-CZ-C2 and T7-C3-CZ-C2) have a similar phase pattern very different from the phase of T7-C3-C4-T8. Common features of the C3-C1-CZ-C2 and T7-C3-CZ-C2 include remaining as a negative phase throughout the frequency range as well as assuming a convex shape from ≈ 1 KHz until 1 MHz (Fig. 9.32). The T7-C3-C4-T8 phase begins as slightly positive and then descends to negative values, the phase follows a concave shape. We can see a frequency band of $\approx 10 - 100$ KHz whereby the greatest separation is achieved between the different phase spectra. As mentioned earlier measurement show the greatest noise (indicated by size of error bars) at low frequencies.

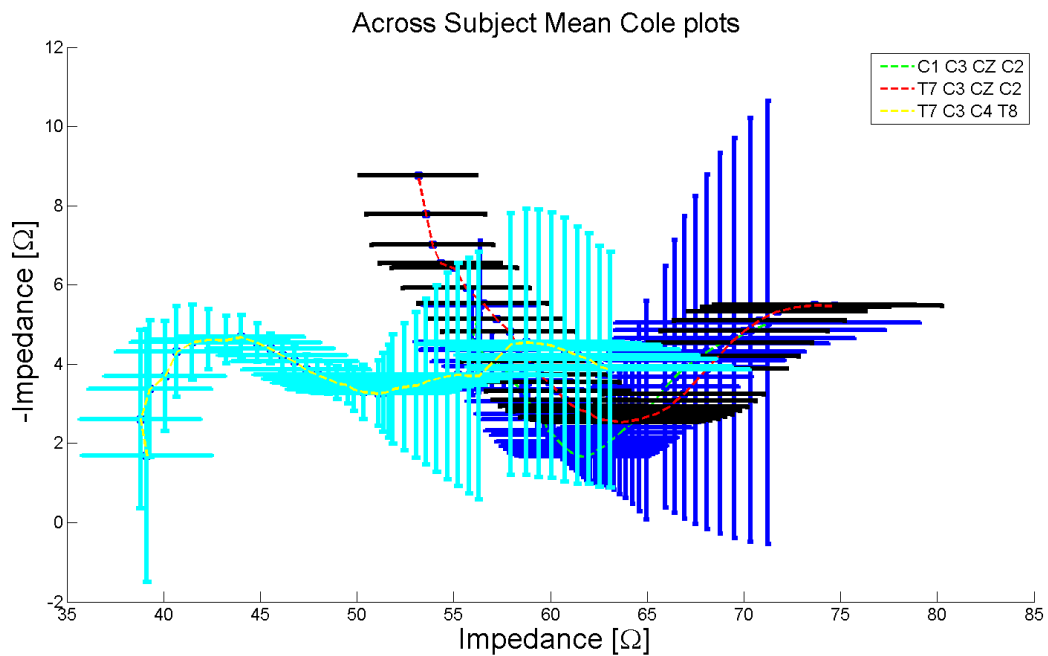
9.5.2.3 Cole Plots and Parameters

In this section we show the results of the mean impedance plotted in a Nyquist or Cole plot. The general shape of the impedance spectra is shown in Fig. 10.4 (a) whereas the inter-subject variability is shown in the form of error bars in Fig. (b). We can see the overall similarity between C3-CZ-C1-C2 and T7-C3-CZ-C2, both spectra show a prominent α semi-circle followed by a steep rise showing part of the β semi-circle. T7-C3-CZ-C2 rises to a higher reactance magnitude and is has a overall higher real impedance than C3-CZ-C1-C2. T7-C3-C4-T8 is shifted significantly to lower values along the real-axis. We can see a semi-circle for the α dispersion followed by a second semi-circle for the β dispersion that descends into negative values (meaning positive phase). We see that the magnitude of the error bars tends to be the largest for the lowest frequencies in the α band. In Figs. 9.34 and 9.35 we show the result of Cole parameter shown in Fig. 10.4. Due to the irregular shapes of the C3-C1-CZ-C2 and T7-C3-CZ-C2 we use the modified Cole fitting approach as described in 9.4.0.1. We use a non-paired t-test to test for statistically significant differences since the parameters here are derived from the mean of different subject measurements (see section 9.4)

We note the following for the α dispersion



(a) Mean Cole plot across all subjects with no error bars



(b) Mean Cole plot across all subjects with error bars added

Figure 9.33: Across Subject Mean Cole plots shown with and without error bars.

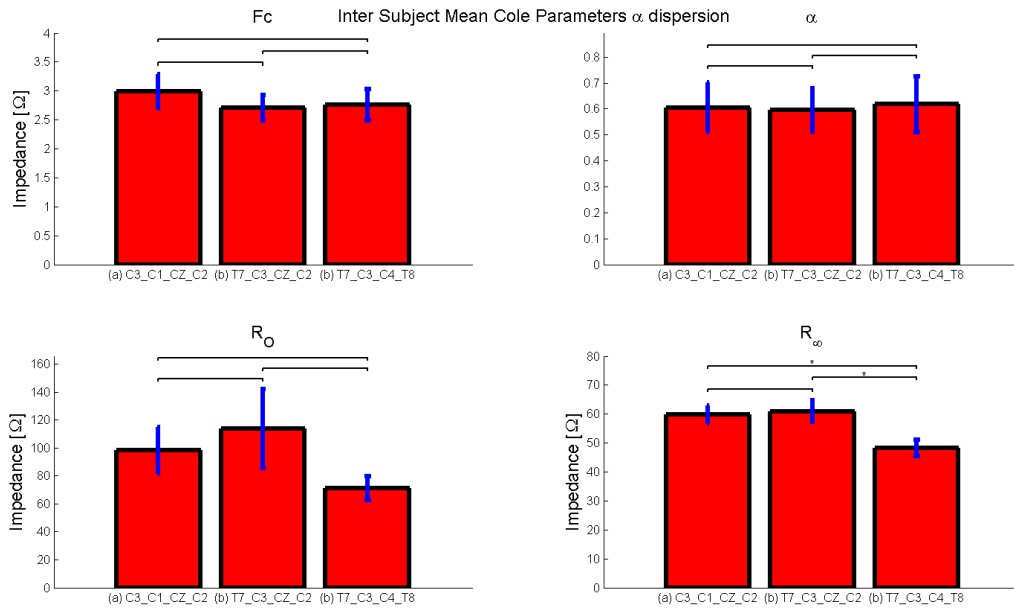


Figure 9.34: Mean across subject α Cole parameter comparison across electrode montages.

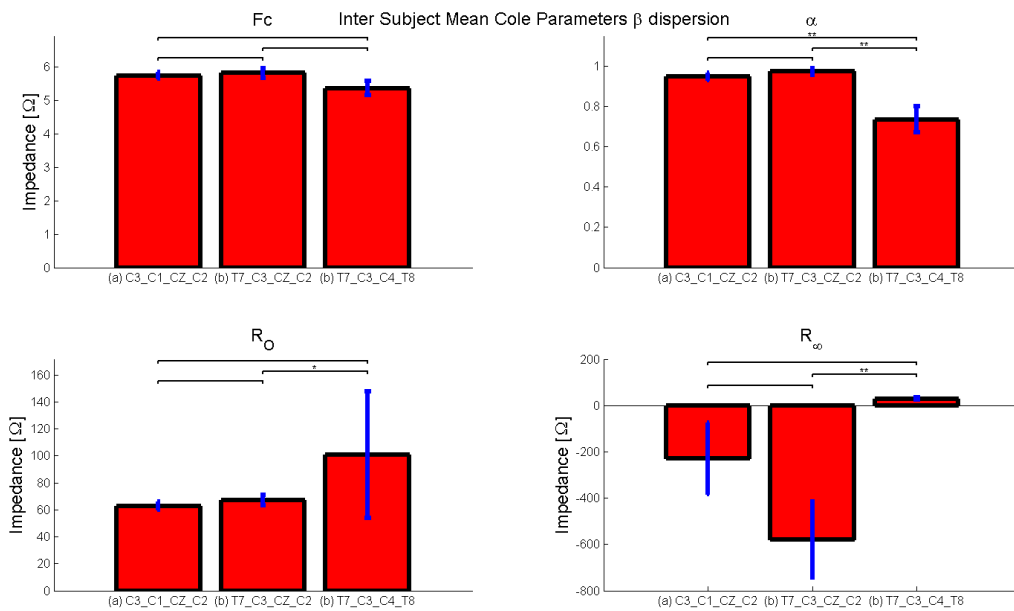


Figure 9.35: Mean across subject β Cole parameter comparison across electrode montages.

- Due to the high error magnitude the only significant difference ($P < .05$) is shown for R_∞ which decreases from C3-C1-CZ-C2 to T7-C3-C4-T8 and from T7-C3-CZ-C2 to T7-C3-C4-T8.
- Non-significant changes include a decrease for f_c , overall stability for α and increase and then decrease for R_0 .

We observe the following for β :

- f_c decreases (non-significantly)
- α decrease significantly from from C3-C1-CZ-C2 to T7-C3-C4-T8 and from T7-C3-CZ-C2 to T7-C3-C4-T8
- R_0 increases significantly from T7-C3-CZ-C2 to T7-C3-C4-T8
- R_∞ increases significantly from T7-C3-CZ-C2 to T7-C3-C4-T8

9.5.2.4 PCA parameters of experimental spectra

We now show results of PCA on impedance spectra pairs where the first montage is used as a reference (pairs are C3-C1-CZ-C2 - T7-C3-CZ-C2, C3-C1-CZ-C2 - T7-C3-C4-T8). See sections 8.2.3 and 8.2.3.1 for some background on PCA as well as the methodology used for our analysis.

Fig. 10.11 shows the loadings (shown as vectors) and the scores of the first 2 principal components of the pair C3-C1-CZ-C2 and T7-C3-CZ-C2. Real results are shown on the left side of the graph and imaginary results on the right. The 2 real scores are shown tightly clustered near the first principal component axis around .4. The imaginary scores are shown more widely dispersed around either side of the negative axis of the first principal component.

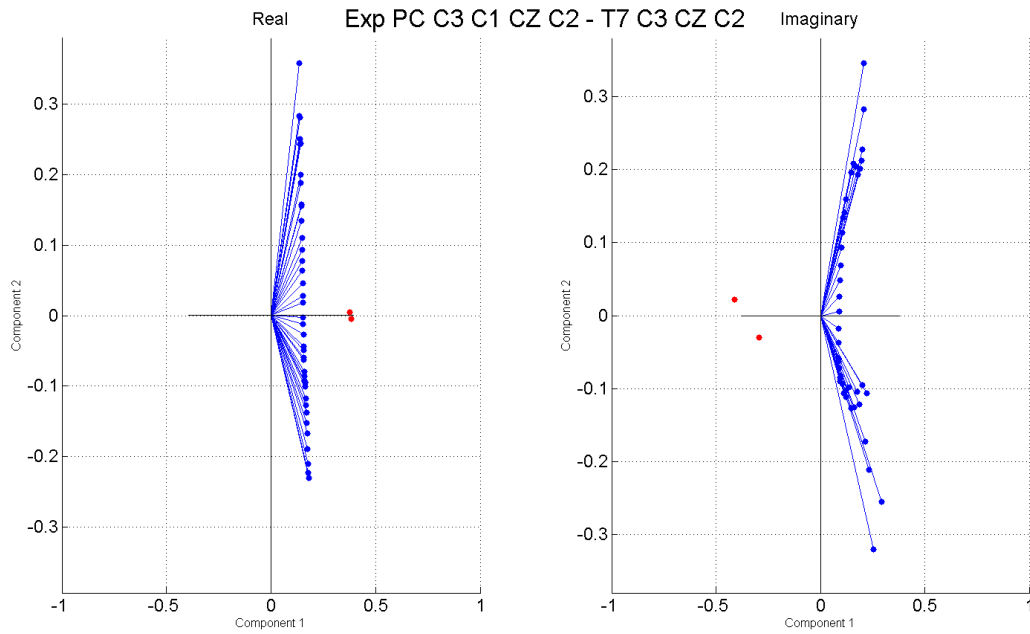


Figure 9.36: Principal components, scores and coefficients shown of real and imaginary components of electrode montages C3-C1-CZ-C2 and T7-C1-CZ-C2

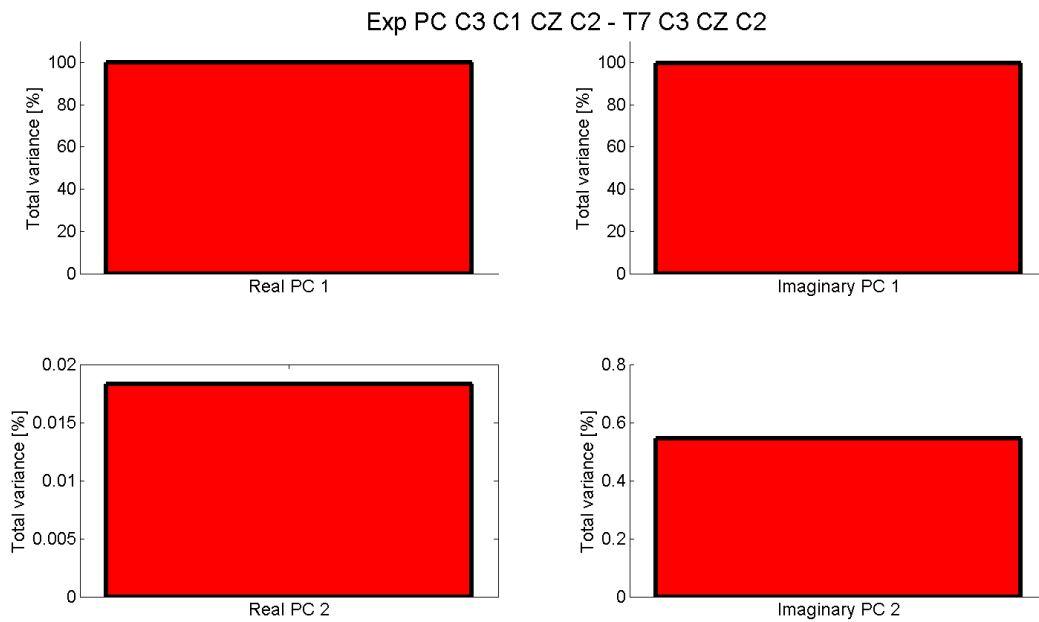


Figure 9.37: Percent of total variance of first and second principal components of real and imaginary components, shown for electrode montages C3-C1-CZ-C2 and T7-C1-CZ-C2.

In Fig. 9.37 we see the percentage of variance described by the first and second real and imaginary components. In both cases the first component describes almost 100% of the variance. For the second principal component we have $\approx .018\%$ variance and $\approx .55\%$ attributed to the real and imaginary components respectively.

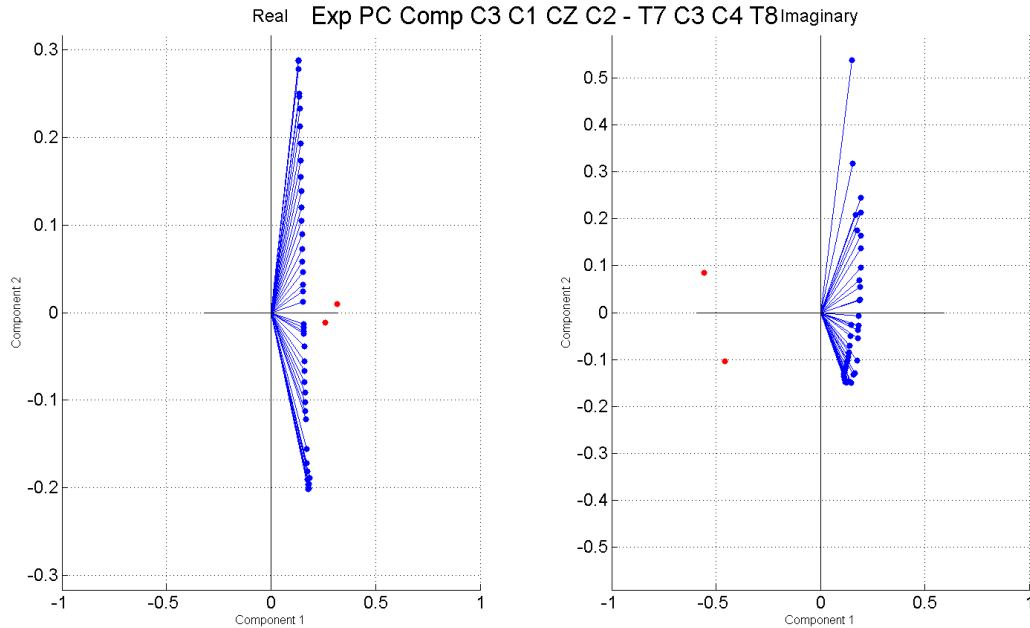


Figure 9.38: Principal components, scores and coefficients shown of real and imaginary components of electrode montages C3-C1-CZ-C2 and T7-C3-C4-T8.

Fig. 10.12 shows the loadings and scores for the pair C3-CZ-C1-C2 and T7-C3-C4-T8.

Here we see that both the real and (especially) imaginary scores are more widely separated.

Fig. 9.39 shows the percent variance explained by the real and imaginary first and second components. Here the percent variance described by the second components has increased by a factor of 10 to $\approx .14\%$ and $\approx 3.3\%$ for the real and imaginary components respectively.

9.5.3 Discussion

After analysis of our experimental we can make a number of observations. Firstly we note the high degree of variability between subjects. A detailed discussion of features of the subject Bode plots showed numerous patterns of impedance response for each montage

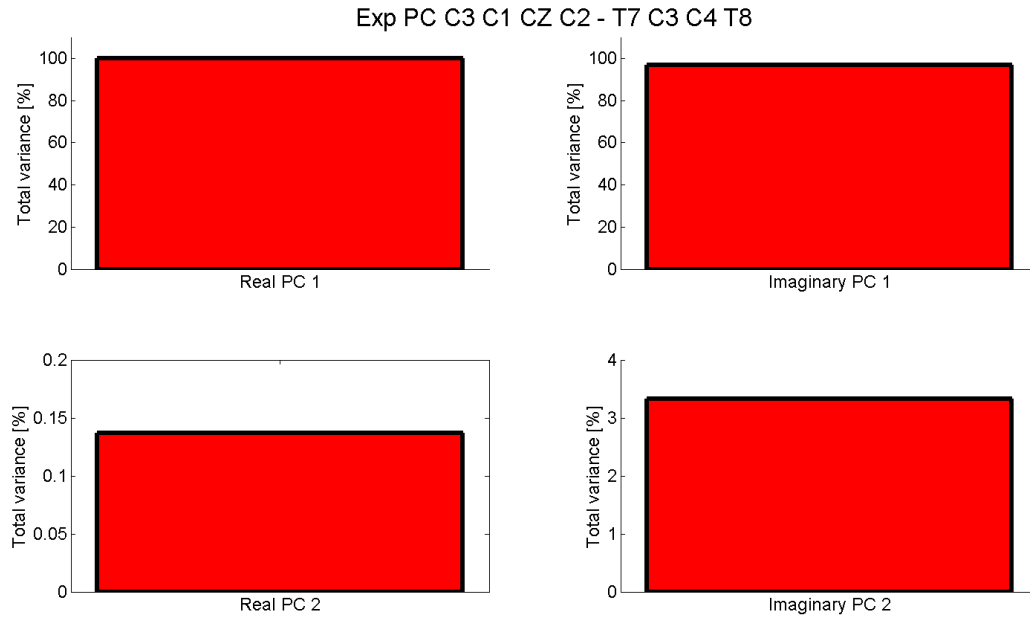


Figure 9.39: Percent of total variance of first and second principal components of real and imaginary components, shown for electrode montages C3-C1-CZ-C2 and T7-C3-C4-T8.

across frequency. We also saw a high degree of variability in the shape of the Cole plots, and the values and trends of the Cole parameters across the different montages. In many cases as well differences between Cole parameters were shown to be non statistically significant.

This high degree of inter-subject variability may be due to a number of reasons. One study has shown that direct bioimpedance measurements are strongly affected by age, gender, and body mass characteristics [244]. In our study, all our subjects were male, however there were differences of age and tissue characteristics. In fact, bioimpedance measurements are known for high variability even within subjects over repeated measurements. Some authors have shown a within subject variability of 3-14 Ω under standardized conditions (fasting, in the morning and an empty bladder in a set position) [245].

In the context of neurostimulation, the variability of tissue properties are a known factor that affect the distribution of the electric field in the brain and hence the purported physiological effects [37, 246, 247]. For instance a study that investigated the electric field

distribution in finite element models constructed from 24 males, found that 50% of the variance could be explained by the thickness of the CSF layer. Others have suggested [37] that a significant cause of inter-subject is driven by anatomical and physiological differences in individuals including factors such as fat levels, skull thickness, shape of the cortex and CSF density [103, 107]. Our findings show large inter-subject variability which is consistent with the reported high between groups variability reported for tDCS neurostimulation effect [18]. Intra-subject measurement error is much lower, however tDCS neurostimulation effect is shown to also have high intra-subject variability [18].

Other factors causing variability may include the thickness and impedance of the stratum corneum. A study has shown that the stratum corneum dominates the impedance response of tissue below 1 KHz [248]. In [249] it was shown that the spectrum of the stratum corneum did not correspond with a Cole model, stripping of this layer with tape did change the impedance to be compatible with the Cole model. Although we have use a 4 electrode measurement, the high impedance of the outer scalp necessitated use of skin pre-conditioning which may cause artifact and error due to voltage mismatch [242, 250].

Despite all the inter-subject variability we do note common patterns across all subjects. In general we were able to identify α and β impedance dispersions across all subjects and differences in mean impedance magnitude and phase are shown across subjects for different electrode montages.

We now discuss in greater details some of the patterns that we identified across subject measurements.

First of all we can identify semi-circles representing the Cole models of α and β dispersion for all subjects- although the exact shape varied quite a bit. We see quite a number of semi-circles part where the characteristic frequency appeared to be beyond the measurement range. This is similar to [251] who simulated a tetrapolar electrode system applied on the fingers factoring in blood pulsatility with current frequency ranging from 5

kHz to 100 MHz. Validation with an instrument only showed part of the semi-circle characterizing blood due to device limitations. Here we see that some Nyquist plots of impedance spectra appear to be linear rather than rounded (for example see top graphs of . 9.7). This posed some challenges for our method of extraction which relies on fitting a semi-circle shape to the impedance spectra. We therefore modified our algorithm (see section 9.4.0.1) and approximated f_c as being the nearest neighbor to a point interpolated near the semi-circle peak. In fact this resulted in a approximate parameter which was often extracted from the peak of the graph representing 1 MHz. Other semi-circles were better defined, for example many of the impedance spectra derived from T7-C3-C4-T8 (see bottom left graph of Fig. 9.7).

Other notable patters included the magnitude of the impedance spectra. We observed generally a decrease in f_c across montages (see for instance Figs. 9.27, 9.24 and 9.18). We also see for instance for a number of subjects (see Figs. 9.13 and 9.19) that the magnitude of T7-C3-C4-T8 is less than that of the other montages (along both the real and imaginary axis).

Despite the commonalities of some of the spectra pattern, it was difficult to find a consistent pattern when comparing across individual subjects. We see clear outliers (i.e. huge differences in magnitude) like for instance the spectrum of the T7-C4-C5-T8 as shown in bottom right Fig.9.25. In many cases the Cole parameters trends across subjects differed considerably. This is line with previous work that showed that Cole parameters are highly susceptible to variability due to noise cause by physiological changes to tissue as well as intrinsic measurement noise [237]

In order to reduce the effect of the inter-subject variability we investigated impedance, Cole and PCA parameters on the mean impedance of all 8 subjects. Here the error bars reflect the inter-subject variability. We note that indeed a distinct curve or frequency behavior is shown resulting from each electrode montage as shown for impedance vs. frequency (Fig. 9.31), phase vs. frequency (Fig. 9.32) and Nyquist plots (Fig. 10.4). Thus despite the large

inter-subject variability, we do see an emergence of pattern for the mean values.

We investigated changes of extracted Cole parameters across the tetrapolar montages. Due to the high-variability across subjects there were very few significant differences. (as tested by an un-paired test). In the α dispersion we see that there is a significant decrease in R_∞ from C3-CZ-C2-C1 to T7-C3-CZ-C2 and from T7-C3-CZ-C2 to T7-c3-c4-T8. In the β dispersion there are significant decreases in α , and a significant increase in R_0 and R_∞ . In no case was there a statistically significant change between the two first montages of C3-CZ-C2-C1 and T7-C3-CZ-C2. Thus we see that only the largest differences between the 2 first montages to T7-C3-C4-T8 were significant enough to emerge through all the inter-subject noise.

We then looked at the scores of the first two real and imaginary principal components. As shown earlier for FEM tetrapolar and bipolar montages, the variation between different impedance spectra pairs is almost 100% explained by the first principal component. The second component increases as the the separation between the electrode montages is increased. Interestingly, PCA on the pair C3-C1-CZ-C2 and T7-C3-CZ-C2 showed that the percent variance along the second imaginary principal component was over 3% (see Fig. 9.39). This is a much more significant variance than that shown for the FEM model (see Fig. 8.34, however, the overall score distribution and trends in changes in variance for different impedance spectra, do appear to closely match results shown on the FEM (see chapter 10).

Thus we conclude our discussion with the observation that despite the inter-subject variability, there are some patterns and trends in the data. This can be seen in the mean results that shows that there are significant differences in the spectra resulting from different montages. The distinct patterns we described may provide insight in how electrode configuration, and measurement frequency shapes internal sensitivity fields patterns in the brain with important implication for neuro-stimulation dose and for neural-measurement applications.

In the next chapter we will discuss in detail how closely the experimental mean impedance characteristics match with results derived from the FEM model.

9.6 Summary

This chapter presents the results of a pilot study measuring and analyzing the head impedance spectra of 8 subjects. We used the Solatron (1294 and 1255b) for acquisition of experimental data. We used a fixed 100 μA current with a frequency range from 100 Hz until 1 MHz with 5 points per decade. Electrode configurations were identical to the simulated tetrapolar montages. We used the Cole model and PCA to analyze the spectra. Results showed high variability of Cole parameters between subjects. Overall each tetrapolar configuration showed unique impedance characteristics (phase, magnitude, nyquist plots) when mean subject spectra was analyzed. PCA analysis of mean subject showed that close to 100% of variance between spectra could be described by a single principal component and that the variance described by the second principal component increase as the inter-electrode angle was increased.

Chapter 10

Comparison of FEM and Experimental Results

In this chapter we compare results derived from mean experimental spectra to that shown for the FEM.

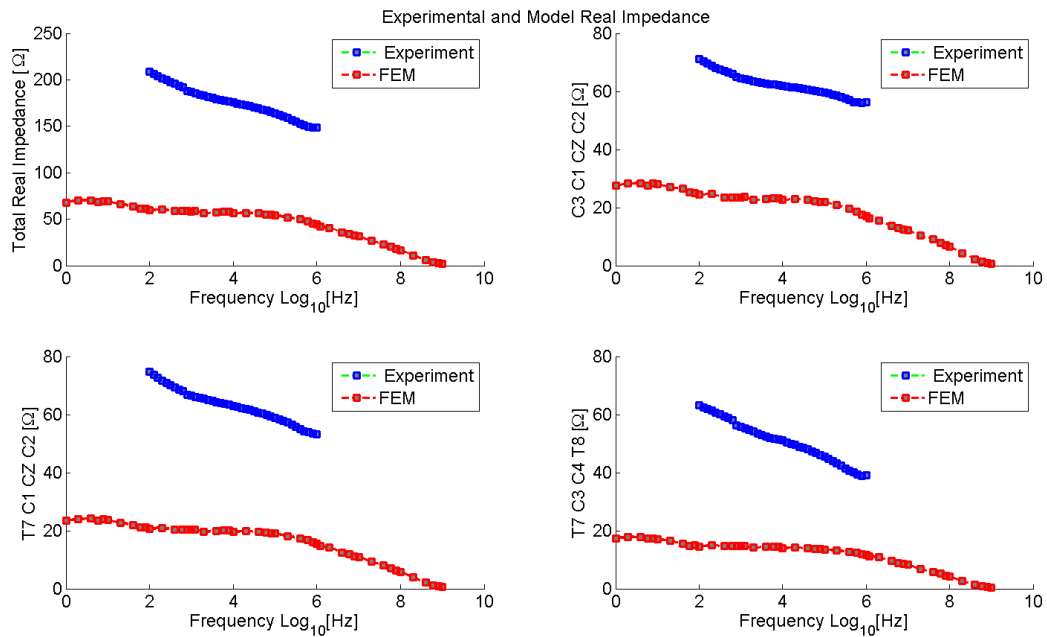


Figure 10.1: Comparison of mean experimental and FEM impedance. From upper left clockwise, Sum of all real impedance across all electrode montages, real impedance of C3-C1-CZ-C2, real impedance of T7-C3-CZ-C2, real impedance of T7-C3-C4-T8.

Fig. 10.1 shows a series of graphs comparing the FEM and mean experimental real impedance. The blue data points represent experimental impedance, whereas red points

are FEM impedance. Experimental data is plotted over the measurement frequency range (100 Hz - 1 MHz) and FEM is plotted over the simulation frequency range (1 Hz - 1 GHz). Specifically we have from upper left moving clockwise: (a) the sum of the real impedances of C3-C1-CZ-C2, T7-C3-CZ-C2 and T7-C3-C4-T8 (b) real impedance of C3-C1-CZ-C2 (c) real impedance of T7-C3-CZ-C2 and (d) real impedance of T7-C3-C4-T8.

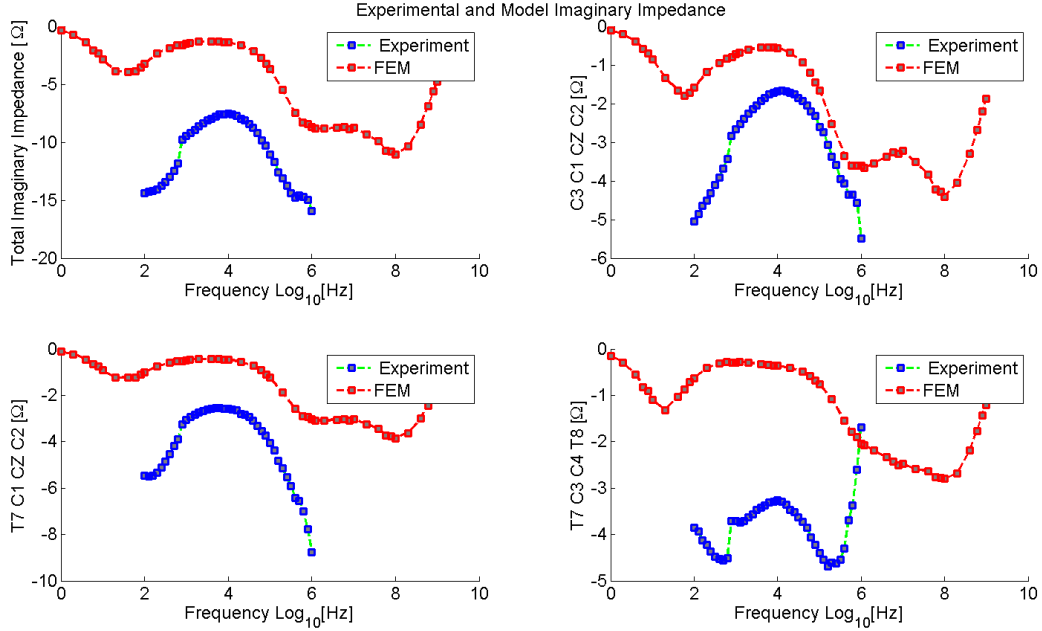


Figure 10.2: Comparison of mean experimental and FEM impedance. From upper left clockwise, Sum of all imaginary impedance across all electrode montages, imaginary impedance of C3-C1-CZ-C2, imaginary impedance of T7-C3-CZ-C2, imaginary impedance of T7-C3-C4-T8.

Fig. 10.2 is presented in the same format as Fig. 10.1 except that the imaginary component of impedance is shown.

We can observe some of the similarities and differences of the experimental and FEM data sets. Firstly we see a difference in the impedance ranges. The experimental data is shown in the \approx range of $40 \Omega < Z_{real} < 80 \Omega$ whereas the FEM is in the \approx range of $1 \Omega < Z_{real} < 30 \Omega$. The imaginary impedances ranges are, for the experimental data: $\approx -15 \Omega < Z_{imaginary} < -2 \Omega$ and for the FEM data: $-10 \Omega < Z_{imaginary} < 0 \Omega$.

Overall we can see that the real impedance FEM and experimental shapes are similar - i.e. descending as a function of frequency, except that the experimental impedance has a greater negative gradient. The imaginary FEM and experimental impedance shapes show good agreement in some cases. We note a clear concavity in the graphs of both impedance sets centered at around 10 kHz. At the end of the experimental frequency we do tend to see a divergence of experimental and FEM imaginary impedances. This is especially clearly shown in the bottom right of Fig. 10.2 for the montage T7-C3-C4-T8 where the tail end of the experimental spectra sharply diverges from the FEM graph.

To further investigate the relationship between the experimental and FEM data we show the Pearson's Linear Correlation coefficients. P-values are shown after testing for the null hypothesis (no significant correlation) with the t-test and an assumed significance level of $\alpha = .05$ (see section 6.1.2).

Impedance	R coefficient	P value
Total Real	0.950	9.365×10^{-17}
Total Imaginary	0.669	2.797×10^{-05}
C3 C1 CZ C2 Real	0.952	5.356×10^{-17}
C3 C1 CZ C2 Imaginary	0.734	1.726×10^{-06}
T7 C3 CZ C2 Real	0.950	1.184×10^{-16}
T7 C3 CZ C2 Imaginary	0.808	2.247×10^{-08}
T7 C3 C4 T8 Real	0.935	5.069×10^{-15}
T7 C3 C4 T8 Imaginary	-0.507	0.003

Table 10.1: Correlation coefficients and p-values for FEM and experimental real and imaginary impedance.

Table 10.1 shows a strong linear correlation ($r > .93$) with low p-values between the real experimental and FEM impedance. Imaginary impedances have a weaker but still significant correlation. The impedances for T7-C3-C4-T8 montage are shown to have a negative correlation of $r = -.507$ with a p-value of .003.

10.1 Comparison of Nyquist plots and Cole Parameters

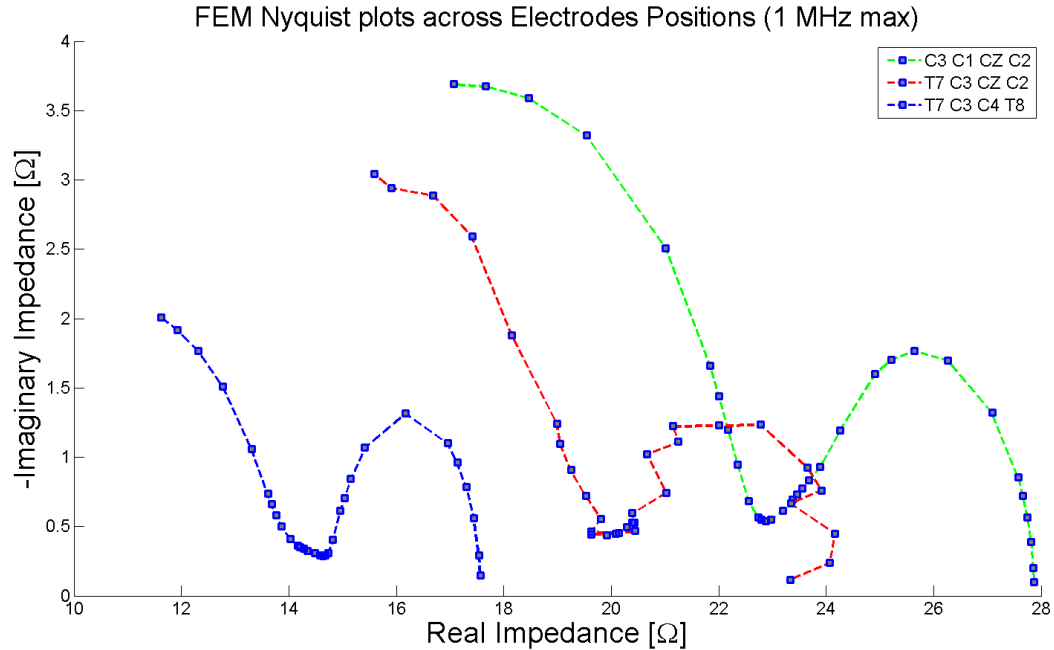


Figure 10.3: FEM Nyquist plots across all electrode montages up until 1 MHz.

We show in Fig. 10.3 Nyquist plots of the FEM for the 3 tetrapolar montages. The frequency range of the plots are limited to 1 MHz to correspond to the maximum frequency used when obtaining experimental data. The plotted impedance is the mean of 6 samples (see section 4.7). We see here a clear difference in impedance magnitude real and imaginary for the different montages. C3-CZ-C1-C2 has the highest impedance magnitude followed by T7-C3-CZ-C2 and then by T7-C3-C4-T8. We observe a change in the shape of the impedance spectra especially at the limit of our frequency range, C3-CZ-C1-C2 shows a rounded semi-circular shape with a peak, this is changed to more of linear rise for T7-C3-CZ-C2 and T7-C3-C4-T8.

Fig. 10.4 shows the mean experimental Nyquist plots over the tetrapolar montages. Here we see that both C1-C3-CZ-C2 and T7-C3-CZ-C2 spectra have an approximately linear rise for β dispersion. T7-C3-CZ-C2 has the greatest magnitude for both real and imaginary

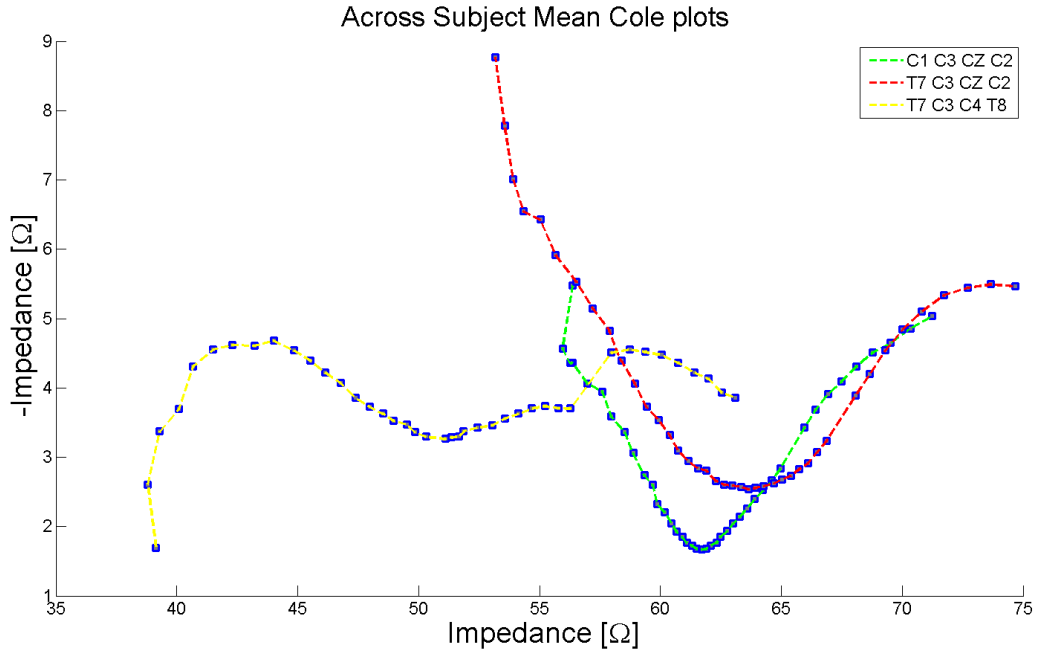


Figure 10.4: Mean Bode plot across all subjects with no error bars.

impedance. T7-C3-C4-T8 has the the lowest real and imaginary magnitude and has a clearly defined semi-circle unlike the other spectra.

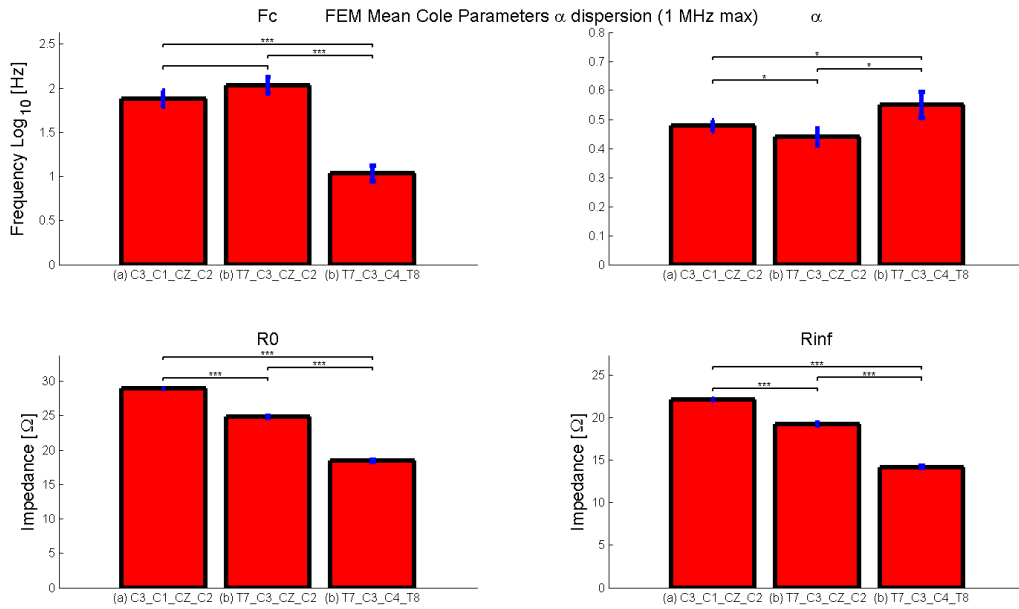


Figure 10.5: FEM α Cole parameter comparison across electrode montages.

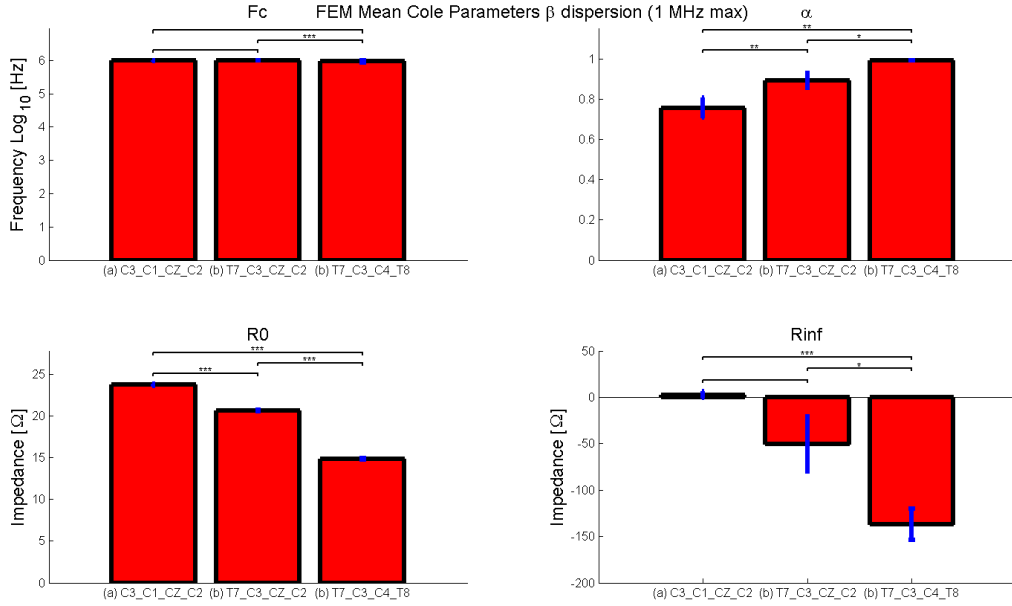


Figure 10.6: FEM β Cole parameter comparison across electrode montages up until 1 MHz.

Figs. 10.5 and 10.6 show a comparison of the FEM Cole parameters for the α and β dispersions.

We note the following for the α dispersion:

- f_c is significantly reduced from C3-C1-CZ-C2 to T7-C3-C4-T8 and from T7-C3-CZ-C2 to T7-C3-C4-T8
- α is reduced from C3-C1-CZ-C2 to T7-C3-CZ-C2 and increased from T7-C3-CZ-C2 to T7-C3-C4-T8 (changes are significant)
- R_0 and R_∞ are significantly reduced (from left to right)

We observe for the β dispersion:

- f_c is significantly decreased from to T7-C3-CZ-C2 and T7-C3-C4-T8
- α significantly increases (from left to right)

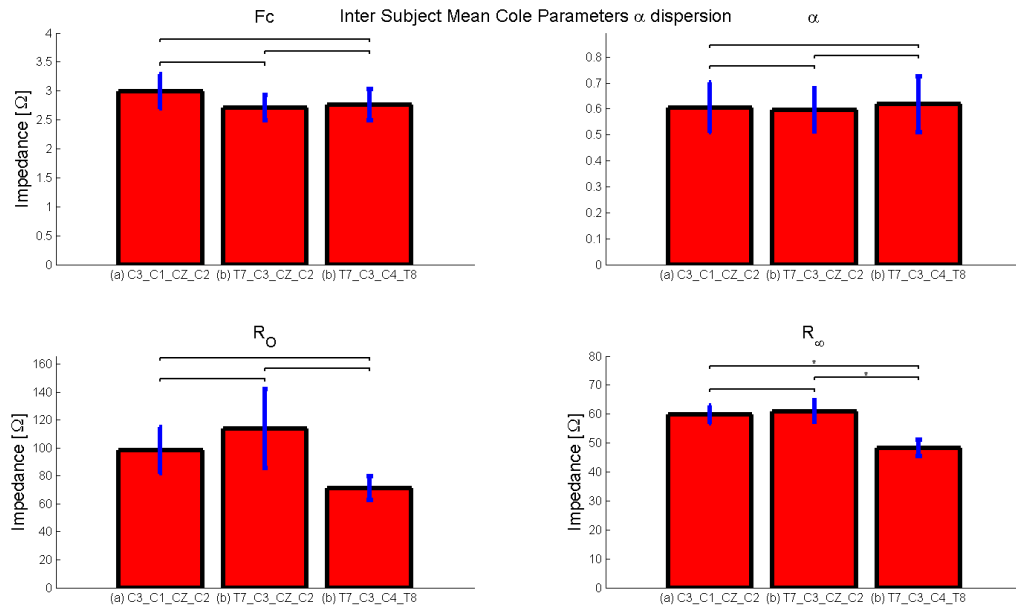


Figure 10.7: Mean inter-subject α Cole parameter comparison across electrode montages.

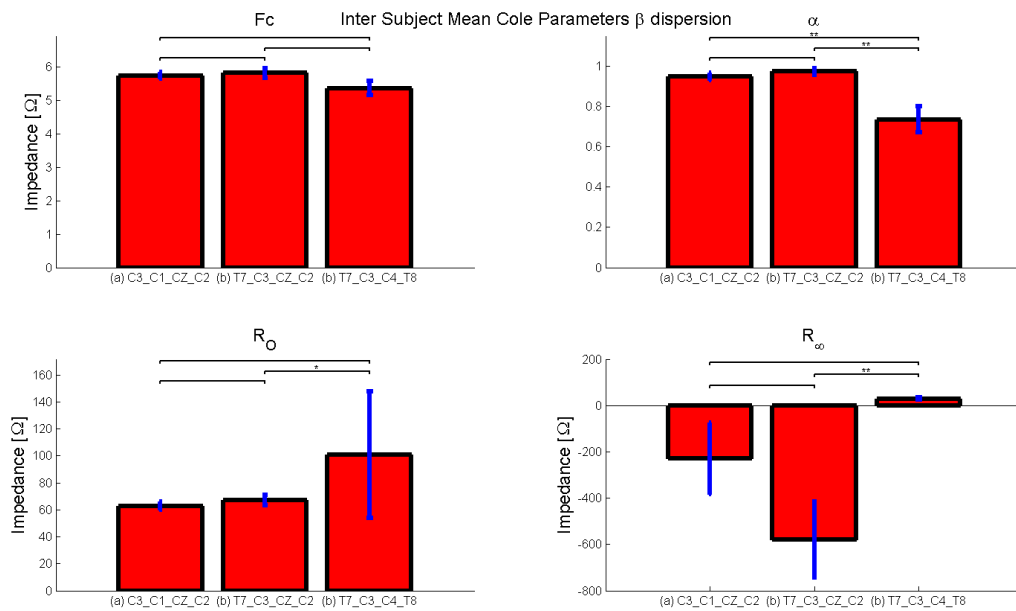


Figure 10.8: Mean inter-subject β Cole parameter comparison across electrode montages.

- R_0 and R_∞ are significantly reduced (from left to right)

Figs. 10.7 and 10.8 show Cole parameter comparison for the mean experimental α and β dispersions. A non-paired t-test is used to test for statistical significance (see section 9.5.2.3).

We note for the α dispersion:

- R_∞ decreases significantly from C3-C1-CZ-C2 to T7-C3-CZ-C2 and from T7-C3-CZ-C2 to T7-C3-C4-T8.
- Other changes are not significant.

We see for the β dispersion:

- f_c decreases (not significantly).
- α decreases significantly from C3-C1-CZ-C2 to T7-C3-CZ-C2 and from T7-C3-CZ-C2 to T7-C3-C4-T8.
- R_0 increases significantly from T7-C3-CZ-C2 to T7-C3-C4-T8
- R_∞ increases significantly from T7-C3-CZ-C2 to T7-C3-C4-T8

10.2 Comparison of PCA parameters

Figs. 10.9 ,10.10, 10.11, 10.12 for the FEM and experimental impedance PCA loadings and scores are reproduced here for the purpose of visual comparison.

Upon inspection of the graph we see clear similarities:

- Real and imaginary scores consist of 2 points around the axis of the first principal component

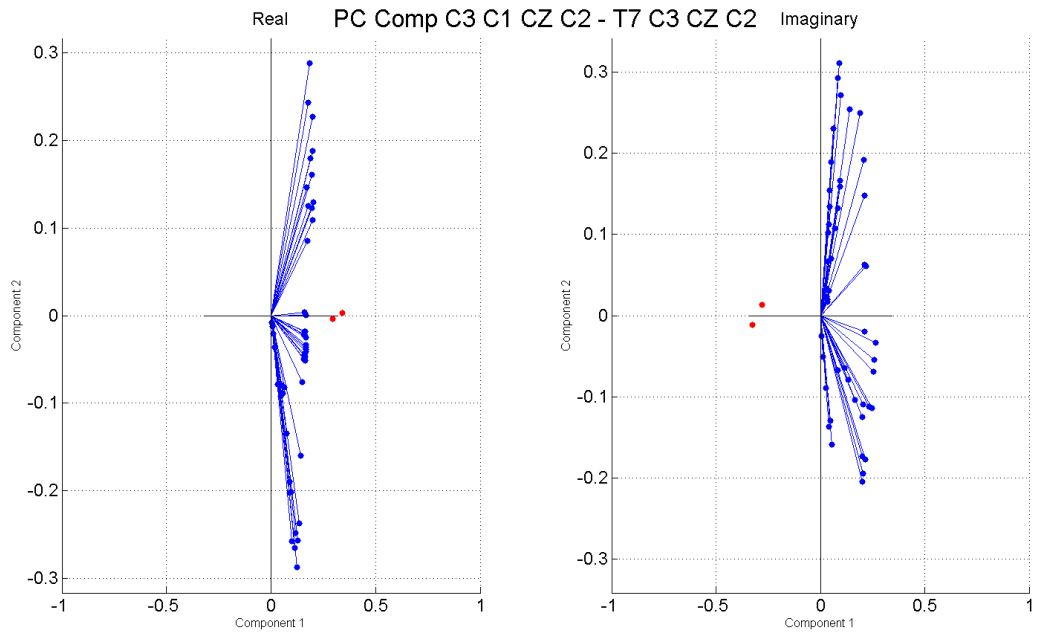


Figure 10.9: Principal components, scores and coefficients shown of real and imaginary components of FEM electrode montages C3-C1-CZ-C2 and T7-C1-CZ-C2.

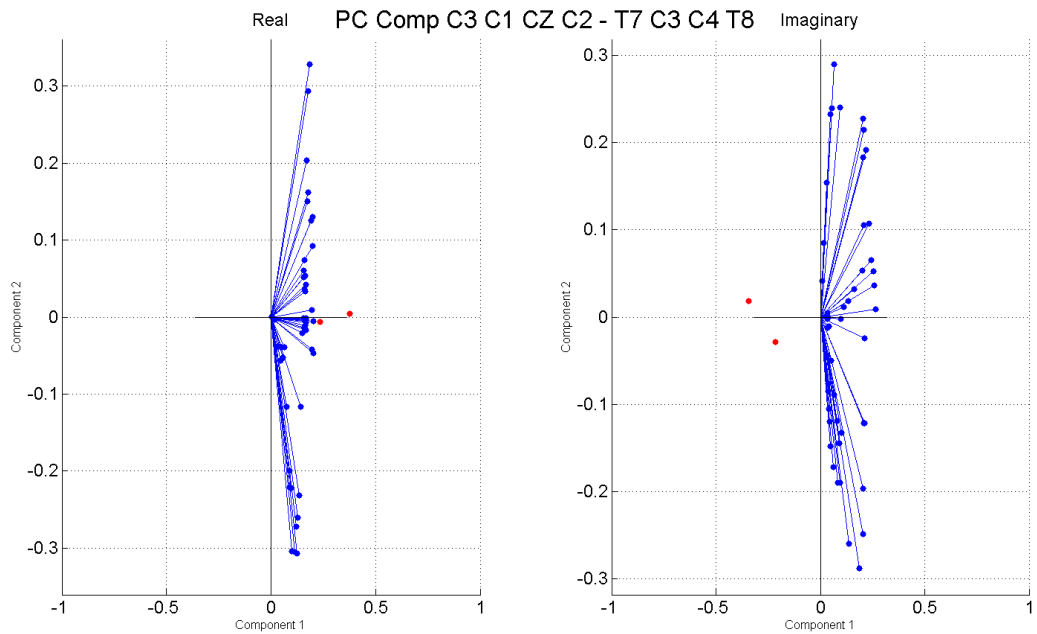


Figure 10.10: Principal components, scores and coefficients shown of real and imaginary components of FEM electrode montages C3-C1-CZ-C2 and T7-C3-C4-T8.

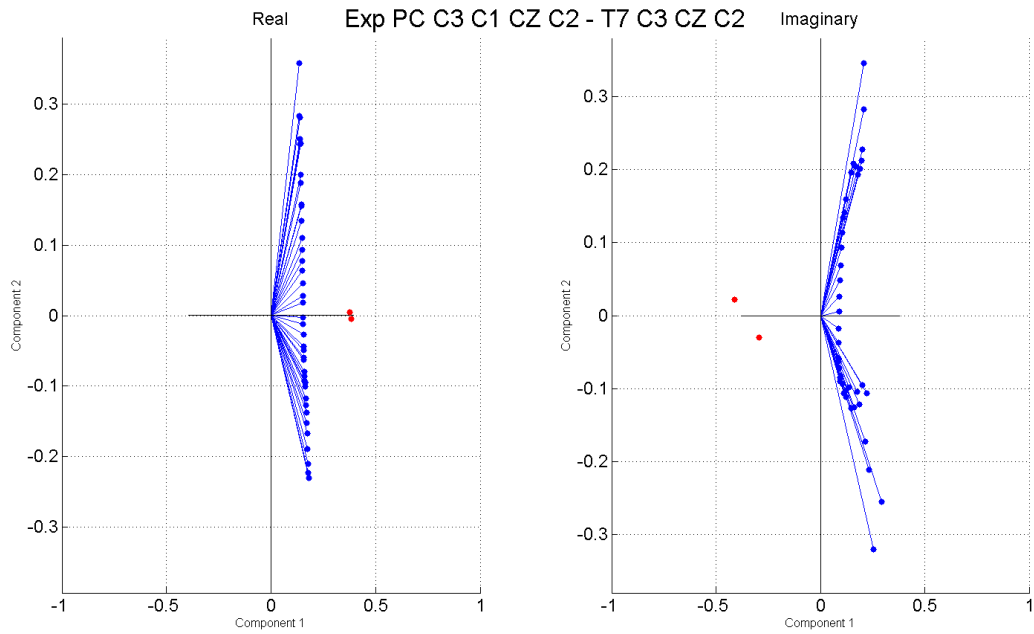


Figure 10.11: Principal components, scores and coefficients shown of real and imaginary components of experimental electrode montages C3-C1-CZ-C2 and T7-C1-CZ-C2.

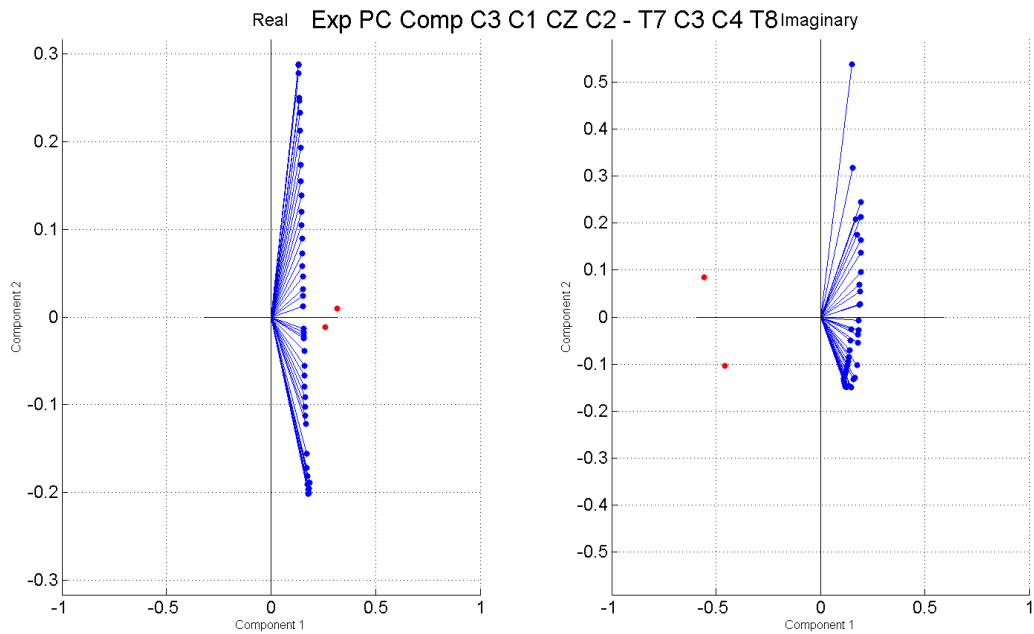


Figure 10.12: Principal components, scores and coefficients shown of real and imaginary components of experimental electrode montages C3-C1-CZ-C2 and T7-C3-C4-T8

- Imaginary components are distributed around the negative axis the first principal component
- Most of the variance between the impedance spectra can be described by the first principal component
- The second principal component explains more of the variance of the imaginary component than the first component
- The variance described by the second principal component increases for the change of impedance pair from C3-CZ-C2-C1 and T7-C3-CZ-C2 to C3-CZ-C2-C1 and T7-C3-C4-T8

Although the trends of the PCA results are the same for the FEM and experimental data, we can also see some differences. For example the variance explained by the second principal component is greater for the experimental impedance as compared to the FEM impedance. In addition scores (real and imaginary) and loadings of the FEM and experimental data are distributed differently.

10.3 Discussion

In the first part of the thesis we have shown separately FEM and experimentally derived results. In this chapter we are interested in comparing experimental and FEM data. Generally agreement between experimental and numerical results is not considered an absolute validation of the model, nevertheless we suggest that similarities between the datasets will allow us to make reasonable inferences concerning the validity of our approach. The comparison of FEM models to experimental data has already been discussed in relation to tDCS dose (for example see [\[239\]](#)). In fact the entire research field of FEM modeling for tDCS optimization is based on the assumption that numerical based results can be applied to clinical settings.

For the first part of our analysis we compared the shape and values of FEM and experimental real (Fig. 10.1) and imaginary (Fig. 10.1) impedance as a function of frequency. We can see that overall the slopes of the decrease of the real impedance are similar and the two data sets are highly correlated ($r > .9$ and $p < 9.36 * 10^{-17}$)(see table 10.1) We also can see that some differences, for example the rate of descent of the the FEM impedance is more gradual in the experimental frequency range ($10^2 Hz < f < 10^6 Hz$). The experimental real data is greater in terms of absolute value by a factor of ≈ 4 for the low frequency values. The agreement between the FEM and experimental data is the highest for the C3-C1-CZ-C2 and the gradually decreases for the T7-C3-CZ-C2 and T7-C3-C4-T8 where T7-C3-C4-T8 has the lowest correlation coefficient.

Similarly we observe the relative agreement of the FEM and experimental imaginary impedance in Fig. 10.2. We see however some clear differences. We can observe that there is a negative offset between the experimental and the FEM imaginary impedance. The peak of the FEM β curve does not coincide exactly with the FEM curve. In addition there is significant error between the high end of the experimental frequency and the FEM. This is especially pronounced for the imaginary experimental impedance T7-C3-C4-T8. The FEM and experimental imaginary impedance of T7-C3-C4-T8 are negatively correlated with a relatively R coefficient ($R = -0.507$, and $p = .003$).

We note that the experimental impedance appears to drop in a more linear fashion than the simulated impedance along the frequency range (x-axis). This may be due to a larger drop in experimental permittivity over frequency as compared to the simulated data-set. The modelling work also does not take into account the frequency dependency of the electrode-tissue interface (see section 4.5).

In addition, differences between experimental and FEM results may be in part due to limitations of the dielectric data provided to the model [39, 54, 55]. In [54] there is a discussion about sources of error in regards to collection of dielectric data. As open ended coaxial probes were used to collect material properties, measurements are susceptible to

electrode polarization at low frequencies and stray capacitance at high frequencies. At frequencies below 1 KHz, electrode polarization may be potentially a significant source, at frequencies below 100 Hz, permittivity values may be erroneous by up to a factor of 2 or 3. Error due to measurement noise was estimated to be at 1%, however variability of dielectric data was estimated to cause an error of 15%-25% for frequencies below 1 MHz. Additionally data was collected from ex-vivo samples which can result in significant differences to dielectric spectra as compared to live samples [220]. As mentioned previously, we based our choice of muscle [150] as a representation of scalp tissue on the work of [151] which modeled scalp tissue as a homogeneous layer of skeletal muscle. This may be a highly inaccurate assumption as it is known that the muscle is highly anisotropic with differing impedance recorded for longitudinal and transverse measurements [252].

Sources of error of our measurement include electrode polarization error (although our measurement is tetrapolar [195]), impedance and voltage mismatch [242] and stray capacitance [155, 156]. The effect of stray capacitance was shown when testing the calibration unit as a deviation of the Nyquist plot at high frequencies (see Fig. 9.2). This error is assumed to have increased by our use of non-shield cables to connect to the Solatron leads (see section 9.3.2). In fact we posit that the sharp divergences of the imaginary curves at high frequencies are largely as a result of stray capacitance error.

We next observe the difference between the FEM and experimental Nyquist plots (see Figs. 10.3 and 10.5). One striking difference between the plots is the difference in order of impedance magnitude for the C3-C1-CZ-C2 and T7-C3-CZ-C2. The FEM shows that C3-C1-CZ-C2 has the highest magnitude (real and imaginary) whereas the mean experimental data indicates that T7-C3-CZ-C2 has the highest impedance. We posit that in fact the experimental C3-C1-CZ-C2 shows the effect of an artifact introduced by the addition of saline to the electrode sites as described in section 9.3.2. Due to the close proximity of the voltage pair C1-CZ, the introduction of saline may have inadvertently created a shunt path through the scalp tissue thus resulting in a lower impedance profile

than predicted by numerical calculations (for an extreme example see the impedance of C3-C1-CZ-C2 in at the bottom graph of Fig. 9.4). We see in the literature that bioimpedance measurements are prone to error due to the creation of surface shunt paths [195] and close placement of current electrodes [253].

Another obvious difference is the shape of the T7-C3-C4-T8 curve which experimentally almost reaches the real-axis (Fig.10.4), whereas the FEM model shows only part of a semi-circle (Fig.10.3). Here possibly the differences between the impedance spectra graphs may have been caused by experimental stray capacitance error at high frequencies.

Since Cole parameters are based on fitting and analysis of the impedance curve, we therefore suggest that these different shaped curves preclude the direct comparison of Cole parameters across the FEM platform and experimental measurements.

Indeed we can see that FEM (Figs. 10.7 and 10.8) and experimental Cole parameters (Figs. 10.5 and 10.6) are very different. There are some similarities (i.e. for the α dispersion f_c decreases (from left to right across the bar charts), however this is not a significant change for the mean experimental parameter. The only α parameter that does match is R_∞ which decreases significantly for both the FEM and experimental data sets. In the β dispersion both the FEM and experimental f_c decreases, however again this is not significant in the experimental case. Contradictory trends are noted in for the α , R_0 and R_∞ parameters; the FEM shows an an increase in α and a decrease in R_0 and R_∞ , conversely the experimental data only shows a statistically significant increase in R_0 and R_∞ from T7-C3-CZ-C1 to T7-C3-C4-T8.

Although there may be some individual trends in the Cole parameters shown for individual subjects that match the FEM, overall each subjects Cole parameters were highly variable and non-consistent (see section 9.5.2.3). This may be the reason that many of the mean Cole parameters did not show statistically significant differences.

The difficulty of Cole parameter variability is discussed in [158], measurement noise and

physiological changes to the tissue are listed as reasons why Cole parameters are highly susceptible to noise [158]. In fact it was shown that Cole parameters extracted from raw data without preprocessing could not be used in a classification task (arm position). Furthermore it was shown that PCA used with K-NN classifier was also had a better classification performance than that achieved using raw Cole parameters [158] In [237] it was shown that SVD (singular value decomposition) could be used as method of preprocessing data by removing uncorrelated noise components and reconstructing the denoised data. It was shown that extraction of Cole parameters from the denoised data could indeed be used accurately in a classification task (prediction of arm position). We thus show here that Cole parameters extracted from raw impedance appear to be too variable for use as a reliable indicator of dose distribution in the brain. On the other hand we do observe that for all the subjects, each electrode montage resulted in a distinct impedance spectrum with a defined α and β dispersion. If we consider the FEM as an approximation of the objective truth, then we can compare subject data with the FEM when there is some agreement between them.

Our motivation for using PCA decomposition as a way of describing the variance between bioimpedance spectra (as well as resulting dose) is thus related to reduction in error caused by discarding elements of the data caused by non-correlated noise elements. We only are looking at the scores of the two first principal components, thus we can assume that most of the variability associated with noise is discarded.

When comparing the PCA parameters for the FEM and experimental data (see Figs. 10.9, 10.10, 10.11, 10.12) we do see a high level of agreement (unlike the Cole parameters). First of all for all impedance spectra pairs, we observe that the first principal component describes close to 100% of the variance. The pattern of the score distribution is similar for the FEM and experimental data. Both scores are clustered around the first principal component with small offsets around the second principal components. The real scores are clustered around the positive part of the first principal component axis; conversely the

imaginary scores are distributed around the negative part of the principal component axis. We find interesting that for both the FEM and experimental impedance, the percent of variance described by the second component increases as the electrode montages are separated. For instance we note for the FEM model the second component variance increases from $\approx 0.17\%$ to $\approx 0.7\%$ when the montage pair is varied from C3-C1-CZ-C2 and T7-C3-CZ-C2 to C3-C1-CZ-C2 and T7-C3-C4-T8. For the experimental impedance we have the same trend albeit different numbers; here the second component variance increases from $\approx 0.7\%$ to $\approx 3.3\%$ for the same change in montage pair. This change of variance can be seen visually in the plots (referenced above) showing the change in the offset of the scores from the first component axis, as the variance along the second axis increases, the distance of the score offset also increases.

The change in variation distribution along the first and second principal components is related to change in impedance which is related to change in sensitivity (see chapter 6). We consider here sensitivity as a quantity related to dose. We see by example from Figs. 6.32 that the intracranial sensitivity does increase when varying electrode montage from C3-C1-CZ-C2 to T7-C3-CZ-C2 and finally to T7-C3-C4-T8. Thus we can consider the changes in the variation percentage of the first and second principal components as a measure of change in dose.

10.4 Summary

This chapter presents the results of comparison of the FEM to the experimental study. We see overall that the experimental Cole parameters are different than the Cole parameters derived from the simulated data. The impedance spectra shapes were plotted showing different patterns for experimental and simulated data. PCA analysis showed a similar trend, both experiment and simulated impedance showed an increase in the variance described by the second principal component as inter-electrode angle is increased. The

results of this PCA analysis can possibly relate changes in impedance spectra to dose.

Chapter 11

Conclusions

11.1 Discussion

At the end of thesis we wish to discuss our results and if and how they conformed to our objectives as described in section [1.2](#).

11.1.1 Objective 1 Results

Our first objective was to simulate sensitivity distribution in our FEM and investigate how changing the electrode configuration (by increasing the inter-electrode gap or θ angle (see section [4.3](#)) affects the sensitivity distribution (2 and 4 electrode configurations described in sections [4.1.1](#) and [4.1.2](#)). We also want to investigate the proportion of sensitivity field distribution in each tissue as well as how sensitivity and focality change as a function of frequency.

Our expectations were that sensitivity and focality are (see section [4.8.4](#)) dependent on electrode distance and that as the inter-electrode gap is increased sensitivity would increase in the brain. We also expect that the total sensitivity will be dominated by the superficial tissue layers of the head and that the brain sensitivity will be less than 5% of the total sensitivity

We do indeed see a clear separation between sensitivity spectra as inter-electrode gap is increased. This is shown for example in Figs. [6.8](#), [6.10](#) and [6.12](#) for the bipolar montages

and in Figs. 6.28, 6.30 and 6.32 for the tetrapolar montages. In general the further the greater inter-electrode gap, the greater the sensitivity distribution in the brain. This pattern is seen for all the brain tissues (GM, WM and GM ROI), with the exception of the WM ROI where greater electrode separation does not necessarily result in a greater sensitivity distribution see Figs. 6.20 6.31)

Conversely as electrode gap is increased, focality is decreased in all the ROIs (for example see for the bipolar montage Figs. 6.19, 6.20 and 6.21 and for the tetrapolar montage Figs. 6.38, 6.39 and 6.40).

These results show the difficulty in optimizing dose as a fundamental tradeoff between magnitude and focality (see for example [120]). Our results showed that brain sensitivity increased as a function of increased inter-electrode angle are in accordance with physical experiments of Burger and Milaan [254], phantom measurements of Rush and Driscoll [87] as well as later FEM studies on the modeling of tDCS current in the brain [71, 105]. Thus we now have a foundation for investigating if a bioimpedance sweep of electrode montage results in a unique spectra that can be linked to the dose distribution.

We also showed the relative sensitivity distribution throughout all the head tissues. For the bipolar measurements sensitivity was highly concentrated in only 2 layers - the scalp and the CSF (see Figs. 6.5 and 6.7). The wide range of sensitivity values for the head tissues is clearly shown in log-log plots of sensitivity vs frequency. These plots also show that scalp followed by CSF have the greatest sensitivity (for example see Fig. 6.13). On the other, sensitivity of the brain tissues is quite low as shown in Figs. 6.8 and 6.10 and on the logarithmic scale in Fig. 6.13. From the values on the graphs we can see that sensitivity of the scalp and CSF are $\approx > 90\%$ (depending on the frequency) of the total sensitivity. This is in line with our expectations. We also see a sharp fall in CSF as a function of frequency (Fig. 6.7) corresponding with an increase of sensitivity in the brain (Figs. 6.8 and 6.10).

The high sensitivity of the bipolar configurations to boundary layers [208] indicates that

the 2 electrode configuration may not be suitable for directly measuring the impedance of the brain (for instance measurements on stroke patients see [236]). In the context of our research, the bipolar configuration may not be optimal for measuring brain impedance and thereby estimating dose.

The tetrapolar sensitivity distribution was more complex. All montages showed a high CSF contribution, however the effect of negative sensitivity caused a large decrease in scalp sensitivity. The montage T7-C3-C4-T8 results in a very low scalp sensitivity which was actually lower than the GM sensitivity at low frequencies (see Fig. 6.35). The implication of these results are that the scalp impedance can almost be entirely removed from the impedance measurement. We also posit that a tetrapolar array of electrodes used in tDCS could be used to increase dose in the brain by reduction of electric field in the scalp in a manner analogous to the field cancellation of the sensitivity field. This may be related to studies in tDCS optimization that show that the electrode field in the brain can be shaped by multiple electrodes in a manner analogous to beam forming [59, 120, 255].

The frequency dependence of sensitivity and focality is clearly shown to increase as frequency rises (see Figs. 6.8 and 6.19). Thus potentially neurostimulation targeting depth could be improving by picking an appropriate current injection frequency. This technique could potentially be used in a form of frequency modulated neurostimulation such as tACS [256]. The improving in focality however has to be balanced against a loss of electric field magnitude as shown in Fig. 6.18. Thus we see again a fundamental tradeoff between focality and magnitude [255].

11.1.2 Objective 2 Results

Our second objective was to investigate if a linear correlation exists between sensitivity and dose (electric field and current density). Our motivation here is to consider the sensitivity field distribution as a proxy for dose variables. Our approach is to measure the impedance spectra of the head. The relation between impedance and sensitivity is shown eq. 4.19 and

4.20. A correlation between sensitivity and dose would then show a link between dose and impedance which ties into our objective of inferring dose from impedance. Our expectation is that a significant linear correlation exists between these variables (p-value below an $\alpha = .05$) and that correlation is high ($> .9$).

We see overall a strong linear correlation between the sensitivity and dose spectra.

For the bipolar montage we have a high correlation between sensitivity and current density. The lowest correlation is for the scalp tissue ($R=0.895$, $p = 9.039 \times 10^{-18}$) and the highest correlation is for the GM ROI ($R = 0.992$, $p = 2.623 \times 10^{-43}$). The correlation between sensitivity and electric field is generally lower with the many of the tissues having a negative correlation. The tissue with the lowest correlation (closest to 0) is the scalp ($R = 0.992$, $p = 2.623 \times 10^{-43}$) and the tissue with highest correlation is the CSF ($R = 0.992$, $p = 2.623 \times 10^{-43}$). See tables 6.1 and 6.2.

For the tetrapolar montage we also have a high correlation between sensitivity and current density. The strongest correlation is for the scalp tissue ($R=0.980$, $p = 3.286 \times 10^{-34}$) and the weakest correlation is for the GM ROI ($R = 0.547$, 6.246×10^{-24}). Correlation of the WM is high but negative ($R = -0.857$, 7.647×10^{-15}). The correlation between sensitivity and electric field is generally weaker with the many of the tissues having a negative correlation. The tissue with the weakest correlation is the scalp ($R = -0.133$, $p = 0.366$) and the tissue with highest correlation is the CSF ($R = 0.982$, $p = 3.392 \times 10^{-35}$). See tables 6.3 and 6.4.

We thus have generally confirmed that there is a high linear correlation between the sensitivity and dose frequency response. We must mention though that the magnitude relationship is non-linear as shown by eq. 6.2. In addition some of the tissues show a weak correlation.

11.1.3 Objective 3 Results

We now wish to examine how electrode montage, frequency, and tissue type affect the impedance measurement of the head. we expect that as electrode gap is increased, the contribution of the brain tissues to the total impedance will increase. We expect that the high impedance skull tissue will have a large contribution to the total impedance of the head since skull conductivity is low. We also expect that the scalp and the CSF will have large contributions to the total impedance. Other tissues will contribute less than 1% of the impedance. Like sensitivity we also expect that the contribution of CSF on impedance will decrease and conversely the brain contribution to impedance will increase as frequency is increased.

First we see that for both bipolar and tetrapolar montages, as electrode gap is increased, impedance of the brain increases as shown in a series of log-log plots (for impedance of bipolar montages see Figs. 7.1, 7.2, 7.3, 7.4; for tetrapolar montages see Figs. 7.5, 7.6, 7.7). For the bipolar montages, we see that the scalp, CSF and skull have the greatest impedance. The impedance of the brain tissues is $\approx < 1\%$ as shown in the graphs above. The impedance of the brain tissues does increase as electrode gap is increased with the largest increase occurring from montage CZ-C1 to CZ-C3.

The tetrapolar montage results in the heighest impedance being in the CSF, skull and CSF. We see clearly the effect of increasing the angle between the voltage and current electrodes and thus generating a negative sensitive field. This is shown as a large reduction of scalp impedance to the extent that the GM impedance is greater than that of the scalp for the low frequencies of the T7-C3-C4-T8 montage.

In general our research objective was met as we showed the impedance measurement of the head is dominated by 2 or 3 tissues. This simplifies the problem of decomposition of the impedance signal as it is mainly generated by only a few tissues. We do note the difficulty of directing measuring the impedance of the brain tissues (this may be the reason for the

development of classifying methods for measuring brains of stroke victims instead of relying on direct measurements [133]. In the context of estimation of dose, our basic approach is to measure shifts in impedance parameters of the head rather than isolating the impedance of the head directly. One exception would be the T7-C3-C4-T8 montage where the the scalp impedance is greatly reduced, even in this case however the CSF impedance is ≈ 10 times greater than the impedance of the brain tissues (GM and WM).

11.1.4 Objective 4 Results

Objective 4 was to extract Cole model and PCA parameters from simulated data and compare the results across bipolar and tetrapolar montages.

As described in section 4.7, 5% Gaussian noise is added to the simulations to mimic experimental noise. For the Cole parameters we expected that there will be significant differences ((p-value below $\alpha = .05$) between the Cole parameters of generated from the impedance of each montage.

Results are shown for Cole parameters from the α , β and γ dispersion of the bipolar (see Figs. 8.10, 8.11 and 8.12) and tetrapolar (see Figs. 8.28, 8.29 and 8.30) montages.

Overall, results are positive, showing statistically significant differences between Cole parameters over all the frequency dispersions. In addition we see clear trends in the variations of the Cole parameters, for instance a slight increases in R_0 as electrode gap is increased. The implications of this are that our measurement is sensitive enough (with our simulated level of noise) to extract Cole parameters of statistically significant differences.

We showed earlier that sensitivity (related to dose) in the brain tissues increases monotonically as electrode gap is increased. Results here show that simulated FEM Cole parameters in many cases also change monotonically (increasing or decreasing) as function of inter-electrode gap. The changes in the Cole parameters correspond to shifts in sensitivity distribution and thus can be related to changes to dose in the brain.

We also wished to investigate the applicability of the linear superposition approximation for bioimpedance spectra. We expect that the total Cole system is composed of the Cole systems of each tissue added in series. Error between the total Cole plot measured across all tissues simultaneously is expected to be below 1%.

Results show indeed that for the bipolar (see Fig. 8.1) and tetrapolar (see Fig. 8.19) the total and added Cole plots are almost identical. The bipolar montage had an error of $.1 \Omega$ corresponding to an error of about .04% for the highest impedance of the spectrum. The tetrapolar montage had an error $\approx 1 \Omega$ corresponding to an error of about 3.5% for the highest impedance of the spectrum. Overall results show that the approximation of linear superposition is valid for impedance spectra. Thus tDCS optimization techniques using multiple electrodes following a beam forming principle which are based on linear superposition [255] can also be applied to the entire impedance spectra.

Another objective is to compare the PCA of bioimpedance spectra pairs (of different electrode montages). We expect a high degree of correlation between 2 bioimpedance spectra, this will be shown if the most of the variance ($> 99\%$) between the spectra is described on a single component. We also expect that as the inter electrode distance is increased the non-linearity of the relation between the bioimpedance spectra will also increase. This will be shown by an increase in the variance of the second principal components.

Results of the bipolar (See Fig. 8.13, 8.14, 8.15, 8.16, 8.17, 8.18) and the tetrapolar montages (See Fig. 10.9, 8.32, 10.10, 8.32) show indeed that $\approx 100\%$ of the variance between the bioimpedance spectra are described along a single principal component. We also see as inter electrode angle is increased the percentage of variance of the second principal component increases.

Thus overall we see that the relationship between bioimpedance is approximately linear (multiplication by a constant). The linear properties of the impedance spectra have

important implications since we may now consider linear operations such subtraction to remove the impedance of tissues external to the brain such as the scalp.

11.1.5 Objective 5 Results

We are looking here to see if the experimental data will be consistent across all montages and that a clear trend of statistically significant differences can be observed across all subjects. We expect that there will be a very high degree of variability between results for different subjects due to measurement error and natural physiological differences.

Overall we do see great variability between subjects as shown in the graphs of Cole parameter comparisons in chapter 9. When looking at the mean of all subject data (Figs. 10.7 and 10.8) we do observe some statistically significant differences between parameters (for example a decrease in α in the β dispersion. Significance for subject mean was measured by an unpaired t-test will be used to measure significance at $\alpha = 0.05$.

Results shows that there are certain patterns and characteristics in the impedance spectra that are not canceled out by inter-subject variability. These patterns and characteristics can then be compared to the FEM.

11.1.6 Objective 6 Results

Our final goal is to compare various impedance characteristics (Nyquist plots, Cole and PCA) of the FEM and the mean experimental data. Similarities can be used to infer relationships between impedance spectra and dose as calculated by the FEM.

Shape of the FEM and experimental impedance plots are shown in Figs. 10.1 and 10.2. Nyquist plots are shown in Figs. 10.3 and 10.5. FEM and Cole parameter comparison is shown in Figs. 10.5, 10.6. 10.7 and 10.8. FEM and experimental PCA plots are shown in Figs. 10.9, 10.10. 10.11 and 10.12.

We see that the real impedance of the FEM and experimental data follow are a similar

pattern and are closely correlated (see table 10.1). The imaginary impedance is also generally highly correlated across the FEM and experimental impedance. The weakest correlation is for the montage T7-C3-C4-T8 (negatively correlation).

Shape of the Nyquist plots are different, some general similarities are that C3-C1-CZ-C2 and T7-C3-CZ-C2 have a large imaginary impedance slope and T7-C3-C4-T8 has a reduced impedance magnitude (real and imaginary). Cole parameters variations were different for the FEM and experimental impedance. Many of the differences in experimental Cole parameters were not significant due to a high level of variability.

Experimental and FEM PCA plots showed overall good agreement. Differences between spectra were composed of 2 scores distributed around the first principal component. As electrode gap was increased the variation described by the second principal component increased for both the FEM and experimental data.

11.2 Conclusions and Future Work

Our motivation for this research was the development of a new method for improving control of tDCS dose. One of the major challenges of tDCS is the variability of individual subject response to the stimulation. Lack of standardization of tDCS dose is one of the key problems inhibiting successful widespread adoption of this technology [37]. Some critics consider tDCS has having no statistically significant effect beyond temporarily altering motor evoked potential (MEP) which raises questions concerning the efficacy of the current treatment system [32].

Our approach was to analysis the frequency response of the head tissues as method of interpretation of dose in the brain. We showed for bipolar and tetrapolar montages that sensitivity distribution in the brain increases as electrodes are moved apart. We also showed how the increase in sensitivity translated into a change in the measured impedance. Changes of impedance parameters (Cole and PCA) for different electrode montages are

then linked to changes in dose.

The simulated data showed expected dispersion regions (characterized by a series of semi-circles in the nyquist plane). The experimental data overall also showed distinct dispersion zones. The α dispersion zone was within range of the Solartron, however the β dispersion was generally only captured when measuring the T7-C3-C4-T8 montage.

Although spectral data can be analyzed by Fourier analysis of a broadband excitation or step signal [257], we chose to directly measure and analyze spectroscopy data acquired from a frequency sweep. This was in part due to the limitations of our instrument which is designed only for frequency sweep measurements. We also did not consider double dispersion Cole model fitting approaches [157] since this requires a priori knowledge of the exact nature of the dispersion of the system under study. In some cases one dispersion may overlap with a second dispersion, thus using a double dispersion methodology might not yield accurate results.

Our method provides a way of quantifying dose by measuring tissue impedance parameters directly related to the spread of current. In the context of neurostimulation, dose is defined by all elements of stimulation controlled by the operator [258]. Traditionally, this has been limited to electrode montage placement based on EEG coordinates, electrode size and amplitude and other characteristics of the injected current [1]. The novelty of our approach is that we also consider the impedance head tissues as another parameter related to control of dose. Although tDCS is our primary focus, we also consider a wide frequency range for analyzing the head impedance. Thus our approach may be applied to other forms of frequency based neurostimulation such as tASC or tRNS [259]. Other applications include optimization of bioimpedance spectroscopy [48] [260].

11.2.1 Limitations and Future Work

It is important to mention some of the limitations of our findings. Firstly we have not addressed the problem of calculation of dose in absolute terms. Our approach is to relate

shifts in impedance spectra to variation of dose. We have however not shown the possibility of directly separating the impedance spectra into components representing each tissue type. Part of our motivation for using PCA was to investigate if change of impedance of each tissue resulting from varying electrode montage, could be interpreted as a separate score along an uncorrelated principal component. We showed that the variance between spectra can almost entirely be described by a single principal component. This shows the linearity of the problem but it also shows the difficulty in separating the global impedance into the impedance of constituent tissues.

In fact a logical continuation of our work would be the use of ICA (independent component analysis) [261] as a method of separating independent contributions of each tissue to the overall impedance. The linear properties of the spectral data suggest that ICA is a suitable technique for separation of the sources [261].

Another limitation of our work is that we only considered changing one variable in our model at a time. For instance all head tissues material properties were kept constant while electrode configuration is changed. This limits our ability to compare the FEM results to experimental data since impedance acquired from subjects may be influenced by changes to multiple variables simultaneously (i.e. change to skin impedance during measurement). In future work, more sophisticated statistical models may be used to analyze the effect of changing multiple variables simultaneously [228].

We used 5% random Gaussian noise to mimic experimental error. For our impedance analysis we used the mean of 6 measurements. Overall we did see statistically significant changes to Cole parameters resulting from varying electrode position. Many of these parameters changes were monotonic (increasing or decreasing) and fit the pattern of change in dose. This was true even for the bipolar electrode measurement which we showed to be dominated by scalp.

Unfortunately we did not find the same trend of Cole parameter change in our

experimental study. Instead we observed a large degree of variability with the some of the patterns close to what we observed with the FEM.

One possible cause of inconsistent experimental results may be due to large variability in the electric properties of subject tissues. In our experimental work we have indeed shown large inter-subject variability which has been discussed in the context of FEM modeling of tDCS [246,262]. Our results indicate that relying on a single FEM model (for example see [263]) for guiding tDCS placement is over simplistic and does not take into account the wide range of inter-individual parameters.

Another potential source of variability is measurement error and noise. Our model may have indeed understated the level of noise inherent in the measurement. The limitations of our instrument include increasing stray capacitance at high frequencies, current shunting for closely spaced electrodes, high skin-electrode contact impedance and voltage mismatch at the pickup electrodes. A further limitation is the fact that gain used by the Solartron instrument was auto adjusted during measurement which may have introduced some artifacts and non-linearities in the experimental data. Furthermore the calibration results show some measurement error above 500 KHz see section 9.2.2. It is also apparent that our instrument range did not capture the characteristic frequency for some of the electrode montages (see for instance nyquist plots of C3-CZ-C1-C2 and T7-C3-CZ-C2). We would expect that a higher frequency range would capture the β and possibly γ dispersion represented as a semi-circle in the nyquist plane. Future work may consider using instrumentation with frequency measurement capabilities at least until 10 MHz. This would allow more direct comparison of the modelling and experimental work.

As discussed in chapter 9, our use of saline to reduce impedance may have altered the uniformity of skin conditions. In addition electrode attachment pressure was not standardized and instead simply relied on the bond created by the adhesive properties of the EEG paste we used.

We note some limitations in regards to our head FEM. Firstly we used the simplifying assumption of regarding tissue domains as isotropic. In reality biological tissue can be highly anisotropic and impedance measurements are sensitive to the orientation of electrodes with respect to tissue structure [252]. In addition we did not incorporate in our model the stratum corneum high impedance layer which has been shown to have a large impact on the dielectric response of tissue [249]. In addition we did not incorporate dynamic elements in the model which affect impedance measurements such as vascular flow throughout the head and cerebral blood flow associated with brain activity [135].

The high variability of the Cole parameters shows the difficulty of using Cole analysis on raw impedance data [237]. We therefore considered PCA as a method of extracting inherent structure in the bioimpedance spectral data, while discarding uncorrelated noise. We indeed saw a good overall agreement between PCA analysis of FEM and experimental data. First of all the first principal component contained close to all of the variance between 2 bioimpedance spectra. Secondly as the gap between electrodes are increased we saw that the variance described by the second principal component increased. The use of PCA for quantifying dose change is interesting especially since the technique reduces much of the impedance spectra dimensionality by removing redundant information. This is a very compact and efficient method of characterizing variation of tissue impedance even for a very large frequency range.

Our relative success comparing FEM and experimental PCA results indicate that this is a logical method of extension of this research. Future work can be comprised of utilization of both the traditional Cole model and PCA or other multivariate analysis techniques. Using the method described in [237] we can use a multivariate analysis technique (PCA or SVD) to remove uncorrelated noise by only considering signal described by the first several eigenvectors. After this preprocessing or denoising step the signal can then be restored and then Cole parameters can be extracted. As shown in [237, 264], reduction of signal dimensionality using SVD has performed well in a classification task despite the inherent

inter subject variability.

Other work that can be done to improve our results (especially in regards to inter subject variability) involves reducing measurement error. Better standardized methods of locating measurement sites as well as ensuring stable low impedance electrode-skin electrode coupling will lower error and the presence of outlier measurements in our data. We should consider improving cable shielding and other factors that affect stray capacitance. We are also interested in extending the experimental frequency range. This is important since many of the Nyquist plots in the β dispersion did not contain the full characteristic semi circle due to limitations on measurement frequency. This caused some difficulty in fitting impedance spectra to the Cole model.

The highest level of model validation of dose distribution in the brain is only available via invasive measurements, however this is suitable only for animal models which differ in significant ways from human physiology and where data may be difficult to obtain. It is therefore important to consider phantom testing as a critical component of validating our results. In future work we would use a phantom that mimics tissue dielectric properties (for example see [265]) since we are interested in analysis of the impedance spectrum.

After reduction of error by improvement of measurement standardization, instrumentation and de-noising processes, we can consider more accurate methods of relating simulated and experimental impedance spectra to dose distribution in the brain. Classifier [243,264] and artificial intelligence algorithms [266] are powerful techniques that can potentially be used to interpret and infer dose from impedance characteristics.

Despite the sources of variability and error, we are overall confident of the quality of the tissue impedance data acquired by use of the Solartron. This is suggested by the good calibration results, low error for repeated measurements, impedance patterns emerging for mean measurements across subjects as well as certain similarities to model data.

11.3 Summary of Contributions

We summarize here the novel contributions of this thesis:

- Our main contribution is that we develop a new simulation and experimental approach of relating bioimpedance spectra of head tissues to dose. The following are a list of sub-contributions that comprise the main contribution
 1. We simulate the dependence of sensitivity, focality and impedance on tissue type, frequency and electrode configuration
 2. We show through simulation the tissue types that provide the largest contribution to sensitivity and impedance
 3. We demonstrate the linear properties of bioimpedance spectra, including the superposition approximation, by showing the total Cole semi-circle of the head is comprised of a sum in series of tissue Cole semi-circles
 4. We further demonstrate the linearity of biompedance spectra by showing the variance between spectra can be approximately described a single principal component
 5. We use the Cole model and multivariate analysis to describe and compare changes to the impedance spectra for different electrode montages as well as to relate these changes to variation in dose. Thus we show how experimental and Cole parameters change for different montages with different dose distributions ($p < .05$)
 6. We show the agreement and high correlation between experimental data and the model in regards to real and imaginary impedance
 7. We demonstrate agreement between the experimental data and the model in regards to trends in the PCA results

8. We demonstrate a new method to fit impedance spectra that are not fully semi-circular in shape to the Cole model

Appendices

Appendix A

Ethics clearance



Office of Research Ethics
5110 Human Computer Interaction Bldg | 1125 Colonel By Drive
| Ottawa, Ontario K1S 5B6
613-520-2600 Ext: 4085
ethics@carleton.ca

CERTIFICATION OF INSTITUTIONAL ETHICS CLEARANCE

The Carleton University Research Ethics Board-B (CUREB-B) at Carleton University has renewed ethics clearance for the research project detailed below. CUREB-B is constituted and operates in compliance with the *Tri-Council Policy Statement: Ethical Conduct for Research Involving Humans* (TCPS2).

Title: In-vivo monitoring of the effect of transcranial direct current stimulation (tDCS) on scalp impedance and voltage [Herschel Caytak]

Protocol #: 102566

Principal Investigator: Andy Adler

Department and Institution: Faculty of Engineering and Design\Systems and Computer Engineering (Department of), Carleton University

Project Team (and Roles): **Andy Adler (Primary Investigator)**

Isar Nejadgholi (Co-Investigator (External))

Miodrag Bolic (Research Supervisor)

Herschel Caytak (Student Research: Ph.D. Student)

Funding Source (If applicable):

Effective: **May 17, 2018**

Expires: **May 31, 2019.**

Please ensure the study clearance number is prominently placed in all recruitment and consent materials: CUREB-B Clearance # 102566.

Restrictions:

This certification is subject to the following conditions:

1. Clearance is granted only for the research and purposes described in the application.
2. Any modification to the approved research must be submitted to CUREB-B. All changes must be approved prior to the continuance of the research.

3. An Annual Application for the renewal of ethics clearance must be submitted and cleared by the above date. Failure to submit the Annual Status Report will result in the closure of the file. If funding is associated, funds will be frozen.

4. A closure request must be sent to CUREB-B when the research is complete or terminated.

5. Should any participant suffer adversely from their participation in the project you are required to report the matter to CUREB-B.

6. It is the responsibility of the student to notify their supervisor of any adverse events, changes to their application, or requests to renew/close the protocol.

7. Failure to conduct the research in accordance with the principles of the *Tri-Council Policy Statement: Ethical Conduct for Research Involving Humans 2nd edition* and the *Carleton University Policies and Procedures for the Ethical Conduct of Research* may result in the suspension or termination of the research project.

Upon reasonable request, it is the policy of CUREB, for cleared protocols, to release the name of the PI, the title of the project, and the date of clearance and any renewal(s).

Please email the Research Compliance Coordinators at ethics@carleton.ca if you have any questions.

CLEARED BY:

Date: May 17, 2018

Bernadette Campbell, PhD, Vice-Chair, CUREB-B

Bibliography

- [1] F. Fregni, M. Nitsche, C. Loo, A. Brunoni, P. Marangolo, J. Leite, S. Carvalho, N. Bolognini, W. Caumo, N. Paik *et al.*, “Regulatory considerations for the clinical and research use of transcranial direct current stimulation (tdcs): review and recommendations from an expert panel,” *Clinical research and regulatory affairs*, vol. 32, no. 1, pp. 22–35, 2015.
- [2] A. R. Brunoni, M. A. Nitsche, N. Bolognini, M. Bikson, T. Wagner, L. Merabet, D. J. Edwards, A. Valero-Cabre, A. Rotenberg, A. Pascual-Leone, R. Ferrucci, A. Priori, P. S. Boggio, and F. Fregni, “Clinical research with transcranial direct current stimulation (tdcs): Challenges and future directions,” *Brain Stimulation*, vol. 5, no. 3, pp. 175 – 195, 2012. [Online]. Available: <http://www.sciencedirect.com/science/article/pii/S1935861X1100026X>
- [3] M. J. Player, J. L. Taylor, C. S. Weickert, A. Alonzo, P. S. Sachdev, D. Martin, P. B. Mitchell, and C. K. Loo, “Increase in pas-induced neuroplasticity after a treatment course of transcranial direct current stimulation for depression,” *Journal of affective disorders*, vol. 167, pp. 140–147, 2014.
- [4] X. Zhang, K. Liu, J. Sun, and Z. Zheng, “Safety and feasibility of repetitive transcranial magnetic stimulation (rtms) as a treatment for major depression during pregnancy,” *Archives of women’s mental health*, vol. 13, no. 4, pp. 369–370, 2010.

- [5] G. Schlaug, V. Renga, and D. Nair, “Transcranial direct current stimulation in stroke recovery,” *Archives of neurology*, vol. 65, no. 12, pp. 1571–1576, 2008.
- [6] F. Fregni, S. Freedman, and A. Pascual-Leone, “Recent advances in the treatment of chronic pain with non-invasive brain stimulation techniques,” *The Lancet Neurology*, vol. 6, no. 2, pp. 188–191, 2007.
- [7] M. A. Nitsche, P. S. Boggio, F. Fregni, and A. Pascual-Leone, “Treatment of depression with transcranial direct current stimulation (tdcs): a review,” *Experimental neurology*, vol. 219, no. 1, pp. 14–19, 2009.
- [8] F. Hummel, P. Celnik, P. Giraux, A. Floel, W.-H. Wu, C. Gerloff, and L. G. Cohen, “Effects of non-invasive cortical stimulation on skilled motor function in chronic stroke,” *Brain*, vol. 128, no. 3, pp. 490–499, 2005.
- [9] A. Monti, F. Cogiamanian, S. Marceglia, R. Ferrucci, F. Mameli, S. Mrakic-Sposta, M. Vergari, S. Zago, and A. Priori, “Improved naming after transcranial direct current stimulation in aphasia,” *Journal of Neurology, Neurosurgery & Psychiatry*, vol. 79, no. 4, pp. 451–453, 2008.
- [10] F. Fregni, R. Gimenes, A. C. Valle, M. J. L. Ferreira, R. R. Rocha, L. Natalle, R. Bravo, S. P. Rigonatti, S. D. Freedman, M. A. Nitsche, A. Pascual-Leone, and P. S. Boggio, “A randomized, sham-controlled, proof of principle study of transcranial direct current stimulation for the treatment of pain in fibromyalgia,” *Arthritis and Rheumatism*, vol. 54, no. 12, pp. 3988–3998, 2006. [Online]. Available: <http://dx.doi.org/10.1002/art.22195>
- [11] P. S. Boggio, P. Liguori, N. Sultani, L. Rezende, S. Fecteau, and F. Fregni, “Cumulative priming effects of cortical stimulation on smoking cue-induced craving,” *Neuroscience letters*, vol. 463, no. 1, pp. 82–86, 2009.

- [12] F. Fregni, F. Orsati, W. Pedrosa, S. Fecteau, F. A. Tome, M. A. Nitsche, T. Mecca, E. C. Macedo, A. Pascual-Leone, and P. S. Boggio, “Transcranial direct current stimulation of the prefrontal cortex modulates the desire for specific foods,” *Appetite*, vol. 51, no. 1, pp. 34–41, 2008.
- [13] P. S. Boggio, S. P. Rigonatti, R. B. Ribeiro, M. L. Myczkowski, M. A. Nitsche, A. Pascual-Leone, and F. Fregni, “A randomized, double-blind clinical trial on the efficacy of cortical direct current stimulation for the treatment of major depression,” *The International Journal of Neuropsychopharmacology*, vol. 11, pp. 249–254, 3 2008.
- [14] R. L. Goldman, J. J. Borckardt, H. A. Frohman, P. M. O’Neil, A. Madan, L. K. Campbell, A. Budak, and M. S. George, “Prefrontal cortex transcranial direct current stimulation (tdcs) temporarily reduces food cravings and increases the self-reported ability to resist food in adults with frequent food craving,” *Appetite*, vol. 56, no. 3, pp. 741–746, 2011.
- [15] M. A. Nitsche, M. S. Nitsche, C. C. Klein, F. Tergau, J. C. Rothwell, and W. Paulus, “Level of action of cathodal dc polarisation induced inhibition of the human motor cortex,” *Clinical Neurophysiology*, vol. 114, no. 4, pp. 600–604, 2003.
- [16] F. Fregni, P. S. Boggio, M. Nitsche, F. Berman, A. Antal, E. Feredoes, M. A. Marcolin, S. P. Rigonatti, M. T. Silva, W. Paulus *et al.*, “Anodal transcranial direct current stimulation of prefrontal cortex enhances working memory,” *Experimental Brain Research*, vol. 166, no. 1, pp. 23–30, 2005.
- [17] R. Sparing, M. Dafotakis, I. G. Meister, N. Thirugnanasambandam, and G. R. Fink, “Enhancing language performance with non-invasive brain stimulation: a transcranial direct current stimulation study in healthy humans,” *Neuropsychologia*, vol. 46, no. 1, pp. 261–268, 2008.

- [18] J. C. Horvath, O. Carter, and J. D. Forte, “Transcranial direct current stimulation: five important issues we aren’t discussing (but probably should be),” *Frontiers in systems neuroscience*, vol. 8, 2014.
- [19] K. Fricke, A. A. Seeber, N. Thirugnanasambandam, W. Paulus, M. A. Nitsche, and J. C. Rothwell, “Time course of the induction of homeostatic plasticity generated by repeated transcranial direct current stimulation of the human motor cortex,” *Journal of Neurophysiology*, vol. 105, no. 3, pp. 1141–1149, 2011.
- [20] S. Tremblay, V. Beaulé, J.-F. Lepage, and H. Théoret, “Anodal transcranial direct current stimulation modulates gabab-related intracortical inhibition in the m1 of healthy individuals,” *Neuroreport*, vol. 24, no. 1, pp. 46–50, 2013.
- [21] K. Fricke, A. A. Seeber, N. Thirugnanasambandam, W. Paulus, M. A. Nitsche, and J. C. Rothwell, “Time course of the induction of homeostatic plasticity generated by repeated transcranial direct current stimulation of the human motor cortex,” *Journal of neurophysiology*, vol. 105, no. 3, pp. 1141–1149, 2011.
- [22] M. A. Nitsche, J. Grundey, D. Liebetanz, N. Lang, F. Tergau, and W. Paulus, “Catecholaminergic consolidation of motor cortical neuroplasticity in humans,” *Cerebral Cortex*, vol. 14, no. 11, pp. 1240–1245, 2004.
- [23] M. A. Nitsche, D. Liebetanz, A. Schlitterlau, U. Henschke, K. Fricke, K. Frommann, N. Lang, S. Henning, W. Paulus, and F. Tergau, “Gabaergic modulation of dc stimulation-induced motor cortex excitability shifts in humans,” *European Journal of Neuroscience*, vol. 19, no. 10, pp. 2720–2726, 2004.
- [24] M. Nitsche, K. Fricke, U. Henschke, A. Schlitterlau, D. Liebetanz, N. Lang, S. Henning, F. Tergau, and W. Paulus, “Pharmacological modulation of cortical excitability shifts induced by transcranial direct current stimulation in humans,” *The Journal of physiology*, vol. 553, no. 1, pp. 293–301, 2003.

- [25] M. A. Nitsche, M.-F. Kuo, R. Karrasch, B. Wächter, D. Liebetanz, and W. Paulus, “Serotonin affects transcranial direct current–induced neuroplasticity in humans,” *Biological psychiatry*, vol. 66, no. 5, pp. 503–508, 2009.
- [26] M. A. Nitsche and W. Paulus, “Sustained excitability elevations induced by transcranial dc motor cortex stimulation in humans,” *Neurology*, vol. 57, no. 10, pp. 1899–1901, 2001.
- [27] S. Tremblay, V. Beaulé, J.-F. Lepage, and H. Théoret, “Anodal transcranial direct current stimulation modulates gabab-related intracortical inhibition in the m1 of healthy individuals,” *Neuroreport*, vol. 24, no. 1, pp. 46–50, 2013.
- [28] K. Monte-Silva, M.-F. Kuo, D. Liebetanz, W. Paulus, and M. A. Nitsche, “Shaping the optimal repetition interval for cathodal transcranial direct current stimulation (tdcs),” *Journal of neurophysiology*, vol. 103, no. 4, pp. 1735–1740, 2010.
- [29] K. Monte-Silva, M.-F. Kuo, S. Hessenthaler, S. Fresnoza, D. Liebetanz, W. Paulus, and M. A. Nitsche, “Induction of late ltp-like plasticity in the human motor cortex by repeated non-invasive brain stimulation,” *Brain stimulation*, vol. 6, no. 3, pp. 424–432, 2013.
- [30] N. E. O’Connell, B. M. Wand, L. Marston, S. Spencer, and L. H. DeSouza, “Non-invasive brain stimulation techniques for chronic pain. a report of a cochrane systematic review and meta-analysis.” *European journal of physical and rehabilitation medicine*, vol. 47, no. 2, pp. 309–326, 2011.
- [31] J. C. Horvath, J. D. Forte, and O. Carter, “Quantitative review finds no evidence of cognitive effects in healthy populations from single-session transcranial direct current stimulation (tdcs),” *Brain stimulation*, vol. 8, no. 3, pp. 535–550, 2015.

- [32] —, “Evidence that transcranial direct current stimulation (tdcs) generates little-to-no reliable neurophysiologic effect beyond mep amplitude modulation in healthy human subjects: a systematic review,” *Neuropsychologia*, vol. 66, pp. 213–236, 2015.
- [33] A. V. Peterchev, T. A. Wagner, P. C. Miranda, M. A. Nitsche, W. Paulus, S. H. Lisanby, A. Pascual-Leone, and M. Bikson, “Fundamentals of transcranial electric and magnetic stimulation dose: definition, selection, and reporting practices,” *Brain Stimulation*, vol. 5, no. 4, pp. 435–453, 2012.
- [34] M. Bikson and A. Datta, “Guidelines for precise and accurate computational models of tdcs,” *Brain stimulation*, vol. 5, no. 3, p. 430, 2012.
- [35] M. A. Nitsche and W. Paulus, “Excitability changes induced in the human motor cortex by weak transcranial direct current stimulation,” *The Journal of physiology*, vol. 527, no. 3, pp. 633–639, 2000.
- [36] A. R. Brunoni, M. A. Nitsche, N. Bolognini, M. Bikson, T. Wagner, L. Merabet, D. J. Edwards, A. Valero-Cabre, A. Rotenberg, A. Pascual-Leone, R. Ferrucci, A. Priori, P. S. Boggio, and F. Fregni, “Clinical research with transcranial direct current stimulation (tdcs): Challenges and future directions,” *Brain Stimulation*, vol. 5, no. 3, pp. 175 – 195, 2012. [Online]. Available: <http://www.sciencedirect.com/science/article/pii/S1935861X1100026X>
- [37] J. C. Horvath, O. Carter, and J. D. Forte, “Transcranial direct current stimulation: five important issues we aren’t discussing (but probably should be),” *Frontiers in systems neuroscience*, vol. 8, p. 2, 2014.
- [38] T. C. Ferree, K. J. Eriksen, and D. M. Tucker, “Regional head tissue conductivity estimation for improved eeg analysis,” *IEEE Transactions on Biomedical Engineering*, vol. 47, no. 12, pp. 1584–1592, 2000.

- [39] S. Gabriel, R. Lau, and C. Gabriel, “The dielectric properties of biological tissues: Ii. measurements in the frequency range 10 hz to 20 ghz,” *Physics in medicine and biology*, vol. 41, no. 11, pp. 2251–2269, 1996.
- [40] —, “The dielectric properties of biological tissues: Iii. parametric models for the dielectric spectrum of tissues,” *Physics in medicine and biology*, vol. 41, no. 11, pp. 2271–2293, 1996.
- [41] H. Caytak, I. Nejadgholi, I. Batkin, and M. Bolic, “Bioimpedance spectroscopy method for investigating changes to intracranial dose during transcranial direct current stimulation,” in *2015 37th Annual International Conference of the IEEE Engineering in Medicine and Biology Society (EMBC)*. IEEE, 2015, pp. 3448–3451.
- [42] I. Nejadgholi, H. Caytak, and M. Bolic, “Using bioimpedance spectroscopy parameters as real-time feedback during tdc,” in *Engineering in Medicine and Biology Society (EMBC), 2016 IEEE 38th Annual International Conference of the*. IEEE, 2016, pp. 5246–5249.
- [43] S. I. Gonçalves, J. C. de Munck, J. P. Verbunt, F. Bijma, R. M. Heethaar, and F. L. da Silva, “In vivo measurement of the brain and skull resistivities using an eit-based method and realistic models for the head,” *IEEE Transactions on Biomedical Engineering*, vol. 50, no. 6, pp. 754–767, 2003.
- [44] Y. Zhang, W. Van Drongelen, and B. He, “Estimation of in vivo brain-to-skull conductivity ratio in humans,” *Applied physics letters*, vol. 89, no. 22, pp. 223 903–2 239 033, 2006.
- [45] A. Cancelli, C. Cottone, F. Tecchio, D. Q. Truong, J. Dmochowski, and M. Bikson, “A simple method for eeg guided transcranial electrical stimulation without models,” *Journal of neural engineering*, vol. 13, no. 3, pp. 1–17, 2016.

- [46] S. Wagner, F. Lucka, J. Vorwerk, C. Herrmann, G. Nolte, M. Burger, and C. H. Wolters, “Using reciprocity for relating the simulation of transcranial current stimulation to the eeg forward problem,” *NeuroImage*, pp. 163–173, 2016.
- [47] E. Ziegler, S. L. Chellappa, G. Gaggioni, J. Q. Ly, G. Vandewalle, E. André, C. Geuzaine, and C. Phillips, “A finite-element reciprocity solution for eeg forward modeling with realistic individual head models,” *NeuroImage*, vol. 103, pp. 542–551, 2014.
- [48] U. G. Kyle, I. Bosaeus, A. D. De Lorenzo, P. Deurenberg, M. Elia, J. M. Gómez, B. L. Heitmann, L. Kent-Smith, J.-C. Melchior, M. Pirlich *et al.*, “Bioelectrical impedance analysis part i: review of principles and methods,” *Clinical nutrition*, vol. 23, no. 5, pp. 1226–1243, 2004.
- [49] O. G. Martinsen and S. Grimnes, *Bioimpedance and bioelectricity basics*. Academic press, 2011.
- [50] L. Chaieb, A. Antal, A. Pisoni, C. Saiote, A. Opitz, G. G. Ambrus, N. Focke, and W. Paulus, “Safety of 5 khz tacs,” *Brain stimulation*, vol. 7, no. 1, pp. 92–96, 2014.
- [51] E. D. Kirson, Z. Gurvich, R. Schneiderman, E. Dekel, A. Itzhaki, Y. Wasserman, R. Schatzberger, and Y. Palti, “Disruption of cancer cell replication by alternating electric fields,” *Cancer research*, vol. 64, no. 9, pp. 3288–3295, 2004.
- [52] D. Terney, L. Chaieb, V. Moliadze, A. Antal, and W. Paulus, “Increasing human brain excitability by transcranial high-frequency random noise stimulation,” *Journal of Neuroscience*, vol. 28, no. 52, pp. 14 147–14 155, 2008.
- [53] C. Gabriel, S. Gabriel, and E. Corthout, “The dielectric properties of biological tissues: I. literature survey,” *Physics in medicine and biology*, vol. 41, no. 11, p. 2231, 1996.

- [54] S. Gabriel, R. Lau, and C. Gabriel, “The dielectric properties of biological tissues: Ii. measurements in the frequency range 10 hz to 20 ghz,” *Physics in medicine and biology*, vol. 41, no. 11, pp. 2251–2269, 1996.
- [55] —, “The dielectric properties of biological tissues: Iii. parametric models for the dielectric spectrum of tissues,” *Physics in medicine and biology*, vol. 41, no. 11, pp. 2271–2293, 1996.
- [56] T. Dai and A. Adler, “In vivo blood characterization from bioimpedance spectroscopy of blood pooling,” *IEEE Transactions on Instrumentation and Measurement*, vol. 58, no. 11, pp. 3831–3838, 2009.
- [57] P. Govyadinov, S. Turovets, A. Gunn, D. Tucker, and P. Luu, “Direct current conditioning to reduce the electrical impedance of the electrode to skin contact in physiological recording and stimulation,” *arXiv preprint arXiv:1711.01059*, 2017.
- [58] D. B. Geselowitz, “An application of electrocardiographic lead theory to impedance plethysmography,” *Biomedical Engineering, IEEE Transactions on*, no. 1, pp. 38–41, 1971.
- [59] J. P. Dmochowski, A. Datta, M. Bikson, Y. Su, and L. C. Parra, “Optimized multi-electrode stimulation increases focality and intensity at target,” *Journal of neural engineering*, vol. 8, no. 4, pp. 1–16, 2011.
- [60] S. Zaghi, M. Acar, B. Hultgren, P. S. Boggio, and F. Fregni, “Noninvasive brain stimulation with low-intensity electrical currents: putative mechanisms of action for direct and alternating current stimulation,” *The Neuroscientist*, vol. 16, no. 3, pp. 285–307, 2009.
- [61] S. Zago, R. Ferrucci, F. Fregni, and A. Priori, “Bartholow, sciamanna, alberti: pioneers in the electrical stimulation of the exposed human cerebral cortex,” *The Neuroscientist*, vol. 14, no. 5, pp. 521–528, 2008.

- [62] A. Priori, “Brain polarization in humans: a reappraisal of an old tool for prolonged non-invasive modulation of brain excitability,” *Clinical Neurophysiology*, vol. 114, no. 4, pp. 589–595, 2003.
- [63] A. Priori, A. Berardelli, S. Rona, N. Accornero, and M. Manfredi, “Polarization of the human motor cortex through the scalp,” *Neuroreport*, vol. 9, no. 10, pp. 2257–2260, 1998.
- [64] L. J. Bindman, O. Lippold, and J. Redfearn, “The action of brief polarizing currents on the cerebral cortex of the rat (1) during current flow and (2) in the production of long-lasting after-effects,” *The Journal of physiology*, vol. 172, no. 3, pp. 369–382, 1964.
- [65] S. R. Weiss, A. Eidsath, X.-L. Li, T. Heynen, and R. M. Post, “Quenching revisited: low level direct current inhibits amygdala-kindled seizures,” *Experimental neurology*, vol. 154, no. 1, pp. 185–192, 1998.
- [66] R. Rehmman, M. Sczesny-Kaiser, M. Lenz, T. Gucia, A. Schliesing, P. Schwenkreis, M. Tegenthoff, and O. Höffken, “Polarity-specific cortical effects of transcranial direct current stimulation in primary somatosensory cortex of healthy humans,” *Frontiers in human neuroscience*, vol. 10, pp. 1–7, 2016.
- [67] A. Antal, T. Z. Kincses, M. A. Nitsche, and W. Paulus, “Manipulation of phosphene thresholds by transcranial direct current stimulation in man,” *Experimental brain research*, vol. 150, no. 3, pp. 375–378, 2003.
- [68] M. A. Nitsche, M. S. Nitsche, C. C. Klein, F. Tergau, J. C. Rothwell, and W. Paulus, “Level of action of cathodal dc polarisation induced inhibition of the human motor cortex,” *Clinical Neurophysiology*, vol. 114, no. 4, pp. 600–604, 2003.
- [69] M. A. Nitsche and W. Paulus, “Transcranial direct current stimulation—update 2011,” *Restorative neurology and neuroscience*, vol. 29, no. 6, pp. 463–492, 2011.

- [70] L. F. Medeiros, I. C. C. de Souza, L. P. Vidor, A. de Souza, A. Deitos, M. S. Volz, F. Fregni, W. Caumo, and I. L. Torres, “Neurobiological effects of transcranial direct current stimulation: a review,” *Frontiers in psychiatry*, pp. 1–11, 2012.
- [71] P. C. Miranda, M. Lomarev, and M. Hallett, “Modeling the current distribution during transcranial direct current stimulation,” *Clinical neurophysiology*, vol. 117, no. 7, pp. 1623–1629, 2006.
- [72] T. Wagner, A. Valero-Cabre, and A. Pascual-Leone, “Noninvasive human brain stimulation,” *Annu. Rev. Biomed. Eng.*, vol. 9, pp. 527–565, 2007.
- [73] M. A. Nitsche, W. Jaussi, D. Liebetanz, N. Lang, F. Tergau, and W. Paulus, “Consolidation of human motor cortical neuroplasticity by d-cycloserine.” *Neuropsychopharmacology*, vol. 29, no. 8, pp. 1573–1578, 2004.
- [74] C. J. Stagg, J. G. Best, M. C. Stephenson, J. O’Shea, M. Wylezinska, Z. T. Kincses, P. G. Morris, P. M. Matthews, and H. Johansen-Berg, “Polarity-sensitive modulation of cortical neurotransmitters by transcranial stimulation,” *The Journal of neuroscience*, vol. 29, no. 16, pp. 5202–5206, 2009.
- [75] M.-F. Kuo, R. Polanía, and M. Nitsche, “Physiology of transcranial direct and alternating current stimulation,” in *Transcranial Direct Current Stimulation in Neuropsychiatric Disorders*. Springer, 2016, pp. 29–46.
- [76] G. Ardolino, B. Bossi, S. Barbieri, and A. Priori, “Non-synaptic mechanisms underlie the after-effects of cathodal transcutaneous direct current stimulation of the human brain,” *The Journal of physiology*, vol. 568, no. 2, pp. 653–663, 2005.
- [77] F. Cogiamanian, M. Vergari, F. Pulecchi, S. Marceglia, and A. Priori, “Effect of spinal transcutaneous direct current stimulation on somatosensory evoked potentials in humans,” *Clinical Neurophysiology*, vol. 119, no. 11, pp. 2636–2640, 2008.

- [78] M. Rango, F. Cogiamanian, S. Marceglia, B. Barberis, A. Arighi, P. Biondetti, and A. Priori, “Myoinositol content in the human brain is modified by transcranial direct current stimulation in a matter of minutes: A 1h-mrs study,” *Magnetic resonance in medicine*, vol. 60, no. 4, pp. 782–789, 2008.
- [79] A. C. Merzagora, G. Foffani, I. Panyavin, L. Mordillo-Mateos, J. Aguilar, B. Onaral, and A. Oliviero, “Prefrontal hemodynamic changes produced by anodal direct current stimulation,” *Neuroimage*, vol. 49, no. 3, pp. 2304–2310, 2010.
- [80] K. Boros, C. Poreisz, A. Münchau, W. Paulus, and M. A. Nitsche, “Premotor transcranial direct current stimulation (tdcs) affects primary motor excitability in humans,” *European Journal of Neuroscience*, vol. 27, no. 5, pp. 1292–1300, 2008.
- [81] L. J. R. Lauro, M. Rosanova, G. Mattavelli, S. Convento, A. Pisoni, A. Opitz, N. Bolognini, and G. Vallar, “Tdcs increases cortical excitability: Direct evidence from tms-eeeg,” *Cortex*, vol. 58, pp. 99–111, 2014.
- [82] H. Kirimoto, K. Ogata, H. Onishi, M. Oyama, Y. Goto, and S. Tobimatsu, “Transcranial direct current stimulation over the motor association cortex induces plastic changes in ipsilateral primary motor and somatosensory cortices,” *Clinical Neurophysiology*, vol. 122, no. 4, pp. 777–783, 2011.
- [83] G. N. Rivera-Urbina, G. Batsikadze, A. Molero-Chamizo, W. Paulus, M.-F. Kuo, and M. A. Nitsche, “Parietal transcranial direct current stimulation modulates primary motor cortex excitability,” *European Journal of Neuroscience*, vol. 41, no. 6, pp. 845–855, 2015.
- [84] A. Datta, V. Bansal, J. Diaz, J. Patel, D. Reato, and M. Bikson, “Gyri-precise head model of transcranial direct current stimulation: improved spatial focality using a ring electrode versus conventional rectangular pad,” *Brain stimulation*, vol. 2, no. 4, pp. 201–207, 2009.

- [85] A. Antal, T. Z. Kincses, M. A. Nitsche, O. Bartfai, and W. Paulus, “Excitability changes induced in the human primary visual cortex by transcranial direct current stimulation: direct electrophysiological evidence,” *Investigative ophthalmology & visual science*, vol. 45, no. 2, pp. 702–707, 2004.
- [86] V. Moliadze, A. Antal, and W. Paulus, “Electrode-distance dependent after-effects of transcranial direct and random noise stimulation with extracephalic reference electrodes,” *Clinical Neurophysiology*, vol. 121, no. 12, pp. 2165–2171, 2010.
- [87] S. Rush and D. A. Driscoll, “Current distribution in the brain from surface electrodes,” *Anesthesia & Analgesia*, vol. 47, no. 6, pp. 717–723, 1968.
- [88] J. T. Francis, B. J. Gluckman, and S. J. Schiff, “Sensitivity of neurons to weak electric fields,” *The Journal of Neuroscience*, vol. 23, no. 19, pp. 7255–7261, 2003.
- [89] R. S. Ghai, M. Bikson, and D. M. Durand, “Effects of applied electric fields on low-calcium epileptiform activity in the ca1 region of rat hippocampal slices,” *Journal of Neurophysiology*, vol. 84, no. 1, pp. 274–280, 2000.
- [90] T. Wagner, F. Fregni, S. Fecteau, A. Grodzinsky, M. Zahn, and A. Pascual-Leone, “Transcranial direct current stimulation: a computer-based human model study,” *Neuroimage*, vol. 35, no. 3, pp. 1113–1124, 2007.
- [91] R. J. Sadleir, T. D. Vannorsdall, D. J. Schretlen, and B. Gordon, “Transcranial direct current stimulation (tdcs) in a realistic head model,” *Neuroimage*, vol. 51, no. 4, pp. 1310–1318, 2010.
- [92] M. Parazzini, S. Fiochi, E. Rossi, A. Paglialonga, and P. Ravazzani, “Transcranial direct current stimulation: estimation of the electric field and of the current density in an anatomical human head model,” *IEEE Transactions on Biomedical Engineering*, vol. 58, no. 6, pp. 1773–1780, 2011.

- [93] S. Wagner, S. Rampersad, Ü. Aydın, J. Vorwerk, T. Oostendorp, T. Neuling, C. Herrmann, D. Stegeman, and C. Wolters, “Investigation of tdc volume conduction effects in a highly realistic head model,” *Journal of neural engineering*, vol. 11, no. 1, pp. 1–14, 2013.
- [94] A. Datta, J. M. Baker, M. Bikson, and J. Fridriksson, “Individualized model predicts brain current flow during transcranial direct-current stimulation treatment in responsive stroke patient,” *Brain stimulation*, vol. 4, no. 3, pp. 169–174, 2011.
- [95] M. Parazzini, S. Fiocchi, and P. Ravazzani, “Electric field and current density distribution in an anatomical head model during transcranial direct current stimulation for tinnitus treatment,” *Bioelectromagnetics*, vol. 33, no. 6, pp. 476–487, 2012.
- [96] S. M. Rampersad, A. M. Janssen, F. Lucka, Ü. Aydın, B. Lanfer, S. Lew, C. H. Wolters, D. F. Stegeman, and T. F. Oostendorp, “Simulating transcranial direct current stimulation with a detailed anisotropic human head model,” *IEEE Transactions on Neural Systems and Rehabilitation Engineering*, vol. 22, no. 3, pp. 441–452, 2014.
- [97] M. Bikson, A. Rahman, and A. Datta, “Computational models of transcranial direct current stimulation,” *Clinical EEG and Neuroscience*, vol. 43, no. 3, pp. 176–183, 2012.
- [98] T. A. Wagner, M. Zahn, A. J. Grodzinsky, and A. Pascual-Leone, “Three-dimensional head model simulation of transcranial magnetic stimulation,” *IEEE Transactions on Biomedical Engineering*, vol. 51, no. 9, pp. 1586–1598, 2004.
- [99] M. E. Mendonca, M. B. Santana, A. F. Baptista, A. Datta, M. Bikson, F. Fregni, and C. P. Araujo, “Transcranial dc stimulation in fibromyalgia: optimized cortical target supported by high-resolution computational models,” *The Journal of Pain*, vol. 12, no. 5, pp. 610–617, 2011.
- [100] W. H. Lee, Z.-D. Deng, T.-S. Kim, A. F. Laine, S. H. Lisanby, and A. V. Peterchev, “Regional electric field induced by electroconvulsive therapy in a realistic finite element

- head model: influence of white matter anisotropic conductivity,” *Neuroimage*, vol. 59, no. 3, pp. 2110–2123, 2012.
- [101] H. S. Suh, W. H. Lee, Y. S. Cho, J.-H. Kim, and T.-S. Kim, “Reduced spatial focality of electrical field in tdcS with ring electrodes due to tissue anisotropy,” in *2010 Annual International Conference of the IEEE Engineering in Medicine and Biology*. IEEE, 2010, pp. 2053–2056.
- [102] H. S. Suh, W. H. Lee, and T.-S. Kim, “Influence of anisotropic conductivity in the skull and white matter on transcranial direct current stimulation via an anatomically realistic finite element head model,” *Physics in medicine and biology*, vol. 57, no. 21, 2012.
- [103] D. Q. Truong, G. Magerowski, G. L. Blackburn, M. Bikson, and M. Alonso-Alonso, “Computational modeling of transcranial direct current stimulation (tdcs) in obesity: impact of head fat and dose guidelines,” *NeuroImage: Clinical*, vol. 2, pp. 759–766, 2013.
- [104] A. Datta, M. Bikson, and F. Fregni, “Transcranial direct current stimulation in patients with skull defects and skull plates: high-resolution computational fem study of factors altering cortical current flow,” *Neuroimage*, vol. 52, no. 4, pp. 1268–1278, 2010.
- [105] P. Faria, M. Hallett, and P. C. Miranda, “A finite element analysis of the effect of electrode area and inter-electrode distance on the spatial distribution of the current density in tdcS,” *Journal of neural engineering*, vol. 8, no. 6, pp. 1–24, 2011.
- [106] M. Bikson, A. Rahman, A. Datta, F. Fregni, and L. Merabet, “High-resolution modeling assisted design of customized and individualized transcranial direct current stimulation protocols,” *Neuromodulation: Technology at the Neural Interface*, vol. 15, no. 4, pp. 306–315, 2012.

- [107] A. Datta, “Inter-individual variation during transcranial direct current stimulation and normalization of dose using mri-derived computational models,” *Frontiers in psychiatry*, vol. 3, pp. 1–8, 2012.
- [108] M. Windhoff, A. Opitz, and A. Thielscher, “Electric field calculations in brain stimulation based on finite elements: an optimized processing pipeline for the generation and usage of accurate individual head models,” *Human brain mapping*, vol. 34, no. 4, pp. 923–935, 2013.
- [109] C.-H. Im, H.-H. Jung, J.-D. Choi, S. Y. Lee, and K.-Y. Jung, “Determination of optimal electrode positions for transcranial direct current stimulation (tdcs),” *Physics in medicine and biology*, vol. 53, no. 11, pp. 219–225, 2008.
- [110] C.-H. Im, H.-K. Jung, J. Y. Han, H. R. Lee, and S. Y. Lee, “Fast and robust localization of brain electrical sources using evolution strategies: Monte-carlo simulation and phantom experiment studies,” *International Journal of Applied Electromagnetics and Mechanics*, vol. 20, no. 3, 4, pp. 197–203, 2004.
- [111] G. Ruffini, M. D. Fox, O. Ripolles, P. C. Miranda, and A. Pascual-Leone, “Optimization of multifocal transcranial current stimulation for weighted cortical pattern targeting from realistic modeling of electric fields,” *Neuroimage*, vol. 89, pp. 216–225, 2014.
- [112] P. C. Miranda, A. Mekonnen, R. Salvador, and G. Ruffini, “The electric field in the cortex during transcranial current stimulation,” *Neuroimage*, vol. 70, pp. 48–58, 2013.
- [113] B. D. Van Veen and K. M. Buckley, “Beamforming: A versatile approach to spatial filtering,” *IEEE assp magazine*, vol. 5, no. 2, pp. 4–24, 1988.
- [114] R. Sadleir, T. D. Vannorsdall, D. J. Schretlen, and B. Gordon, “Target optimization in transcranial direct current stimulation,” *frontiers in psychiatry*, vol. 3, pp. 1–13, 2012.

- [115] R. A. Waltz, J. L. Morales, J. Nocedal, and D. Orban, “An interior algorithm for nonlinear optimization that combines line search and trust region steps,” *Mathematical programming*, vol. 107, no. 3, pp. 391–408, 2006.
- [116] A. Dutta, “Using electromagnetic reciprocity and magnetic resonance current density imaging to fit multi-electrode montage for non-invasive brain stimulation,” in *Neural Engineering (NER), 2013 6th International IEEE/EMBS Conference on*. IEEE, 2013, pp. 447–451.
- [117] G. Ruffini, “Application of the reciprocity to eeg inversion and optimization of eeg-driven transcranial current stimulation (tcs, including tdc, tacs, trns),” *arXiv preprint arXiv:1506.04835*, 2015.
- [118] M. Fernandez Corazza, S. Turovets, P. Luu, E. Anderson, and D. Tucker, “Transcranial electrical neuromodulation based on the reciprocity principle,” *Frontiers in Psychiatry*, vol. 7, p. 87, 2016.
- [119] P. Luu, E. M. E. Arumugam, E. Anderson, A. Gunn, D. Rech, S. Turovets, and D. M. Tucker, “Slow-frequency pulsed transcranial electrical stimulation for modulation of cortical plasticity based on reciprocity targeting with precision electrical head modeling,” *Frontiers in Human Neuroscience*, vol. 10, 2016.
- [120] J. P. Dmochowski, L. Koessler, L. C. Parra, M. Bikson, and A. M. Norcia, “Targeted electrical stimulation of active brain sources using reciprocity,” *bioRxiv*, pp. 1–13, 2016.
- [121] M. L. Joy, “Mr current density and conductivity imaging: the state of the art,” in *Engineering in Medicine and Biology Society, 2004. IEMBS’04. 26th Annual International Conference of the IEEE*, vol. 2. IEEE, 2004, pp. 5315–5319.
- [122] G. Ruffini, J. Marco, and C. Grau, “Spherical harmonics interpolation, computation of laplacians and gauge theory,” *arXiv preprint physics/0206007*, 2002.

- [123] C.-T. Tai, “Complementary reciprocity theorems in electromagnetic theory,” *IEEE Transactions on Antennas and Propagation*, vol. 40, no. 6, pp. 675–681, 1992.
- [124] P. C. Miranda, A. Mekonnen, R. Salvador, and P. J. Basser, “Predicting the electric field distribution in the brain for the treatment of glioblastoma,” *Physics in medicine and biology*, vol. 59, no. 15, p. 4137, 2014.
- [125] G. H. Klem, H. O. Lüders, H. Jasper, C. Elger *et al.*, “The ten-twenty electrode system of the international federation,” *Electroencephalogr Clin Neurophysiol*, vol. 52, no. 3, pp. 3–6, 1999.
- [126] M. A. Nitsche, S. Doemkes, T. Karakoese, A. Antal, D. Liebetanz, N. Lang, F. Tergau, and W. Paulus, “Shaping the effects of transcranial direct current stimulation of the human motor cortex,” *Journal of neurophysiology*, vol. 97, no. 4, pp. 3109–3117, 2007.
- [127] A. Antal, T. Z. Kincses, M. A. Nitsche, and W. Paulus, “Manipulation of phosphene thresholds by transcranial direct current stimulation in man,” *Experimental brain research*, vol. 150, no. 3, pp. 375–378, 2003.
- [128] T. Z. Kincses, A. Antal, M. A. Nitsche, O. Bártfai, and W. Paulus, “Facilitation of probabilistic classification learning by transcranial direct current stimulation of the prefrontal cortex in the human,” *Neuropsychologia*, vol. 42, no. 1, pp. 113–117, 2004.
- [129] K. Matsunaga, M. A. Nitsche, S. Tsuji, and J. C. Rothwell, “Effect of transcranial dc sensorimotor cortex stimulation on somatosensory evoked potentials in humans,” *Clinical Neurophysiology*, vol. 115, no. 2, pp. 456–460, 2004.
- [130] R. J. Sadleir, T. D. Vannorsdall, D. J. Schretlen, and B. Gordon, “Target optimization in transcranial direct current stimulation,” *Frontiers in psychiatry*, vol. 3, pp. 1–13, 2012.

- [131] R. D. Fields, “White matter matters,” *Scientific American*, vol. 298, no. 3, pp. 54–61, 2008.
- [132] S. R. Atefi, F. Seoane, and K. Lindecrantz, “Electrical bioimpedance cerebral monitoring. preliminary results from measurements on stroke patients,” in *Engineering in Medicine and Biology Society (EMBC), 2012 Annual International Conference of the IEEE*. IEEE, 2012, pp. 126–129.
- [133] S. R. Atefi, F. Seoane, T. Thorlin, and K. Lindecrantz, “Stroke damage detection using classification trees on electrical bioimpedance cerebral spectroscopy measurements,” *Sensors*, vol. 13, no. 8, pp. 10 074–10 086, 2013.
- [134] D. S. Holder, *Electrical impedance tomography: methods, history and applications*. CRC Press, 2004.
- [135] T. Tidswell, A. Gibson, R. H. Bayford, and D. S. Holder, “Three-dimensional electrical impedance tomography of human brain activity,” *NeuroImage*, vol. 13, no. 2, pp. 283–294, 2001.
- [136] R. Salvador, F. Ramirez, M. V’yacheslavovna, and P. Miranda, “Effects of tissue dielectric properties on the electric field induced in tdc: a sensitivity analysis,” in *Engineering in Medicine and Biology Society (EMBC), 2012 Annual International Conference of the IEEE*. IEEE, 2012, pp. 787–790.
- [137] A. Opitz, W. Paulus, S. Will, A. Antunes, and A. Thielscher, “Determinants of the electric field during transcranial direct current stimulation,” *Neuroimage*, vol. 109, pp. 140–150, 2015.
- [138] “Spherical polar coordinate graph,” http://en.citizendium.org/images/2/2f/Spherical_polar.png, accessed: 2017-12-25.

- [139] P. C. Miranda, A. Mekonnen, R. Salvador, and G. Ruffini, “The electric field in the cortex during transcranial current stimulation,” *NeuroImage*, vol. 70, no. 0, pp. 48 – 58, 2013. [Online]. Available: <http://www.sciencedirect.com/science/article/pii/S1053811912012190>
- [140] C.-H. Im, H.-H. Jung, J.-D. Choi, S. Y. Lee, and K.-Y. Jung, “Determination of optimal electrode positions for transcranial direct current stimulation (tdcs),” *Physics in medicine and biology*, vol. 53, no. 11, pp. 219–225, 2008.
- [141] A. Datta, M. Elwassif, F. Battaglia, and M. Bikson, “Transcranial current stimulation focality using disc and ring electrode configurations: Fem analysis,” *Journal of neural engineering*, vol. 5, no. 2, p. 163, 2008.
- [142] C. Gabriel, “Compilation of the dielectric properties of body tissues at rf and microwave frequencies.” KING’S COLL LONDON (UNITED KINGDOM) DEPT OF PHYSICS, Tech. Rep., 1996.
- [143] P. Dimbylow, “The development of realistic voxel phantoms for electromagnetic field dosimetry,” in *Proc. Workshop on Voxel Phantom Development, Chilton, UK, 1996*, 1996, pp. 1–7.
- [144] H. P. Schwan, “Electrical properties of tissue and cell suspensions,” in *Advances in biological and medical physics*. Elsevier, 1957, vol. 5, pp. 147–209.
- [145] H. P. Schwan and K. R. Foster, “Rf-field interactions with biological systems: electrical properties and biophysical mechanisms,” *Proceedings of the IEEE*, vol. 68, no. 1, pp. 104–113, 1980.
- [146] R. Pethig, “Dielectric properties of biological materials: Biophysical and medical applications,” *IEEE Transactions on Electrical Insulation*, no. 5, pp. 453–474, 1984.

- [147] R. Pethig and D. B. Kell, “The passive electrical properties of biological systems: their significance in physiology, biophysics and biotechnology,” *Physics in medicine and biology*, vol. 32, no. 8, p. 933, 1987.
- [148] K. Foster and H. Schwan, “Dielectric properties of tissues and biological materials: a critical review, crc crit,” *Rev. Biomed. Eng*, vol. 17, pp. 25–104, 1989.
- [149] M. Stuchly and S. Stuchly, “Dielectric properties of biological substances tabulated,” *Journal of Microwave Power*, vol. 15, no. 1, pp. 19–25, 1980.
- [150] P. Hasgall, F. D. Gennaro, C. Baumgartner, E. Neufeld, M. Gosselin, D. Payne, A. Klingebek, and K. N., “Itis database for thermal and electromagnetic parameters of biological tissues, version 3.0,” www.itis.ethz.ch/database DOI: 10.13099/VIP21000-03-0., 2015-09-01 (accessed on 2016-08-18).
- [151] L. Horesh, “Some novel approaches in modelling and image reconstruction for multi frequency electrical impedance tomography of the human brain,” *University of London, PhD Thesis*, 2006.
- [152] *Field Variables and Scalar Variables*, the Comsol Multiphysics User Guide p. 149 2018.
- [153] H. S. Suh, S. H. Kim, W. H. Lee, and T.-S. Kim, “Realistic simulation of transcranial direct current stimulation via 3-d high-resolution finite element analysis: effect of tissue anisotropy,” in *Engineering in Medicine and Biology Society, 2009. EMBC 2009. Annual International Conference of the IEEE*. IEEE, 2009, pp. 638–641.
- [154] P. Høyum, H. Kalvøy, Ø. G. Martinsen, and S. Grimnes, “A finite element model of needle electrode spatial sensitivity,” *Physiological measurement*, vol. 31, no. 10, pp. 1369–1379, 2010.

- [155] M. Bolton, L. Ward, A. Khan, I. Campbell, P. Nightingale, O. Dewit, and M. Elia, “Sources of error in bioimpedance spectroscopy,” *Physiological measurement*, vol. 19, no. 2, p. 235, 1998.
- [156] H. Scharfetter, P. Hartinger, H. Hinghofer-Szalkay, and H. Hutten, “A model of artefacts produced by stray capacitance during whole body or segmental bioimpedance spectroscopy,” *Physiological measurement*, vol. 19, no. 2, p. 247, 1998.
- [157] T. J. Freeborn, B. Maundy, and A. S. Elwakil, “Extracting the parameters of the double-dispersion cole bioimpedance model from magnitude response measurements,” *Medical & biological engineering & computing*, vol. 52, no. 9, pp. 749–758, 2014.
- [158] I. Nejadgholi and M. Bolic, “A comparative study of pca, simca and cole model for classification of bioimpedance spectroscopy measurements,” *Computers in biology and medicine*, vol. 63, pp. 42–51, 2015.
- [159] L. A. Levin, “One way functions and pseudorandom generators,” *Combinatorica*, vol. 7, no. 4, pp. 357–363, 1987.
- [160] Y. Hattori, A. Moriwaki, and Y. Hori, “Biphasic effects of polarizing current on adenosine-sensitive generation of cyclic amp in rat cerebral cortex,” *Neuroscience letters*, vol. 116, no. 3, pp. 320–324, 1990.
- [161] A. Moriwaki, “Polarizing currents increase noradrenaline-elicited accumulation of cyclic amp in rat cerebral cortex,” *Brain research*, vol. 544, no. 2, pp. 248–252, 1991.
- [162] P. C. Miranda, M. Lomarev, and M. Hallett, “Modeling the current distribution during transcranial direct current stimulation,” *Clinical Neurophysiology*, vol. 117, no. 7, pp. 1623–1629, 2006.
- [163] K.-A. Ho, J. L. Taylor, T. Chew, V. Gálvez, A. Alonzo, S. Bai, S. Dokos, and C. K. Loo, “The effect of transcranial direct current stimulation (tdcs) electrode size and current

- intensity on motor cortical excitability: evidence from single and repeated sessions,” *Brain Stimulation: Basic, Translational, and Clinical Research in Neuromodulation*, vol. 9, no. 1, pp. 1–7, 2016.
- [164] A. F. DaSilva, M. S. Volz, M. Bikson, and F. Fregni, “Electrode positioning and montage in transcranial direct current stimulation,” *Journal of visualized experiments: JoVE*, no. 51, 2011.
- [165] P. Minhas, M. Bikson, A. J. Woods, A. R. Rosen, and S. K. Kessler, “Transcranial direct current stimulation in pediatric brain: a computational modeling study,” in *Engineering in Medicine and Biology Society (EMBC), 2012 Annual International Conference of the IEEE*. IEEE, 2012, pp. 859–862.
- [166] P. C. Miranda, P. Faria, and M. Hallett, “What does the ratio of injected current to electrode area tell us about current density in the brain during tdcS?” *Clinical Neurophysiology*, vol. 120, no. 6, pp. 1183–1187, 2009.
- [167] T. Neuling, S. Wagner, C. H. Wolters, T. Zaehle, and C. S. Herrmann, “Finite-element model predicts current density distribution for clinical applications of tdcS and tacs,” *Frontiers in psychiatry*, vol. 3, pp. 83–93, 2012.
- [168] H. Helmholtz, “Ueber einige gesetze der vertheilung elektrischer ströme in körperlichen leitern mit anwendung auf die thierisch-elektrischen versuch,” *Ann. Physik und Chemie*, vol. 89:, pp. 211–233, 1853.
- [169] J. Malmivuo and R. Plonsey, *Bioelectromagnetism: principles and applications of bioelectric and biomagnetic fields*. Oxford University Press, 1995.
- [170] R. MCFEE and F. D. JOHNSTON, “Electrocardiographic leads i. introduction,” *Circulation*, vol. 8, no. 4, pp. 554–568, 1953.

- [171] J. Lehr, “A vector derivation useful in impedance plethysmographic field calculations,” *IEEE Transactions on Biomedical Engineering*, no. 2, pp. 156–157, 1972.
- [172] E. R. Larson, M. D. Feldman, J. W. Valvano, and J. A. Pearce, “Analysis of the spatial sensitivity of conductance/admittance catheter ventricular volume estimation,” *Biomedical Engineering, IEEE Transactions on*, vol. 60, no. 8, pp. 2316–2324, 2013.
- [173] Ø. G. Martinsen and S. Grimnes, “The concept of transfer impedance in bioimpedance measurements,” in *4th European Conference of the International Federation for Medical and Biological Engineering*. Springer, 2009, pp. 1078–1079.
- [174] W. Frei, “Solutions to linear systems of equations: Direct and iterative solvers,” <https://www.comsol.com/blogs/solutions-linear-systems-equations-direct-iterative-solvers/>, 2013-11-13 (accessed on 2018-01-22).
- [175] “MUMPS: A parallel sparse direct solver,” mumps.enseeiht.fr, 2017-10 (accessed on 2018-01-22).
- [176] P. R. Amestoy, A. Guermouche, J.-Y. L’Excellent, and S. Pralet, “Hybrid scheduling for the parallel solution of linear systems,” *Parallel computing*, vol. 32, no. 2, pp. 136–156, 2006.
- [177] P. R. Amestoy, I. S. Duff, J.-Y. L’Excellent, and J. Koster, “A fully asynchronous multifrontal solver using distributed dynamic scheduling,” *SIAM Journal on Matrix Analysis and Applications*, vol. 23, no. 1, pp. 15–41, 2001.
- [178] “PARDISO 6.1.0: Solver project (january 2018),” www.pardiso-project.org, (accessed on 2018-01-22).
- [179] C. G. Petra, O. Schenk, M. Lubin, and K. Gärtner, “An augmented incomplete factorization approach for computing the schur complement in stochastic optimization,” *SIAM Journal on Scientific Computing*, vol. 36, no. 2, pp. C139–C162, 2014.

- [180] C. G. Petra, O. Schenk, and M. Anitescu, “Real-time stochastic optimization of complex energy systems on high-performance computers,” *IEEE Computing in Science & Engineering*, vol. 16, no. 5, pp. 32–42, 2014.
- [181] “SPOOLES 2.2: Sparse object oriented linear equations solver,” www.netlib.org/linalg/spooles/spooles.2.2.html, (accessed on 2018-01-22).
- [182] E. W. Weisstein, “Lu decomposition,” From Mathworld—A Wolfram Web Resource.<http://mathworld.wolfram.com/LUDecomposition.html>, (accessed on 2018-01-22).
- [183] N. Jamil, “A comparison of direct and indirect solvers for linear systems of equations,” *International Journal of Emerging Sciences*, vol. 2, no. 2, pp. 310–321, 2012.
- [184] “Conjugate gradient method,” From Mathworld—A Wolfram Web Resource.<http://mathworld.wolfram.com/ConjugateGradientMethod.html>, (accessed on 2018-02-03).
- [185] A. M. Bruaset, *A survey of preconditioned iterative methods*. CRC Press, 1995, vol. 328.
- [186] H. A. Van der Vorst, “Bi-cgstab: A fast and smoothly converging variant of bi-cg for the solution of nonsymmetric linear systems,” *SIAM Journal on scientific and Statistical Computing*, vol. 13, no. 2, pp. 631–644, 1992.
- [187] Y. Saad and M. H. Schultz, “Gmres: A generalized minimal residual algorithm for solving nonsymmetric linear systems,” *SIAM Journal on scientific and statistical computing*, vol. 7, no. 3, pp. 856–869, 1986.
- [188] R. Barrett, M. W. Berry, T. F. Chan, J. Demmel, J. Donato, J. Dongarra, V. Eijkhout, R. Pozo, C. Romine, and H. Van der Vorst, *Templates for the solution of linear systems: building blocks for iterative methods*. Siam, 1994, vol. 43.

- [189] S. M. N. Black, “Generalized minimal residual method,” From Mathworld—A Wolfram Web Resource. <http://mathworld.wolfram.com/GeneralizedMinimalResidualMethod.html>, (accessed on 2018-02-03).
- [190] H. Yserentant, “Hierarchical bases give conjugate gradient type methods a multigrid speed of convergence,” *Applied Mathematics and Computation*, vol. 19, no. 1-4, pp. 347–358, 1986.
- [191] V. Marra, “On solvers: Multigrid methods,” From Comsol <https://www.comsol.com/blogs/on-solvers-multigrid-methods/>, (accessed on 2018-02-03).
- [192] —, “On solvers: The v cycle multigrid,” From Comsol <https://www.comsol.com/blogs/on-solvers-v-cycle-multigrid/>, (accessed on 2018-02-03).
- [193] K. Stüben, “A review of algebraic multigrid,” in *Partial Differential Equations*. Elsevier, 2001, pp. 281–309.
- [194] J. Malmivuo and R. Plonsey, *Bioelectromagnetism: principles and applications of bioelectric and biomagnetic fields*. Oxford University Press, USA, 1995.
- [195] S. Grimnes and Ø. G. Martinsen, “Sources of error in tetrapolar impedance measurements on biomaterials and other ionic conductors,” *Journal of Physics D: Applied Physics*, vol. 40, no. 1, pp. 9–14, 2006.
- [196] D. C. Baird and J. A. Simpson, “Experimentation: an introduction to measurement theory and experimental design,” *Physics Today*, vol. 15, 1962.
- [197] R. A. Fisher, “Statistical methods for research workers,” in *Breakthroughs in statistics*. Springer, 1992, pp. 66–70.

- [198] M. G. Kendall *et al.*, “The advanced theory of statistics.” *The advanced theory of statistics.*, no. 2nd Ed, 1946.
- [199] H. P. Zaveri, R. B. Duckrow, and S. S. Spencer, “On the use of bipolar montages for time-series analysis of intracranial electroencephalograms,” *Clinical neurophysiology*, vol. 117, no. 9, pp. 2102–2108, 2006.
- [200] E. Urrestarazu, J. Iriarte, M. Alegre, M. Valencia, C. Viteri, and J. Artieda, “Independent component analysis removing artifacts in ictal recordings,” *Epilepsia*, vol. 45, no. 9, pp. 1071–1078, 2004.
- [201] P. Nasser, M. A. Nitsche, and H. Ekhtiari, “A framework for categorizing electrode montages in transcranial direct current stimulation,” *Frontiers in human neuroscience*, vol. 9, pp. 1–5, 2015.
- [202] A. Antal and W. Paulus, “Transcranial alternating current stimulation (tacs),” *Frontiers in human neuroscience*, vol. 7, pp. 1–4, 2013.
- [203] J. Jossinet and G. Kardous, “Physical study of the sensitivity distribution in multi-electrode systems,” *Clinical Physics and Physiological Measurement*, vol. 8, no. 4A, 1987.
- [204] K. Wendel, N. G. Narra, M. Hannula, P. Kauppinen, and J. Malmivuo, “The influence of csf on eeg sensitivity distributions of multilayered head models,” *IEEE Transactions on Biomedical Engineering*, vol. 55, no. 4, pp. 1454–1456, 2008.
- [205] U. Birgersson, E. Birgersson, P. Åberg, I. Nicander, and S. Ollmar, “Non-invasive bioimpedance of intact skin: mathematical modeling and experiments,” *Physiological measurement*, vol. 32, no. 1, pp. 1–18, 2010.
- [206] Y. Huang and L. C. Parra, “Can transcranial electric stimulation with multiple electrodes reach deep targets?” *bioRxiv*, pp. 1–19, 2018.

- [207] A. Ragheb, L. Geddes, J. Bourland, and W. Tacker, “Tetrapolar electrode system for measuring physiological events by impedance,” *Medical and Biological Engineering and Computing*, vol. 30, no. 1, pp. 115–117, 1992.
- [208] B. Brown, A. Wilson, and P. Bertemes-Filho, “Bipolar and tetrapolar transfer impedance measurements from volume conductor,” *Electronics Letters*, vol. 36, no. 25, p. 1, 2000.
- [209] Y. Mahajan and G. McArthur, “Does combing the scalp reduce scalp electrode impedances?” *Journal of neuroscience methods*, vol. 188, no. 2, pp. 287–289, 2010.
- [210] M. F. Villamar, P. Wivatvongvana, J. Patumanond, M. Bikson, D. Q. Truong, A. Datta, and F. Fregni, “Focal modulation of the primary motor cortex in fibromyalgia using 4×1 -ring high-definition transcranial direct current stimulation (hd-tDCS): immediate and delayed analgesic effects of cathodal and anodal stimulation,” *The Journal of Pain*, vol. 14, no. 4, pp. 371–383, 2013.
- [211] N. Grossman, D. Bono, N. Dedic, S. B. Kodandaramaiah, A. Rudenko, H.-J. Suk, A. M. Cassara, E. Neufeld, N. Kuster, L.-H. Tsai *et al.*, “Noninvasive deep brain stimulation via temporally interfering electric fields,” *Cell*, vol. 169, no. 6, pp. 1029–1041, 2017.
- [212] M. Vöröslakos, Y. Takeuchi, K. Brinyiczki, T. Zombori, A. Oliva, A. Fernández-Ruiz, G. Kozák, Z. T. Kincses, B. Iványi, G. Buzsáki *et al.*, “Direct effects of transcranial electric stimulation on brain circuits in rats and humans,” *Nature communications*, vol. 9, no. 1, pp. 1–17, 2018.
- [213] O. Seibt, A. R. Brunoni, Y. Huang, and M. Bikson, “The pursuit of dlPFC: non-neuronavigated methods to target the left dorsolateral pre-frontal cortex with symmetric bicephalic transcranial direct current stimulation (tDCS),” *Brain stimulation*, vol. 8, no. 3, pp. 590–602, 2015.

- [214] P. S. Boggio, S. Zaghi, A. B. Villani, S. Fecteau, A. Pascual-Leone, and F. Fregni, “Modulation of risk-taking in marijuana users by transcranial direct current stimulation (tdcs) of the dorsolateral prefrontal cortex (dlpfc),” *Drug and alcohol dependence*, vol. 112, no. 3, pp. 220–225, 2010.
- [215] S. Roizenblatt, F. Fregni, R. Gimenez, T. Wetzel, S. P. Rigonatti, S. Tufik, P. S. Boggio, and A. C. Valle, “Site-specific effects of transcranial direct current stimulation on sleep and pain in fibromyalgia: A randomized, sham-controlled study,” *Pain Practice*, vol. 7, no. 4, pp. 297–306, 2007.
- [216] C. Hahn, J. Rice, S. Macuff, P. Minhas, A. Rahman, and M. Bikson, “Methods for extra-low voltage transcranial direct current stimulation: current and time dependent impedance decreases,” *Clinical Neurophysiology*, vol. 124, no. 3, pp. 551–556, 2013.
- [217] P. Kauppinen, J. Hyttinen, and J. Malmivuo, “Sensitivity distribution simulations of impedance tomography electrode combinations,” in *BEM & NFSI Conference Proceedings*, vol. 7, no. 1, 2005, pp. 344–347.
- [218] K. S. Cole, “Permeability and impermeability of cell membranes for ions,” in *Cold Spring Harbor Symposia on Quantitative Biology*. Cold Spring Harbor Laboratory Press, 1940, vol. 8, pp. 110–122.
- [219] S. Grimnes and O. G. Martinsen, “Cole electrical impedance model—a critique and an alternative,” *IEEE transactions on biomedical engineering*, vol. 52, no. 1, pp. 132–135, 2005.
- [220] O. G. Martinsen and S. Grimnes, *Bioimpedance and bioelectricity basics*, 2011.
- [221] L. Nazareth, “A relationship between the bfgs and conjugate gradient algorithms and its implications for new algorithms,” *SIAM Journal on Numerical Analysis*, vol. 16, no. 5, pp. 794–800, 1979.

- [222] Z. W. Geem, "Parameter estimation for the nonlinear muskingum model using the bfgs technique," *Journal of irrigation and drainage engineering*, vol. 132, no. 5, pp. 474–478, 2006.
- [223] A. Geletu, "Solving optimization problems using the matlab optimization toolbox-a tutorial," *TU-Ilmenau, Fakultät für Mathematik und Naturwissenschaften*, 2007.
- [224] Mathworks, *Unconstrained Nonlinear Optimization Algorithms*, 2018 (accessed December 17, 2018), <http://www.mathworks.com/help/optim/ug/unconstrained-nonlinear-optimization-algorithms.html#brnpcye>.
- [225] H. Hsu and P. A. Lachenbruch, "Paired t test," *Wiley StatsRef: Statistics Reference Online*, 2014.
- [226] M. D. Van Loan, P. Withers, J. Matthie, and P. L. Mayclin, "Use of bioimpedance spectroscopy to determine extracellular fluid, intracellular fluid, total body water, and fat-free mass," in *Human body composition*. Springer, 1993, pp. 67–70.
- [227] D. Smith Jr, M. Johnson, and T. Nagy, "Precision and accuracy of bioimpedance spectroscopy for determination of in vivo body composition in rats," *International journal of body composition research*, vol. 7, no. 1, p. 21, 2009.
- [228] C. Tronstad and A. H. Pripp, "Statistical methods for bioimpedance analysis," *Journal of Electrical Bioimpedance*, vol. 5, no. 1, pp. 14–27, 2014.
- [229] J. Nyström, B. Lindholm-Sethson, L. Stenberg, S. Ollmar, J. W. Eriksson, and P. Geladi, "Combined near-infrared spectroscopy and multifrequency bio-impedance investigation of skin alterations in diabetes patients based on multivariate analyses," *Medical and Biological Engineering and Computing*, vol. 41, no. 3, pp. 324–329, 2003.

- [230] T. Zagar and D. Krizaj, “Multivariate analysis of electrical impedance spectra for relaxed and contracted skeletal muscle,” *Physiological measurement*, vol. 29, no. 6, p. S365, 2008.
- [231] H.-R. Tränkler, O. Kanoun, M. Min, and M. Rist, “Smart sensor systems using impedance spectroscopy,” *Proc. Estonian Acad. Sci. Eng*, vol. 13, no. 4, pp. 455–478, 2007.
- [232] I. Bodén, J. Nyström, P. Geladi, P. Naredi, and B. Lindholm-Sethson, “Nir and skin impedance spectroscopic measurements for studying the effect of coffee and alcohol on skin, and dysplastic naevi,” *Skin research and technology*, vol. 18, no. 4, pp. 486–494, 2012.
- [233] D. Kamat, A. P. Chavan, and P. Patil, “Bio-impedance measurement system for analysis of skin diseases,” *International Journal of Application or Innovation in Engineering & Management*, vol. 3, no. 2, pp. 1–5, 2014.
- [234] J.-H. Park, S. B. Hong, D.-W. Kim, M. Suh, and C.-H. Im, “A novel array-type transcranial direct current stimulation (tdcs) system for accurate focusing on targeted brain areas,” *Magnetics, IEEE Transactions on*, vol. 47, no. 5, pp. 882–885, 2011.
- [235] M. Bikson, A. Datta, and M. Elwassif, “Establishing safety limits for transcranial direct current stimulation,” *Clinical Neurophysiology*, vol. 120, no. 6, pp. 1033–1034, 2009.
- [236] F. Seoane, M. Lu, M. Persson, and K. Lindcrantz, “Electrical bioimpedance cerebral monitoring. a study of the current density distribution and impedance sensitivity maps on a 3d realistic head model,” in *Neural Engineering, 2007. CNE’07. 3rd International IEEE/EMBS Conference on*. IEEE, 2007, pp. 256–260.

- [237] I. Nejadgholi, H. Caytak, M. Bolic, I. Batkin, and S. Shirmohammadi, “Preprocessing and parameterizing bioimpedance spectroscopy measurements by singular value decomposition,” *Physiological measurement*, vol. 36, no. 5, pp. 1–19, 2015.
- [238] C. Brüning, S. Hellweg, S. Dambach, D. Lipinsky, and H. Arlinghaus, “Improving the interpretation of tof-sims measurements on adsorbed proteins using pca,” *Surface and Interface Analysis: An International Journal devoted to the development and application of techniques for the analysis of surfaces, interfaces and thin films*, vol. 38, no. 4, pp. 191–193, 2006.
- [239] A. Datta, X. Zhou, Y. Su, L. C. Parra, and M. Bikson, “Validation of finite element model of transcranial electrical stimulation using scalp potentials: implications for clinical dose,” *Journal of neural engineering*, vol. 10, no. 3, pp. 1–11, 2013.
- [240] M. Bikson, P. Grossman, C. Thomas, A. L. Zannou, J. Jiang, T. Adnan, A. P. Mourdoukoutas, G. Kronberg, D. Truong, P. Boggio *et al.*, “Safety of transcranial direct current stimulation: evidence based update 2016,” *Brain stimulation*, vol. 9, no. 5, pp. 641–661, 2016.
- [241] T. Chanchairujira and R. L. Mehta, “Assessing fluid change in hemodialysis: whole body versus sum of segmental bioimpedance spectroscopy,” *Kidney international*, vol. 60, no. 6, pp. 2337–2342, 2001.
- [242] R. Buendía, P. Bogónez-Franco, L. Nescolarde, and F. Seoane, “Influence of electrode mismatch on cole parameter estimation from total right side electrical bioimpedance spectroscopy measurements,” *Medical engineering & physics*, vol. 34, no. 7, pp. 1024–1028, 2012.
- [243] D. Ayllón, R. Gil-Pita, and F. Seoane, “Detection and classification of measurement errors in bioimpedance spectroscopy,” *PLoS one*, vol. 11, no. 6, pp. 1–19, 2016.

- [244] M. Dittmar, “Reliability and variability of bioimpedance measures in normal adults: effects of age, gender, and body mass,” *American Journal of Physical Anthropology: The Official Publication of the American Association of Physical Anthropologists*, vol. 122, no. 4, pp. 361–370, 2003.
- [245] E. Gualdi-Russo and S. Toselli, “Influence of various factors on the measurement of multifrequency bioimpedance,” *HOMO-Journal of Comparative Human Biology*, vol. 53, no. 1, pp. 1–16, 2002.
- [246] I. Laakso, S. Tanaka, S. Koyama, V. De Santis, and A. Hirata, “Inter-subject variability in electric fields of motor cortical tdc,” *Brain stimulation*, vol. 8, no. 5, pp. 906–913, 2015.
- [247] V. López-Alonso, B. Cheeran, D. Río-Rodríguez, and M. Fernández-del Olmo, “Inter-individual variability in response to non-invasive brain stimulation paradigms,” *Brain stimulation*, vol. 7, no. 3, pp. 372–380, 2014.
- [248] Ø. G. Martinsen, S. Grimnes, and E. Haug, “Measuring depth depends on frequency in electrical skin impedance measurements,” *Skin research and technology*, vol. 5, no. 3, pp. 179–181, 1999.
- [249] T. Yamamoto and Y. Yamamoto, “Electrical properties of the epidermal stratum corneum,” *Medical and biological engineering*, vol. 14, no. 2, pp. 151–158, 1976.
- [250] P. Bogonez-Franco, L. Nescolarde, R. Bragos, J. Rosell-Ferrer, and I. Yandiola, “Measurement errors in multifrequency bioelectrical impedance analyzers with and without impedance electrode mismatch,” *Physiological measurement*, vol. 30, no. 7, p. 573, 2009.
- [251] T. Dai and A. Adler, “Blood impedance characterization from pulsatile measurements,” in *2006 Canadian Conference on Electrical and Computer Engineering*. IEEE, 2006, pp. 983–986.

- [252] R. Aaron, M. Huang, and C. Shiffman, “Anisotropy of human muscle via non-invasive impedance measurements,” *Physics in Medicine & Biology*, vol. 42, no. 7, p. 1245, 1997.
- [253] C. Shiffman, “Adverse effects of near current-electrode placement in non-invasive bio-impedance measurements,” *Physiological measurement*, vol. 34, no. 11, p. 1513, 2013.
- [254] H. Burger and J. Van Milaan, “Measurements of the specific resistance of the human body to direct current,” *Acta Medica Scandinavica*, vol. 114, no. 6, pp. 584–607, 1943.
- [255] J. P. Dmochowski, A. Datta, Y. Huang, J. D. Richardson, M. Bikson, J. Fridriksson, and L. C. Parra, “Targeted transcranial direct current stimulation for rehabilitation after stroke,” *Neuroimage*, vol. 75, pp. 12–19, 2013.
- [256] D. Reato, A. Rahman, M. Bikson, and L. C. Parra, “Effects of weak transcranial alternating current stimulation on brain activity: a review of known mechanisms from animal studies,” *Frontiers in human neuroscience*, vol. 7, pp. 1–8, 2013.
- [257] B. Sanchez, G. Vandersteen, R. Bragos, and J. Schoukens, “Basics of broadband impedance spectroscopy measurements using periodic excitations,” *Measurement Science and Technology*, vol. 23, no. 10, 2012.
- [258] A. V. Peterchev, T. A. Wagner, P. C. Miranda, M. A. Nitsche, W. Paulus, S. H. Lisanby, A. Pascual-Leone, and M. Bikson, “Fundamentals of transcranial electric and magnetic stimulation dose: definition, selection, and reporting practices,” *Brain stimulation*, vol. 5, no. 4, pp. 435–453, 2012.
- [259] W. Paulus, “Transcranial electrical stimulation (tes–tdcs; trns, tacs) methods,” *Neuropsychological rehabilitation*, vol. 21, no. 5, pp. 602–617, 2011.
- [260] B. H. Brown, “Electrical impedance tomography (eit): a review,” *Journal of medical engineering & technology*, vol. 27, no. 3, pp. 97–108, 2003.

- [261] A. Hyvriinen, “Survey on independent component analysis,” *Neural Computing Surveys*, vol. 2, no. 4, pp. 94–128, 1999.
- [262] J.-H. Kim, D.-W. Kim, W. H. Chang, Y.-H. Kim, K. Kim, and C.-H. Im, “Inconsistent outcomes of transcranial direct current stimulation may originate from anatomical differences among individuals: electric field simulation using individual mri data,” *Neuroscience letters*, vol. 564, pp. 6–10, 2014.
- [263] T. Wagner, A. Valero-Cabre, and A. Pascual-Leone, “Noninvasive human brain stimulation,” *Annu. Rev. Biomed. Eng.*, vol. 9, pp. 527–565, 2007.
- [264] I. Nejadgholi, T. Davidson, C. Blais, F. Tremblay, and M. Bolic, “Classification of responders versus non-responders to tdc by analyzing voltage between anode and cathode during treatment session,” in *World Congress on Medical Physics and Biomedical Engineering, June 7-12, 2015, Toronto, Canada*. Springer, 2015, pp. 990–993.
- [265] H. Griffiths, “A cole phantom for eit,” *Physiological measurement*, vol. 16, no. 3A, p. A29, 1995.
- [266] A. Pandya, A. Arimoto, A. Agarwal, and Y. Kinouchi, “A novel approach for measuring electrical impedance tomography for local tissue with artificial intelligent algorithm,” *International Journal of Biometrics and Bioinformatics*, vol. 3, no. 5, pp. 1–16, 2009.